Electrolyte Performance In Proton exchange membrane Fuel Cells

By

Oliver Edward Fernihough

A Thesis submitted to the University of Birmingham
for the degree of
DOCTOR OF PHILOSOPHY

Centre for Fuel Cells and Hydrogen Research
School of Chemical Engineering
College of Engineering and Physical Sciences
University of Birmingham
December 2022

Abstract

This thesis explores the production and performance of polymer electrolyte membranes patterned using Laser Induced Periodic Surface Structures (LIPSS). The study investigates how microscale patterning impacts the hydrophobicity, water management, and overall performance of the membranes in fuel cells. Patterns including flat, lotus, lines, and sharklet were created on steel moulds and transferred to Nafion membranes. Contact angle measurements and scanning electron microscopy (SEM) images confirmed that the patterning significantly increased the hydrophobicity of the membrane surfaces, with the sharklet pattern exhibiting the highest contact angle.

The bulk properties of the patterned membranes were assessed by evaluating ion exchange capacity (IEC), water uptake, and membrane swelling. The results indicated stable IEC across all patterns, while the sharklet pattern demonstrated the best water management, reducing dimensional change without affecting water uptake. Hydrogen crossover measurements revealed that patterns with greater depth exhibited higher crossover currents, suggesting thinner regions in the membrane.

Polarization curve analyses showed that the sharklet pattern achieved the highest power density, with a significant increase at both high and low relative humidity levels. This enhancement was attributed to the larger electrochemical surface area (ECSA) and improved water transport properties, confirmed through cyclic voltammetry and impedance

spectroscopy. The sharklet pattern also maintained lower high-frequency resistance under varied humidity conditions, indicating better ionic conductivity and reduced ohmic losses.

In contrast, the lotus and lines patterns showed increased ohmic resistance and diminished performance under low humidity conditions, highlighting the importance of optimizing pattern feature size and depth. These findings suggest that while patterning can significantly enhance membrane performance, careful design is crucial to avoid adverse effects on functional properties.

In conclusion, this research demonstrates that microscale patterning, particularly the sharklet design, can significantly improve the mechanical and transport properties of polymer electrolyte membranes, leading to sustained fuel cell performance under diverse operational conditions. Future work should focus on refining the pattern designs, ensuring scalability, and assessing the long-term durability of the patterned membranes in practical fuel cell systems.

Additionally, this thesis investigates the performance and modelling of Polymer Electrolyte Fuel Cells (PEFCs) utilizing Nafion 211 membranes under various operational conditions, focusing on elevated temperatures (80ºC, 100ºC, and 120ºC) and relative humidities (40-100%). The research aims to elucidate how these conditions affect fuel cell performance and develop robust models for predicting fuel cell behaviour. Experimental results indicate that while increasing temperature enhances mass transport and mitigates water flooding, it also leads to significant dehydration and reduced ionic conductivity, particularly beyond 100ºC. At higher temperatures, membrane hydration decreases, causing a rise in ohmic resistance and a decline in overall performance.

High-pressure operation significantly enhanced performance by maintaining better

water balance and ensuring adequate oxygen availability. The study extends empirical relationships for water content (lambda, λ) and ionic conductivity to higher temperatures, highlighting the necessity for accurate fitting parameters such as water activity. 1D modelling techniques were employed, showing good agreement with experimental results in the ohmic region of the polarization curve, thus validating their use for pre-emptive design adjustments and operational strategies.

The research also delves into the degradation mechanisms affecting the membranes, identifying the need for developing new materials or modifying existing perfluorosulfonic acid (PFSA) membranes to enhance thermal stability and water retention. The findings emphasize the complex interplay between thermal, mechanical, and chemical degradation pathways and the importance of robust membrane formulations.

The study concludes that while operating Nafion-based fuel cells at higher temperatures offers potential benefits, it also presents significant challenges. Higher operational pressures, necessary to maintain adequate humidity levels and oxygen availability, increase the energy requirements for air pumps and water vaporization. Despite these challenges, the research outlines a clear path forward for advancing PEFC technology through targeted improvements in membrane materials, operational strategies, and predictive modelling. The findings provide a foundation for developing more robust, efficient, and durable PEFC systems, marking a significant step forward in sustainable energy technologies. Further research into high-pressure operational scenarios could unlock new potentials for overcoming current performance limitations in fuel cell technologies.

Lastly, this thesis investigates the performance and modelling of composite graphene oxide Nafion (GO-Nafion) membranes for polymer electrolyte fuel cells (PEFCs) operat-

ing at intermediate temperatures (80-120ºC). The experimental study involved fabricating GO-Nafion membranes via solution casting, incorporating 4 wt% graphene oxide. The performance of these membranes was evaluated using polarization curves and impedance spectra at 80ºC, 100ºC, and 120ºC across various relative humidity levels (40-100%).

The results demonstrated that GO-Nafion membranes enhanced water retention and overall performance at elevated temperatures compared to pure Nafion. However, significant performance degradation occurred at lower relative humidity due to membrane dehydration. At 80ºC, GO-Nafion membranes maintained performance across a wide humidity range, while at 100ºC and 120ºC, performance was more sensitive to humidity changes, with notable declines at lower humidity levels.

Two modelling approaches were developed to predict the performance of the GO-Nafion membranes: a polynomial model based on a rule-of-mixtures approach and a power-law model. The polynomial model accurately predicted performance at 80ºC ($R^2 > 0.96$) and 100ºC ($R^2 > 0.84$) but was less accurate at 120ºC ($R^2 < 0.57$) due to complex dehydration and reactant crossover effects. The power-law model showed reasonable fits across all temperatures but lacked a clear physical basis, limiting its application for full fuel cell modelling.

Incorporating the polynomial model into a single-cell fuel cell model revealed good agreement with experimental data at 80ºC and reasonable fits at 100ºC, though the model overpredicted mass transport resistance at high humidity. At 120ºC, the model struggled to capture performance accurately, particularly at low relative humidity.

Overall, this thesis provides valuable insights into the potential of GO-Nafion membranes for intermediate temperature PEFCs and presents a comprehensive modelling frame-

work. While the polynomial model shows promise for predicting water sorption behaviour and membrane performance, further refinement is needed for higher temperature predictions. Future work should explore advanced water sorption models and comprehensive mass transport effects to enhance predictive accuracy across all temperatures.

Acknowledgements

I want to Acknowledge the help and support of my family and friends during the write up and corrections. It was pivotal in my execution and success.

I would also like to acknowledge all of the people who inspired me with their kind words and those who spent many hours encouraging and supporting me.

Thank you all for your time, without it, I might not have finished this chapter of my life.

Contents

List of Figures

List of Tables

Nomenclature

Abbreviations

- BET: Brunauer – Emmet – Teller
- CFD: Computational Fluid Dynamics
- CHP: Combined Heat and Power
- CL: Catalyst Layer
- DI: Deionized
- DMFC: Direct Methanol Fuel Cell
- DRT: Distributed Relaxation Time
- EC: Equivalent Circuit
- ECSA: Electrochemical Surface Area
- EIS: Electrochemical Impedance Spectroscopy
- GDL: Gas Diffusion Layer
- GO: Graphene Oxide

- GTT: Glass Transition Temperature
- HFR: High Frequency Resistance
- IEC: Ion Exchange Capacity
- IEM: Ion Exchange Membranes
- IMRS: Inverse-Micro-Raman-Spectroscopy
- IPA: Isopropyl Alcohol
- LIPSS: Laser Induced Periodic Surface Structures
- MEA: Membrane Electrode Assembly
- MPL: Microporous Layer
- NSTF: Nanostructured Thin Film
- OCV: Open Circuit Voltage
- ORR: Oxygen Reduction Reaction
- PEFCs: Polymer Electrolyte Fuel Cells
- PEM: Polymer Electrolyte Membrane
- PTFE: Polytetrafluoroethylene
- PVP: Polyvinylpropylene
- RH: Relative Humidity
- SEM: Scanning Electron Microscopy

- TPB: Triple Phase Boundary

Symbols

- A_{Pt}^{eff} [m^2]: Effective area of platinum available in the cathode catalyst layer.
- C_i, C_i^{ref} [mol m^{-3}]: Concentrations and reference concentrations of species i.
- C_{NaOH} [mol L^{-1}]: Concentration of NaOH.
- $C_{H_2}^{\text{an}}, C_{H_2}^{\text{cath}}$ [mol m^{-3}]: Concentration of hydrogen at the anode and cathode.
- $D_{H_2}^{\text{eff}}$ [$m^2 s^{-1}$]: Effective diffusivity of hydrogen.
- D_{jk}^{eff} [$m^2 s^{-1}$]: Effective diffusivity of species j in material k.
- ΔG_f [J mol^{-1}]: Gibbs free energy change of the fuel cell reaction.
- $\Delta H_{combustion}$ [J mol^{-1}]: Enthalpy of combustion.
- ΔT [K]: Temperature Difference.
- E [V]: Cell potential under non-standard conditions.
- E^0 [V]: Standard cell potential.
- e^- [Coulomb]: Electron (charge of a single electron).
- F [C mol^{-1}]: Faraday's constant (≈ 96485 C mol^{-1}).
- $G_{f\text{Products}}, G_{f\text{Reactants}}$ [J mol^{-1}]: Gibbs free energy of products and reactants.
- H_2 : Hydrogen gas.

- H^+ : Proton.
- H_i [Pa m^{3}mol^{-1}]: Henry's law coefficient for species i.
- H_2O : Water.
- i [A m^{-2}]: Current density.
- i_0 [A m^{-2}]: Exchange current density.
- i_{act} [A m^{-2}]: Activation overpotential current.
- i_{CO} [A m^{-2}]: Crossover current due to hydrogen permeation.
- i_{l} [A m^{-2}]: Limiting current density.
- $IM_{O_2}, IM_{H_2}, M_{H_2O}$ [g mol^{-1}]: Molecular weights of oxygen, hydrogen, and water respectively.
- $I_{o,a}, I_{o,c}$ [A m^{-2}]: Reference exchange current density for anode and cathode.
- $\mathbf{N}j$ [mol m^{-2}s^{-1}]: Mass flux of species j.
- O_2 [gas]: Oxygen gas.
- p [Pa]: Pressure.
- p_0 [Pa]: Reference pressure.
- $P_{H_2}, P_{O_2}, P_{H_2O}$ [Pa]: Partial pressures of hydrogen, oxygen, and water.
- R [J mol^{-1}K^{-1}]: Universal gas constant.
- r [Ω]: Internal resistance of the fuel cell.

- S [dimensionless]: Saturation.
- S_j [mol $m^{-3}s^{-1}$]: Source term for species j.
- S_s [mol $m^{-3}s^{-1}$]: Saturation source term.
- T [K]: Temperature.
- T_0 [K]: Reference temperature.
- T_{Wet}, T_{Dry} [m]: Wet and dry thickness respectively.
- t_{dif} [m]: Diffusion thickness.
- V [V]: Cell voltage.
- α_a, α_c [dimensionless]: Anodic and cathodic transfer coefficients.
- ϵ [dimensionless]: Porosity.
- η [V]: Overpotential.
- η_{conc} [V]: Concentration overpotential.
- η_{max} [dimensionless]: Maximum theoretical efficiency of the fuel cell.
- m_{Wet}, m_{Dry} [kg]: Wet and dry mass respectively.
- ϕ_s, ϕ_m [V]: Solid phase potential, membrane phase potential.
- σ [S m^{-1}]: Conductivity.
- $\sigma_s^{eff}, \sigma_m^{eff}$ [S m^{-1}]: Effective electrical conductivity of the solid phase and membrane respectively.

CHAPTER ONE

INTRODUCTION

"Meeting the needs of the current generation without compromising the ability of future generations to meet theirs."

World commission on environment and development, Our Common Future [1]

1.1 Background

The concept of sustainability, as defined in Our Common Future sometimes called the Brundtland Report of 1987, encompasses the responsible management of resources to ensure future generations can meet their needs. This principle has since guided evaluations and improvements across various sectors, including energy, food, and infrastructure, in pursuit of a sustainable future [2].

Sustainability involves the stewardship of "physical capital" (infrastructure like roads and hospitals), "human capital" (knowledge and skills), and "environmental capital" (natural resources and ecosystems). The urgency to address environmental issues has led to global efforts such as life cycle assessments, the Kyoto Protocol, and the Paris 2020 Agreement. Climate change, recognized as a factual concern by 97% of the scientific

community, drives these initiatives [3–7].

To mitigate climate change, various international agreements and national policies have been adopted. The Paris 2020 Agreement, endorsed by the United Nations, sets out a roadmap for countries to reduce greenhouse gas emissions. Japan, for instance, is advancing a hydrogen economy with strategies like domestic micro CHP systems and subsidies for fuel cell vehicles [8, 9]. Notably, China aims to increase its non-fossil energy share to 20% by 2030, while the European Union targets a 40% increase in the same timeframe [10–12]. These policies often focus on reducing CO2 emissions and their carbon footprint, quantifying environmental impact in terms of CO2 equivalents [13]. Despite challenges, renewable energy technologies have seen a steady growth, driven by global sustainable energy policies [14].

1.1.1 History of Fuel Cells

The concept of the fuel cell traces back to Sir William Robert Grove's "gaseous voltaic battery," which combined oxygen and hydrogen using platinum electrodes in a sulfuric acid solution. This invention laid the groundwork for modern fuel cells. Unlike batteries, fuel cells continuously convert fuel to energy as long as the fuel supply is maintained. This technology gained significant public exposure through its use in the Gemini and Apollo space missions, and later in the space shuttle program where they employed Ion Exchange Membranes (IEMs) made of sulfonated polystyrene [15]. This exposure spurred investments from companies like General Motors, leading to the mass-market introduction of fuel cells in vehicles like Toyota's 'Mirai' in 2014 [16].

1.1.2 Fuel Cell Thermodynamics

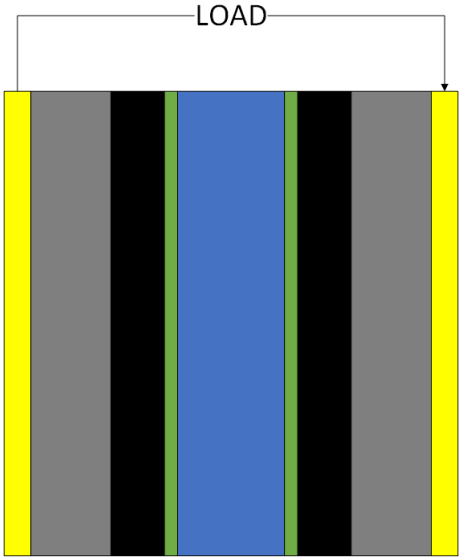

Figure 1.1: Fuel Cell Diagram;
from left to right: Current collectors (yellow), Bipolar plates (grey), Gas diffusion layer (Black), Catalyst Layer (green), Electrolyte (blue), the components are repeated in reverse order on the other side.

A Polymer Electrolyte Membrane (PEM) fuel cell operates as an electrochemical device at low temperatures and offers high efficiency. As shown in Figure 1.1, it comprises essential components like the Gas Diffusion Layer (GDL), catalyst layer, membrane, and bipolar plate. Unlike traditional thermal engines bound by the Carnot efficiency limit, fuel cells directly convert chemical energy into electrical energy, though they are still subject to the limitations of the second law of thermodynamics [17]. PEM fuel cells find applications in various domains, including household CHP systems, transportation, and spacecraft, primarily because their hydrogen fuel generates only water as a byproduct [18].

Hydrogen serves as an energy carrier rather than a primary energy source, necessitating an initial energy input for its production. Although hydrogen has a high energy density per weight (120 MJ kg^{-1}), its volumetric energy density is relatively low (0.01

MJ L^{-1}), highlighting the importance of efficient storage methods, such as high-pressure tanks or metal hydrides [19, 20]. The most common method for hydrogen production is steam methane reforming, which, although widespread, generates carbon dioxide as a byproduct. Alternative, greener methods like water electrolysis exist but face challenges including cell degradation at large scales, and electricity running cost when not coupled with green energy generation. When compared to steam methane reforming the main barrier is cost of generation where electricity can be 3 times more expensive [21].

Current research in fuel cells focuses extensively on materials science, exploring advancements in catalysts, supports, membranes, and bipolar plate materials. To comprehensively assess the performance of new materials, both in situ (within actual operating conditions) and ex situ (under simulated conditions) testing are crucial. Historically, many studies relied on ex situ evaluations, which may not accurately reflect in situ performance.

Fuel cells offer practical efficiencies up to approximately 60%, significantly higher than the maximum 45% efficiency of combustion engines. This high efficiency, coupled with the continuous operation as long as fuel is supplied, positions fuel cells as an attractive energy conversion technology. They also have advantages like quiet operation, minimal vibration, and higher system energy density compared to combustion engines. Despite these benefits, several challenges persist in cost, lack of infrastructure for refueling, hydrogen availability, fuel cell reliability, material development, and large-scale deployment, as exemplified by vehicles like the Toyota Mirai and Hyundai ix35 [22].

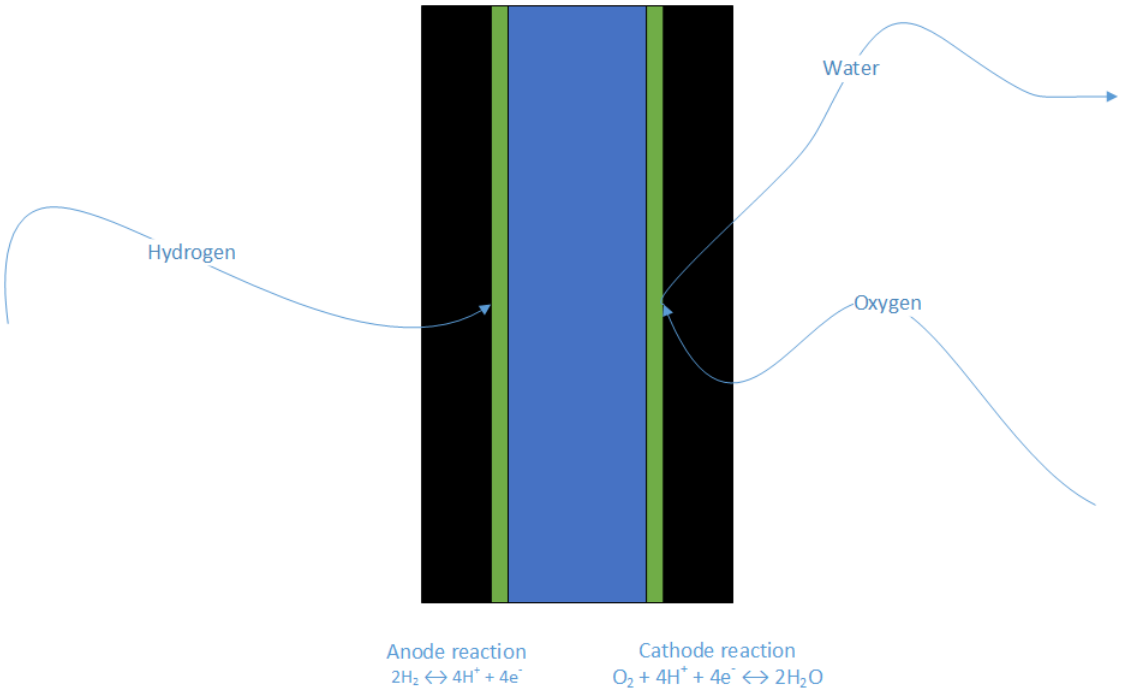

Figure 1.2: Fuel Cell Reaction Diagram; with half cell reactions

1.2 Principals of Polymer Electrolyte Membrane Fuel Cells

In fuel cells, chemical energy is converted into electrical energy through electrochemical processes. The reaction equilibrium is influenced by the external load applied to the fuel cell. Drawing more current drives the reaction forward, facilitating water formation, while supplying current can induce water splitting as the reaction is thermodynamically favourable.

The Open Circuit Voltage (OCV) represents the equilibrium voltage arising from the electrochemical reaction equilibrium. It is the potential observed when no external load is applied. The choice of catalyst critically influences the OCV as it determines the equilibrium potential of the half-cell reactions [23] shown in equations 1.1 and 1.2.

$$2H_2 \rightarrow 4H^+ + 4e^- \tag{1.1}$$

$$O_2 + 4H^+ + 4e^- \rightarrow 2H_2O \tag{1.2}$$

Figure 1.3 illustrates the 'classical split' of internal energy in an exothermic reaction. This demonstrates that a reaction requires a certain energy threshold, termed activation energy, to proceed. While activation energy is typically represented as thermal energy, it remains constant across temperatures. Catalysts can lower the activation energy by altering the reactants' transition state, making the reaction more favourable. In fuel cells, a combination of catalysts, increased electrode area, and elevated temperatures are used to enhance overall efficiency. However, the temperature of low-temperature fuel cells is limited to 120°C or lower due to membrane stability considerations. The efficiency of a fuel cell can be described using the 'Gibbs free energy of formation' for the cell's products—water, in this case—divided by the total internal energy of the reactants. The free energy change for a system, representing the maximum electrical energy available from a given reaction, is defined as follows:

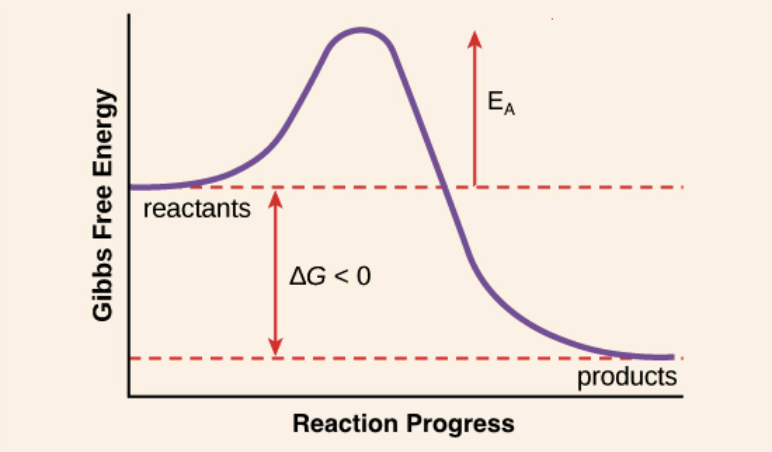

Figure 1.3: Gibbs free energy vs Reaction coordinate, reproduced from [24]

$$\Delta G_f = G_{f\text{Products}} - G_{f\text{Reactants}} \tag{1.3}$$

For a low-temperature fuel cell, the equation is:

$$\Delta G_f = (\bar{G}_f)_{H_2O} - (\bar{G}_f)_{H_2} - 0.5(\bar{G}_f)_{O_2} \tag{1.4}$$

The standard formation free energies for O_2 and H_2 are zero at standard conditions (25°C and 0.01 MPa), making the electrical energy output of a fuel cell proportional to the Gibbs free energy of water formation.

The total energy of a fuel cell system can be defined as the enthalpy of combustion of the reactants to form the products. This definition introduces a discrepancy. Combustion enthalpies can be calculated including the heat of vaporization of water, known as the Higher Heating Value (HHV), or excluding it, referred to as the Lower Heating Value (LHV). Industry typically uses the LHV which results in a seemingly higher efficiency by neglecting the vaporization enthalpy of water. However, for low-temperature fuel cells, the HHV is more appropriate as the product water remains below 100°C and does not vaporize.

$$E^0 = \frac{-\Delta G_f}{2F} \tag{1.5}$$

Equation 1.5 represents the standard potential of a reaction, relating to the Gibbs free energy divided by the number of electrons transferred and Faraday's constant. Where E^0 is the standard potential, and F is Faraday's constant 94685 C mol^{-1}. The maximum thermodynamic efficiency of a fuel cell is given by

$$\eta_{max} = \frac{\Delta G_f}{\Delta H_{combustion}} \tag{1.6}$$

where η_{max} is the efficiency, and $\Delta H_{combusiton}$ is the enthalpy of combustion.

Fuel cells are constrained by the Second Law of Thermodynamics due to irreversibilities. Entropy Generation: Irreversibilities such as Ohmic losses, activation losses, and mass transport losses result in entropy generation and heat dissipation, reducing the practical efficiency.

The Nernst equation describes how concentrations or partial pressures of reactants cause a reduction in voltage

$$E = E^o + \frac{RT}{2F} \ln \left(\frac{P_{H_2} \cdot P_{O_2}^{1/2}}{P_{H_2O}} \right) \tag{1.7}$$

where R is the universal gas constant 8.431 J mol^{-1} K^{-1}, T is the temperature in kelvin, P_{H_2} is the partial pressure of hydrogen, P_{O_2} is the partial pressure of oxygen, and P_{H_2O} is the partial pressure of water. This equation shows that any product formation deviates the open circuit voltage (OCV) from the thermodynamic equilibrium value.

The Nernst potential accounts for losses associated with the redox couple's concentration so it is affected by things such as side reactions, catalyst oxidation, and fuel crossover.

Figure 1.4 demonstrates the polarization curve of a typical PEM fuel cell. As the electrode reactions move away from equilibrium, various loss mechanisms cause a reduction in voltage with increasing current. The curve's shape is defined by activation and kinetic losses at low current densities, ohmic resistance in the mid-range, and mass transport limitations at high current densities.

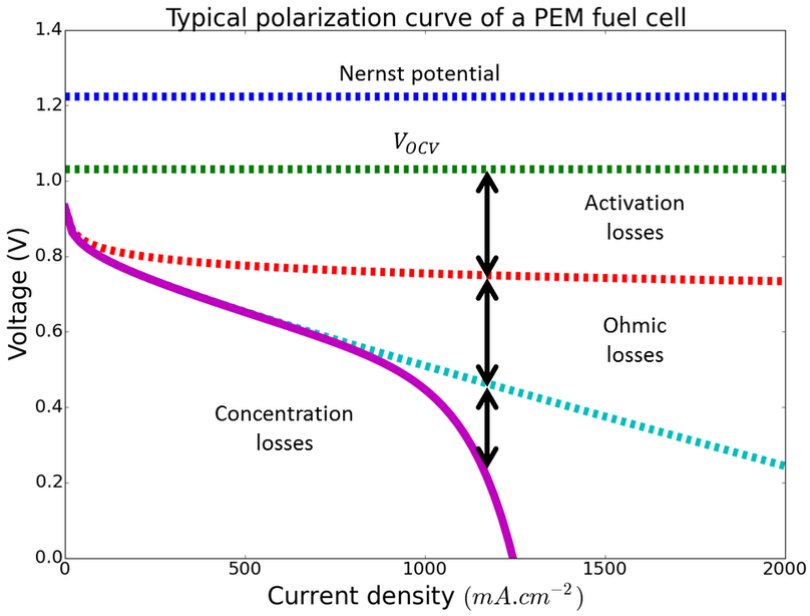

Figure 1.4: Typical PEM Fuel cell polarisation curve, reproduced from [25]

1.3 General Losses associated with Fuel Cells

This section outlines the general losses encountered in fuel cell technology, focusing on issues pertinent to the electrolyte. More detailed discussions on these challenges will be presented in subsequent chapters.

1.3.1 Activation Losses

Activation losses represent the energy required to ensure the completion of each half-cell reaction, predominantly influencing the low current density region. It can be mathematically expressed using the Butler-Volmer equation, given by

$$i_{\text{act}} = i_0 \left(\exp\left(\frac{\alpha_a F \eta}{RT}\right) - \exp\left(-\frac{\alpha_c F \eta}{RT}\right) \right) \tag{1.8}$$

This equation calculates the activation loss current density (i_{act}) from the overpoten-

tial (η), exchange current density (i_0), anodic transfer coefficient (α_a), cathodic transfer coefficient (α_c), Faraday's constant (F), universal gas constant (R), and temperature (T). The exchange current density (i_0) is a measure of the rate at which the electrochemical reaction occurs at equilibrium, reflecting the intrinsic catalytic activity of the electrode for a given reaction.

1.3.2 Hydrogen Crossover

The electrolyte in a fuel cell, typically a Polymer Electrolyte Membrane (PEM), is selected for: its high ionic conductivity, minimal electronic conductivity and barrier to reactants. Hydrogen crossover in PEM fuel cells occurs due to the physical diffusion of hydrogen through the membrane. Influenced by the gas permeability of the electrolyte and the structural properties of the membrane, this diffusion results in hydrogen loss from the anode to the cathode side. As the membrane fills with water, it reduces the ability of the gas to crossover in the free pore space, however hydrogen permeability can be higher than that of dry Nafion due to: (1) increased pore diameter due to membrane swelling, and (2) dissolution of hydrogen in the water absorbed by the membrane, resulting in diffusion through water channels

This loss of fuel reduces the fuel cell's overall efficiency as the crossover hydrogen does not contribute to electricity generation. Additionally, hydrogen crossover contributes to mixed potential losses. The crossover hydrogen prematurely reacts with the oxygen reduction reaction (ORR) at the cathode, decreasing the cell's efficiency. Consequently, the Open Circuit Voltage (OCV) of the fuel cell is lower than expected. The mass flow rate of hydrogen crossover, $\dot{M}_{H_2}$, a critical factor in determining these losses, is given by

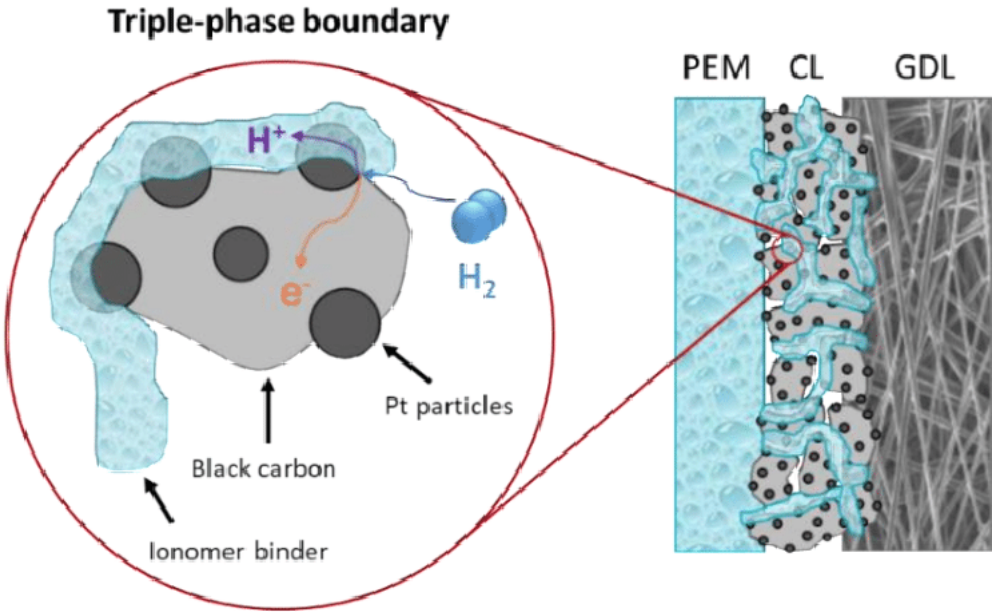

Figure 1.5: Representation of a fuel cell triple phase boundary reproduced from [26]

$$\dot{M}_{H_2} = D_{H_2}^{\text{eff}} \frac{C_{H_2}^{\text{an}} - C_{H_2}^{\text{cath}}}{t_{\text{dif}}} \tag{1.9}$$

where $C_{H_2}^{\text{an}}$ and $C_{H_2}^{\text{cath}}$ are the concentrations of hydrogen at the anode and cathode, respectively, and t_{dif} is the diffusion path length. The crossover current, i_{CO}, resulting from the hydrogen crossover is calculated using Faraday's law:

$$i_{\text{CO}} = \frac{2F \cdot \dot{M}_{H_2}}{M_{\text{H}_2}} \tag{1.10}$$

Here, F is Faraday's constant, and M_{H_2} is the molar mass of hydrogen. This loss of hydrogen due to crossover is a crucial factor in the overall efficiency and performance of PEM fuel cells as it leads to reduced fuel efficiency and increased crossover current.

1.3.3 Electrode Processes and Electrolyte

The triple phase boundary is where electronic conductivity, ionic conductivity, and chemical reaction converge, enabling fresh reactant movement to the catalytic site and product movement through electronic and ionic pathways. Achieving a uniform triple phase boundary distribution is critical for optimal electrolyte and electrode performance. The interfacial resistance between the catalyst layer and electrolyte results from the complex interaction of materials and properties. The electrolyte's thickness and acid content significantly influence its ionic resistance and mechanical properties. Thicker electrolytes offer lower ionic conductivity but are mechanically more robust, while higher acid content increases conductivity but can lead to structural instability.

$$V = ir \tag{1.11}$$

Equation 1.11 describes the performance losses due to membrane resistance, following Ohm's law, where i is the current density, and r is the area-specific resistance.

1.3.4 Mass Transport Losses in Low Temperature Polymer Electrolyte Fuel Cells

Mass transport losses in low temperature polymer electrolyte fuel cells (PEFCs) are a significant factor affecting their performance, particularly at high current densities. These losses are attributed to the limitations in the supply of reactants (hydrogen at the anode and oxygen at the cathode) to the electrochemical reaction sites and the effective removal of products (like water) from these sites.

One of the critical parameters in quantifying mass transport losses is the limiting current density (i_l), which is the maximum current density achievable under the given conditions of reactant supply. The concentration overpotential (η_{conc}) associated with mass transport losses can be described by

$$\eta_{conc} = \frac{RT}{nF} \ln\left(1 - \frac{i}{i_l}\right) \tag{1.12}$$

where R is the universal gas constant, T is the temperature, n is the number of electrons involved in the electrochemical reaction (1 for hydrogen oxidation and 4 for oxygen reduction), F is Faraday's constant, i is the operating current density, and i_l is the limiting current density. This equation highlights how the concentration overpotential increases as the operating current density approaches the limiting current density, indicating a higher degree of mass transport limitation.

It is important to note that the actual values of i_l and η_{conc} are dependent on various factors such as the fuel cell design, operating conditions, and the properties of the membrane electrode assembly (MEA). Therefore, a detailed understanding of these parameters is crucial for optimizing the performance of low temperature PEFCs.

1.4 Overview

This work investigates the improvement of Polymer Electrolyte Fuel Cell (PEFC) performance through various approaches, including membrane patterning, operation at increased temperatures, and the use of composite membranes. The study encompasses both experimental and modeling methodologies to evaluate these strategies.

- Chapter 2 presents a comprehensive literature review on the development of electrolyte membranes, exploring techniques like patterning, intermediate temperatures, and composite materials.

- Chapter 3 details the materials and methods employed in this investigation.

- Chapter 4 details the production of Nafion membranes with patterning of the cathode side using laser induced periodic surface structures (LIPSS) moulds. Membrane patterning is a promising method to increase the current density of fuel cells by improving catalyst utilisation.

- Chapter 5 details the development of a fuel cell model capable of describing the material behaviour of the electrolyte at intermediate temperature ($\leq$ 120°C). It was trained to fuel cell data and used to investigate a range of temperature and humidity conditions, giving a clear picture of the performance.

- Chapter 6 used a similar fuel cell model, but this time to investigate the effect of graphene oxide on the membrane's high-temperature performance. The behaviour of the composite material was described using two different mathematical approaches, using an experimental investigation to confirm the model.

CHAPTER TWO

LITERATURE REVIEW

2.1 Nafion structure

Nafion is a sulfonated tetrafluoroethylene based fluoropolymer-copolymer. Figure 2.1 shows the chemical structure of the repeated units within the Nafion polymer. The backbone (noted between the brackets marked x), is made of repeated units of tetrafluoroethylene a hydrophobic polymer. This backbone is spaced with branches (noted by the brackets marked y); these are similar in chemical structure to the backbone units but have one of the fluorine atoms replaced with an oxygen bond attached to chain of fluorocarbons (noted by the brackets marked z), ending with an oxygen bond to a fluorocarbon chain containing a sulphonic acid group [27, 28]. Nafion was one of the first in a new class of

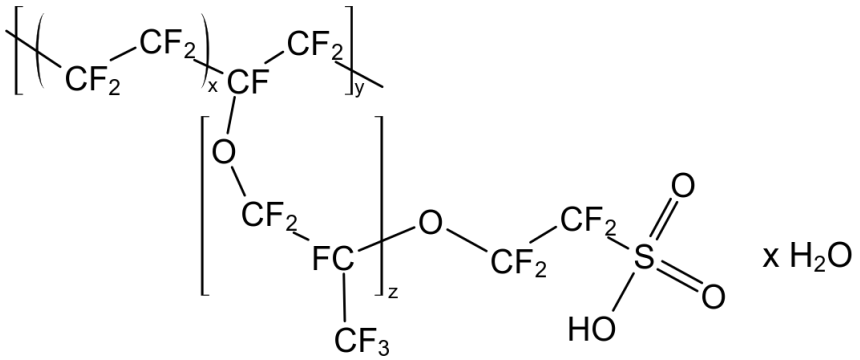

Figure 2.1: Chemical structure of Nafion

polymers called 'ionomers', which have good electrical resistivity but can conduct ions. Nafion also has excellent chemical and mechanical stability, which allowed it to gain significant attention in fuel cells [28]. The ionic conductivity of Nafion is enhanced by the presence of water, the water surrounds the sulphonic acid groups and at critical mass enables the transition from vehicular proton transport to proton hopping (Grotthus transport) [29–32]. The membrane is highly selective to protons.

2.2 History of Electrolyte Development

The Nafion membrane material was developed in the 1960s and first commercialized in the 1990s for fuel cell applications, starting with the 1100 series. These membranes were relatively thick and ranged from 127 to 254 μm, a design requirement to meet expected fuel cell life, echoing the original NASA design [33]. As the 1100 series gained widespread market adoption it underwent extensive study, with both modelling and experimental work focusing on key performance parameters, such as membrane thickness and durability [34, 35]. These membranes were produced via an extrusion casting method, which involved pulling the material through a fixed gap to set the thickness. This manufacturing process offered two primary advantages: first, its simplicity, as extrusion is a common industrial technique; second, the resulting membranes were generally denser compared to those produced by other methods, effectively reducing gas crossover [36].

A significant turning point in membrane development occurred with the rising demand to integrate large, powerful stacks into automotive applications. The primary performance metrics for automotive fuel cell stacks were size, power, and cost. Concurrent advancements in catalysis significantly reduced platinum loading from 4 mg cm^{-2} to

0.4 mg cm^{-2} [37] (1999), which influenced membrane technology. Thinner membranes became feasible through a dispersion casting method known as solution casting [38]. This innovation led to the development of membranes as thin as 50 μm (Nafion 212, 2000) and eventually 25 μm (Nafion 211, 2000). Considering typical automotive stacks comprise around 300 cells, the reduction in membrane thickness offered considerable savings in both weight and cost. Interestingly, these thinner dispersion-cast membranes exhibited a marked increase in conductivity, using the same material, suggesting that the extrusion casting method had previously imposed limitations on proton mobility, consequently affecting conductivity [39].

Recent advancements are focused on creating membranes with thicknesses below 10 μm [40] (2015). However, these ultra-thin membranes pose significant challenges including, compromised mechanical strength, increased fuel crossover, and reduced durability [41]. Nevertheless, the potential for enhanced performance is substantial. Ongoing research explores alternative materials such as Polybenzimidazole (PBI) [42] and blended polymers [43, 44](2011), which might offer thinner yet more robust membranes. Additionally, advancements are being made in three-dimensional electrolyte interface design, including texturing the surface to expand the available triple-phase boundary area [29](2018).

Improving the membrane involves optimizing several key performance indicators: gas crossover, thickness, and operating temperature [45]. Thicker membranes exhibit reduced gas crossover but necessitate a more intricate water balance [46]. This complex balance can lead to performance losses due to membrane drying. Fundamental proton transport mechanisms, vehicular and Grotthus transport, are significantly influenced by hydration

levels [47]. Grotthus transport, involving proton hopping between ionic groups, occurs only under high hydration conditions [29, 31, 48]. In contrast, the vehicular mechanism is prevalent at lower hydration levels but is considerably slower as it relies on the movement of larger hydronium ions. By reducing membrane thickness it is possible to maintain higher hydration levels with less effort due to the efficient movement of water across the membrane facilitated by electro-osmotic drag in proton diffusion. However, thinner membranes present challenges in mechanical strength, particularly in fuel cells operating with pressurized gas streams. During system initiation, the pressure differential can exceed the mechanical strength of Nafion leading to ruptures and the formation of holes. Additionally, durability is influenced by the surface area to volume ratio; radicals attacking the membrane surface can more rapidly form holes in thinner membranes compared to thicker ones.

Gas crossover is closely linked to membrane thickness; a thicker layer or denser structure can inhibit it [49, 50]. However, increased thickness also hinders performance by extending the distance protons must travel [51]. Managing water transport in thicker membranes is a complex task. Enhancing membrane density using fillers or by crosslinking with other polymers can reduce the mean free path for gas transport [52]. Generally, a fully hydrated membrane exhibits lower gas crossover than one that is partially hydrated [36], leading to significant research interest in fillers that can augment the membrane's water content [53, 54].

Operating temperature is predominantly dictated by the material's properties. Nafion remains thermally stable up to 130°C, its glass transition temperature [23, 39]. Beyond this point, the polymer structure becomes susceptible to morphological changes, such as

hole and dendrite formation, theoretically constraining the operating conditions of the membrane. However, considering the need for water incorporation into the membrane structure for proton conductivity, the practical operational temperature limit is further reduced [55]. Typically, 80°C is considered the optimal operating temperature, beyond which water rapidly approaches its vaporisation enthalpy which leads to swift evaporation. The Sorption and Vaporisation enthalpy are critical factors as they indicate the ease of water to become physically associated with the membrane structure and the ease of phase change conditions. Those enthalpies decrease as temperature increases, this is discussed in further detail in section 2.9. Additionally, water vapour sorption and solubility drop as temperature rises because the exothermic sorption process becomes less favourable. Pressurizing gas streams can elevate the boiling point, reducing vapour formation and partially mitigating water transport issues [19]. Alternatively, incorporating fillers to increase water retention within the membrane enables operation at temperatures above 80°C [56], thereby exploiting the advantages of high-temperature operation [29].

This review will focus on key areas of membrane development, including:

- Reinforcement through fibres and fillers
- Utilization of peroxide scavengers
- Texture and patterning of the membrane interface
- Advantages of higher temperature operation
- Polymer electrolyte membrane modelling

2.3 Texturing

Enhancing the performance of fuel cell membranes through surface texturing has been identified as a promising strategy to increase the triple-phase boundary (TPB), thereby improving the efficiency of Membrane Electrode Assemblies (MEAs). Such texturing techniques, which include the introduction of micro- or nano-scale patterns on the membrane surface, offer a direct path to augmenting the active sites available for electrochemical reactions. Nonetheless, the introduction of these textures raises several concerns that warrant careful consideration. First, an increased surface area is believed to heighten the membrane's vulnerability to radical attacks, a phenomenon exacerbated in regions where stagnant flow regimes prevail, thereby facilitating radical formation and subsequent membrane degradation[57]. Moreover, the process of texturing often results in a reduction of membrane thickness, which, while beneficial for enhancing ion transport, may compromise mechanical durability. Additionally, they might inadvertently facilitate shorter pathways for gas crossover through the recesses created by the patterning, potentially impacting the efficiency of the fuel cell by altering the shortest path through the membrane and affecting diffusion processes. These complexities highlight the necessity of a balanced approach in membrane texturing, where the benefits of increased TPB area and enhanced ion transport must be weighed against the potential for increased degradation and reduced mechanical stability.

2.3.1 Nano Structured Catalysts with Electrode Focused Design (3M)

3M developed a nanostructured thin film (NSTF) catalyst layer, significantly reducing platinum loading while enhancing durability. Figure 2.2 shows the structure of the NSTF;

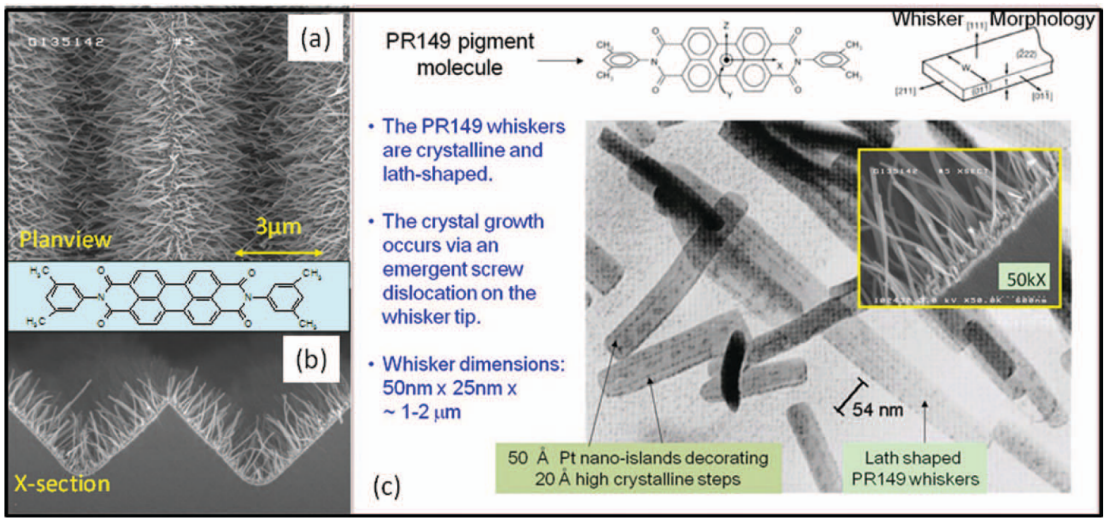

Figure 2.2: NSTF planar and cross-section view from [61]

this innovative material incorporated a sputter-coated platinum layer as its catalyst. Unlike standard MEAs, their design, focusing on high surface area catalyst support, tackled interfacial issues and lead to improved MEA performance. The NSTF featured whisker-like structures, composed of chemically and electronically inert organic materials and backed by a 'Zig Zag' patterned substrate. The catalyst was applied to these whiskers via sputtering, followed by transferring the NSTF to a membrane through a roll-to-roll process. This process led to a slight collapse of the support material but allowed for a thinner catalyst layer [58–61].

Performance comparisons were made against conventional platinum on carbon hot-pressed electrodes. The NSTF electrode, with a lower catalyst loading of 0.15 mg cm^{-2}, demonstrated comparable performance to the 0.4 mg cm^{-2} platinum on carbon electrode. Crucially, the NSTF showed greater resistance to high potential operation ranges, characteristic of startup/shutdown and hydrogen starvation scenarios [58].

Further investigations by the same team focused on the NSTF's response to high current density situations. They used existing research and their results to develop a zero-

dimensional model using physisorption and kinetic gas theory, explaining high current density losses in both standard Pt/C and NSTF catalysts. The model also highlighted how the distinct structure of the catalyst layer and support mitigates significant losses in NSTF [59].

An additional study emphasized the NSTF's lower loading as a key factor in outperforming a hot-pressed MEA with 0.4 mg cm^{-2} loading, particularly under reduced humidity conditions. The NSTF's performance drastically declined with lower humidity, primarily due to its weakened proton conductivity. The NSTF layer, lacking effective water management techniques, dried out and diminished catalyst utilization at the interfacial region. The employed model correlated the NSTF whiskers' proton conductivity with relative humidity, indicating substantial performance losses at reduced humidity and high current densities [60].

In conclusion, the NSTF catalyst layer offers a topographical strategy to enhance fuel cell performance, significantly reducing platinum loading compared to standard MEAs and demonstrating robustness against extreme operational conditions. However, its primary limitation lies in its sensitivity to operation at relative humidities below 100%, which poses challenges at the system level in terms of water and power requirements.

2.3.2 Patterned Membranes

Following the approach in Section2.3.1, various groups have explored altering the cathode side electrode's effective surface area by patterning the membrane. Techniques such as hot hydraulic imprinting and solution casting have been employed to create these patterns. The objective is to augment the TPB, thereby improving catalyst utilization, reactant ac-

cessibility, and water transport, culminating in enhanced fuel cell performance.

Kim et al.[62] demonstrated a 50% increase in fuel cell performance in air using Nafion 212 and a hot hydraulic imprinting method to create an ”asymmetric pattern” shown in figure 2.3. This design reduced membrane resistance, improved water transport, and increased the Electrochemically Active Surface Area (ECSA) of the catalyst. Their usage of 0.12 mg cm^{-2} for both patterned and flat membrane MEAs, along with Scanning Electron Microscopy (SEM) images of the finished catalyst layer, provided insight into the pattern's efficacy. Notably, contact angle measurements indicated a high hydrophobicity of the catalyst layer, potentially aiding in water transport away from the cathode side catalyst layer

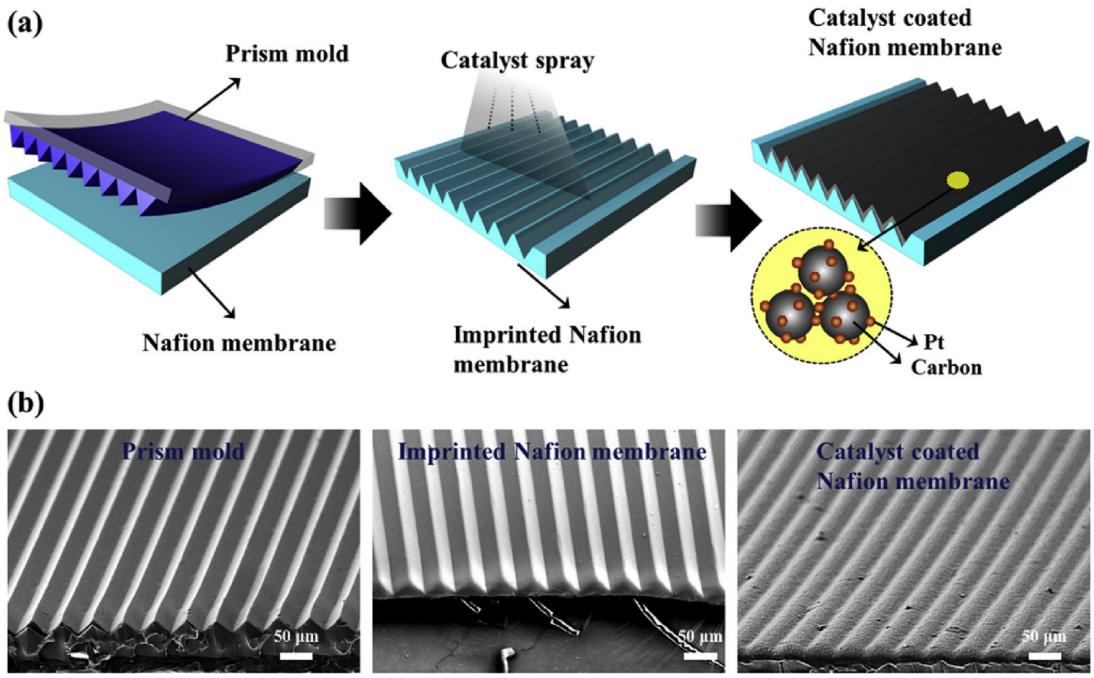

Figure 2.3: Production of asymmetric pattern from [62]

Zhou et al. [63] utilized a poly acrylate film, patterned via soft lithography, to enhance performance. Their work, although focused on methanol fuel cells, demonstrated that cathode side patterning could yield a performance increase of approximately 50%

compared to standard flat arrangements. They investigated various square patterns with differing thicknesses.

Yildirim et al. [64] also employed hot hydraulic imprinting on Nafion 117 for Direct Methanol Fuel Cells (DMFCs) shown in Figure 2.4. Despite achieving good pattern replication, the patterns were compromised during the hot pressing of MEAs as shown in the accompanying SEM images. Consequently, the performance benefits were negated when pattern integrity was lost.

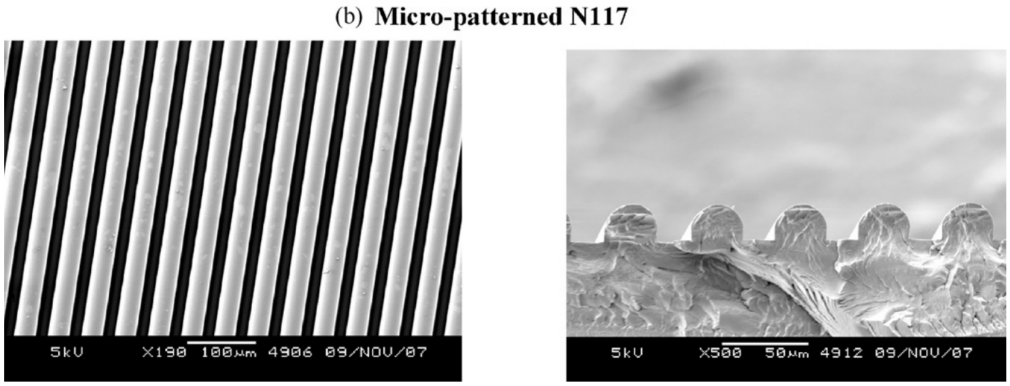

Figure 2.4: Pattern planar and cross-section view from [64]

Omosebi and Besser [51] adopted electron beam patterning to create a master pattern on a silicon wafer, which was then transferred to the Nafion membrane using multi-step lithography. Comparing this patterned membrane with an e-beam exposed and pristine Nafion sheet, they observed enhanced power density performance but increased fuel crossover, attributed to the e-beam's interaction with the Nafion backbone (-CF_2-CF_2- bonds) creating additional surface pores.

Jeon et al. [65] evaluated various highly ordered patterns displaced in figure 2.5, discovering that feature size and shape significantly influenced the catalyst-electrolyte interface layer's operational effectiveness. Their results indicated an impressive 80% power density increase with 0.4 mg cm^{-2} catalyst loading. Additionally, they reported high

power densities of 1555 mW cm^{-2} with a reduced loading of 0.2 mg cm^{-2}.

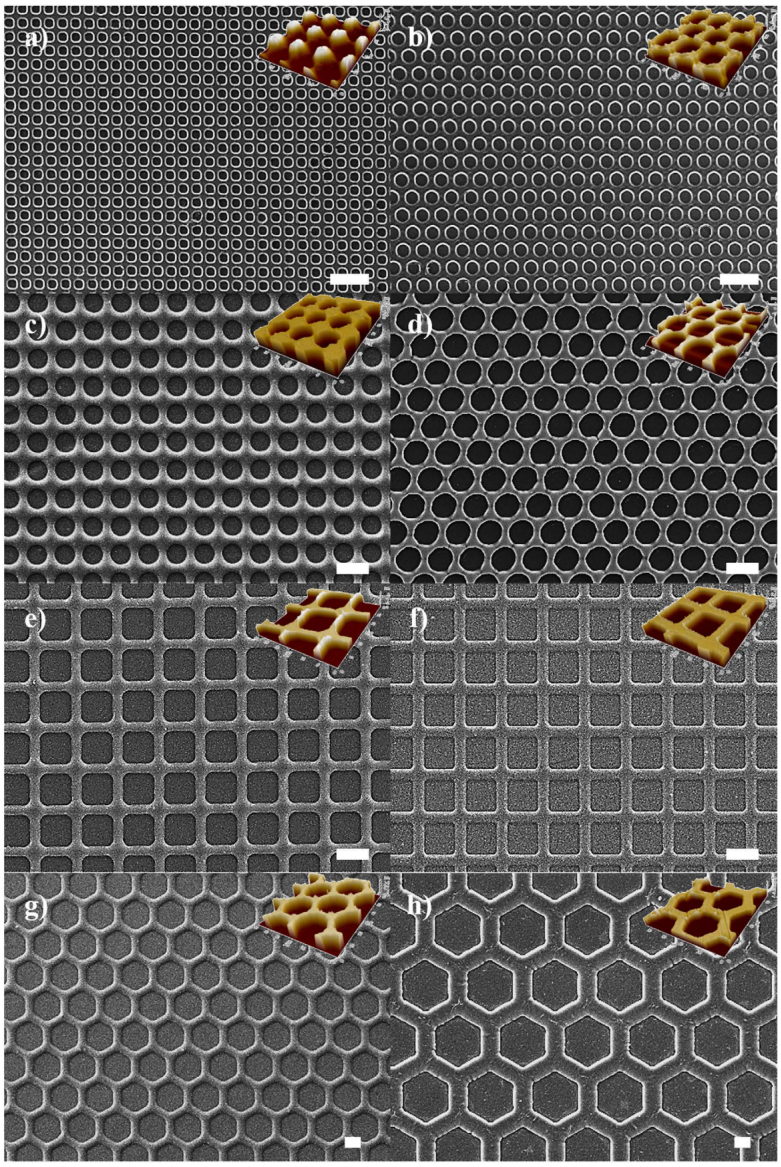

Figure 2.5: planar view of patterns explored by Jeon et al. from [65]

Patterned membranes have been utilized in both direct methanol and hydrogen fuel cells, achieving performance improvements of up to 80% depending on the fabrication technique and catalyst loading. The primary advantage is the enhanced catalyst utilization which leads to increased power density. The most common types of patterns are arranged in a linear style of repeating triangular or polygon shapes through the cross-section of one plane i.e the 'asymmetric' pattern by Kim et al.[39] or NSTF from 3M[61].

They tend to make up 20-50% of the total thickness of the membrane, which is good for increasing power density but can thin the membrane and increase fuel crossover[51]. Other patterns include much less depth, only comprising 1-10% of the membrane thickness. The patterns are repeating geometric shapes i.e. the work done by Jeon et al.[65] in Figure 2.5. The improvement of power density is attributed to the improved connection between platinum and the electrolyte, fostering a more homogeneous TPB. The topology of the catalyst layer also reported enhanced water transport, potentially mitigating flooding phenomena. However, challenges such as the durability of thinner catalyst layers and fabrication complexities at scale may limit their application to laboratory settings.

2.4 Other Material Effects

This section explores the impact of various components in the Membrane Electrode Assembly (MEA) on performance, akin to the effects observed in the electrolyte membrane. These components include ionomer catalyst distribution, carbon support, and gas diffusion layer (GDL) effects.

2.4.1 Ionomer Catalyst Distribution

The triple phase boundary (TPB) comprises three fundamental connections: electronic, ionic, and mass transport, centered around a catalytic site. This configuration ensures that the diffusion of reaction products, electrons, and protons is directed to their respective destinations. The ionomer content within the catalyst layer plays a crucial role in the mechanics of the TPB. Excessive ionomer can hinder reactant percolation and decrease performance, while insufficient ionomer forces ions to diffuse to an ionomer chain. Lit-

erature suggests that the optimal ionomer content for the cathode side catalyst layer is approximately 30%, primarily in traditional membrane geometries. However, the influence of ionic conductivity from just the catalyst contact with the membrane itself is less explored.

Optimizing the amount of ionomer in catalyst layer inks is vital to avoid adding additional electronic resistance. Kim, K., et al. [66], found that reducing ionomer loading from 0.8 mg mg_{Carbon}^{-1} to 0.3 mg mg_{Carbon}^{-1} on the cathode side led to performance improvements in ohmic and mass transport regions, as well as a slight increase in Open Circuit Voltage (OCV). This improvement was attributed to better connectivity between the catalyst ink and the membrane. Higher ionomer weights in samples increased resistance to diffusion and blocked some catalyst sites due to excess ionomer. A similar study on the anode side identified an optimal ionomer weight of 0.25 mg mg_{Carbon}^{-1}, though the performance benefit was less pronounced than on the cathode side. This was attributed to the higher reaction rate at the anode and the high diffusivity of hydrogen through the electrode.

Yu, H., et al. [67] observed similar results, with the optimum cathode side loading being 0.2 mg mg_{Carbon}^{-1}. Their analysis of the total and average pore volume through nitrogen adsorption isotherm indicated that the 0.2 and 0.3 mg mg_{Carbon}^{-1} loadings had smaller total pore volumes and a more narrow distribution of pore size. This was deemed a result of the ionomer infiltrating the larger carbon pores, thereby narrowing them and enhancing Pt-ionomer connectivity.

Chaparro, A.M., et al. [68] focused on the effect of ionomer loading in electrospraying 20% Pt/C catalyst ink. They discovered that the best performance was achieved with

15% ionomer content in the ink. This performance boost was linked to improved contact between the catalyst and ionomer, as confirmed by testing the catalytic activity of the layer, which was highest with 15% ionomer loading.

Jeon, S., et al. [69] examined the impact of ionomer content (ranging from 10 to 40%) under various humidity levels (25 to 95%) in decal transfer catalyst coated membranes. They found optimal performance at 95% humidity for 30% and 20% ionomer loading on the cathode side. Interestingly, at 25% humidity, the best performance was achieved with a 40% ionomer content in the catalyst layer. This suggested that high ionomer contact, unrestricted by water content, allowed the cell to maintain operation even under low humidification.

Suzuki, A., et al. [70] investigated the effects of ionomer content in the catalyst layer on diffusion mechanisms and performance. They developed a 3D model of the GDL based on percolation theory and an effective diffusion coefficient by computing relative pore tortuosity to simulate the distribution of reactands and products within the GDL. The model incorporated the zero-dimensional springer model for membrane water transport and conductivity, and their electrochemical model was from the first principles. Their model results confirmed an optimal range of approximately 33% ionomer content in the catalyst layer, using a concentration of 0.1 mg cm^{-2} of platinum and 0.24 mg cm^{-2} ionomer.

2.4.2 Influence of GDL on Performance of Fuel Cell

The GDL is a critical component in MEAs, facilitating even gas movement from the flow field plate to the catalyst layer. At the cathode, the GDL plays a pivotal role in removing excess water from the catalyst layer and conducting electrons to the catalyst. Its ability to

control hydration levels is crucial in preventing flooding phenomena commonly observed in low-temperature fuel cells. Researchers have extensively utilized fundamental and bulk effect modeling to characterize this phenomenon and predict the effectiveness of varying hydrophobic coatings and Microporous Layers (MPL). The consensus in the research community is that for normal Pt/C catalysts, the inclusion of MPL is essential.

A Microporous Layer (MPL) is a thin, carbon-based layer applied between the catalyst layer and the gas diffusion layer (GDL) in a fuel cell. It is needed to improve water management and reactant distribution by:

- **Water Management:** Enhancing water transport and preventing flooding by promoting uniform water removal through the GDL.
- **Reactant Distribution:** Facilitating better reactant gas distribution across the catalyst layer, improving overall fuel cell performance.

El-kharouf, A., et al. [71, 72] delved into the various transport properties affected by the introduction of different carbon support materials and coatings. Chu, H., et al. [73], examined the impact of relative pore density from the GDL to the catalyst layer, using a model-based approach to assess the effective porosity of both the catalyst layer and GDL on overall cell performance. They discovered that the porous network could be disrupted by an excessive presence of water at the interface between the catalyst layer and GDL. Flooding at high current densities was found to be proportional to the GDL's porosity.

Hyun Nam, J., et al. [74] studied the microporous layer's role in water morphology and breakthrough. They developed a model to describe the behavior observed through Environmental Scanning Electron Microscopy (E-SEM) and demonstrated the impact of various microporous layer structures on water distribution through the GDL.

Lim, C., et al. [75] characterized the effects of varying amounts of hydrophobic polymer (ranging from 10 to 40%) in the GDL on a fuel cell system's performance. They found that a GDL with 10% polymer content was optimal as it significantly enhanced back pumping of water through the membrane. Effective water transport through the membrane is vital for operating the catalyst layer without flooding, while still maintaining ionic conductivity.

Shimpalee, S., et al. [76] analyzed the impact of GDL flooding on the overall cell performance. Their study utilized a numerical model to predict performance degradation in experiments where water was artificially introduced to hinder transport. The model's predictions aligned with experimental results, confirming the benefits of using hydrophobic coatings and MPL in managing flooding issues.

2.4.3 Carbon Support Material Effects

The catalyst support is a crucial element in the catalyst layer, significantly influencing performance. New and innovative materials have been extensively researched and characterized; however, these materials are often not fully optimized, leading to a gap in their full potential exploration.

The catalyst layer in a Proton Exchange Membrane (PEM) fuel cell typically consists of platinum on carbon, where platinum serves as the catalyst, and carbon reduces the amount of required platinum while maintaining electronic conductivity. The morphology of the carbon support dictates the region's hydrophobic or hydrophilic nature as it is influenced by its production method.

Soboleva, T., et al. [77] explored the role of carbon in the catalyst layer, distinguish-

ing between Vulcan XC-72 and Ketjen black carbon supports. They linked the support morphology to the hydrophilic properties of the catalyst layer, emphasizing the importance of selecting the right carbon support and ionomer amount to ensure adequate water retention for lower humidity operation. Their findings corroborated previous studies highlighting the significant influence of ionomer content in the cathode side catalyst layer on performance.

Mardle, P., et al. [78] challenged the notion that graphene is a suitable support material for the catalyst layer. Their research indicated that water accumulation in the catalyst layer, due to the hydrophilic nature of reduced graphene oxide sheets, impedes active reaction sites. However, they suggested that aligning graphene sheets parallel to gas transport could potentially make it an effective support material.

Wang, X., et al. [79] reported ex situ results using carbon nanotubes as catalyst support. Their findings revealed that carbon nanotubes could match the performance of Pt/c catalyst materials and demonstrated resistance to degradation under ex situ conditions. After undergoing an accelerated degradation test for 169 hours, consisting of holding the potential at 0.9 V vs SHE and recording a linear sweep at regular intervals, the nanotube-supported catalysts retained 30% more surface area than standard Pt/C catalysts. This increased durability was attributed to a more uniform electronic structure of the support material.

2.5 Composite Membranes

Composite membranes in fuel cells are electrolyte materials composed of more than one component. For example, Nafion XL consists of Nafion polymer reinforced with ex-

panded polytetrafluoroethylene fibers. These composites can be constructed from a variety of materials, primarily added for improved stability. Additionally, some fillers, like ceria, are incorporated as free radical scavengers.

2.5.1 Metal Oxides

Di Noto et al. [80, 81] explored Nafion membranes blended with various metal oxides to enhance mechanical properties and conductivity at elevated temperatures. They observed that most metal oxides restrained the relaxation profile, suggesting a limitation on polymer structure swelling and performance degradation. Interestingly, the conductivity at 135°C remained relatively stable for additives like titanium, zirconium, tungsten, and hafnium, while tantalum exhibited a conductivity loss of about 33%.

Adjemain et al. [82] investigated the performance of membranes integrated with silicon, titanium, aluminum, and zirconium. Tested in situ at 130°C, the membranes showed promising performance, particularly with titanium and silicon additives which also demonstrated carbon monoxide tolerance up to 500 ppm at 130°C.

Sacca et al. [83] focused on zirconium as a filler in Nafion membranes. In single cell tests, they reported a 20% improvement in membrane resistance at both 110 and 130°C, compared to pristine Nafion, by incorporating 10% zirconium.

Sahu et al. [84] examined the performance of silica composite membranes. They found that membranes with 5 and 10wt% silica displayed significantly enhanced performance at 100°C, as opposed to pristine and 15 wt% silica-incorporated samples.

2.5.2 Hybrid Fillers

Di Noto et al. [44] demonstrated the effectiveness of a hybrid filler comprising a silica core functionalized with fluoroalkyl surface units. This material proved stable up to 240°C and exhibited peak conductivity for the composite membrane at 155°C. Their single cell performance tests at 85°C, using both air and oxygen, confirmed superior performance of the composite membrane.

Griffin et al. [85] investigated a hybrid silicon filler doped with sulfate. Their findings indicated enhanced conductivity with the addition of sulfate groups, even under dry conditions at 120°C.

D'Epifanio et al. [54] explored the use of sulphated zirconia as a membrane filler. Their results showed increased water uptake, proton conductivity, and water diffusivity in the membranes. Single cell tests revealed notable performance improvements at a cell temperature of 70°C, particularly in the ohmic region.

Costamanga et al. [86] incorporated zirconium phosphate as a filler in Nafion membranes. When tested in situ at 130°C they observed a four-fold performance increase at 0.45 V. The filler was found to stabilize Nafion above its normal glass transition temperature, in contrast to the significant degradation observed in conventional samples.

Further investigations on similar fillers, including different structures like nanowires or carbon nanotubes mixed with Nafion, have aimed to enhance temperature resistance and performance beyond the standard 80°C. These studies are detailed in various publications [53, 87–91].

2.5.3 Graphene Composites

Carbon fillers, particularly graphene composites, have garnered interest due to their cost-effectiveness and abundance. Graphene oxide, known for its hydrophilic properties, is often functionalized with additional ionically conductive species like sulphate and phosphate [92].

Sahu et al. [93] utilized a composite membrane incorporating graphene filler functionalized with sulphonic acid groups. Remarkably, they reported a fivefold increase in conductivity at 20% Relative Humidity (RH), translating to an 80 $mWcm^{-2}$ peak power increase compared to pristine Nafion.

Lee et al. [94] compared composites of graphene oxide and graphene oxide functionalized with platinum nanoparticles. They observed that functionalized graphene sheets exhibited higher performance, attributing the poor performance of normal graphene at low RH to its hydrophobic nature. Furthermore, Lee et al. [95] combined the platinum-graphene concept with an additional silicate filler which improved performance when combined correctly; though membrane resistance increased significantly with a combined filler percentage over 4%.

Yang et al. [96] prepared similar composites with graphene oxide and a hybrid platinum-titania filler. By fixing the total filler weight at 1% and varying the proportions of each filler, they demonstrated improved membrane operation at low RH. The synthesized graphene oxide's high oxygen content was aligned with enhanced water retention. Their most notable improvement was observed with 20% graphene oxide and 80% platinum-titania filler.

Ibrahim et al. [97] observed a 20% increase in maximum power density at 100°C

with 4% graphene oxide Nafion composite, directly affecting the ohmic resistance and improving mechanical strength. However, performance at 120°C was not as optimal as at 100°C.

Kumar et al. [98] investigated sulfonated poly(ether ether ketone) (SPEEK) and sulfonated graphene oxide composites. They reported increased conductivity across various temperatures and RH levels, with conductivity doubling at 80°C compared to virgin SPEEK. This enhancement translated to improved performance at low RH.

Uregen et al. [56] used a PBI graphene oxide composite membrane, testing 2 and 5 wt% graphene oxide. The 2 wt% graphene oxide composite exhibited the best proton conductivity across all temperatures and showed a modest power density improvement at 165°C, when compared to PBI and the other composite.

Xue et al. [99] incorporated a butyl group into modified PBI, along with functionalizing graphene oxide with icacyanate groups (iGO). Testing various concentrations and mixtures, they discovered that 10 wt% iGO yielded the highest proton conductivity.

Xu et al. [89] prepared membranes with PBI and sulfonated graphene oxide, demonstrating significantly higher conductivity across a range of temperatures. In single cell tests, they achieved a maximum power density of 450 $\mathrm{mWcm^{-2}}$.

Abouzari-Lotf et al. [42] created a composite membrane using phosphonated graphene oxide and PBI, showing a 75% increase in maximum power density compared to conventional membranes at 120°C under anhydrous conditions.

2.5.4 Other Carbon Composites

Kim et al. [43] investigated sulfonated carbon nanotubes combined with sulfonated di-block copolymer (SDBC) based on PEEK and partially fluorinated poly(arylene ether sulphone). They reported enhanced conductivity at 20% RH and 120°C, with both ex situ and in situ tests showing similar improvements.

Kannan et al. [100] combined phosphonated carbon nanotubes with PBI, resulting in a 25% increase in maximum power density at 140°C compared to unmodified PBI. Conductivity enhancement was observed across all temperature ranges.

2.5.5 Fuel Cell Composite Membranes – Other Materials

High-temperature polymer electrolyte fuel cells often employ non-Nafion materials for membranes as these do not require high water saturation for ionic conductivity. A notable material is Poly-benzimidazole (PBI), typically doped with phosphoric acid to enhance proton conductivity [101]. However, PBI has limitations in transporting dissolved gases [102] and phosphoric acid can adsorb onto the platinum catalyst, reducing the electro-chemical surface area [103–105]. PBI membranes can operate up to 200°C [106] and require less water for conductivity [107]. Nonetheless, their suitability for the automotive industry is limited due to challenges in cold start protocols [108, 109]. Other approaches to elevate operating temperatures involve using additives with Nafion to improve mechan-ical strength limitations, focusing on enhancing thermal stability and conductivity through hydrophilic additives or ionically conductive species.

2.5.6 Multi-Discipline Approach

Jang et al. [110] combined patterning with a multi-layered approach, creating membranes featuring a prism-patterned titania-Nafion layer on the cathode side. Compared with commercial Nafion 211 and standard flat titania-Nafion layers, their design significantly improved performance in the ohmic region of the polarization curve. Testing across temperatures from 80 to 120°C, and at low humidity conditions, the patterned multi-layer membrane outperformed Nafion 211, particularly at 35% RH and 120°C, with a notable increase in current density.

2.5.7 Summary

A summary table of all the materials surveyed in the literature is available in Table 2.1. They are generally broken up into 3 desired effects: increased durability to both chemical and mechanical degradation, increased ionic conductivity, and increased operational temperature. All of these factors can contribute to power density and lifetime of the membrane and the fuel cell as a whole. Graphene is of particular interest as it has large through-plane resistance, as well as good mechanical strength and chemical stability[111]. When it is oxidised to graphene oxide, it could also contribute to the ionic transport of the membrane; the OH groups also contribute to a reduction in the in-plane conductivity. The challenge in using graphene oxide is controlling its shape as the membrane is manufactured in order to reduce any in-plane conductive effects. There is a general lack of models containing composite materials in the literature including any attempt to align the physics with the bulk properties of the composite.

Table 2.1: Summary of Composite Membrane Materials

Material	Type of filler	Proposed Function	References
Ceria	Metal oxide	Reduce chemical degradation from radical H_2O_2 attack	[41]
Titania, Zirconia, Tungsten oxide, Hafnium oxide, Tantalum oxide	Metal oxide	Enhance mechanical properties and conductivity at elevated temperatures	[80, 81]
Silica, Alumina	Metal oxide	Improved performance and CO tolerance	[82]
Zirconia	Metal oxide	Improve membrane resistance	[83]
Silica	Metal oxide	Enhanced power density and water transport at 100°C	[84]
Silica Core with Fluoroalkyl Surface Units	Doped metal oxide	Stable up to 240°C with peak conductivity at 155°C	[44]
Sulfate-Doped Silica	Doped metal oxide	Enhanced conductivity even under dry conditions	[85]
Sulphated Zirconia	Doped metal oxide	Increased water uptake, proton conductivity, and water diffusivity	[54]
Zirconium Phosphate	Doped metal oxide	Stabilize Nafion above its glass transition temperature	[86]
Graphene Oxide	Carbon	Enhance water retention and conductivity	[97]
Functionalized Graphene	Acid doped carbon	Increase ionic conductivity, especially at low RH	[93]
Graphene Oxide with Platinum-Titania	Metal oxide doped carbon	Improve membrane operation at low RH	[96]
Sulphonated Graphene oxide and Sulfonated Polyether Ether Ketone (SPEEK)	Acid doped carbon	Increased ionic conductivity across various temperatures and RH levels	[112]
PBI Graphene Oxide	Carbon	Increase ionic conductivity	[56]
Butyl Group Modified PBI with Isocyanate Graphene oxide	Organic carbon composite	Increase ionic conductivity	[99]
Sulfonated Graphene Oxide	Acid doped carbon	Significantly higher conductivity across a range of temperatures	[89]
Phosphonated Graphene Oxide	Acid doped carbon	Increase maximum power density at 120°C under anhydrous conditions	[42]
Sulfonated Carbon Nanotubes	Acid doped carbon	Enhanced conductivity at 20% RH and 120°C	[43]
Phosphonated Carbon Nanotubes	Acid doped carbon	Increase in maximum power density at 140°C	[100]

2.6 High-Temperature Benefits for Fuel Cells

While operating fuel cells at higher temperatures offers several advantages, it also introduces specific challenges. This section explores these benefits and challenges, and the need for a strategic approach in high-temperature fuel cell applications.

2.6.1 Improved Cathode Kinetics

In Polymer Electrolyte Fuel Cells (PEFCs), the cathode side often presents a limitation, particularly the Oxygen Reduction Reaction (ORR). The kinetics of the ORR are slower than those of the anode side reaction, the Hydrogen Oxidation Reaction (HOR), at standard operating temperatures like 80°C [113]. Enhancing cathode kinetics is a pivotal area of research in fuel cell technology. Increasing the temperature is a classic method to speed up reaction kinetics, as the reaction rate generally increases with temperature according to the Arrhenius equation. The Arrhenius equation is given by

$$k = Ae^{\frac{-E_a}{RT}} \tag{2.1}$$

where k is the rate constant, indicating the speed of the reaction; A is the pre-exponential factor, also known as the frequency factor, which factors in the frequency of collisions with the correct orientation for reaction; E_a is the activation energy required for the reaction to proceed; R is the universal gas constant; and T is the temperature in Kelvin. Two terms here are affected by a change of temperature, the temperature and the frequency factor. Both will increase with an increase in temperature, which is how the rate of reaction increases.

The exchange current density is an important parameter in this context, indicating the ease with which a catalyst can facilitate a reaction and thus influencing cell performance [114]. Research by Song et al. [113] demonstrated that both HOR and ORR rates improve with higher temperatures.

Wakabayashi et al. [115] discusses in detail the thermal effects alongside an ex-situ characterisation of platinum on carbon electrodes for temperatures 20-80°C in acidic electrolyte. They showed that the rate increases with temperature, and discussed the various kinetic effects. Their conclusions also discuss the dependency of the absolute values on the electrolyte used comparing their work to other authors using different acids.

Temperature changes also affect the reference potential and Open Circuit Voltage (OCV) of the cell, as described by the Tafel and Nernst equations (2.2,2.3) [116]. This equation shows that increasing temperature reduces the reversible voltage, especially below 100°C due to the phase transition of water to vapour:

$$E = E_{\text{rev}} + \alpha + b \log i_0 - b \log i \tag{2.2}$$

In this equation, b is the slope, E_{rev} is the Nernst voltage, and i is the current.

$$\eta_{\text{act}} = b \log \left(\frac{i}{i_0} \right) = b \log i - b \log i_0$$

Here is an alternative form of the tafel equation where η represents the cell overpotential, or the $E - E_{\text{rev}}$.

The Nernst voltage can be calculated as

$$E_{\text{rev}} = E^0_{\text{rev}} + (\frac{\delta E_{\text{rev}}}{\delta T})_P(T - 298) = E^0_{\text{rev}} + (\frac{\Delta S}{nF})_P(T - 298) \tag{2.3}$$

Xu et al. [117] reported that the theoretical OCV is influenced by the partial pressures of the reactants according to equation (2.4):

$$\mathrm{OCV} = 1.23 - 0.9 \times 10^{-3}(\mathrm{T} - 298) + \frac{\mathrm{RT}}{4\mathrm{F}} \ln \frac{\mathrm{P}^2_{\mathrm{H_2}}\mathrm{P}_{\mathrm{O_2}}}{\mathrm{P}^2_{\mathrm{H_2O}}} \tag{2.4}$$

The effect of temperature on the Tafel slope, assuming an independent reaction mechanism and transfer coefficient α, is shown in equation (2.5):

$$\frac{\delta b}{\delta T} = \frac{-2.3R}{\alpha nF} \tag{2.5}$$

Experimental studies by Parthasarathy et al. [118] have indicated a linear relationship between the Tafel slope and temperature at low current densities. At higher current densities, the Tafel slope increases, indicating a change in the reaction mechanism due to temperature. An increase in the Tafel slope at both high and low current densities typically implies an increase in coverage of intermediates on the catalyst surface, increase of adsorption to catalyst sites, or a change in the reaction mechanism. The impact of temperature on the exchange current density, a fundamental property of the catalyst that varies with pressure and temperature, has been documented to increase with temperature [113], confirming a faster reaction rate at elevated temperatures.

2.6.2 Improved tolerance of CO

Most fuel cells operate using hydrogen with a purity of 99.9995% because of the sensitivity of the Pt catalyst to being poisoned by CO. Producing such high purity hydrogen is energy intensive. Several studies have demonstrated that increasing temperature creates a negative entropy for CO adsorption, making it highly unfavorable [119, 120]. It is important to note that much of the research on CO adsorption utilized phosphoric acid membranes up to 200°C. The tolerance to CO shows only marginal improvement when approaching the temperature limit (120°C) of PTFE-based materials like Nafion.

2.6.3 Effect of temperature on oxygen transport

In a fuel cell, oxygen transport is critical as the cathode reaction is considerably slower than the anode reaction. With the mole fraction of oxygen in the cathode gas stream ranging from 0.05 to 0.21, depending on RH, the diffusion coefficient significantly impacts performance. It has been found that the diffusion coefficient of oxygen in liquid water increases with temperature [121]. Oxygen diffusion through water vapour is faster than through liquid water, and at higher temperatures, more water is in vapour form, effectively ensuring higher diffusion coefficients. The presence of ionomer in the catalyst layer can also significantly reduce oxygen transport, this is because oxygen diffusion through PFSA type materials is extremely slow. Tuning the amount of ionomer in the catalyst layer to allow for adequate unhindered gas transport was investigated by Yakkolev, Y. et al.[122] where they showed that ionic transport resistance made up $\tilde{1}0\%$ of the total transport resistance for catalyst layers with ionomer carbon ratios of 0.3 and 0.6.

2.6.4 Water management

Water management in fuel cells is a dominant area of research [123]. High-temperature operation could simplify this challenge. Poor water management manifests in two forms: dehydration, where insufficient water leads to reduced conductivity and performance, and flooding, where excess water hinders reactant/product transport and reduces voltage [124–126]. High-temperature operation minimizes flooding by ensuring that most water outside the membrane is in vapour form, facilitating removal. Dehydration, characterized by insufficient water in the membrane, can cause significant conductivity drops. This issue is exacerbated at higher temperatures [127, 128].

2.6.5 Thermal management

Fuel cells primarily generate heat through the formation of water and joule heating, making it essential to effectively manage and remove this heat to maintain optimal operation, as outlined in the water management section. The equation for heat transfer by convection is given as

$$Q_{\text{conv}} = hA(T_{\text{cell\_out\_boundary}} - T_{\text{coolant}}) \tag{2.6}$$

where Q_{conv} denotes the convective heat transfer rate, h is the convective heat transfer coefficient, A represents the surface area through which heat transfer occurs, $T_{\text{cell\_out\_boundary}}$ is the temperature at the cell's outer boundary, and T_{coolant} is the coolant temperature. This equation emphasizes that the driving force for heat transfer is the temperature difference between the fuel cell's operating temperature and the coolant temperature.

While in equation 2.7 ΔT indicates the initial and final temperatures of the coolant, it

primarily aids in determining the required mass flow-rate of the coolant for a given total heat transfer. It is crucial to understand that achieving the operating temperature of the fuel cell necessitates a large heat exchange area, as the log-mean temperature difference for heat transfer approaches small values.

Operating at higher temperatures increases this temperature difference (ΔT) acting as the driving force for heat transfer. For low-temperature fuel cells, a typical ΔT for heat removal ranges from 55 to 65°C, requiring a high mass flow-rate of coolant to remove the generated heat, as per:

$$Q = mC_p\Delta T \tag{2.7}$$

However, increasing the operating temperature can elevate ΔT to between 95 and 105°C, which significantly reduces the required coolant mass flow-rate. This reduction simplifies the heat exchange design by decreasing the necessary coolant volume, thereby affecting the overall heat exchange area required and the heat transfer coefficient, h. Optimizing these factors is crucial for effective fuel cell heat management, though the detailed design of heat exchangers falls outside the scope of this discussion.

2.6.6 Degradation of engineering materials and mechanical failure

Fuel cell components are exposed to corrosive agents from gas streams during operation. For instance, bipolar plates encounter fuel and oxidant, facing oxidative and reductive environments. They also are generally made from carbon which can corrode when the cell operates with a high overpotential. Metallic bipolar plates can leech transition metals which can cause side reactions with the other materials of the MEA in the acidic operat-

ing conditions. Hydrogen peroxide formation from fuel rich and flooding of the cell with water, can lead to membrane degradation further degrading various components, including bipolar plates and ancillary hardware. Degradation escalates with rising temperatures [129–131].

2.6.7 Membrane conductivity and degradation

In low-temperature fuel cells, membrane degradation arises from a vulnerability in the side chain susceptible to peroxide attack. Several mechanisms contribute to peroxide formation, especially under non-steady-state conditions such as prolonged OCV periods [132]. The glass transition temperature of Nafion's PTFE backbone ranges from 110 to 130°C [133], and the side chain relaxation is near 100°C [134]. These factors pose challenges for membrane performance above these temperatures as relaxation increases porosity and diminishes membrane stability.

2.6.8 Additive effects on membrane degradation

The conductivity of Nafion membranes is closely linked to their water content [23]. Composite materials can reduce the total Nafion content, so understanding their impact on water balance is crucial for high-temperature operation. Significant changes in water balance could diminish proton conductivity. However, additives generally enhance membrane resistance to degradation, potentially providing a net positive effect on the overall system.

2.6.9 Summary

High-temperature operation of fuel cells offers promising benefits including increased reaction kinetics, increased tolerance to carbon monoxide, increased diffusion coefficients, better thermal management, and lower flooding risk. However, it also poses significant challenges such as dry cell conditions, increased degradation of engineering materials, and lower membrane conductivity. To address these challenges, it is essential to understand the limitations of current materials and explore alternative operating modes and new materials.

2.7 Introduction to Polymer Electrolyte Modelling

Nafion, a perfluorosulfonic acid (PFSA) membrane, is produced by Du Pont and is the industry standard solid electrolyte in polymer electrolyte fuel cells. It is extensively used in various electrochemical applications [46, 135]. As discussed in section 2.1, the membrane's morphology eludes a consistent structural description from the molecular to the macroscopic level [135–137]. Crucial to understanding polymer membranes is the relationship between their ionic conductivity properties and structure, often focusing on their water uptake characteristics, as water is essential for enabling ionic conductivity in most electrolytes. This complex relationship is predominantly described empirically. However, the experiments forming the basis of these models often utilize outdated techniques, highlighting a need for updated methods [138]. Therefore, developing new membrane materials requires a reassessment of Nafion's current limitations, such as high production costs, diminished proton conductivity at elevated temperatures [139], and hydrogen

crossover during fuel cell operation [140].

Experimentally discerning the structure of PFSA membranes, like Nafion, is challenging due to their low spatial order, which complicates obtaining unambiguous structural information [141, 142]. This necessitates the complementary use of diagnostic and prognostic modelling techniques to enhance understanding, such as computing proton diffusion [143]. The difficulty in correlating observed macroscopic effects with the membrane's structure has led to most fuel cell membrane models being empirically-derived [144–147]. Atomistic models employing empirical potential functions have been developed to represent the PFSA system [148–150]. Additionally, quantum chemical methods which involve solving the Schrödinger equation using time-independent approximations have been utilized [151–153]. Although these methods offer high accuracy in predicting chemical phenomena essential for proton conductivity, such as charge transfer and bonding [154, 155], they are limited to localised structural units.

Molecular dynamics methods can simulate multiple ionic clusters, which play a crucial role in proton transfer mechanics [156, 157]. Despite the development of sophisticated force fields for PFSA [158–160], there is debate over whether these simulations accurately represent the local structures of hydrated ionic groups, especially considering the diffusion via the Grothuss mechanism. The latter is often ignored in classical force fields but is acknowledged as the dominant proton transport mechanism at high hydration levels [29].

Large-scale modelling of membrane proton transfer mechanisms often relies on empirical observations of membrane hydration under various humidification levels [34, 161]. These models measure conductivity while progressively hydrating the membrane, estab-

lishing a secondary correlation [47, 162]. These correlations are then used to define the observed bulk properties of the membrane, influencing its performance in situ.

2.8 Fuel Cell membrane Models

The modeling of perfluorosulfonic acid (PFSA) membranes, such as Nafion, has been a subject of extensive research. Elliott et al. [163] explored the membrane's structure, predicting the size, shape, and inter-connectivity of the channels within the membrane matrix. Their work revealed how membrane structure adapts to water content and the dynamics of proton transport in a hydrated environment. Interestingly, they found that the actual membrane structure differs significantly from the traditional pore and chamber model, yet this divergence does not impede proton transport. However, they observed that the mechanisms of proton mobility did not always correlate with effective proton diffusion, sometimes even reducing it.

Costamagna et al. [164] introduced a proton conductivity model based on percolation theory. They posited that bulk proton conductivity originates from water within the membrane, influenced by adsorption and capillary condensation. These phenomena were modeled using the Brunauer – Emmet – Teller (BET) and the Kelvin – Cohan equations, respectively. Their model aligned well with existing literature and proved applicable under varying relative humidity conditions, extending to high temperatures and different membrane materials.

The BET equation is foundational in the analysis of gas adsorption data, providing a

method to calculate the specific surface area of materials. It is expressed as

$$\frac{P}{V(P_0 - P)} = \frac{1}{V_m C} + \frac{(C-1)P}{V_m C P_0} \tag{2.8}$$

where P is the equilibrium pressure of the adsorbate gas, P_0 is the saturation pressure of the adsorbate at the temperature of adsorption, V is the volume of gas adsorbed at pressure P, V_m is the monolayer adsorbed gas volume, and C is the BET constant. This equation models multilayer adsorption and is pivotal in determining the surface area of porous materials.

The Kelvin-Cohan equation describes the equilibrium vapour pressure over curved surfaces, which is essential for understanding capillary condensation. It is given by

$$\ln\left(\frac{P}{P_0}\right) = -\frac{2\gamma V_m}{RTr} \tag{2.9}$$

where P is the equilibrium vapour pressure over a curved surface, P_0 is the equilibrium vapour pressure over a flat surface, γ is the surface tension of the liquid, V_m is the molar volume of the liquid, R is the universal gas constant, T is the absolute temperature, and r is the radius of curvature of the meniscus. The Kelvin equation plays a crucial role in the study of phenomena such as cloud formation and the behaviour of fluids in porous media.

Spohr [165] conducted molecular dynamics simulations to examine the impact of pore structure and water content on proton transfer dynamics in Nafion membranes. This study explored the interplay between water content, side chain density, and proton transport at a molecular level.

Wohr et al. [166] developed a model for a single cell and stack, incorporating mass

transport limitations and considering heat and water transport. Their findings highlighted the significant impact of membrane humidification on performance, recommending temperature and pressure management to preserve membrane hydration. They also suggested enhancing the porosity of the anode gas diffusion layer to facilitate water flux to the anode interface.

Yi [167] proposed a model accounting for water and heat transport along-the-channel of a low temperature fuel cell. This model included natural convection to address water and heat losses and emphasized the advantage of maintaining a positive pressure gradient between the cathode and anode for efficient water management across the membrane.

Giner-Sanz et al. [50] focused on modelling losses due to internal short circuits and hydrogen crossover. Their approach involved a series resistance model, which effectively characterized these losses and demonstrated a linear relationship between hydrogen crossover and anode pressure, independent of cathode pressure. However, the influence of relative humidity was not explored in their model.

Taherkhani et al. [30] investigated the effects of temperature and water content on Nafion 117 membranes through a thermodynamic lens. Their study emphasized the significant role of the Grotthus mechanism in proton transport at higher temperatures and water content levels, urging its consideration in related models.

Huang et al. [168] reviewed various modelling methods related to the catalyst layer and the role of ionomer within it. Their analysis indicated a clear benefit in understanding proton conduction without ionomer presence, leading to performance improvements in ultra-thin catalyst layers.

Biyikoglu [106] provided a comprehensive review of fuel cell models, categorizing

them mainly into finite element and Computational Fluid Dynamics (CFD) models. This review highlighted the predominance of 1D models and the scarcity of 3D modelling in this field.

Kone [169] reviewed 3D fuel cell models employing CFD, covering various aspects such as: transport phenomena, geometry, and operating conditions. These models are generally built upon the dynamic models initially introduced by Springer et al. [170] in 1991, with some modifications from subsequent research.

Finally, Commer et al. [45] discussed proton transport mechanisms in different PFSA membranes. Their review across multiple papers highlighted the need to bridge different length scales to gain a comprehensive understanding of membrane behaviour.

2.9 Membrane Thermodynamic Theory

The absorption of water by polymers is governed by a set of general theories that explain how variations in conditions like temperature, pressure, and changes in polymer structures affect water sorption behavior. A foundational theory was elaborated by Enderby in 1954 [171], which modeled the sorption behavior of water in cellulose, providing a comprehensive examination of the theory, beginning with the Helmholtz free energy of a sorption system:

$$F = F_p + F_w \tag{2.10}$$

Here, the Helmholtz free energy (F) is the sum of the free energy of the dry polymer (F_p) and the free energy of water absorbed into the structure (F_w), expressed as

$$F_w = -kT\left[N \ln \Phi_w(T) + \ln \frac{Q_N}{N!}\right] \tag{2.11}$$

where $\Phi_w(T)$ is a function of temperature related to the internal and momentum coordinates of a single water molecule, Q_N is the configuration integral for the water molecules in the potential field, N is the number of water molecules, k is the sorption constant, and T is the temperature. Enderby et al. further described this methodology [171].

Sorption behavior can also be described in terms of sorption enthalpy, which is the energy required to transfer a unit mass from a vapour state into the polymer structure. It is a sum of the condensation enthalpy ($\Delta_{cond}h$) and the mixing enthalpy ($\Delta_{mix}h$) [172, 173]:

$$\Delta_{sorp}h = \Delta_{cond}h + \Delta_{mix}h \tag{2.12}$$

Water activity and moisture content are parameters in the sorption/mixing process. The mixing enthalpy represents the interaction between liquid-phase water and solid-phase polymer. This interaction is typically examined by subtracting the condensation enthalpy from the sorption enthalpies, essentially being the excess heat generated during the condensation process. The mixing enthalpy involves interactions between liquid water and the polymer, with multiple interactions occurring across hydrophilic and hydrophobic regions, forming bonded, unbonded, and clustered water. Water diffusion coefficients change with water content, increasing with volume fraction and then decreasing due to clustering. In our model, the assumption of a constant $D_{\mathrm{H_2O}}$ presents a limitation as it

doesn't capture these variations. A schematic diagram was adapted from Wadso et al. [172]:

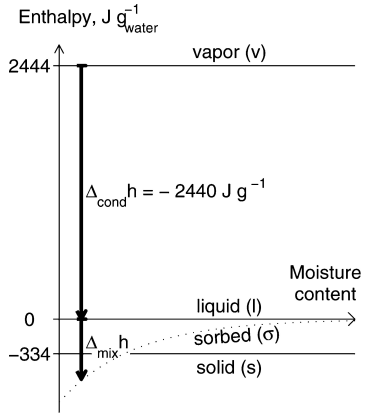

Figure 2.6: Enthalpy diagram for water sorption in polymers at 25°C, adapted from Wadso et al. [172].

Figure 2.6 demonstrates that as water sorption occurs, the mixing enthalpy becomes less due to less reorganisation required to accommodate water into the structure. In some cases, the mixing enthalpy can become positive and is driven by entropic processes. Water properties, such as boiling point and enthalpy, have been extensively tabulated in steam tables. The following table was created using data from the engineering toolbox steam table [174]:

Table 2.2: Enthalpy of saturated liquid water and enthalpy of saturated water vapour for different pressures and temperatures.

Absolute pressure (bar)	Boiling point (°C)	Specific enthalpy of liquid water at saturation (kJ kg^{-1})	enthalpy of water vapour at saturation (kJ kg^{-1})
0.5	81.35	340.57	2645.99
1	99.63	417.51	2675.43
2	120.23	504.71	2706.3
3	133.34	561.44	2724.22

In high moisture content polymers like fully hydrated Nafion, the heat of sorption approaches the difference between the enthalpy of saturated liquid water and the enthalpy

of saturated vapour. As seen from table 2.2, these values converge at higher temperatures and pressures, suggesting that water sorption into the polymer structure becomes more favourable as the reorganisation becomes less exothermic. This implies that under higher temperature conditions, more water molecules are absorbed into the structure. This thermodynamic measure does not account for the balancing of water within the membrane, where water can condense out of the membrane causing the formation of liquid droplets within the structure. Under the definition of activity provided by springer this would account activities higher than 1.

2.10 Schroeder's Paradox

Schroeder's paradox is an observation made in 1903 by Paul von Schroeder, noted that gelatin exhibited a significantly lower water uptake from 100% relative humidity (RH) compared to liquid water at the same temperature [175]. This paradox stands in contrast to the thermodynamics of crosslinked polymers, where the chemical potential typically determines sorption behaviour rather than the solvent state. Despite this inconsistency, several researchers, including Zawodzinski [34], Hirata [176], and Pushpa [177], have referenced this paradox in explaining their observations of lower vapour equilibration compared to liquid equilibration.

Water vapour pressure, saturation pressure, and water activity are fundamental concepts in understanding water sorption in solid polymer electrolytes like Nafion. Water activity (a_{H_2O}) in the gas phase, derived from the ideal gas law and Van't Hoff/Nernst equations, correlates with relative humidity in aqueous solutions. In Nafion, different forms of water (bonded to sulfonic groups, as hydronium ions, or free in hydrophobic

domains/pores) interact with the polymer, influencing the sorption process. The driving force for sorption is the chemical potential gradient between the gas and polymer phases. However, Schroeder's paradox reveals discrepancies between vapour sorption and liquid water sorption: Nafion membranes exhibit higher hydration when immersed in liquid water compared to 99% relative humidity. This inconsistency could be due to the reorientation of functional groups, polymer chain relaxation, and hydrostatic pressure when in contact with liquid water. Manufacturing processes, membrane clamping to prevent relaxation, and additional membrane layers to stop direct liquid contact affect this phenomenon. Although some suggest higher water activity (>1) in the vapour phase as an explanation, however this is only a means of pseudo approximation for the effect of the water as if it were vapour. Instead, uncontrolled factors likely contribute to the extra uptake from liquid water. Therefore, the rapid hydration increase observed in liquid water cannot be fully captured by sorption models alone.

Various mathematical correlations have been drawn from these measurements [178–182], with some studies adjusting the activity range from 0 to 1 to 0 to 3 to account for both liquid and vapour equilibrations under the same pseudo two phase approximation. This two phase approximation uses the mol fraction of water in the membrane multiplied by the system pressure divided by the saturation pressure as the definition for activity. This definition creates a dimensionless quantity similar to the partial pressure divided by the saturation pressure. The result is that the mol fraction may exceed the saturation pressure creating values up to 3, that are attempting to account for the liquid phase, according to springer. Jeck et al. [183] demonstrated that Schroeder's paradox is resolved for activities between 0.75 and 1. They conducted comparative examinations of water sorption

under both liquid and vapour conditions, showing that the equilibration measurements for both states were identical and suggesting that small experimental errors might present a paradox.

Their gas equilibrated experiments utilized Inverse-Micro-Raman-Spectroscopy (IMRS) on a glass slide with tight control over temperature and humidity (to within 0.1°C), limiting activity change to 0.1%. For the liquid equilibrated experiment, high molecular weight polyvinylpropylene (PVP) was used as a barrier to control liquid flow into the test area and to prevent any swelling and deswelling effects.

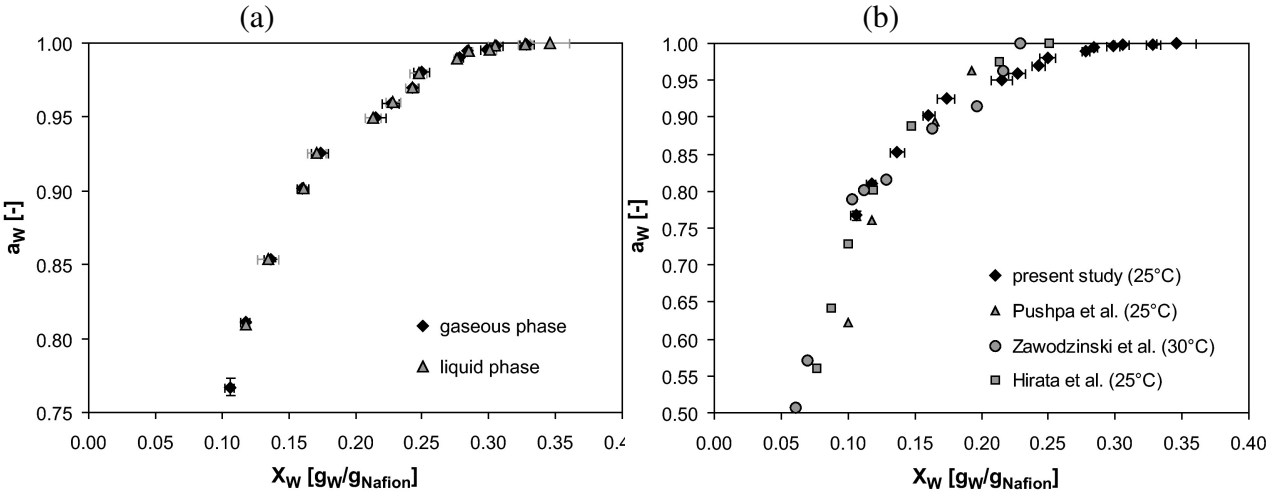

Figure 2.7: (a) Water sorption for gaseous and liquid phase measurements from Jeck et al. [183], (b) Gas phase water sorption curves comparing studies from various authors [34, 176, 177, 183].

In Figure 2.7(a), each point for the gas phase comprises 45 data points: 5 different sample points on the membrane taken a few hours apart, with equilibration recorded every 2-3 days, and 3 separate samples used. The error bars represent the standard deviation for each point. The liquid phase data, collected with the same technique, is plotted in the same figure. Figure 2.7(b) compares gas phase data with previous literature, showing significant deviation in the 0.95 to 1 a_w range. The membrane's water content on the x-axis is measured in units of grams of water per grams of nafion. Typically it is represented

as lambda (λ) which is defined as the molar quantity of water per mole of sulphonic acid side group.

Jeck et al.'s findings indicate that water content is extremely sensitive to changes in activity, with a 1 to 0.99 change resulting in a 5% shift in weight fraction. This observation is corroborated by other studies [184, 185], which employed different methods to analyze water activity and conductivity in Nafion membranes. They also left a piece of Nafion in 30°C 100% RH environment for 2.5 months to see what the maximum lambda would be, which resulted in the middle of the two values measured with increasing and decreasing temperature. They also noted that the 80°C measurement had the same water uptake, regardless of if the temperature were increasing or decreasing. They say that this might explain why evidence of the Schroeder paradox is seemingly present in many measurements. They also showed through a meta-analysis of other work with different experimental samples with two distinct thermal histories, either predried or not, that the water uptake was significantly different between the two groups explaining further why the paradox is consistently found. Taking the thermal history of the membrane into account appears extremely important when understanding the water sorption.

Onishi et al. [185] used impedance spectroscopy to determine the ex-situ conductivity of membrane samples, adopting an equivalent circuit (EC) model as discussed in Yuan X et al. [186]. Water uptake measurements were performed in a custom-built apparatus within a constant temperature chamber. Their findings showed that conductivity measurements for liquid and gas phases were within 1% of each other, aligning with mass calculations for water uptake. They observed higher water uptake at elevated temperatures and identified differences in water uptake based on the thermal history of the membrane,

suggesting that this history is crucial in understanding water sorption behaviour.

A recent review of the process by which the Schroder paradox operates within fuel cell membranes like Nafion, concluded that the dimensional swelling of the membrane was a key parameter in the understanding of the effect. Although they did not directly contradict the work by Jeck, the authors pointed out that they believed there was evidence for the paradox based upon the swelling of the membrane aligning with Onishi, saying that the thermal history of the membrane and if its structure had been thermally reorganised then liquid swelling would not be similar to the swelling observed by purely vapour equilibrated membranes [187]. If two samples with identical thermal histories are subsequently equilibrated with saturated vapour and liquid, it is unclear why the vapour equilibrated membrane would not continue swelling to a maximum extent comparable to that of liquid water at the same temperature. The net energy available for membrane reorganization should be equivalent in both cases, suggesting the same equilibrium state.

However, both perspectives present challenges. If the Schröder paradox is disregarded, the assumption must be that the membrane has a maximum swelling thickness, making maximum water sorption proportional to this limit. A model must either accurately account for the dimensional expansion of the membrane or accept that sorption will appear artificially higher due to the absence of this expansion, affecting inferred water activity. Conversely, if the Schröder paradox holds, a precise understanding is required of how liquid water condenses within the membrane during vapour equilibration and how this process is influenced by microporous boundary layers, which repel water back into the membrane.

2.11 Low Temperature Membrane Models

Modelling plays a crucial role in reducing the cost of designing and building prototypes, offering insights into complex systems where experimentation can be challenging. The development of low-temperature membrane models has been extensively reviewed by Dickinson and Smith [46], with key figures and points reproduced here with permission. The models discussed in this section have been formulated based on comprehensive empirical analyses, incorporating polynomial fitting of extensive datasets derived from experimental observations. These models, while not strictly developed from fundamental first principles, incorporate a sophisticated level of empirical rigour. The closest association with fundamental physics is observed in their structural resemblance to the Langmuir isotherm, providing a conceptual link to physical adsorption processes. This approach represents the forefront of existing methodologies to characterize the specific behaviour under investigation. To the best of the author's knowledge, these models stand as the most advanced and currently available representations, developed to encapsulate the observed phenomena within the constraints of empirical data and theoretical frameworks available in the literature. This methodology underscores a commitment to an exhaustive and technically rigorous exploration of the phenomena, balancing empirical accuracy with theoretical insights, and advancing the field's understanding through a careful synthesis of observed data and conceptual modelling strategies.

Membrane modelling began in earnest with Springer et al. [188] in 1991, who built upon the empirical relationship between water movement through the membrane and water activity established by Zawodzinski et al. [34]. Springer et al. successfully incorporated electro-osmotic drag into their model. This work initiated the modelling of mem-

brane processes using Nafion 117, which was the state-of-the-art material at the time. Zawodzinski et al. measured the weight increase of the membrane with increasing relative humidity at 30°C, deriving an activity equation. Kusoglu and Weber [27] offered an alternative polynomial fit to the same data, as shown in Figure 2.8. Hinatsu et al. [179], measured water sorption at 80 ºC their relationship was based on their own data. Pasaogullari et al. [180] also presented a fit to the [189] data, in vapour equilibrated state. Kulikovski et al. [181] added the supersaturated vapour condition to Pasaogullari et al. It should be noted that these two relationships return lower values of lambda than Springer at and close to 1. This is due to the normal activity term not including liquids, as activity below 1 is considered to be purely vapour. Activities above 1 are considered to have a mixture of water and vapour aligned with the assumption made in the original springer et al. [170] model of a pseudo two-phase approximation. Meier and Eigenberger [190] presented an isotherm that accounts for liquid equilibration, without exceeding an activity of 1. Karpenko-Jereb et al. [182] proposed an alternative solution with a smoothed jump between activity of 0.97 and 1 to account for Schroeder's paradox, where there is not temperature dependence of the vapour equilibrium. A temperature dependence was incorporated into the liquid equilibration instead. Peron et al. [47], proposed an empirical sorption isotherm based off data they collected. Unlike the other sorption isotherms included in Figure 2.8 this one is based on dispersion cast Nafion 211. It is known to behave differently to the Nafion 1100 series membranes, which are extrusion cast.

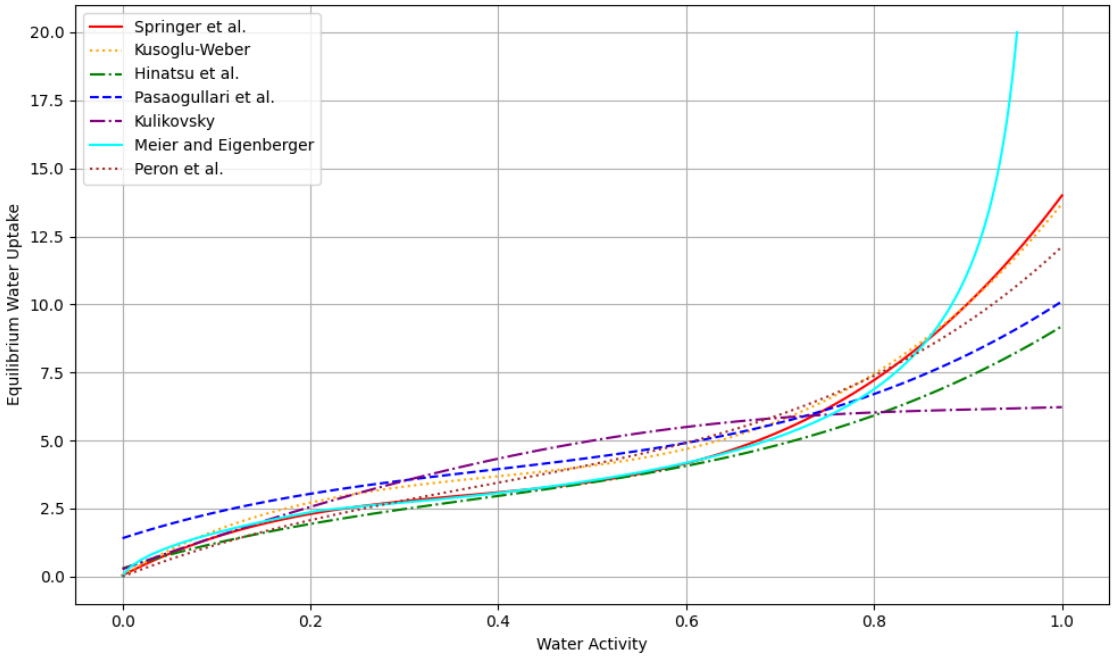

Figure 2.8: Water sorption curves at 80°C by various authors [47, 179–182, 188, 190, 191].

Springer et al. [188] also explored the relationship between conductivity and lambda, developing a model that could predict conductivity based on water content and temperature. This model integrated the activation energy for water diffusion through the membrane, based on measurements by Yeo and Eisenburg [189]. Springer et al. put this all together to develop a relationship of diffusion coefficient relative to lambda, activation energy, and temperature. Newer Nafion materials are made by using dispersion casting. This method uses dispersed ionomer, and casting rather than extruding. This allows the production of thinner membranes, the drawback of which is slightly lower mechanical strength and lower acid content. This means that the behaviour will fundamentally differ to the previously described Nafion 117. In 2012 the relationship for Nafion 211 was described by Peron et al. [47]. They used a similar method to Zawodzinski [34], including liquid equilibration at a range of temperatures. Their new relationship updated the Springer model by including the sorption isotherm suggested by Mittelsteadt and Liu

[192]. They also described a relationship between conductivity and lambda for Nafion 211.

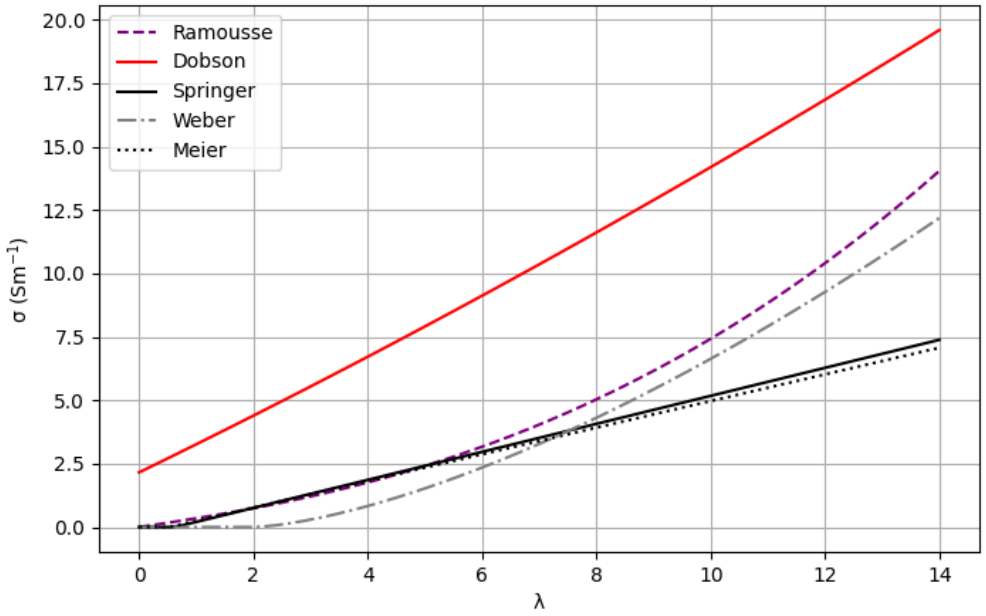

Figure 2.9: Conductivity vs Lambda at 80°C by various authors [188, 190, 193–195].

Figure 2.9 illustrates different conductivity relationships versus lambda. The models by Springer et al. [188], Weber et al. [193], and others show varying approaches to incorporating different factors. The general conductivity equation used in these models is:

$$\sigma = 0, \quad \lambda < \lambda_0 \tag{2.13}$$

$$\sigma = \sigma_0(\lambda - \lambda_0)^{n_{cond}} e^{(\theta_{cond}(1/T_0 - 1/T))}, \quad \lambda \geq \lambda_0 \tag{2.14}$$

Here, λ_0 is the minimum lambda value, θ_{cond} is the thermal coefficient, n_{cond} is the conductivity coefficient, and T and T_0 are the temperature and reference temperatures, respectively. The parameters of each model are listed in Table 2.3.

Table 2.3: Conductivity parameters.

Source	σ_0 S/m	λ_0	θ_{cond} K	n_{cond}
Springer [188]	0.5139	0.6344	1260	1
Kulikovsky [181]	0.5736	1.253	undefined	1
Weber [193]	0.2646	2	1800	1.5
Wiezell [196]	0.45	0.222	undefined	1
Meier [190]	0.491	0.543	1190	1

Ramousse et al. [194] presented data repeated from Neubrand [197], with a higher order polynomial fit given by

$$\sigma = (2.0634 + 1.052\lambda + 0.010125\lambda^2)\exp(\theta_{\text{cond}}(\frac{1}{T_0} - \frac{1}{T})) \tag{2.15}$$

where the symbols have the same meanings as the above equation 2.14. The higher-order polynomial fit was justified as a better fit of the data; however, no metric was shown as to what the better fit meant.

The sorption and conductivity behaviours of Nafion membranes, particularly the differences between the 1100 and 2000 series, are evident when comparing models like Springer et al.'s with those of Dobson et al. and Peron et al. This comparison is depicted in Figure 2.10.

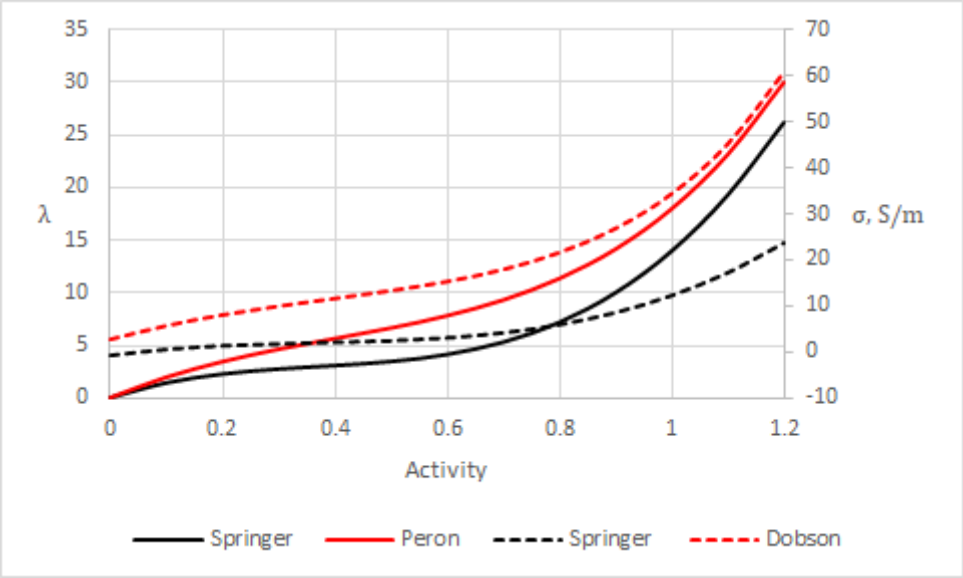

Figure 2.10: Water sorption and conductivity comparison.

Figure 2.10 shows the lambda and conductivity behaviours of the Springer [170] and Dobson/Peron [47, 195] models. These models include the redefined activity accounting for liquid water using the same pseudo two-phase approximation earlier cited. The distinct behaviours of extruded versus dispersion cast membranes are apparent. The dispersion cast membranes exhibit higher conductivity relative to water sorption, attributed to the greater mobility of polymer chains within the structure which enhances proton mobility and conductivity [47, 195].

The models discussed in this section have been formulated based on comprehensive empirical analyses, incorporating polynomial fitting of extensive datasets derived from experimental observations. These models, while not strictly developed from fundamental first principles, incorporate a sophisticated level of empirical rigour. The closest association with fundamental physics is observed in their structural resemblance to the Langmuir isotherm, providing a conceptual link to physical adsorption processes. This approach represents the forefront of existing methodologies to characterize the specific behaviour

under investigation. To the best of the author's knowledge, these models stand as the most advanced and currently available representations, developed to encapsulate the observed phenomena within the constraints of empirical data and theoretical frameworks available in the literature. This methodology underscores a commitment to an exhaustive and technically rigorous exploration of the phenomena, balancing empirical accuracy with theoretical insights, and advancing the field's understanding through a careful synthesis of observed data and conceptual modeling strategies.

2.11.1 Nafion Modelling at High Temperatures

Current research lacks comprehensive whole cell models for Nafion sorption behaviour above 90°C. While some studies, such as that by Cheng et al. [198], have investigated the effect of temperature on hydrogen crossover at higher temperatures, these studies have not fully accounted for changes in saturation pressure necessary to achieve 100% RH above 100°C. Therefore, a gap remains in fully understanding and modelling Nafion's sorption behaviour at these elevated temperatures. It could be possible to apply existing models to these temperatures, which will be the basis for the investigation into higher temperature modelling in chapter 5.

2.11.2 Modelling Composite Membrane Materials

To date, there are no known membrane or whole cell water sorption models for composite membrane materials in PEM fuel cells. An ex-situ model addressing the fatigue cracking mechanism in Nafion membranes reinforced with expanded PTFE fibres was reported by Singh et al. [55]. This model detailed the material behaviours (stress and strain) related

to the mechanical strength of fibre-reinforced Nafion membranes. However, it did not provide information on the water uptake or sorption characteristics of these composite materials. Thus, a significant research opportunity exists in developing models that encompass both the mechanical and absorptive properties of composite membrane materials in fuel cells.

CHAPTER THREE

METHODOLOGY AND MATERIALS

3.1 Experimental Methods

3.1.1 Membrane Preparation

Membrane patterns were created using the laser-induced periodic surface structures (LIPSS) technique, as described and provided by Romano et al. [199]. This technique involves removing material from a stainless steel surface with a controlled laser beam to leave a pattern behind. The patterned stainless steel samples served as masters for solution casting. Before casting, the masters and glassware were thoroughly cleaned.

The preparation of membranes required chemically clean glassware to avoid impurities affecting the final properties and stability of the membranes. The cleaning process involved three washes with acetone (Fisher Chemical), isopropyl alcohol (IPA) (Fisher Chemical), deionised water (DIW) (milipore), and ethanol (Fisher Chemical), followed by drying in an oven at 50°C. The acetone is there to break down any remaining polymer from previous castings, IPA is there to help remove any acetone remaining incase it is dried to the glassware. DIW is added to ensure no ions that were present are washed off, and finally ethanol is used in a small rinse to aid in faster drying, and because it is used as

the primary solvent for the casting it doesn't matter if there is a small amount remaining on the glassware surface.

The casting process, adapted from Ding et al. [200], involved using Nafion solution (DuPont) by first measuring out the required amount for a specific thickness into a clean sample vial. For example, using approximately 14 ml of 5% Nafion solution in water and 1-propanol, it was possible to prepare a 50 micron membrane [201]. The solution was degassed by using a desiccator and vacuum pump, operating at about 200 mbar, to remove any dissolved gases overnight, preventing the gas from being liberated during casting, forming bubbles and imperfections in the final membrane. The degassed Nafion solution (Du Pont) was then poured gently into the clean glassware as to prevent any further stirring of the solution and entrapment of gases and put into the oven.

The casting process generally has two phases. The first phase is the evaporation phase, where a large amount of the continuous phase of the solution is removed so that the polymer chains are all in contact with one another so that in the second phase, the annealing phase, they can form an advantageous pore structure for proton transport. This is important in generating good mechanical properties due to reorganisation of the polymer chains. To ensure both phases are adequately completed, an hour of time for each phase is allowed so that homogeneous properties can be built across the entire membrane. For the Nafion solution (Du Pont) prepared an hour at 100ºC then an hour at 120ºC this was sufficient time to create a mechanically robust membrane. To make a patterned membrane the procedure was the same, but a stainless steel plate cleaned in the same manner as the

glassware was added face up in the petri dish as part of the casting surface, then the Nafion solution (Du Pont) is added in the same manner as above, following the same procedure for evaporation and annealing. Once cast, the membrane was removed from the mould (petri dish) by soaking the membrane in water and heating in the oven to 50°C for approximately 15 minutes. This enables simple removal of the membrane from the moulds, minimising the risk of tearing or rupture of the polymer. Solution cast membranes have random ordered structures, therefore it is important to terminate the ends of the polymer chains with extra sulphonic acid groups to maximise ionic conductivity.

The activation procedure was as follows. First the membrane was heated in DIW at 80ºC for 1 hour to fully hydrate the structure and enable the easy passage of other chemical species. The membrane was then heated to 80ºC in a 3%(w/v) solution of hydrogen peroxide (Sigma Aldrich) for 1 hour to remove any organic leftovers from the dispersant and imperfections in the membrane. Then the water step was repeated to remove any leftover hydrogen peroxide in the structure, the membrane was then submerged in a solution of 0.1 M sulphuric acid (Fisher Chemical) at 80ºC for 1 hour to help with fully protonating all of the sulphonic acid side groups and ensuring good water transport, and finally the water step was repeated again to remove any excess sulphuric acid from the surface and structure [201].

3.1.2 Membrane Electrode Assembly (MEA) Manufacture

To test the membrane's performance in situ within a fuel cell, it was necessary to incorporate it into an MEA. The MEA was assembled using specific stencils (Scribner Associates) for cutting the anode and cathode from Carbon paper with a microporous carbon layer on

top (sigracet 29B) into a 5 cm^2 area. The anode was an industrially made gas diffusion electrode from Johnson Matthey, the cathode was made in-house as a one-sided catalyst coated membrane and GDL hot pressed together. The membrane was either Nafion 212, Nafion 211, or a membrane made in-house with the base polymer as Nafion. For catalyst layer application, a silicon mask was used with a hole of 5 cm^2 so that the final MEA would have a catalyst layer of appropriate platinum loading.

Catalyst ink preparation involved combining 10 mg of 40% platinum on carbon hispec 3000 (Johnson Matthey), 0.064 ml of Nafion solution (Du Pont), and 0.936 ml of ethanol (Fisher Chemicals) as a dispersant, followed by sonication for 10 minutes (5 s on 5 s off) at 20% power. The mixture was created as to provide a 0.4 mg cm^{-2} loading on the final CCM. The ink was then applied to the cathode side of the membrane using an airbrush (Fengda), dried and weighed, to find the loading. The MEA components were assembled by stacking and hot pressing at 130°C, applying 0.1 Tonne of pressure to seal the assembly into a single cell for testing.

3.1.3 Characterisation

3.1.3.1 Swelling

The purpose of swelling measurements is to identify the dimensional changes expected from the membrane as it hydrates during operation. Of chief importance for membrane swelling is the Z direction or swelling through the thickness, it can cause an increase in the compression of the other layers as well as enhance some of the mechanical degradation processes. It is important to note that swelling in Nafion membranes is inherently anisotropic, affecting different dimensions to varying degrees. In this study, we report

only on the swelling of the membrane's thickness. This approach presents a limitation, as significant increases in water uptake might not correspond proportionally to changes in thickness but could instead manifest predominantly in the X-Y dimensions. This aspect should be considered in future analyses, particularly when discrepancies in hydration and dimensional swelling are discussed in subsequent chapters.

Swelling measurements were taken by cutting the membrane into small pieces with dimensions of 1 cm x 2 cm area. They were dried in an oven for 24 hrs at 50°C, once dried the membrane's thickness was measured using a micrometre (RS Pro). The membrane was then submerged in deionised water for a further 24 hrs and the swollen thickness of the membrane was taken. Using the following equation it was possible to calculate the swelling factor for the membrane. Measurements of the wet thickness at 50 °C is also taken, a total of 5 repeats were taken for each membrane.

$$Swelling\% = \frac{(T_{Wet} - T_{Dry})}{T_{Wet}} \tag{3.1}$$

Where T_{Wet} and T_{Dry} represent the wet and dry thickness respectively. When hot pressing, the electrode is bound to the dry membrane area on both sides which dimensionally stabilizes the X and Y directions, otherwise, the electrode would delaminate. The membrane will transport water in the X and Y directions so there will be some dimensional change outside of the active area but inside the active area it should primarily happen in the Z direction.

3.1.3.2 Water uptake

Water uptake is an important measurement of a membrane, as Nafion and other PFSA-type membranes rely on water to enhance the proton transport properties of the membrane. In a similar way to the swelling measurements, water uptake requires a dry measurement and a wet measurement. The weight of sample was taken in this case. The procedure of drying and wetting the sample remained the same and the size of sample was similar, as a smaller piece reduced the influence of surface bound water droplets. A total of 5 repeats per sample were taken. Water uptake was given as a percentage also using the following equation.

$$WaterUptake\% = \frac{(m_{Wet} - m_{Dry})}{m_{Wet}} \tag{3.2}$$

Where m_{Wet} and m_{Dry} represent the wet and dry mass respectively.

3.1.3.3 Ion exchange capacity

Ion exchange capacity (IEC) is a measure of the membranes capacity to hold ions. This capacity is proportional with conductivity. It shouldn't change as it is a property of the base polymer and therefore should remain constant for the same polymer. IEC measurements were taken by a titration method. First the samples were soaked in water saturated with NaCl for 72 hrs. Then the membrane was washed with DI water before titrating NaOH and phenolphthalein until the solution changes colour. Equation 3.3 was applied to the results to calculate the IEC [202] , given by

$$IEC = \frac{(V_{NaOH} \cdot C_{NaOH})}{m_{Dry}} \tag{3.3}$$

where V is the volume of NaOH, C is the concentration of NaOH, and m is the dry mass of the membrane [98].

3.1.3.4 Surface and cross-section characterisation by SEM

Nafion is an insulating material, so SEM characterisation is difficult for high resolution. Usually this requires high energy beams which can cause the membrane to melt or change shape. Therefore, samples which require high resolution imaging have to be coated in gold using a sputter coater. For samples that will look at the cross-section of the membrane, they must be freeze-cracked as exposing the membrane to shear will cause the polymer chains to align in the direction of shear which will not be truly representative of the cross-sectional structure.

3.1.4 Contact Angle Measurement

Contact angle measurements were taken using a theta optical tensiometer (biolin scientific). The measurements involved placing a droplet of water on the surface of the test material while a camera relayed an image through software to determine the angle of contact between the droplet and the surface. The droplets were targeted to three points on the patterned surface, to get 3 repeats of the angle measurement. The measurements were taken using DI water.

3.1.5 Fuel cell testing

Electrochemical testing of fuel cells, such as using methods like polarization curves, electrochemical impedance spectroscopy (EIS), and cyclic voltammetry, serves to evaluate

key performance metrics such as cell voltage, current density, and overall efficiency under varying operational conditions. This testing facilitates the characterization of the electrocatalytic activity and stability of the fuel cell components, providing insights into reaction kinetics, charge transfer processes, and the degradation mechanisms. Ultimately, these measurements enable optimization of the cell design and operational parameters to enhance durability, efficiency, and cost-effectiveness of the fuel cell systems. Prepared MEA's are ready to be used in the fuel cell test stand (Scribner 850e). The EU harmonisation protocol for breaking in new cells was conducted before performing measurements [203].

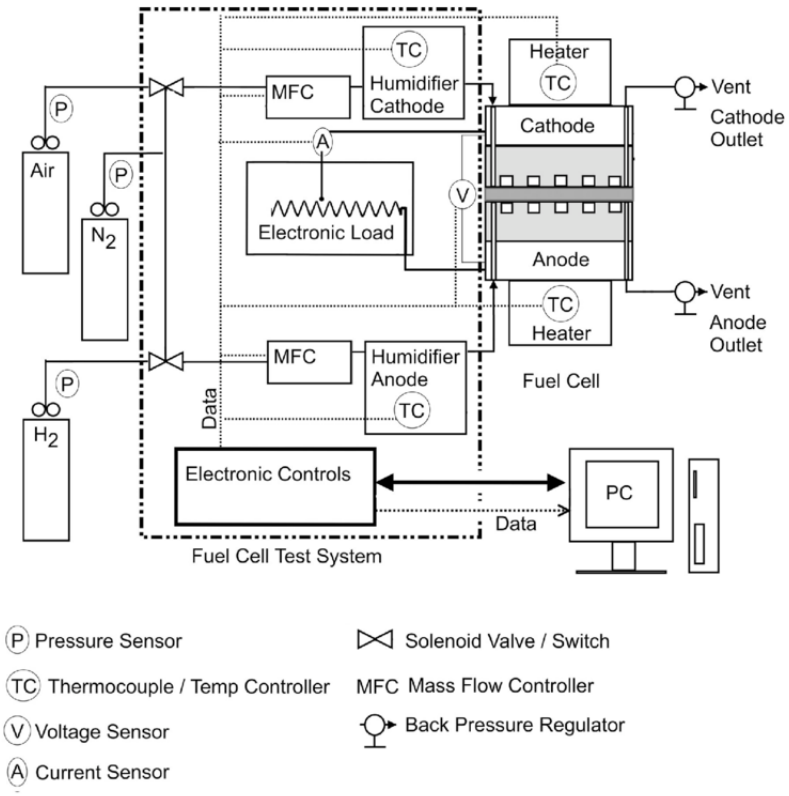

Figure 3.1: Schematic of fuel cell test stand from [204]

Figure 3.1 shows the schematic for a Scribner fuel cell test station and contains all the components in the test system which allow the tests to proceed; the system has software

which can test the components and ensure they're functioning within their specification. The humidity function of the test stand is set using the temperature of the humidifier. This allows time to come to equilibrium and then the temperature of the humidifier is expected to keep up with the mass flow rate of gas. This is guaranteed by Scribner when specifying the test station at 2 standard litres per minute (SLPM) for the anode and 5 SLPM for the cathode.

3.1.5.1 IV curve procedure (Polarisation)

After assembling the sample holder and setting up the 4 electrode system, hydrogen and air were supplied to the anode and cathode side, respectively, using a flow rate of 120 mlmin^{-1} for the anode and 300 mlmin^{-1} for the cathode. The flow rates were chosen based upon a 1.5 stoichiometric flow rate at 2 Acm^{-2}. The back pressure could then be set for both sides, 1.5 bar for the anode and 1.3 bar for the cathode. The test software is used to set the cell temperature, gas temperatures, and humidity to 80°C. The cell is then set at a constant potential of 0.6 V for at least 6 hrs, often overnight. In the morning the anode and cathode relative humidity were both set to 50% which is done by setting a humidifier temperature of approximately 64°C. Then a voltage scan was set between OCV and 0.35 V and back to OCV with a step size of 0.05 V and 5 minutes measuring per point. This enabled each point in the scan to reach equilibrium before data was recorded to ensure the minimisation of transient voltage effects.

For the modelling work, the back pressures were set to 2 barg on both sides to account for the higher temperatures used in operation. The remainder of the procedure was the same, when varying the relative humidity the cell was left at 0.6 V and the humidifiers

were allowed to cool over a 2-6 hour period depending on the temperature difference. The lowest relative humidities were performed first after break in. The wait time required from break in conditions to 30% RH steady state was approximately 6 hours. Once the total battery of tests were performed at 30% RH the the cells were set to the next relative humidity step up and allowed 2 hours to heat up and reach equilibrium at 0.6 V. The reason 0.6 V holds were chosen is to minimise the flooding of the cathode which can enhance degradation over the short term when idling, and to ensure that stead-state conditions were attained before each test.

3.1.5.2 Hydrogen crossover

By removing the air from the system and instead running the cell with nitrogen, it was possible to get a parasitic current of hydrogen crossover. By using the potentiostat built into the Scribner 850e it was possible to scan voltage from OCV to 0.1 V to determine hydrogen crossover. The hydrogen diffusion limiting region of 0.3 to 0.35 V was chosen as this was where a response was expected [50].

3.1.5.3 Electrochemical surface area (ECSA) measurement

Similar to the measurement of crossover, the air from the system was removed by holding the cell at 0.6 V and switching gases from air to nitrogen. Limiting the flow rate of nitrogen to 1 $\mathrm{mlmin^{-1}cm^{-2}}$ as per the findings of Carter et al. [205], and reducing the cell temperature to 30°C as discussed by Garrik et al. [206] to avoid loss in accuracy due to weakening the hydrogen adsorption process. Using the potentiostat in the Scribner 850e test rig, it was possible to run a constant voltage (CV) between 0 and 1.2 V vs reference electrode (RE). This graph is analysed using the trapezium rule to find the area under the

curve, the total charge of the H^+ adsorption peak [205, 207].

3.1.6 Electrochemical Impedance Spectroscopy

Electrochemical impedance spectroscopy (EIS) is a non-destructive method used to study electrochemical systems, often performed in-operando with a two-electrode setup in polymer electrolyte fuel cells (PEFCs). It uses a frequency response analyser which is a component of the electronic load, and therefore uses the same set up in figure 3.1. The results are typically presented in a Nyquist plot, with imaginary impedance on the y-axis and real impedance on the x-axis across a range of frequencies, creating a spectrum [208]. A typical impedance spectrum includes three general features shown in figure 3.2:

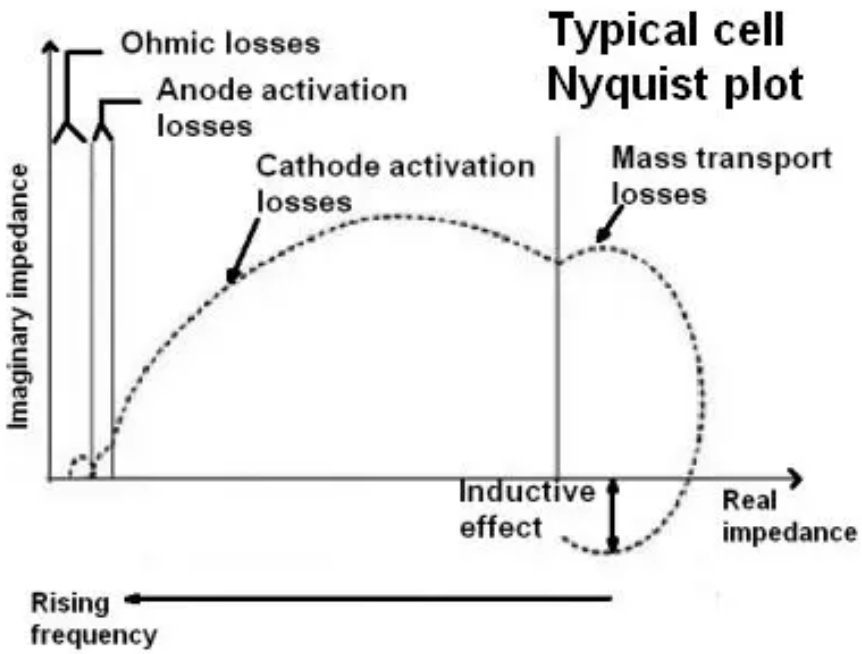

Figure 3.2: Generic fuel cell impedance spectra

- The high-frequency region is associated with the internal ohmic resistance of the membrane, catalyst layer, and bipolar plates, predominantly attributed to the membrane resistance [186, 196, 209].

- The medium-frequency region is represented by an arc reflecting the effective charge-transfer resistance linked with the oxygen reduction reaction (ORR) and the double-layer capacitance within the catalyst layer (CL). The ORR is the dominant resistance in this spectrum section [162, 210, 211].

- The low-frequency element, another arc, mainly reflects the mass-transport limitations within the gas diffusion layer (GDL) and CL, often due to water flooding of the cathode [208].

The Scribner 850e supports 4 electrode cell measurements, 2 load and 2 sense. This allows the removal of the load resistance effects from the impedance measurement, which would appear as an additional resistance and inductance in the impedance spectra. As such a 4 electrode set up for an impedance measurement could facilitate the addition of a 3rd reference electrode, however the cell hardware and seals does not account for this in the standard design. As the standard cell holder from Scribner was not modified, the EIS measurements taken represent the whole cell. According to the book Electrochemical Impedance spectroscopy in PEM fuel cells [208], this means when analysing the results there will a combination of anode and cathode processes in the EIS spectra. The ohmic portion will remain as the high-frequency resistance. It means that a half cell fitting using the Randles circuit becomes more complicated, and does not allow for differentiation between processes on the sides.

3.1.6.1 Equivalent Circuit Analysis

Impedance analysis often involves constructing an equivalent circuit (EC) that replicates the impedance response of the fuel cell. To create an EC model, Bode plots (magnitude

vs. frequency and phase vs. frequency) are used, as shown in Figure 3.4.

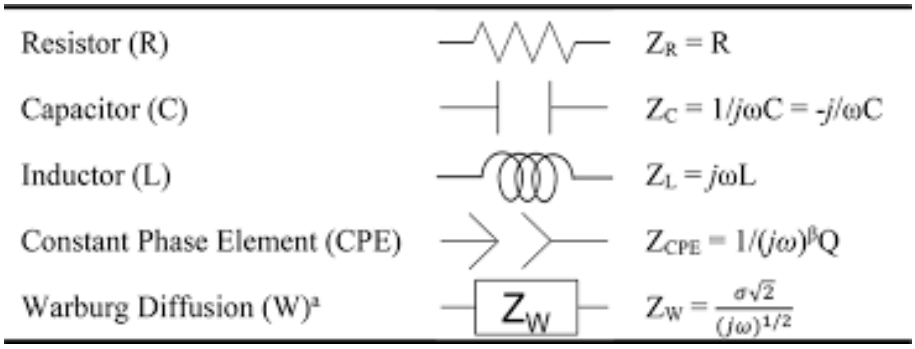

Figure 3.3: Key of elements used in equivalent circuits, and their impedance equations

3.1.6.2 Typical experimental conditions

These measurements were made by setting a constant current or voltage, then applying a 5% AC signal at different frequencies between 100 mHz and 10 kHz, and measuring the phase angle of the response. The settings used here were 0.45 A, 0.6 V, and 0.4 V for our low, medium, and high current measurements, respectively. These measurements gave readings in the three major resistance phenomena regions, so the relative resistance could be compared with a baseline.

3.2 Modelling

This section details a 1-dimensional MEA model incorporating 1D gas flows, water sorption, saturation physics, and thermal modelling, implemented using COMSOL Multiphysics.

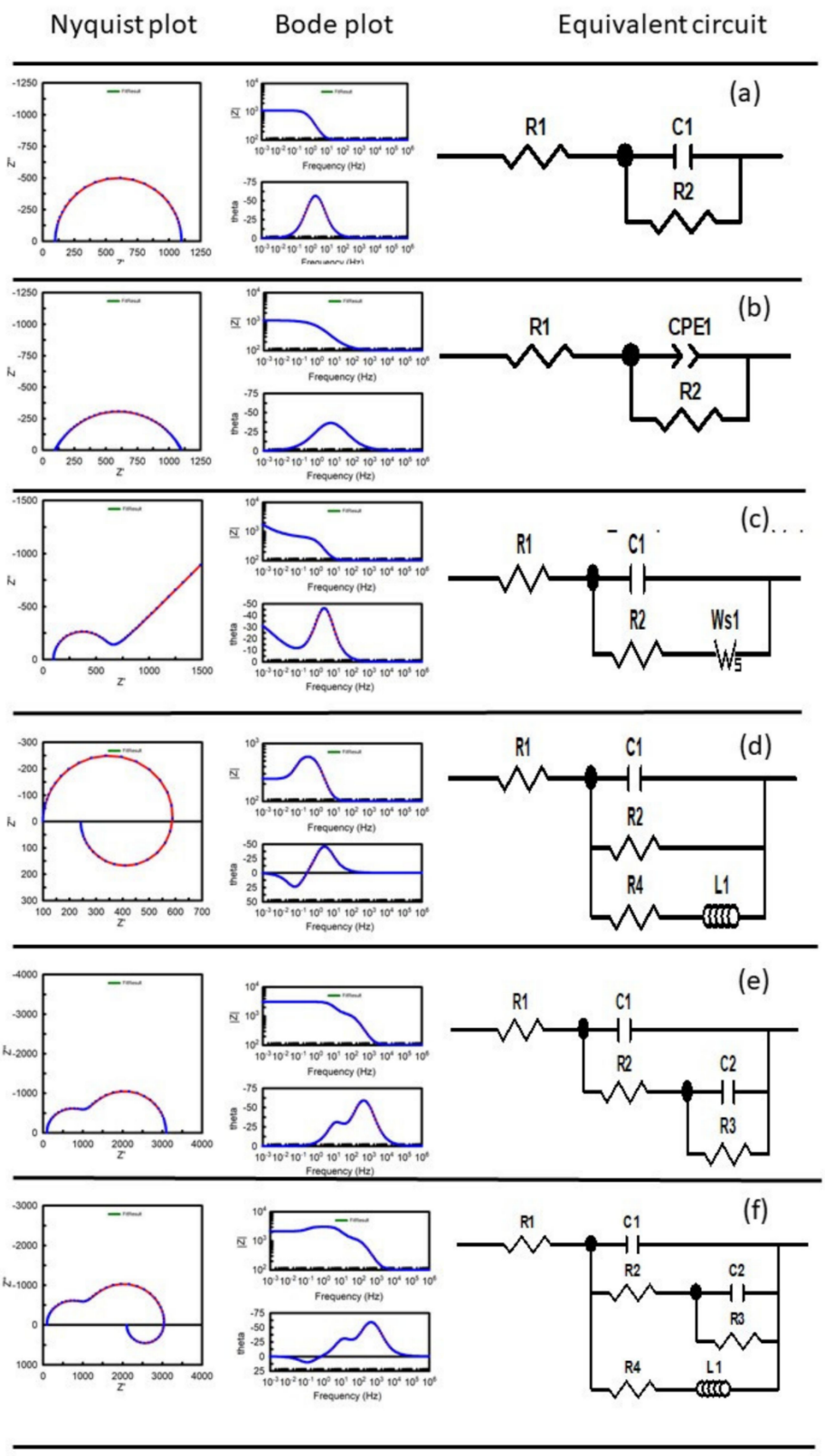

Figure 3.4: Common shapes of Bode and Nyquist plots interpreted as ECs, adapted from Feliu et al. [212].

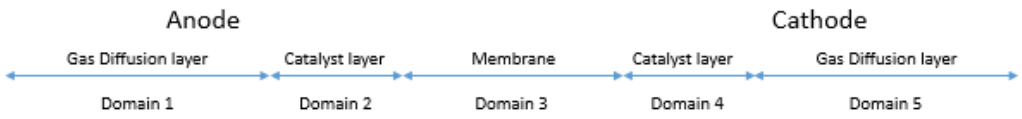

Figure 3.5: Modelling domain diagram

3.2.1 Simplifications and Assumptions

The gas streams in the model are treated as laminar flows of concentrated multi-species ideal gas streams within their respective domains. The anode and cathode gas streams consist of mixtures of hydrogen, oxygen, nitrogen, water vapour, and some inert components. These streams are described by conventional conservation equations with known mixture properties and specified pressure boundary conditions. The MEA, separating the two gas streams, is modelled as a collection of variables and boundaries, with layers assumed to have uniform material properties for computational simplicity.

Water in the gas streams and the catalyst layer, either as vapour or liquid, is treated as a finely dispersed mist. Within the membrane, the water-vapour mixture is considered in the conductivity profile, with water treated as dissolved water for the governing transport equations. The correlations used for the membrane are based on data collected at 30 to 50°C and atmospheric pressure. Due to the lack of specific data on transport phenomena inside the membrane at higher temperatures and pressures, these correlations are assumed to remain valid under these conditions.

3.2.2 Transport of Chemical Species

The transport of concentrated chemical species in the model is governed by equations that account for convective, diffusive, and reactive sources. These equations describe the general physics governing the behaviour of these species under the conditions modelled.

$$\nabla \cdot \mathbf{N}_j = S_j \tag{3.4}$$

where $\mathbf{N}_j$ and S_j are the mass flux and source terms of species j (i.e. O_2, H_2O, or N_2), respectively. $\mathbf{N}_j$ is obtained using the Maxwell-Stefan equation.

$$, \mathbf{N}_j = -\rho\omega_j \sum_k D_{jk}^{eff} \frac{M}{M_k} \left(\nabla\omega_k + \omega_k \frac{\nabla M}{M} \right) \tag{3.5}$$

with

$$M = \sum x_j M_j \tag{3.6}$$

$$\rho = \frac{pM}{RT} \tag{3.7}$$

As reported here[213] the Bruggeman approximation overpredicts the diffusivity in the GDL by up to a factor of 2 so the empirically derived equation 3.8 from the source was used instead. The effective diffusivity of the gases into the gas diffusion layer is given as [144, 147, 213]

$$D_{jk}^{eff} = 0.008 \exp(4.81\epsilon) D_{jk} \tag{3.8}$$

where ϵ is the porosity and D_{jk} is the diffusivity of species j in material k. The effective diffusivities within the catalyst layers were estimated using the Bruggeman approximation:

$$D_{jk}^{eff} = \epsilon_{CL}^{1.5} D_{jk} \tag{3.9}$$

The diffusivities were corrected for pressure and temperature using the following equation [214]

$$D_{ij} = D_{ij}(T_0, p_0)\frac{p_0}{p}\left(\frac{T}{T_0}\right)^{1.5} \tag{3.10}$$

The reference pressure p_0 was set to 1 atm, and the values for the reference temperatures T_0 were 298 to 307.5 K, taken from Berning et al. [214]. The source term in equation 3.4 is the consumption/production rate of oxygen, hydrogen, and water vapour:

$$S_{O_2} = -\frac{IM_{O_2}}{4F} \tag{3.11}$$

$$S_{H_2} = -\frac{IM_{H_2}}{2F} \tag{3.12}$$

$$S_{H_2O} = I\left(\frac{nd}{F} + \frac{M_{H_2O}}{2F}\right) \tag{3.13}$$

Where I is the volumetric current density (Am^{-3}), M_{O_2}, M_{H_2}, and M_{H_2O} are the molecular weight of oxygen, hydrogen, and water, respectively, F is Faraday's constant and nd is the net-drag coefficient that is calculated as follows:

$$nd = \frac{2.5\lambda}{22} \tag{3.14}$$

where λ is water content and explained in equation 3.31

3.2.3 Transport of electronic and ionic charge

The following equations govern the transport of electrons and protons in the electrically and ionically conductive components.

$$\nabla(-\sigma_s^{eff}\nabla\phi_s) = \nabla \cdot i \tag{3.15}$$

$$\nabla(-\sigma_m^{eff}\nabla\phi_m) = \nabla \cdot i \tag{3.16}$$

where the solid phase potential is ϕ_s, the membrane phase potential is ϕ_m, and i is the volumetric current density (Am^{-3}). σ_s^{eff} and σ_m^{eff} are the effective electrical conductivity of the solid phase and effective membrane conductivity, respectively. The gas diffusion layer effective conductivity σ_{GDL}^{eff} is provided in Table 3.3. The electrical conductivity of the catalyst layer is calculated as

$$\sigma_{cat}^{eff} = \sigma_{GDL}^{eff}[(1-\epsilon_{cat})(1-\nu_{naf})]^{1.5} \tag{3.17}$$

where ϵ_{cat} is the porosity of the catalyst layer and ν_{naf} is the volume fraction of the ionomer phase in the catalyst layer. Subsection 3.2.5 defines the effective membrane conductivity. The activation overpotential η for the anode (η_a) and cathode (η_c) electrodes are obtained as

$$\eta_a = \phi_s - \phi_m \tag{3.18}$$

$$\eta_c = \phi_s - \phi_m - E \tag{3.19}$$

where E is the equilibrium potential and is given by

$$E = E_0 + \frac{RT}{2F} \ln \left(p_{H_2} \cdot p_{O_2}^{1/2} \right) \tag{3.20}$$

Where E_0 is the reference equilibrium potential at ambient temperature $(1.23V)$ and, p_{H_2} and p_{O_2} are the partial pressures of hydrogen and oxygen respectively. The above activation overpotential is required to calculate the anodic (I_a) and cathodic (I_c) volumetric current densities through Butler-Volmer equations:

$$I_a = I_{0,a} \frac{C_{H_2}}{C_{H_2}^{ref} H_{H_2}} \left(\exp \frac{-(1-\alpha_a) F \eta_\alpha}{RT} - \exp \frac{\alpha_a F \eta_\alpha}{RT} \right) \tag{3.21}$$

$$I_c = A_{Pt}^{eff} i_{0,c} (1-S) \frac{C_{O_2}}{C_{O_2}^{ref} H_{O_2}} \left(- \exp \frac{-\alpha_c F \eta_c}{RT} \right) \tag{3.22}$$

Where $I_{o,a}$ is the volumetric anodic exchange current density (Am^{-3}), $I_{o,c}$ is the cathodic exchange current density which is multiplied by the specific area m^{-1}, A_{Pt}^{eff} to give the volumetric exchange current density, C_i is the concentrations of the species i (H_2 or O_2), C_i^{ref} is the reference concentration for the species i (H_2 or O_2), and H_i is the Henry's law coefficient for the species i (H_2 or O_2). R is the universal gas constant, F is Faraday's constant and S is the saturation term. Note the water saturation is accounted for in the Butler-Volmer equation of the cathode electrode (i.e. equation 3.22), the term $(1-S)$ represents liquid water restricting the gas diffusion pathway making it more tortuous and difficult. To convert the exchange current density to the volumetric exchange current density, we consider the specific area of the catalyst layer. The specific area A_{spec} (measured in $\mathrm{m}^2\mathrm{m}^{-3}$) indicates the surface area of the catalyst per unit volume. The volumetric exchange current density i_{a} can be derived by multiplying i_0 with A_{spec} :

$$I_{\text{o,a}} = I_0 \cdot A_{\text{spec}} \tag{3.23}$$

The effective area of platinum available throughout the cathode catalyst layer, A_{Pt}^{eff}, is given by

$$A_{Pt}^{eff} = \frac{A_{Pt} \cdot m_{Pt}}{L_{cat}} \tag{3.24}$$

where A_{Pt} is the specific area of platinum, m_{Pt} is the mass of platinum, and L_{cat} is the thickness of the catalyst layer.

3.2.4 Transport of heat

The following equation [214] governs the heat transfer in the various components of the model:

$$\nabla \cdot (k_s \nabla T) + S_e = 0 \tag{3.25}$$

Where k is the thermal conductivity and S_e is the heat (or energy) source term. The source terms for each component are given in Table 3.1.

Table 3.1: Heat transport variables across the modelling domains

Component	***Source term***
Gas diffusion Layers	$\sigma_{GDL}\phi_s^2$
Catalyst layers	$-\eta_{c/a}I_{c/a} + \sigma_{CL}^{eff}\phi_s^2 + \sigma_{mem}^{eff}\phi_m^2$
Membrane	$\sigma_m\phi_m^2$

In the fuel cell model, the heat contribution from the $T\Delta S$ term in the catalyst layer is often neglected due to its relatively small impact compared to the dominant heat sources such as reaction enthalpy and ohmic heating. This simplification, which reduces the com-

plexity of the model without significantly affecting accuracy, is justified by the minimal entropy changes and stable operational temperatures expected in this model.

3.2.5 Water transport in the membrane phase

The dissolved water in the membrane phase (in the membrane and the membrane phase in the catalyst layers) is represented by water content λ, and the following conservation equations govern its physics:

$$\nabla \cdot \left(-D_w \frac{\rho_{mem}}{EW}\right) = \nabla \left(\frac{nd\sigma_{mem}^{eff} \nabla \phi_m}{F}\right) \text{ in the catalyst layers} \tag{3.26}$$

$$\nabla \cdot \left(-D_w \frac{\rho_{mem}}{EW}\right) = \nabla \left(\frac{nd\sigma_{mem} \nabla \phi_m}{F}\right) \text{ in the membrane electrolyte} \tag{3.27}$$

Water transport within the membrane phase, including the catalyst layers and membrane electrolyte, is governed by Equations 3.26 and 3.27 which are essential for understanding and managing water movement to enhance fuel cell efficiency. These equations describe the divergence of water flux $\nabla \cdot \left(-D_w \frac{\rho_{mem}}{EW}\right)$ in terms of membrane properties like water diffusivity D_w, density ρ_{mem}, and equivalent weight EW, against concentration gradients according to Fick's law. Additionally, they account for electro-osmotic drag, where $\nabla \left(\frac{nd\sigma_{mem}^{eff} \nabla \phi_m}{F}\right)$ in the catalyst layers and $\nabla \left(\frac{nd\sigma_{mem} \nabla \phi_m}{F}\right)$ in the membrane electrolyte depict proton transport through varying conductivity scenarios. These dynamics crucially impact the fuel cell's performance, particularly through hydration management, which ensures optimal proton conductivity and operational efficiency, while preventing issues like flooding or drying that could severely impair function.

$$D_w = 10^{-6} \exp\left(\frac{2416}{273+T}\right)\left(2.563 - 0.33\lambda + 0.0264\lambda^2 - 0.000671\lambda^3\right) \tag{3.28}$$

The equation 3.28 models the diffusion coefficient of waterD_w in the membrane as a function of the hydration level λ and cell temperature T_{cell} [188], incorporating a temperature-dependent exponential term to reflect the activation energy dynamics and a polynomial in λ to capture the non-linear effects of water content on diffusion. The diffusion coefficient decreases with increasing λ due to the increasing congestion of water pathways, while the exponential term accounts for the enhanced mobility of water molecules at higher temperatures.

The membrane ionic conductivity for Nafion 211 is a correlation based on measurements by BekkTech LLC, their assets were bought by Scribner Associates however the data is no longer available at the source. Similar data with NR-212 supplied by Bekktech LLC are available in work by Cooper [215]. Here curves for conductivity are given at 80, 100, and 120°C. Therefore, it is likely that the correlation is based on data in a similar range and valid for temperatures up to 120°C. Membrane conductivity is given as [195]

$$\sigma_{mem} = (2.0634 + 1.052\lambda + 0.010125\lambda^2) \exp\left[751.4\left(\frac{1}{303} - \frac{1}{T}\right)\right] \tag{3.29}$$

where the conductivity is in Sm^{-1}, the original is in Scm^{-1} but has been adapted in this form to give Sm^{-1}, λ is the water content per sulfonic acid group in the membrane, and T is the temperature in Kelvin.

The conductivity of the membrane phase in the catalyst layers is corrected as

$$\sigma_{mem}^{eff} = \sigma_{mem} \left((1 - \epsilon_{cat})\nu_{naf}\right)^{1.5} \tag{3.30}$$

where σ_{mem}^{eff} is the effective membrane conductivity, ϵ_{cat} is the porosity of the catalyst layer, and ν_{naf} is the volume fraction of Nafion in the catalyst layer and are defined in Table 3.3. Boundary condition values of water content at the interfaces between the gas diffusion layers and the catalyst layers are required to solve equation 3.27; these boundary conditions water contents λ_{BC} are given using the following equation [195] where the temperature is given in Celsius:

$$\lambda_{BC} = (1 + 0.2352a^2 \cdot \left(\frac{T - 30}{30}\right)) \cdot (14.22a^3 - 18.92a^2 + 13.41a) \tag{3.31}$$

This correlation is an update of the Springer et al[188] model measured and suggested by Mittlestead and Liu[192] using a form similar to Brunauer-Emmett-Teller sorption isotherm model. Its form was applied successfully to several materials up to 80% relative humidity at 80°C. The model was then further used to correlate relative humidity and temperature up to 95°C for nafion type membranes and other PFSA based membranes up to 120°C. A conditional statement was included to limit the calculation of activity to that measured by high frequency intercept impedance spectroscopy, in this way the maximum conductivity is converted to a value of lambda and then converted into an activity, allowing the model to not over-predict the activity. This was implemented using an IF statement which overrides the calculation of lambda when values of activity exceed the

maximum from the experiment. In this way the water may accumulate in the gas streams; however, it might not all be useful in increasing the conductivity of the membrane or ionic components.

a is the water activity and is given by

$$a = \frac{p_w}{p_s} \tag{3.32}$$

where p_w is the partial pressure of water vapour and p_s is the saturation pressure of water vapour and obtained (in atm) as

$$\log_{10}(p_s) = -2.1794 + 0.02953(T - 273.15) - 9.1837 \times 10^{-5}(T - 273.15)^2 + 1.4454 \times 10^{-7}(T - 273.15)^3 \tag{3.33}$$

In cases where there is liquid water accumulation within the fuel cell, the membrane hydration will exceed the level predicted by water activity alone. To account for the increased water saturation, the concept of 'activity' is extended beyond 1. Springer et al. first proposed a model that includes the mole fraction of water (X_w) multiplied by the system pressure (P) and divided by the saturation pressure (p_s). This approach accounts for liquid water by considering the mole fraction of water as inclusive of both liquid and vapour phases. It essentially represents a pseudo-two-phase approximation where liquid water is treated as additional vapour without extra momentum considerations. Although more detailed two-phase models exist, the following approximation is utilized in this work:

$$a = \frac{X_w \cdot P}{p_s} \tag{3.34}$$

Where a represents the water activity. This formulation allows for a more accurate representation of water transport and membrane hydration in scenarios where liquid water is present in the fuel cell.

Poullet's law was used to evaluate the membrane conductivity and convert it into resistance to be compared with the high-frequency resistance.

$$R = \frac{t_{mem}}{\sigma A} \tag{3.35}$$

Where R is the resistance, σ is the membrane conductivity, t_{mem} is the thickness of the membrane, and A is the surface area of the membrane.

3.2.6 Water vapour saturation

The transport of liquid water in the porous media (i.e.the gas diffusion layers and the catalyst layers) is accounted for through the conservation equation of effective water vapour saturation, s [145, 146]:

The effective water saturation, which disregards the impact of the immobile saturated water, is crucial in the context of fuel cell performance. Immobile water represents the fraction of pore space filled with water that is unable to contribute to liquid water transport due to its inability to flow or move through the pores. Therefore, the effective saturation is the portion that significantly influences the performance of the fuel cell.

$$\nabla \cdot \left(\frac{\rho_w K s^3}{\mu_w} \frac{dp_c}{ds} \right) \nabla S = S_s \tag{3.36}$$

Equation 3.36 quantifies the transport of liquid water through the porous media of fuel

cells, where $\nabla \cdot \left(\frac{\rho_w K s^3}{\mu_w} \frac{dp_c}{ds} \right) \nabla S$ represents the divergence of water flux, driven by capillary pressure gradients. This expression combines the hydraulic properties of the media, such as permeability (K) and saturation (s), with the fluid properties (ρ_w, μ_w) to model how capillary forces and water viscosity influence water movement through the pores, critical for maintaining optimal cell hydration and efficiency.

where s is the effective saturation and is given by equation 3.37:

$$s = \frac{s - s_{\text{im}}}{1 - s_{\text{im}}} \tag{3.37}$$

where s_{im} is the immobile saturation which represents the portion of the pore space filled with water that cannot move or contribute to flow.

p_c is the capillary pressure which is given by:

$$p_c = \frac{\sigma_w cos(\theta)}{\sqrt{\frac{K}{\epsilon}}} 1.417s - 2.12s^2 + 1.263s^3 \tag{3.38}$$

where σ_w is the surface tension of liquid water, and θ is the contact angle. S_s is the saturation source term and is obtained by:

$$S_s = \gamma M_{H_2O}(1 - s)\frac{(p_w - p_s)}{RT} \quad if \quad p_w > p_s \tag{3.39}$$

$$S_s = \gamma M_{H_2O} s \frac{(p_w - p_s)}{RT} \quad if \quad p_w \leq p_s \tag{3.40}$$

where γ is the condensation rate constant.

$$\gamma = 0.1 * A_s \tag{3.41}$$

where A_s is the saturation specific area.

Note that the conservation equation of effective saturation was only applied to the cathodic gas diffusion layer and the catalyst layer (where water is produced) and was not applied to the anode side as water condensation is unlikely.

$$s = \frac{s - s_{\text{im}}}{1 - s_{\text{im}}} \tag{3.42}$$

3.2.7 Boundary conditions and numerical procedure

Dirichlet boundary conditions (i.e. specific values) were prescribed for the chemical species, the temperature, the saturation, and solid-phase potential at the edges of the gas diffusion layers. Likewise, Dirichlet boundary conditions were set for the membrane phase potential and water content at the interfaces between the gas diffusion and catalyst layers. Table 3.2 lists the boundary conditions used for the model.

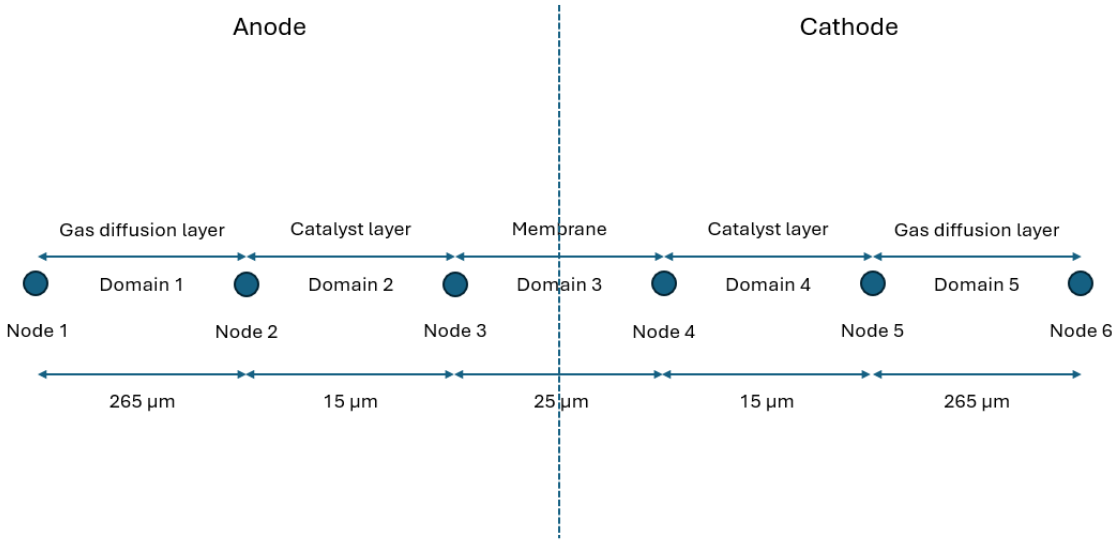

Figure 3.6: Modelling domain boundary diagram

The equations governing mass transport of gases and water vapour act within the do-

Table 3.2: Dirichlet boundary conditions used for the model. Note that the boundary conditions water contents are calculated using equation 3.31.

$\boldsymbol{Variable}$	$\boldsymbol{Value}$	Domain	Node
Mol fraction of oxygen at the cathode	$(1 - x_{H_2O}) * 0.21$		6
Mol fraction of water vapour at anode and cathode	$P_H 20/P$		6
mass fraction of hydrogen	$(1 - x_{H_2O})$		1
Voltage of cathodic terminal	0.3-1 V		6
Voltage of anodic terminal	0 V		1
Saturation	s_{im}		5
Temperature	80,100,120$^\circ C$		1 & 6

Figure 3.7: Model Mesh

mains of the gas diffusion and catalyst layers on both sides (domains 1,2,4,5), the ionic transport physics acts along the membrane and catalyst layers (domains 2,3,4), the electronic transport equations act along the catalyst and gas diffusion layers (domains 1,2,4,5). The heat transport acts across all domains with boundary conditions set at each of the edge nodes. The boundary condition for the model was a fixed temperature, equal to the respective cell temperature being studied. The membrane water transport is bound to the membrane and ionomer (domains 2,3,4). Finally the water vapour saturation physics acts in the cathode environment (domains 4 and 5).

The governing equations of the model were solved using the COMSOL multiphysics©5.6 solver using the Newton non-linear method and the default settings. The initial conditions were gathered from the 0D solutions to the equations allowing the initial values to be constant across each of the domains. The computational domain was discretised and refined using the presents in COMSOL until a mesh-independent solution was obtained; the number of elements that achieved this was 2615. Table 3.3 shows the parameters used in the model. Figure 3.7 shows the model mesh.

The mesh independence was determined by running the model until the output values of current density were unchanging, This occurred when moving the mesh size from coarse to fine along the slider in COMSOL, additional refinement was suggested by and performed with the help of Mohammed Ismail to make the mesh finer at the interfaces of the membrane and catalyst layers. This was assumed valid for all of the subsequent runs of the model.

Table 3.3: Parameters used for the model [214, 218–220].

Symbol	Value	Units	Description
A_{pt}	40	$\mathrm{m^2\ g^{-1}}$	Catalyst specific area
A_s	1000	$\mathrm{m^{-1}}$	Saturation specific area
C	96485	$\mathrm{C\ mol^{-1}}$	Faraday's constant
$\mathrm{C}_{H_2}^{\mathrm{Ref}}$	56.4	$\mathrm{mol\ m^{-3}}$	Reference concentration for H_2 [216]
$C_{\mathrm{o2}}^{\mathrm{Ref}}$	0.85111	$\mathrm{mol\ m^{-3}}$	Reference concentration for O_2[217]
$\mathrm{D}_{\mathrm{o_2,naf}}$	8.45×10^{-10}	$\mathrm{m^2\ s^{-1}}$	Diffusivity of O_2 in Nafion
EW	1000	$\mathrm{g\ mol^{-1}}$	Equivalent weight
$\mathrm{H}_{\mathrm{H_2}}$	4.56×10^3	$\mathrm{Pa\ m^3\ mol^{-1}}$	Henry's constant for H_2
$\mathrm{H}_{\mathrm{O_2}}$	3.17×10^4	$\mathrm{Pa\ m^3\ mol^{-1}}$	Henry's constant for O_2
$\mathrm{I}_{o,a}$	1.4×10^{10}	$\mathrm{A\ m^{-3}}$	Anodic volumetric reference exchange current density
$\mathrm{I}_{\mathrm{o,c}}$	0.05	$\mathrm{A\ m^{-2}}$	Reference exchange current density cathode
K	1×10^{-13}	$\mathrm{m^2}$	Absolute permeability
L_{cat}	15	μm	Catalyst layer thickness
L_{GDL}	265	μm	Gas diffusion layer thickness
$\mathrm{L}_{\mathrm{mem}}$	25	μm	Membrane thickness
$\mathrm{M}_{\mathrm{H_2}}$	2	$\mathrm{g\ mol^{-1}}$	Molecular weight hydrogen
$M_{\mathrm{H_2O}}$	18	$\mathrm{g\ mol^{-1}}$	Molecular weight water
$\mathrm{M}_{\mathrm{N_2}}$	28	$\mathrm{g\ mol^{-1}}$	Molecular weight nitrogen
$\mathrm{M}_{\mathrm{o_2}}$	32	$\mathrm{g\ mol^{-1}}$	Molecular weight oxygen
M_{Pt}	0.4	$\mathrm{mg\ cm^{-2}}$	Platinum Loading
nd	1		Electro-osmotic drag Coefficient
P	3	bar	Pressure
R	8.314	$\mathrm{J\ mol^{-1}\ K^{-1}}$	Universal gas constant
α_{a}	0.5		Anode charge transfer coefficient
α_{c}	0.8		Cathode charge transfer coefficient
ϵ_{cat}	0.48		Porosity of catalyst layer
ϵ_{GDL}	0.45		Porosity of gas diffusion layer
μ_w	4.05×10^{-4}	Pa s	Viscosity of water
ν_{naf}	0.25		Electrolyte volume fraction
ν_{sol}	0.48		Volume fraction of solid phase
ρ_{mem}	2000	$\mathrm{kg\ m^{-3}}$	Membrane density
ρ_w	1000	$\mathrm{kg\ m^{-3}}$	Density of water
σ_{GDL}	100	$\mathrm{S\ m^{-1}}$	Gas diffusion layer conductivity
σ_w	0.0644	$\mathrm{N\ m^{-1}}$	Surface tension
θ	105	degree	Contact angle

CHAPTER FOUR

PATTERNED MEMBRANES

4.1 Membrane Manufacture

This section details the production of membranes using the LIPSS moulds described in section 3.1.1, one of each mould was created for evaluation. Each mould was used to create between 3 and 5 membranes which were tested in-situ. SEM images were taken of the membranes and moulds during all stages of the production to ensure none of the processes were affecting the morphology of the membrane surface in ways other than patterning.

Patterning a surface at the microscale introduces a complex interplay between surface roughness and wettability that can significantly increase the contact angle, thereby enhancing hydrophobicity. This effect is fundamentally rooted in the Wenzel and Cassie-Baxter theories, where the presence of micro- or nano-scale structures modifies the surface topography to create heterogeneous wetting states[221]. In the Wenzel state, liquid fills the grooves of the roughened surface, increasing the actual contact area and potentially enhancing hydrophilicity if the intrinsic surface chemistry is hydrophilic. Conversely, in the Cassie-Baxter state, air pockets are trapped within the surface irregularities,

reducing the real contact area between the liquid and the solid surface. This air layer acts as a barrier, preventing the liquid from fully wetting the surface, thus increasing the contact angle dramatically. By carefully designing the pattern dimensions and distributions (e.g., through lithography, etching, or laser ablation [199]), it is possible to favour the Cassie-Baxter state over the Wenzel state, promoting higher contact angles and greater hydrophobicity.

4.1.1 Patterns in this chapter

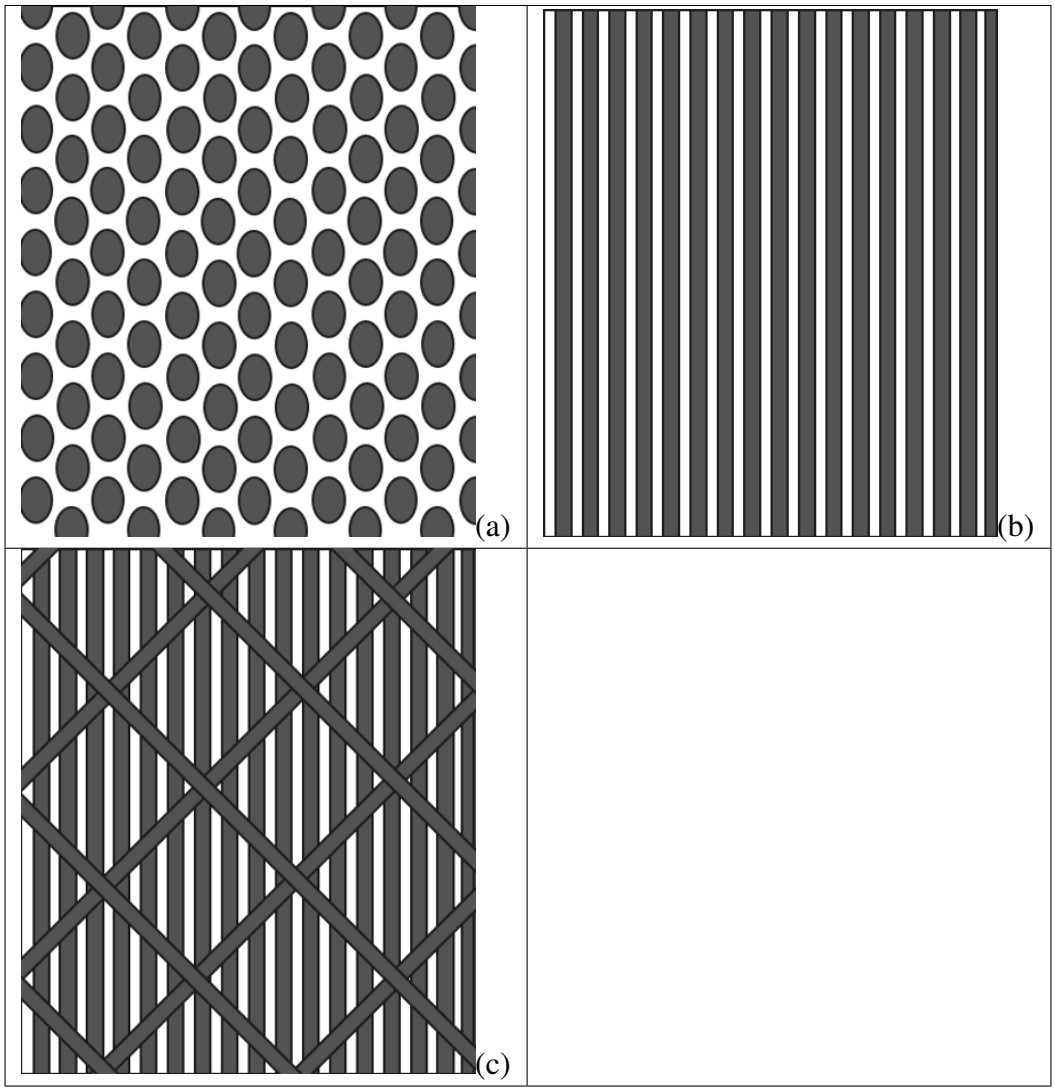

Figure 4.1: Pattern Schematics of each of the moulds used in this chapter (a) lotus, (b) lines, (c) sharklet, the width of the ovals and pitch of the lines is approximately 25 μm the other major dimensions are available in table 4.3

Figure 4.1 shows the pattern schematics for each of the patterns used to create the stainless steel moulds. Each of the patterns was chosen as an example of a hydrophobic surface, with the Lotus mimicking the natural surface pattern of a Lotus leaf with oval structures. The Lines pattern was intended to have a simple set of lines as features that could exhibit hydrophobicity. The Sharklet went one step further and attempted to enhance the Lines

pattern hydrophobicity with the addition of a diagonal grid overlaid on the lines.

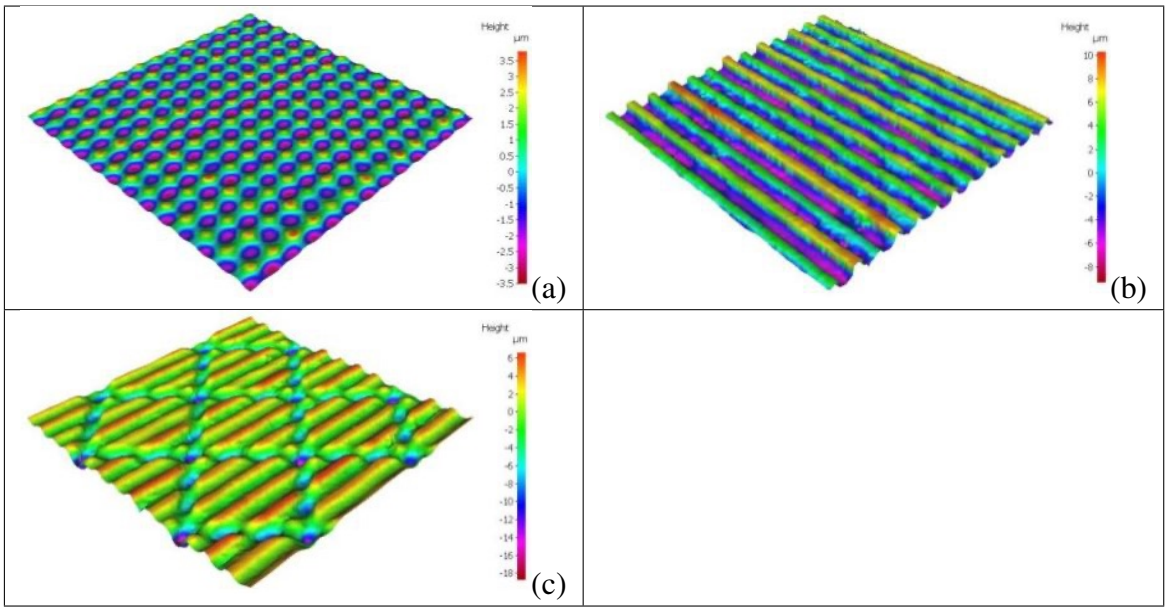

Figure 4.2: Interferometer images of the stainless steel moulds courtesy of JM Romano.

Figure 4.2 shows the stainless steel mould patterns measured by interferometer. The lotus pattern is similar to that of the leaf of a lotus leaf. The lines is a basic hydrophobic pattern with repeating lines. The sharklet pattern is a mixture of lines with diagonal square pattern cut over the top, mimicking a similar pattern to the skin of a shark. They are all based upon hydrophobic patterns, as discussed in the literature review many other authors used similar hydrophobic patterns as a basis for membrane patterning.

4.1.2 Contact Angle Measurements

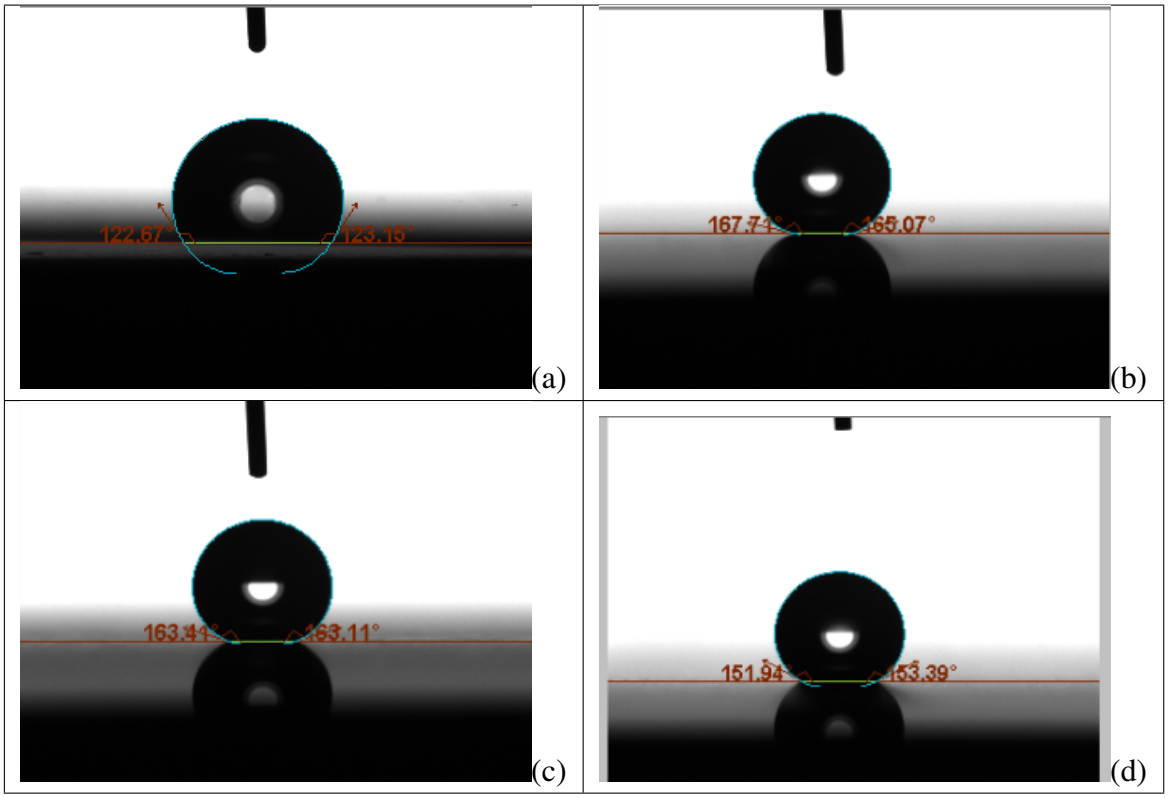

Figure 4.3: Contact angle measurements of the bare steel moulds, (a) flat (b) Lotus (c) Lines (d) Sharklet

Table 4.1: Contact angles measured from steel mould surfaces

Pattern	Contact angle
Flat	122.9°± 0.3
Lotus	166.4°± 1.3
Lines	163.3°± 0.2
Sharklet	152.7°± 0.7

Figure 4.3 shows the LIPSS patterning conferred a big increase in contact angle over unpatterned with all patterns, meaning each pattern was more hydrophobic than the bare steel. Kim et al. [62] gave some insight that hydrophobic properties of the pattern may lead to some enhanced water transport. In order to obtain a clear benchmark, all the patterns were chosen with different feature sizes but similar contact angle measurements; i.e. the same or at least similar hydrophobic properties. Jean-Michel Romano carried out

an optimisation of the features for the patterns to achieve a similar contact angle value similarly to his published work [199].

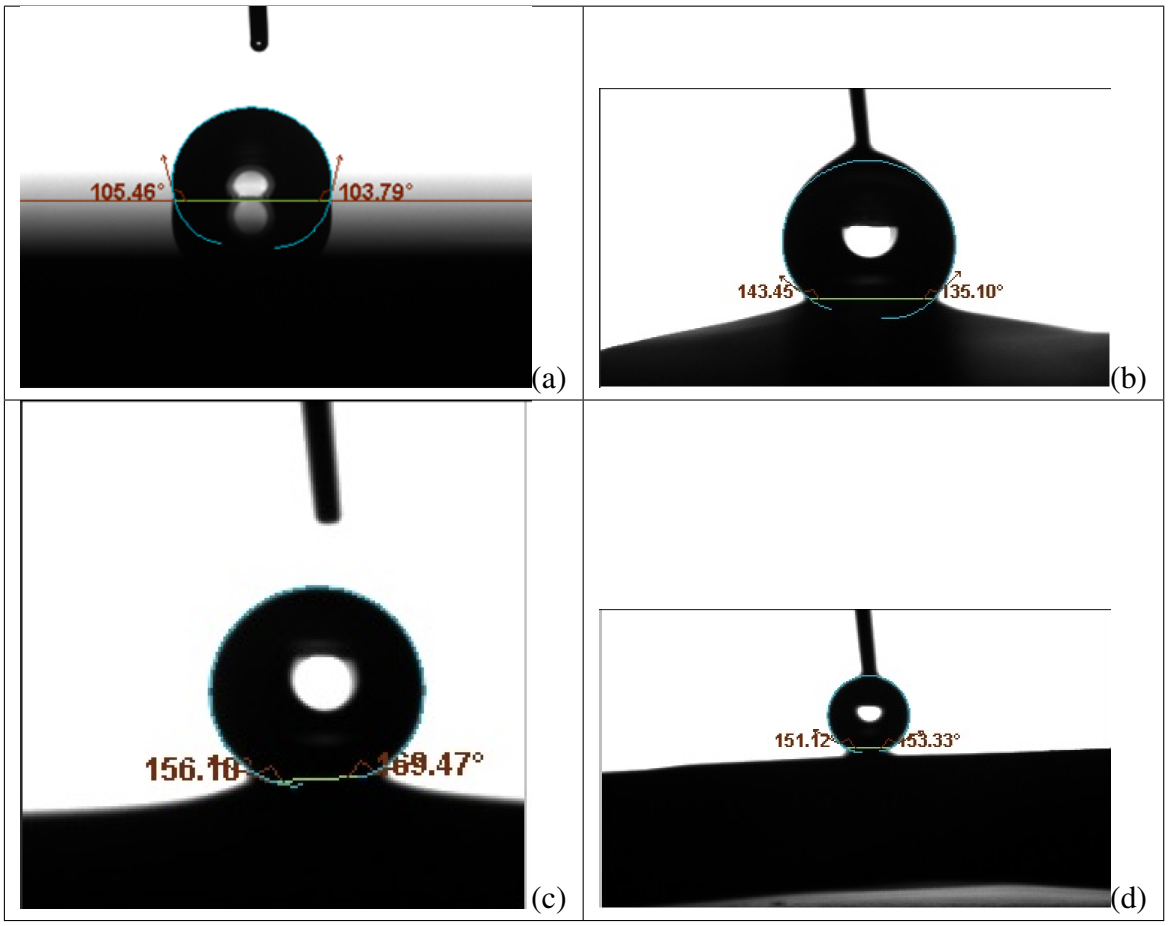

Figure 4.4: Contact angle measurements of the patterned membranes, (a) Flat membrane (b) Lotus (c) Lines (d) Sharklet

Table 4.2: Contact angles measured from patterned membrane surfaces

Pattern	Contact angle
Flat	104.6°± 0.84
Lotus	139.3°± 4.2
Lines	162.8°± 6.7
Sharklet	152.2°± 1.1

Figure 4.4 shows the contact angle of the patterned membranes after being removed from their moulds and dried in an oven for 24h at 50°C. Table 4.2 shows the range of data for the replicated contact angle, each one of the membranes was quite difficult to measure

as the water droplet would over time start to swell towards the droplet skewing the image and the measurement. The images were taken at the same interval between applying the droplet and capturing the image which was 5 seconds. There was good replication of the contact angle between the lines and sharklet pattern; however, the lotus pattern did make a difference when compared to the unpatterned but it was much further away from the steel mould measurement than the other patterns.

4.1.3 SEM Images

	Lotus	Lines	Sharklet
Master Mould (plan view)	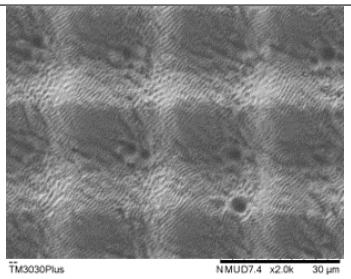	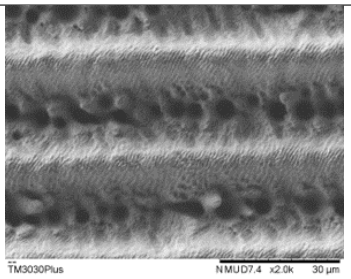	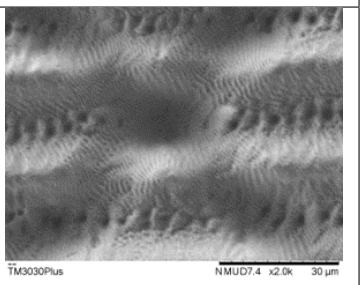
Cast Nafion (plan view)	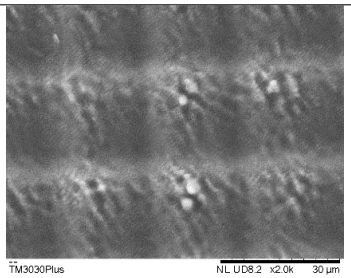	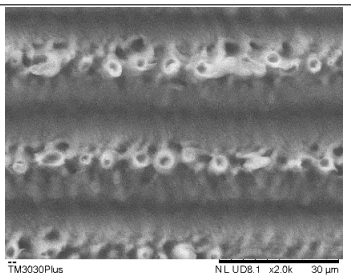	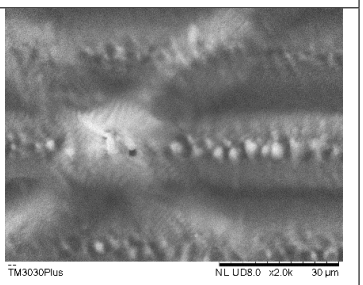
Post Activation (plan view)	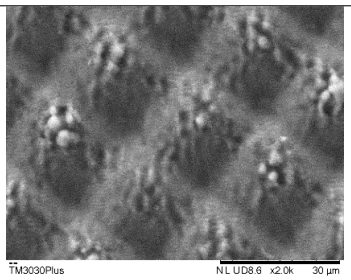	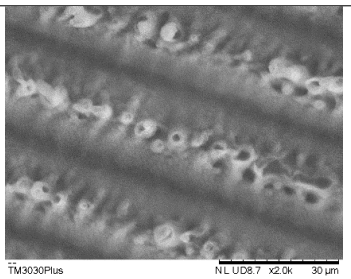	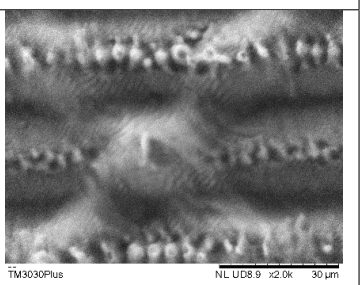
Cross Section (side view)	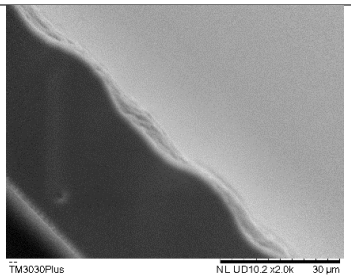	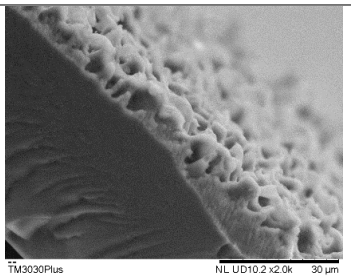	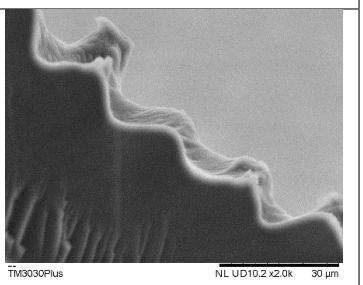
Spray-coated Cross Section (side view)	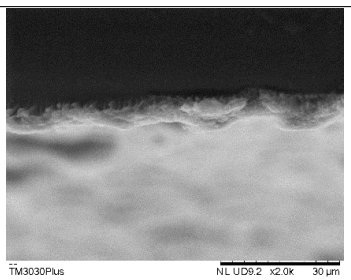	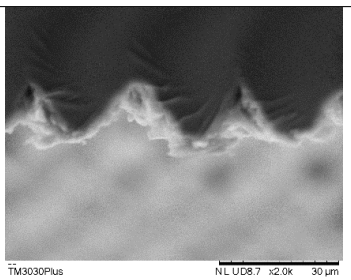	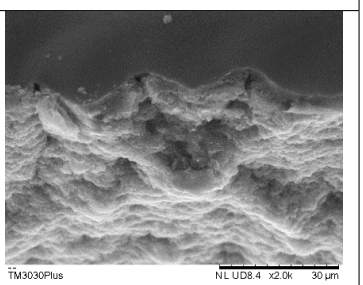

Figure 4.5: Detailed images of different stages of membrane production and treatment for various patterns.

In Figure 4.5, each of the patterns showed good replication from the front view after casting. The small defects in each of the patterns can be seen in the recesses, this is a thermal effect of the laser when material is removed, and the Nafion replicated these features with a high degree of accuracy. Figure 4.6 shows an example of the features within the cross-section images.

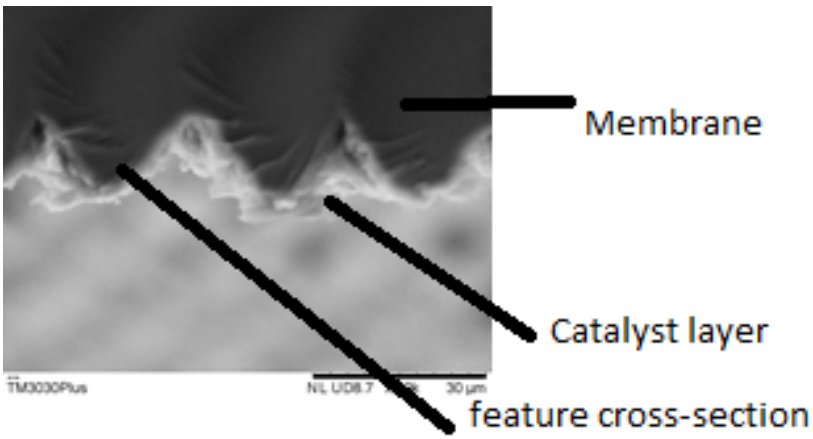

Figure 4.6: Example cross-section image

The lotus pattern had the shallowest features. The defects were not as noticeable on this pattern due to the material not having as much time under the laser light to impose the pattern. As expected, the pattern survived activation, however was smoothed out by the application of the catalyst layer. The lines pattern had very large feature sizes and the frequency of the defects was greater than the lotus and the sharklet. It held up well to both casting and activation, the extent of the defects can be seen in the unsprayed cross section Figure 4.5 row 5, and the catalyst layer conformed to the large features while smoothing some of the defects within its layer. The sharklet pattern had similarly spread defects to the lines pattern, but less intense. This was due to the laser protocol being faster to create shallower features for the sharklet. It was replicated well by casting and held up to activation as with the other two types. The catalyst layer conformed to the shape of

the pattern, with the medium features being seen as well as the large features, the defects again smoothed slightly by the catalyst layer. It was expected that the smaller patterns would be smoothed out by the catalyst layer and that there would be a trade-off between too much smoothing, leading to no effect and enormous feature sizes that were so far apart they had no effect [64, 222].

Table 4.3: Feature size dimensions of patterns including length separation, diagonal feature separation and average, maximum depth of feature, and percentage of area with a reduced thickness .

	Lotus	Lines	Sharklet
Length	25 μm	25 μm	25μm
Diagonal	5.1μm	n/a	18.08μm
Depth (Average)	3.2 $\pm$1.1μm	28 $\pm$0.1μm	4.6 $\pm$4μm
Depth (Max)	3.5μm	28.1μm	16μm
% Area of reduced thickness	50	50	25

Table 4.3 shows the feature size of each of the patterns: their depth, spacing length, and diagonal spacing for the lotus and sharklet patterns. Each of the patterns had a similar spacing length and a variance only in the spread of the depth of the feature sizes. It also shows the percentage of the area that has a reduced thickness, this is a high level estimate from the laser mold of the patterns. As a high level estimate there should be a reduction proportional to the area of reduced thickness to the ohmic resistance from the membrane as well as a proportionate increase in the permeation through the membrane.

4.2 Characterisation

This section will detail all the characterisation techniques used to analyse the membrane performance, starting with ex-situ characterisation and finishing with in-situ characterisation.

4.2.1 Ion Exchange Capacity, Water Uptake and Membrane Swelling

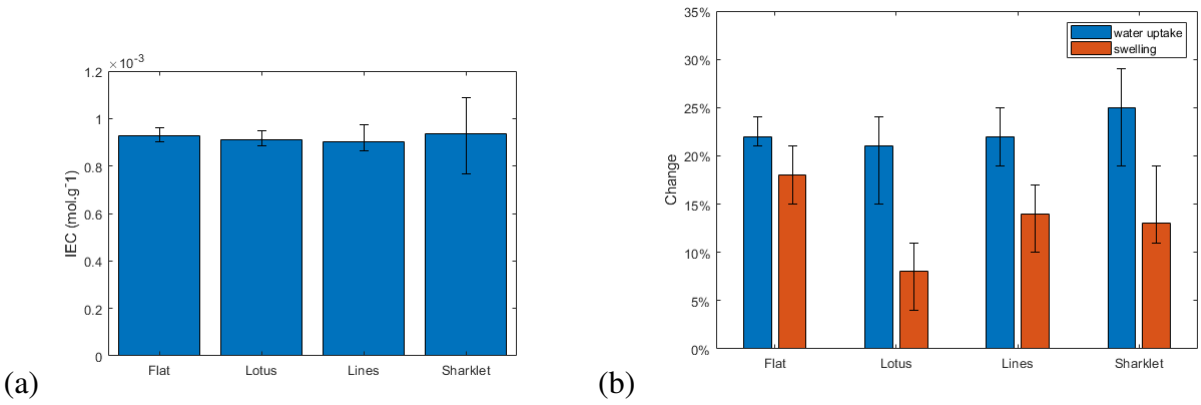

Figure 4.7: (a) Ion exchange capacity, (b) water uptake, and (b) swelling measurements for all samples; Flat, lotus, lines, and sharklet.

Figure 4.7a showed that the ion exchange capacity (IEC) was seen to be very stable which makes sense due to all the membranes being made from the same batch of Nafion. The pattern should not interfere with the bulk properties of the membrane. The dimensional change and water uptake shown in figure 4.7b were slightly unexpected. The same amount of water absorbed by the membrane should produce roughly the same dimensional change; however, the dimensional change was lower due to the patterning. This is believed to be because of the pattern shape, as the swelling could occur into the pattern gaps as well as through the bulk material, showing less bulk dimensional change even though the same amount of water was absorbed. Shown in table 4.4 are the swelling to water uptake ratios for each pattern. A low swelling to water uptake ratio is preferable because it can reduce the mechanical stress on the MEA during operation, reducing the stress forces through hydration and drying cycles thus improving membrane durability [223]. The dry thicknesses and an estimate of the density assuming the thickness is consistent i.e. there is no pattern is presented. The density should be closer to 2 gcm^{-3} like the

flat membrane. This difference gives a measure of the empty space created by the pattern.

Table 4.4: Dry Thickness, Density, and Swelling to Water Uptake Ratio for Each Pattern

Sample	Dry Thickness (μm)	Dry Density (g cm^{-3})	Swelling to Water Uptake Ratio	Standard Deviation
Flat	52 ± 0.5	1.91 ± 0.12	0.80	0.13
Lotus	59 ± 2	1.86 ± 0.11	0.38	0.25
Lines	64 ± 1	1.40 ± 0.12	0.68	0.25
Sharklet	64 ± 2	1.40 ± 0.15	0.50	0.26

Swelling of the pattern is a concern due to the shape change that may occur at the surface which may reduce the ability of the modification to aid in the removal of water from the surface. Work by Zhou et al [224] showed that for flat membranes the typical clamping pressure applied constrains the Z dimension reasonably well, leading to reduced contact resistance and therefore better performance. In the case of the patterns, the catalyst layer applied is shown in the SEM images in Figure 4.5. This sprayed cross-section shows the pattern is preserved in the lines and sharklet patterns, meaning that the pattern will be moulded in part to the carbon paper GDL during hot pressing. Similarly to the Nanostructured thin film catalysts by 3M [61, 225], the hot pressing changed the shape but overall the structuring remained after hot pressing which gives confidence that the same would happen here.

Table 4.5: Hydrogen Crossover at different relative humidity for each pattern, (mA cm^{-2})

Relative humidity (%)	Flat	Lotus	Lines	Sharklet
25	3.05 ± 0.15	2.65 ± 0.20	9.1 ± 0.3	16.9 ± 1.3
50	3.3 ± 0.2	2.95 ± 0.25	8.2 ± 0.33	16.7 ± 2.2
75	3.35 ± 0.11	2.83 ± 0.11	7.3 ± 0.21	15.4 ± 1.7
100	2.43 ± 0.05	2.11 ± 0.42	3.9 ± 1.1	14.1 ± 1.2

Table 4.5 illustrates that patterns with greater depth exhibited significantly higher hydrogen crossover currents. This likely stems from the local thinning of the membrane in its shallowest regions, which reduces the diffusion length compared to a uni-

formly flat cast surface. The lotus pattern and the flat membrane demonstrated comparable behaviours, attributed to the minimal alteration in the bulk thickness of the membrane by the lotus pattern. In contrast, the lines and sharklet patterns exhibited markedly higher crossovers. Notably, the sharklet pattern displayed pronounced crossover, which is thought to be a consequence of overlapping laser scans at the points of deepest pattern indentation. While the lines pattern featured the most substantial depth, it involved a single laser scan suggesting these factors jointly contributed to the observed differences in crossover behaviour.

Literature confirms that the crossover current is higher for thinner membranes and the patterns with significant pattern depth have thinner regions [36, 226, 227]. The drop in hydrogen crossover with increasing relative humidity can be explained with the increasing water content of the membrane restricting the pathways for hydrogen crossover [49, 198]. However there is a lot of overlapping error between the different relative humidities, which warrants the need for further work to investigate the crossover relationship with relative humidity. The Sharklet pattern had the highest crossover; however it did not have the greatest depth, this could be due to some variance in the moulding process, creating a more porous structure; further analysis would be required to confirm this. The crossover explains the relatively lower open circuit voltage (OCV) for the lines and sharklet patterns.

4.2.2 Polarisation Curve

Figure 4.8 shows that the lotus pattern and flat pattern performed almost identically. There was some deviation in the lotus pattern as the relative humidity went below 25 %, but this was expected due to the minor change to the TPB and bulk membrane. The lines pattern

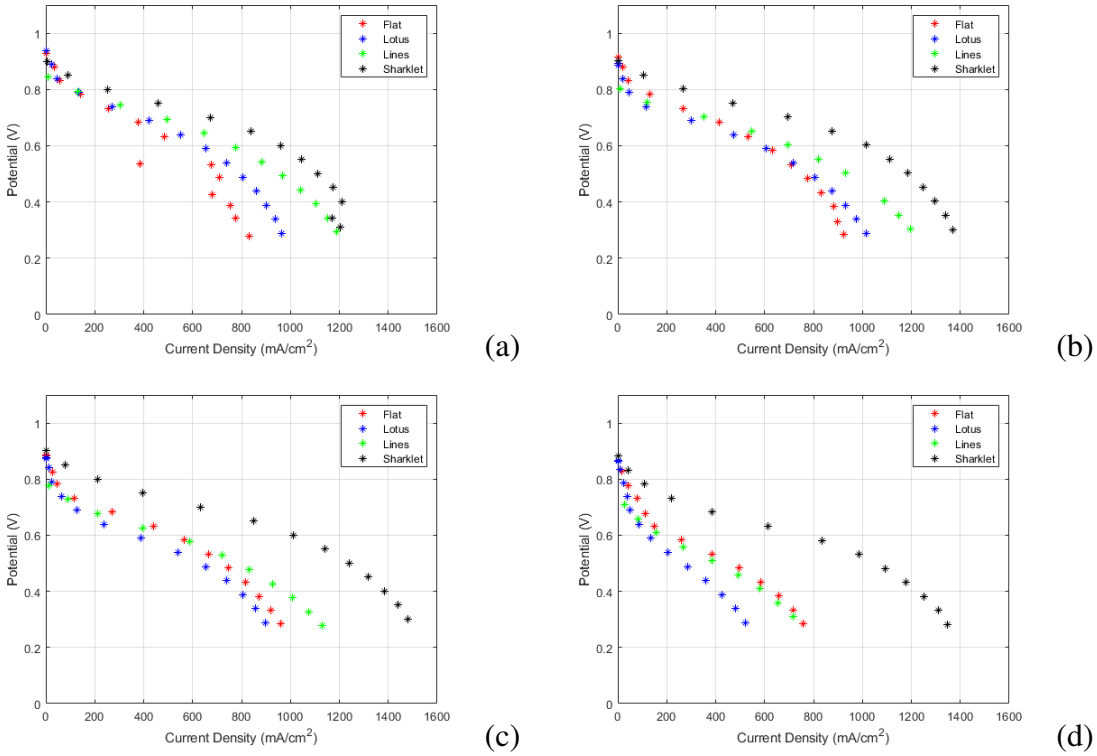

Figure 4.8: Cell Performance at different relative humidity levels a) 100%, b) 75%, c) 50%, d) 25%.

showed some improvement at 75 % RH, probably due to the large feature sizes. The available TPB was larger making mass transport less hindered at higher current densities. The sharklet pattern showed best overall performance through all RH values. The improvement seen the most was in the mass transport region, but there was also a shallower ohmic region through the middle of the polarisation curve, meaning the membrane's average thickness was less and therefore had lower ionic flow resistance. The sharklet pattern showed improvement in the activation region of the polarisation curve. This indicates that there are faster kinetics leading to a lower overpotential. However this could actually be because of the increased electrochemical surface area which would have more available reaction sites which would also lead to a lower overpotential. This in turn can have a knock on effect throughout the polarisation curve due to increased water generation

leading to better hydration and lower ohmic resistance, and higher limiting current which would reduce mass transfer resistance.

To calculate the power density from a polarization curve of a fuel cell, multiply the cell voltage V by the current density i. The power density P at each point on the curve is given by

$$P = V \times i$$

where P is the power density in watts per square centimetre (Wcm^{-2}), V is the cell voltage in volts (V), and i is the current density in amperes per square centimetre (Acm^{-2}). This equation allows for the evaluation of the fuel cell's performance across various operating conditions directly from the polarisation curve.

The drop in performance of the sharklet pattern from 100 % to 25 % RH was about 20 % at 0.6 V, when compared to the flat membrane this loss was 40 %. The lotus shows loss of 80 % and the lines pattern showed a loss of 85 %, again at 0.6 V. The power density at 100 % RH of the flat membrane at 0.6V is 0.3 Wcm^{-2}, compared to the Sharklet pattern which is 0.57 Wcm^{-2}, an increase of 90%. When compared to low humidity conditions 25 % RH, the flat membrane has a power density of 0.12 Wcm^{-2} and the Sharklet pattern 0.48 Wcm^{-2}, a 4-fold increase measured at 0.6 V. Due to a difference in the step size (-50 mV from OCV to 0.3 V) a linear interpolation was used to calculate between the nearest two values.

Figure 4.9 shows the relative power density data interpolated between 0.8 and 0.3 V. The relative power density was calculated by taking the power at each voltage and dividing it by the power at each voltage for the Flat membrane. In this way, the increase in power density is quantified vs the power density of the flat membrane. Here the large effect of

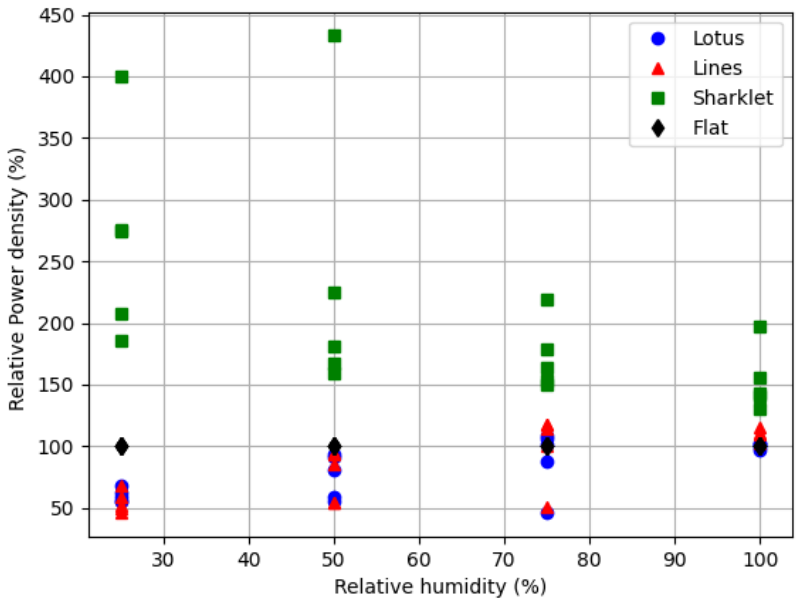

Figure 4.9: Plot of power density against relative humidity for each of the patterns

the Sharklet pattern can be observed, it shows peak power density increases across the relative humidity range with a minimum of 200 % increase, and a maximum of 430 %.

Figure 4.10 shows the approximate ASR for each of the patterns at different relative humidities. This was calculated using an approximation for the overpotential assuming the OCV is constant at all points of the polarisation curve. This is not strictly accurate as the OCV is governed by the Nernst equation and the major shifts in Nernst potential come from concentration and temperature variations. As the fuel cell increases in current density the water production will reduce the partial pressure of reactants at the cathode, and the back diffusion of water through the membrane can alter the concentration of hydrogen at the anode, although these effects would be small they will still shift the OCV downwards making the ASR an approximation. The ASR's shown in this way show that the sharklet has a far reduced ASR, which when coupled with the increased ECSA measured below. Shows that when more surface area is available there should be a reduction

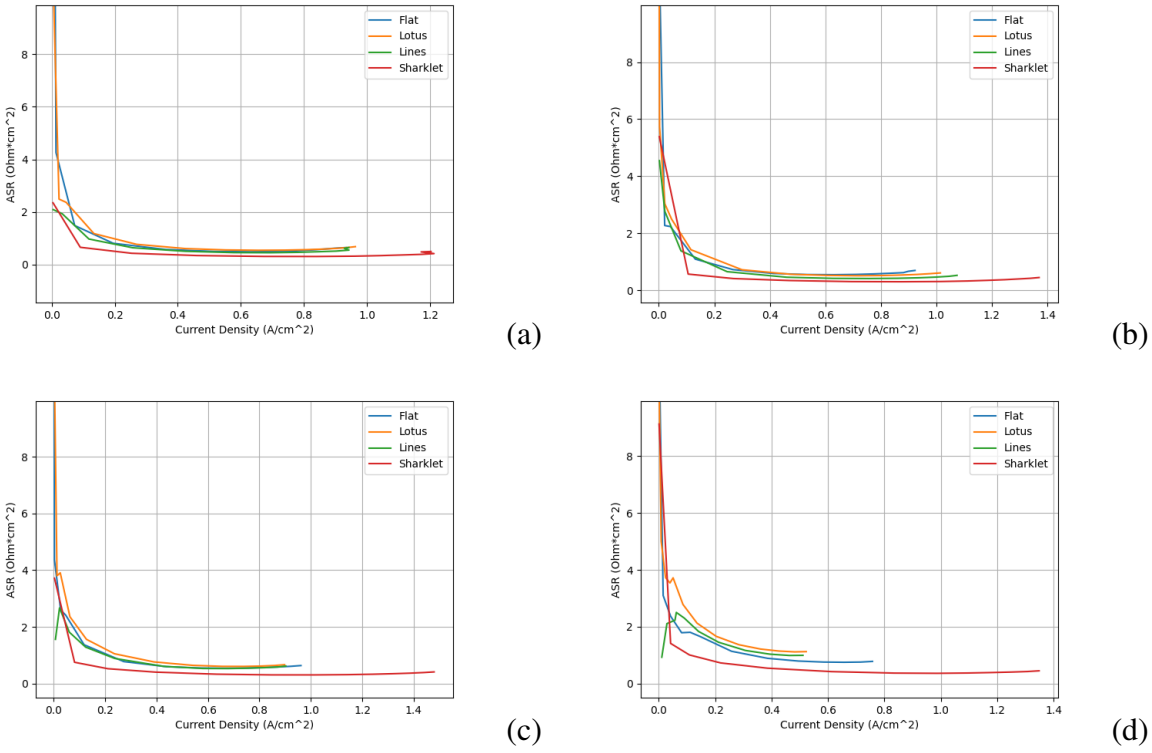

Figure 4.10: Approximate Area specific resistance vs current density at different relative humidity levels a) 100%, b) 75%, c) 50%, d) 25%.

in the resistance as the current increases which aligns with Butler-Volmer equation. The ASR is also a reflection of the full cell resistance like the low frequency intercept of an impedance spectra.

4.2.3 Impedance measurements

This section will detail the impedance results from the patterned membrane tests.

Table 4.6: High frequency resistance (ohm.cm^2) measured under 0.4 A load

Relative humidity (%)	Lotus	Lines	Sharklet	Flat
25	0.095	0.12	0.08	0.08
50	0.035	0.032	0.035	0.03
75	0.022	0.0251	0.025	0.025
100	0.02	0.02	0.02	0.025

Table 4.6 shows the high-frequency intercept for the low current impedance measure-

ments, they are consistent with the expected values, and the lines pattern showed the largest resistance at 25% relative humidity. This indicates that the membrane is drying.

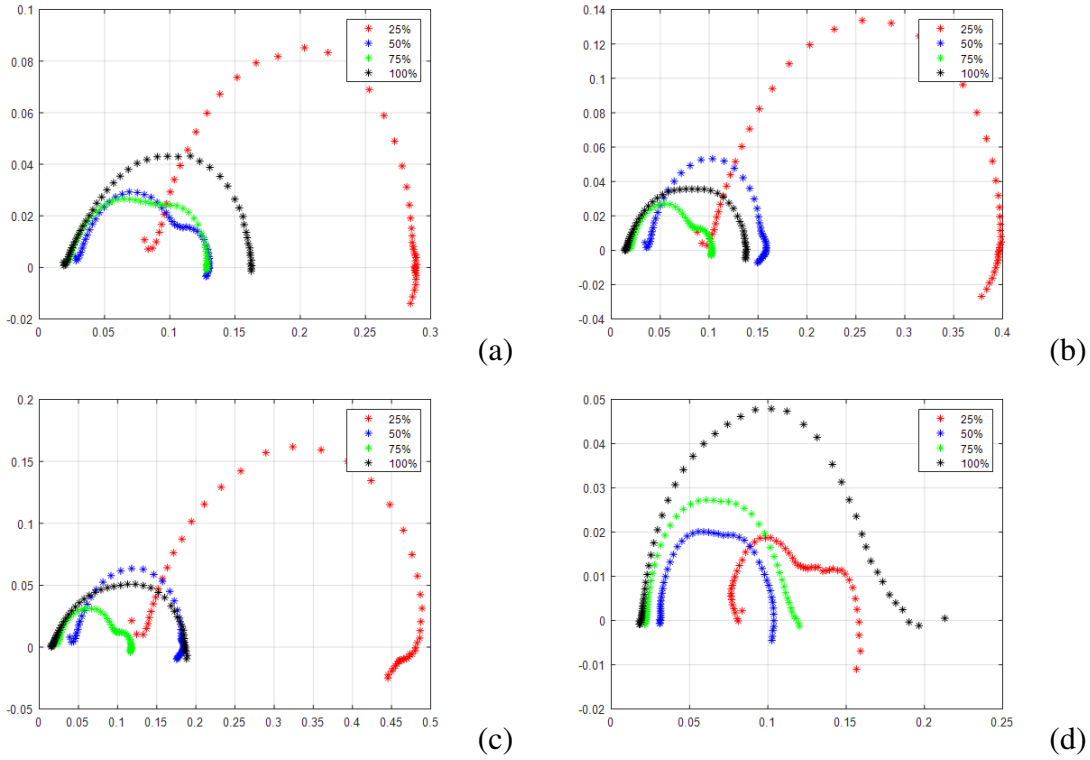

Figure 4.11: Impedance spectroscopy measurement @ 0.65 V a) Flat, b) Lotus, c) Lines, d) Sharklet patterns.

Table 4.7: Difference between high and low frequency resistance (ohm.cm^2) measured under 0.65 V

Relative humidity (%)	Flat	Lotus	Lines	Sharklet
25	0.2	0.3	0.355	0.08
50	0.095	0.12	0.13	0.09
75	0.1	0.075	0.1	0.085
100	0.135	0.118	0.155	0.168

Figure 4.11 and table 4.7 shows the impedance measurements at 0.65 V for each of the patterns and the difference between the high and low frequency impedances. The key highlight is the low frequency intercepts of the sharklet pattern are low for relative humidities below 100%. All of the samples show similar performances at 100% relative humidity, with the flat and lotus patterns showing the lowest low frequency intercepts.

The HFR for each of the patterns are shifting in a similar manner. With small shifts above 50% relative humidity and a bigger shift from 50% to 25%. The shift in low frequency intercept indicates an increase in the charge transfer resistance. The shift in the high frequency resistance implies that there could be a dehydration of the membrane and ionomer. This general trend is broken with the sharklet pattern which appears to have only a very slight shift in the charge transfer resistance at 25% relative humidity, it appears that for this pattern that the majority of the performance drop at 25% relative humidity is the shifting high frequency resistance, indicating that the membrane or ionomer dehydration is dominating at this region of the polarisation curve.

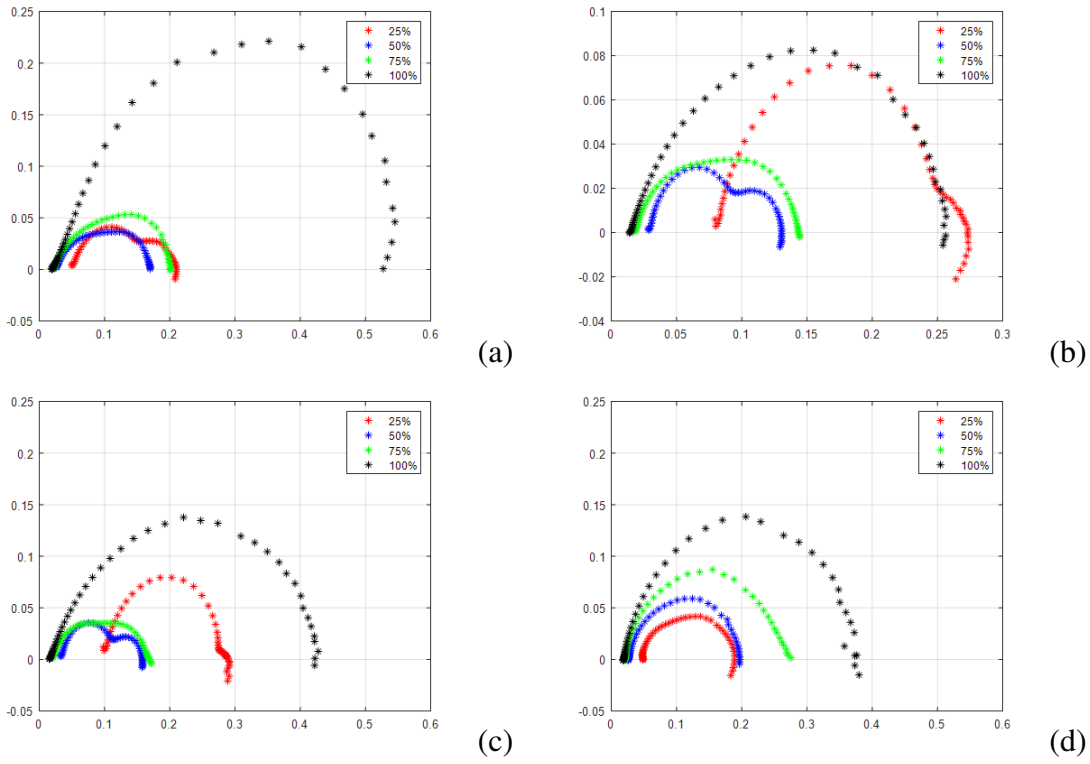

Figure 4.12: Impedance spectroscopy measurements @ 0.4 V for a) flat, b) lotus, c) lines, d) Sharklet patterns.

Figure 4.12 and table 4.8 shows the impedance measurement and difference between the low and high frequency resistances. They confirmed the reduction in mass transport

Table 4.8: Difference between high and low frequency resistance (ohm.cm^2) measured under 0.4 V

Relative humidity (%)	Flat	Lotus	Lines	Sharklet
25	0.16	0.195	0.19	0.13
50	0.159	0.095	0.135	0.16
75	0.18	0.115	0.15	0.255
100	0.501	0.238	0.395	0.357

losses for the sharklet pattern through the reduction in low frequency intercept, however what is not clear is why the flat pattern showed a lower resistance when the performance was greater for the sharklet at the same current density. It could indicate that the performance lies in greater electrochemically active surface area. The initial intersection with the x-axis showed the ohmic resistance was lower. The second intersection shows the low frequency intercept and this is a measure of the total cell resistance at this point, so if the resistance is lower then a greater performance is expected. The lotus pattern shows similar size and position to the flat membrane apart from 100 % RH where they diverged. When looking at the mass transport region of both polarisation curves, the impedance agrees as the flat membrane showed a sharper drop at 100 % RH than the lotus pattern. The lines pattern showed an improvement in the 50 & 75% resistance, but greater resistance at 100 & 25 % RH.

Figure 4.13 shows the high frequency resistances at all conditions for all patterns. here it can be seen that the Sharklet showed the lowest resistance for the majority of humidity conditions, fairing the best at low relative humidity. This also confirms that it was probably thinned the most out of all the patterns.

The similarities in mass transfer resistance between the sharklet and flat membranes, observed when measurements were conducted at a fixed voltage of 0.4 V rather than at specific current densities, might initially mask the benefits of the sharklet pattern. Despite

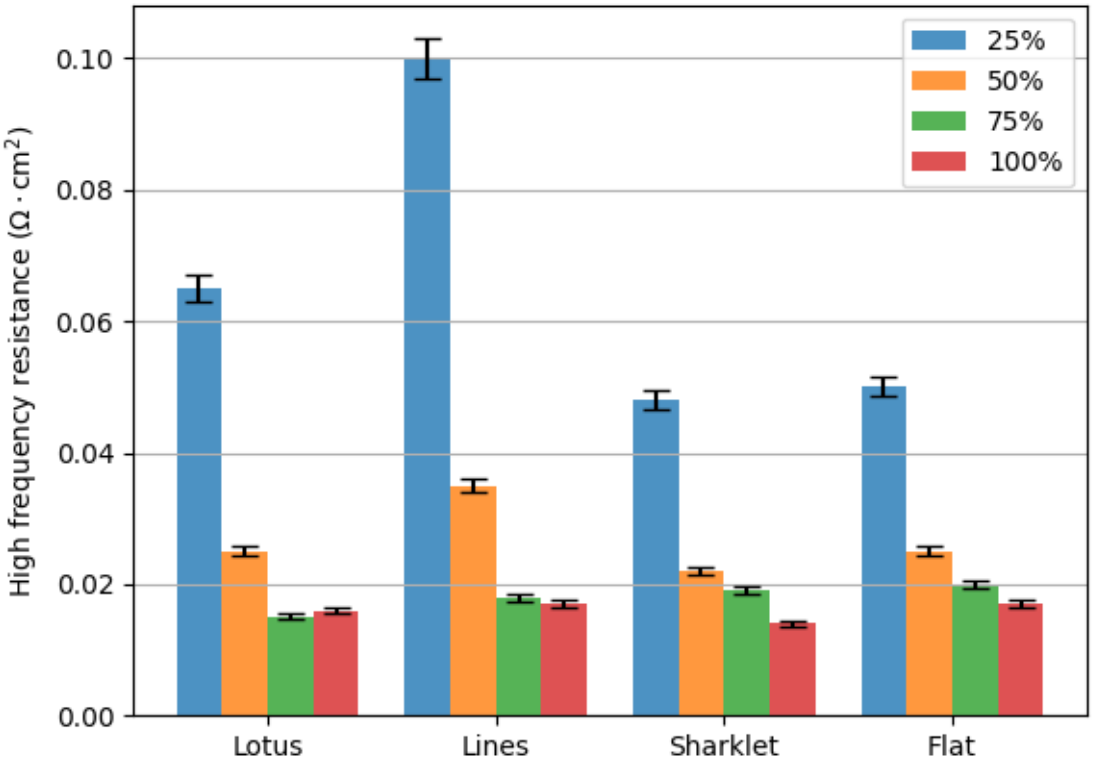

Figure 4.13: High-Frequency resistance across all conditions

showing similar resistance values, the sharklet pattern supported higher current densities. This suggests an enhanced capability for water management within the catalyst layer, allowing for more efficient exchange of reactants and products at the same level of mass transfer resistance. Essentially, the sharklet design facilitates better removal of water from the catalyst layer, thereby reducing the likelihood of flooding and improving reactant access to active sites.

Integrating the results from both the impedance measurements and the polarization curves, it becomes evident that the sharklet pattern leads to significant enhancements in water transport and overall power density of the fuel cell. These improvements are crucial for optimizing fuel cell performance, especially under challenging conditions such as low

RH where maintaining adequate hydration is pivotal for sustaining ionic conductivity and minimizing performance losses due to mass transport limitations.

The combination of EIS and LSV data thus reveals a comprehensive picture, where the benefits of the sharklet pattern are underscored not only in terms of maintaining hydration but also in enhancing the overall electrochemical efficiency of the fuel cell system.

4.2.3.1 Electrochemical surface area measurements

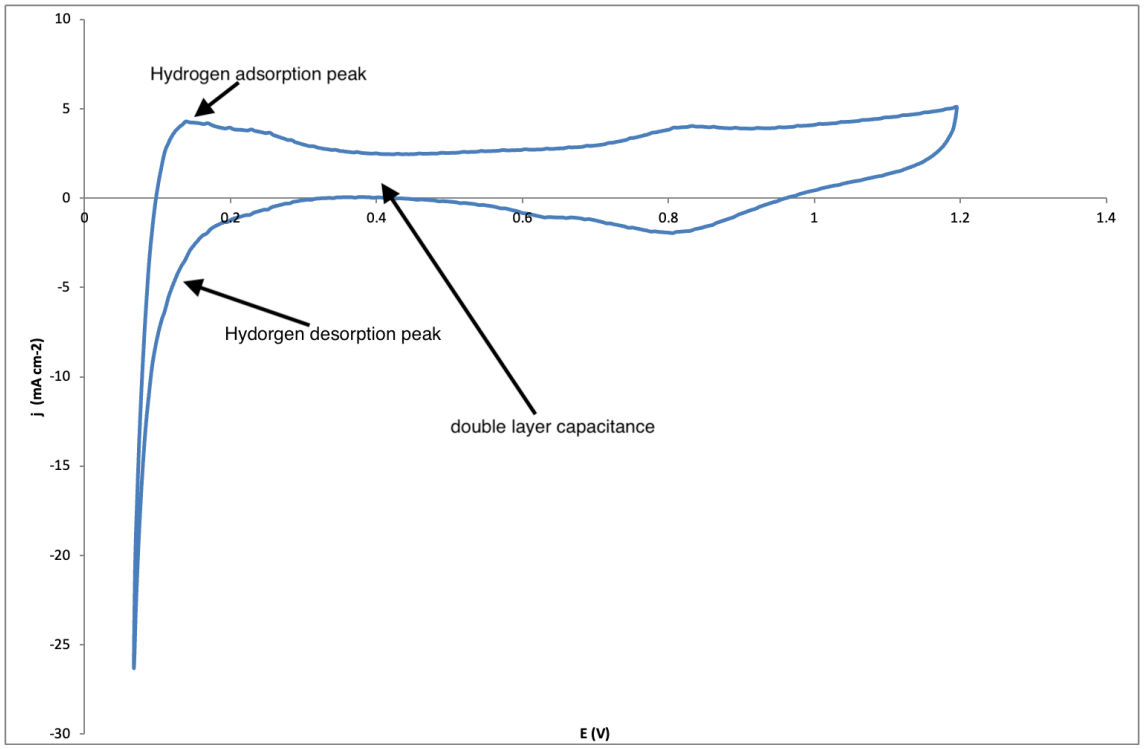

Figure 4.14: Example cyclic voltammagram showing the typical platinum shape

Figure 4.14 shows a typical platinum cyclic voltammogram (CV) from a Membrane Electrode Assembly (MEA), highlighting three specific regions: the hydrogen adsorption peak, the hydrogen desorption peak, and the double layer capacitance region. The electrochemical surface area (ECSA) can be calculated from the hydrogen adsorption and desorption peaks, using the double layer capacitance as the baseline to integrate the area that

represents the surface area of platinum accessible to hydrogen. ECSA may differ between an aqueous electrolyte and a fuel cell due to varying ion mobility and the electrochemical environment. In aqueous solutions, ion conductivity is generally higher, leading to more uniform electrochemical activity across the catalyst surface. Conversely, in a fuel cell, the presence of gas phases and polymer electrolyte membranes can restrict ion access and diffusion, thereby reducing the effective surface area for reactions.

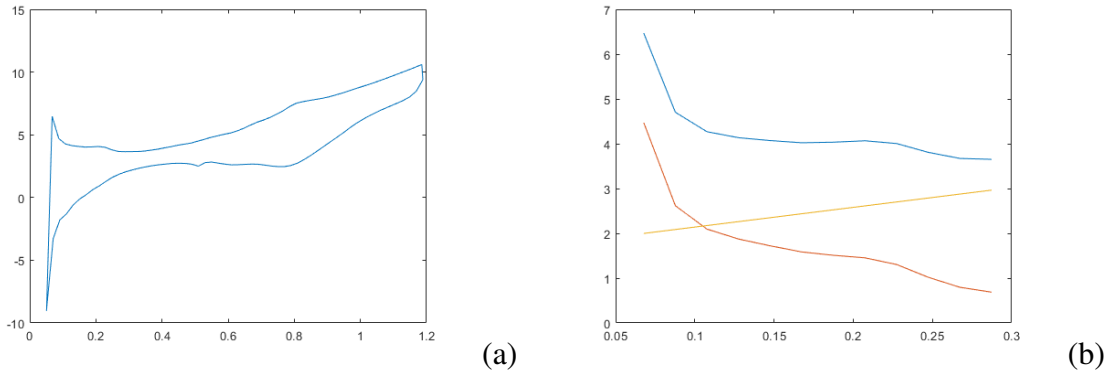

(a) (b)

Figure 4.15: Example cyclic voltammagram of sharklet pattern MEA (a) and the isolated Hydrogen adsorption peak with (red) and without (blue) subtracted double layer baseline (yellow) Voltage (V) on the X-axis and current density (mA^{-2})on the Y axis

Figure 4.15a shows a measurement of the ECSA from a sharklet pattern MEA. Figure 4.15b displays the isolated hydrogen adsorption peak in blue. The double layer region, shown in yellow, was extrapolated by examining the slope of the line and back-calculating its trajectory underneath the hydrogen adsorption peak. This double layer region was then subtracted from the adsorption peak to yield a double layer-free adsorption peak. The area under this curve is equivalent to the ECSA.

Table 4.9: Electrochemical surface area measured from the H+ adsorption peak in-situ.

Pattern	ECSA m^2g^{-1}
Flat	18.4 ± 0.3
Lotus	12.5 ± 2.1
Lines	17.5 ± 1.2
Sharklet	20.2 ± 0.7

Table 4.9 shows the ECSA calculated using the trapezium rule from the corrected H+ adsorption peak. It can be seen that the sharklet pattern has the highest ECSA of all the patterns, with approximately a 10% increase in ECSA when compared with the flat cast membrane. The lower ECSA for the other patterns is probably due to the application of the catalyst layer on the membrane surface; for the lines pattern where the feature size was large, this probably caused a disconnection between the catalyst layer and the electrolyte, meaning a higher transport resistance of the interface. In the lotus case, the ink probably penetrated the membrane more deeply due to the tiny feature size, again reducing the TPB connectivity and increasing transport resistance, making it unavailable to react [67].

4.3 Discussion

The combination of the right feature size and pattern depth yielded the best results. The best performing pattern in this work, the sharklet, did so because of its effects in both the ohmic and mass transport regions. These improvements were confirmed through in situ testing of the ECSA which showed that it was approximately 10% larger than that of the unpatterned membrane. In a fuel cell stack, such an enhancement in ECSA would contribute to higher catalytic efficiency across the entire system, leading to improved overall power output and system performance, especially under low humidity conditions.

The membrane material and thickness govern the ohmic region; the patterning changes the thickness of the membrane in some areas and makes it thicker in others. It also affects the dimensional change when the membrane is hydrated, swelling into the pattern before the bulk thickness is affected. The swelling results, show this effect with the membranes having smaller dimensional changes versus the unpatterned membranes; however, overall

water uptake is unaffected. With a thinner membrane, it is confirmed that the membrane will have a lower ohmic resistance. In a stack configuration, this reduction in ohmic resistance would mean lower energy losses across the cells and improved voltage efficiency under various operational conditions.

Losses in the mass transport region occur when rate of reaction is limited by mass transfer. This causes a drop in performance to the level that the electrochemical potential collapses. The mass transfer limiting current is the point at which the electrochemical process is no longer governed purely by the butler-volmer equation, and it is additionally diffusion limited. In this case, the patterned surfaces showed that by increasing the available TPB surface area, it was possible to mitigate these losses at higher current densities. Larger TPB was expressed in a higher ECSA, despite the loading of the CCMs being similar between the samples, indicating that there was a better catalyst utilisation. This translates to enhanced performance under high load conditions in a stack, reducing losses associated with limited reactant supply and improving reactant accessibility and product removal.

In Figure 4.8, the sharp drop in performance of the lotus and lines patterns as the RH dropped showed a sharp increase in the slope throughout the ohmic region. This means that the pattern negatively affected the membrane's water transport properties, drying it out and increasing the membrane's resistance. However, the sharklet pattern showed a stable ohmic region through to 25% RH. This indicates that water was effectively redistributed and retained within the membrane, keeping the conductivity high, a feature that is advantageous in a stack by ensuring stable operation across a range of environmental conditions and reducing the risk of dry-out or flooding within the cells.

The sharklet pattern shows a noticeable performance increase in the kinetic region of the polarisaiton curve, this confirmed by the low charge transfer resistance throughout the impedance measurements. The lower charge transfer resistance could be a result of the pattern favourably moving water away from the catalyst layer, enabling more effective charge transfer at high current densities as well as other points throughout the polarisation curve.

Some of the performance gains can be explained due to the increase in ECSA; this effect, coupled with the improved water transport characteristics on the cathode side, seemed to yield a significant performance improvement. When applied in a stack, such targeted patterning can help maintain more consistent performance across cells, even under challenging operating conditions.

The pattern feature size seemed to play an important role; the patterns with too shallow features behaved like standard membrane surfaces or hindered improved performance. The large feature size patterns had an effect, but it was minor, and other areas became worse than the original surface. However, the medium feature size and depth pattern performed very well. Furthering this work would involve investigating a range of different feature sizes and relative depths on power density and durability, using the sharklet pattern, especially considering cell integration into stacks for enhanced system reliability and efficiency. This is corroborated by the measurement of hydrogen crossover rates, which were much higher for patterns with significant depths, leading to a decrease in open circuit voltage (OCV) for the sharklet and lines patterns. The critical aspect of transferring this successful patterning from experimental to practical applications in stacks involves primarily understanding production repeatability, transitioning from batch to continuous

manufacturing methods, assessing the durability of the patterned membrane, and comprehending how these factors interact with the overall effects observed.

4.4 Conclusions

The research presented in this chapter highlights the successful implementation of steel molds modified by the Laser Induced Periodic Surface Structures (LIPSS) technique to fabricate patterned membranes. These membranes demonstrated enhanced performance characteristics, particularly in the mass transport and ohmic regions of the polarization curve. The contact angle measurements and subsequent SEM analysis confirm the effective replication of microscale patterns onto the membrane surfaces, which significantly influenced their hydrophobic properties and surface morphology.

Quantitative assessments revealed that the sharklet patterned membranes exhibited up to a 4-fold in power density, with marked improvements observed across varying relative humidity conditions. Specifically, the sharklet pattern maintained higher catalytic utilisation, as evidenced by an electrochemical surface area (ECSA) increase of approximately 10% compared to the flat membrane. This suggests a more effective utilization of the catalyst and therefore an increase in the kinetic region, likely due to better connectivity at the three-phase boundary (TPB). The sharklet pattern facilitated higher power density and maximum current densities, which is exhibited by the improved mass transfer resistance due to TPB.

Impedance spectroscopy further supported these findings, indicating reduced high-frequency resistance in the sharklet pattern under varied operational conditions, implying lower ohmic losses and enhanced ionic conductivity. Notably, the hydrogen crossover

measurements for the sharklet pattern, though higher compared to the flat and other patterned membranes, did not adversely affect the overall cell performance. This could be attributed to the membrane's ability to maintain hydration and conductivity, even at lower relative humidities, which helps mitigate the potential drawbacks of increased crossover.

In contrast, other patterns such as the lotus and lines demonstrated certain limitations under low humidity conditions, as shown by their increased ohmic resistance and diminished performance on the polarization curves. This suggests that while patterning can significantly impact membrane performance, the feature size and depth must be carefully optimized to harness beneficial effects without incurring negative consequences on the membrane's functional properties.

In conclusion, this research underscores the critical role of pattern design in optimizing membrane performance for fuel cell applications. The sharklet pattern emerges as a particularly promising design, enhancing both mechanical and transport properties of the membrane, thus supporting sustained performance under a variety of operational conditions. Future work should focus on further refining this pattern and exploring the scalability of this approach, ensuring the repeatability and reliability of these patterns in larger-scale fuel cell systems. Moreover, the integration of these findings into practical applications would require a detailed examination of the long-term stability and durability of patterned membranes, particularly in terms of their resistance to mechanical stresses and chemical degradation over extended operational periods.

CHAPTER FIVE

INTERMEDIATE TEMPERATURE PEFC'S WITH NAFION^{TM} 211 MEMBRANE ELECTROLYTES: AN EXPERIMENTAL AND NUMERICAL STUDY

5.1 Introduction

A significant portion of the research effort on Polymer Electrolyte Fuel Cell (PEFC) has focused on cathode catalyst material and layer optimisation. The cathode kinetics are much slower than those of the anode [228] and are therefore considered the cell reaction rate-determining step [229–231]. Most research has been focused on conventional operating temperatures (60 to 80°C); however, increasing the operating temperature also improves cathode kinetics, as reported by Song et al. [113]. Moreover, higher temperatures increase the saturation pressure of water vapour and decrease the likelihood of

water flooding. Elevated temperatures also improve the fuel cell tolerance to CO impurities in hydrogen. Increased temperature makes the adsorption of CO to the platinum surface unfavourable [119, 120, 232]. As with many transport phenomena, oxygen transport increases with temperature. The diffusion of oxygen in water is greater at higher temperatures [121], enabling significant enhancements in the transfer of reactants to the catalyst active sites, which has a knock-on effect on performance.

Perfluorosulfonic acid (PFSA) based membranes, namely Nafion, are today's PEFC industry standard [52]. The central role of the membrane is to separate electronic and ionic charges and provide an impermeable barrier to gases at the anode and cathode [23]. PFSA membranes are made of a hydrophobic polytetrafluoroethylene (PTFE) backbone and a side chain terminating in a sulphonic acid group, which require high hydration to conduct protons [233]. Consequently, the membrane is the main component limiting the operational temperature of PEFCs. Higher temperatures mean less dissolved water and more steam. This phase difference significantly affects water transport through the cell, although it improves mass transport at the interface. The extra water movement reduces the membrane's ability to accumulate and retain water and results in dehydration [234]. This has a detrimental effect on PEFC performance as conductivity drops with reduced water content.

For low-temperature fuel cells, degradation of the membrane occurs through three primary mechanisms: chemical, thermal, and mechanical. Thermal degradation is the breakdown of the polymer chain from heat, such as thermal relaxation to the point of plastic deformation and pinhole formation at hot spots; mechanical degradation results from the swelling and contraction of the membrane with varying hydration levels and

the pressure differential across the membrane [130]. The swelling and contraction of the membrane are independent of the pressure gradient and usually due to the water content of the membrane. The pressure gradient depends on operational conditions; therefore, they can align constructively or destructively. Chemical degradation comes from weak sulphonic acid side chains that are vulnerable to peroxide attack. Peroxide is formed due to hydrogen crossover across the membrane, exacerbated by non-steady-state operation and time spent at open circuit voltage (OCV) [132]. Higher operating temperatures can enhance all membrane degradation mechanisms, reducing the cell's lifetime. Researchers have been investigating alternatives or modifications to the currently used PFSAs [32, 43, 83, 97]. The structural characteristics of PFSA membranes that make them susceptible to these types of mechanical degradation include the base polymer backbone, whose mechanical properties can dominate. If the polymer has a long side chain versus a short side chain, there can be a reduction in bulk strength due to the length and packing density of the polymer structure, as well as the frequency of side chains.

The glass transition temperature in polymers represents a temperature above which bulk morphological relaxation takes place. A relaxation of the polymer chains causes a destabilisation of the structure of the polymer; small relaxations are elastic, but large relaxations can mean the complete separation of the crosslinking within the polymer structure. Nafion comprises two polymer chains: a backbone of PTFE and the side chain containing the sulphonic groups. The backbone has a glass transition temperature of 110 to 130°C [133, 134]. As discussed by Calleja et al. [133], the relaxation of the backbone has stages, and the relative change in relaxation is low up to 125°C. Sidechain relaxation is characterised near temperatures of 100°C [134], posing a problem for the performance

of the membrane at temperatures above 100°C because relaxation increases porosity and decreases the stability of the membrane.

PFSA membrane development has focused on increasing the performance of the membrane while maintaining the desired lifetime for PEFC applications. Membrane thicknesses were reduced from Nafion 117, which had a thickness of 183 μm, to Nafion 211 at a thickness of 25 μm [123]. Improvements in manufacturing, such as the change from extrusion to dispersion casting, have yielded high-performance membranes with very high conductivities [47] whilst maintaining mechanical strength and durability. Nafion 117, is produced through an extrusion process that yields a denser and more tightly packed polymer structure, limiting its ability to swell and retain water. In contrast, Nafion 211 is manufactured via dispersion casting, resulting in a less dense, more porous membrane with a higher internal surface area. This structural difference makes Nafion 211 more adept at absorbing and managing water, enhancing its performance in fuel cell applications, especially under normal operational temperatures ($\leq$ 80°C) where effective hydration is crucial. Reinforcement with other polymer fibres such as PTFE and PBI can increase mechanical strength and durability [27, 235, 236]. Finally, dopants such as cerium oxide are now used as radical scavengers to reduce the chemical degradation of the membrane [237], helping to extend lifetime. The next area for development would now be an increase in the operating temperature, with benefits as described [138].

Modelling is advantageous in the research process as it can reduce costs associated with designing and fabricating prototypes and allow investigations beyond the limit of the current experiments. They can give insights into complex systems where experimentation can be difficult or expensive. The Springer et al. model [188] is the most famous

empirical model for Nafion membranes; it enables the estimation of the ionic conductivity of the membrane electrolyte with the knowledge of water content and temperature. Many authors have used it as the foundation of membrane modelling [46, 163, 213, 234]. The model developed by Springer et al. [188] was partly based on Yeo and Eisenburg's measurements that described the activation energy and diffusion of water in Nafion 117 [189].

The main limitation of the Springer model is that it was based on a limited range of temperatures (30 to 80°C) and pressures (1 atm). However, many real-life fuel cells operate at higher pressures to increase performance [238]. The behaviour of water was studied extensively, leading to the production of steam tables; they show the thermodynamic properties of saturated steam [239]. Steam tables are helpful as they give insight into the relative behaviour of water at different pressures, temperatures, and saturation levels. The data surrounding water sorption into the Nafion phase at elevated temperatures and pressures are still lacking due to the complexity of the experimentation.

Nafion 211 and Nafion 117 are similar as they share the same base polymer unit; however, they differ in thickness and production method: Nafion 211 is 25 μm thick and made by dispersion casting; while Nafion 117 is 183 μm thick and made by an extrusion process. Dispersion casting results in a more relaxed polymer structure, which changes the water sorption and membrane swelling behaviour. Dobson et al. [195] presented the sorption isotherm measured by Mittlestead and Liu [240], who measured the water sorption vs activity of Nafion 211 and suggested a model similar to that of Springer et al. in [170]. However, they did not account for elevated temperatures (< 100°C) and the phase of water (vapour and liquid).

Fuel cell performance decreases with increasing temperature beyond 100ºC, which is due to the issues mentioned above of water accumulation and retention at these temperatures. Research into composite Nafion membranes showed the potential of operating Nafion at temperatures up to 120°C [97]. However, in addition to the polymer modification, the operating conditions, such as the operating pressure, need to be increased with increasing operating temperature to enable the correct relative humidity and therefore water sorption [176, 177, 184].

For the first time, this work attempts to assess the performance of a PEFC equipped with a Nafion 211 membrane under elevated temperatures (80°C, 100°C, and 120°C) and various relative humidity (40 to 100%). Temperatures were selected to be as high as possible while remaining below the glass transition temperature to ensure the membrane stays in a glassy state. Additionally, a midpoint was chosen between the two temperatures. Membrane performance was assessed in a single PEFC cell. The experimental results were used to extend the model of Nafion 211 in order to adapt it to elevated temperatures and enable the investigation of optimum operating pressures and relative humidity at these operating temperatures.

5.2 Methodology

This work used the experimental membrane electrode assembly fabrication technique shown in section 3.1.2 and the modelling method included in section 3.2. It is important to note that the materials used in this section were acquired from industrial suppliers, assembled and tested. They are different from the materials in the previous chapter because the materials were all created using the full manufacturing method from scratch.

Lambda (λ) represents the equivalent water content, denoting the number of water molecules per acid molecule in the membrane structure. It links the activity of water in the gas streams to the water content of the membrane, and subsequently to its conductivity, using equations 3.31 and 3.29 respectively.

5.3 Results

Figure 5.1 shows the experimental polarisation and electrochemical impedance spectroscopy results (EIS) for the membrane electrode assembly (MEA) testing at different operating temperatures and reactants' relative humidities. The trend for the data at 80°C (Figures 5.1a and 5.1b) shows a decrease in performance as the relative humidity increased; this was due to the accumulation of water in the cathode at high current density, causing an increase in the mass transport polarisation. The EIS taken at 0.6 V show that the ohmic resistance does not vary much for all relative humidity conditions. Towards the low-frequency end of the impedance data, there is a clear shift in the total cell resistance as the mass transport effects cut in. The relationship is inverse due to the oxygen concentration decreasing with increasing relative humidity, and the minor onset of flooding behaviour.

The results at 100°C are shown in Figures 5.1c and 5.1d. Generally, the cell shows an increase in the maximum performance achieved, as the average current density at 80°C, 0.6 V was 1200 $mAcm^{-2}$ and at 100°C, 0.6 V was 1400 $mAcm^{-2}$. The trend here was reversed compared to that seen at 80°C, and the highest performance was achieved at high relative humidities between 60 and 100%, whilst at 40% relative humidity, the cell showed signs of dehydration with a significant increase in the cell resistance compared

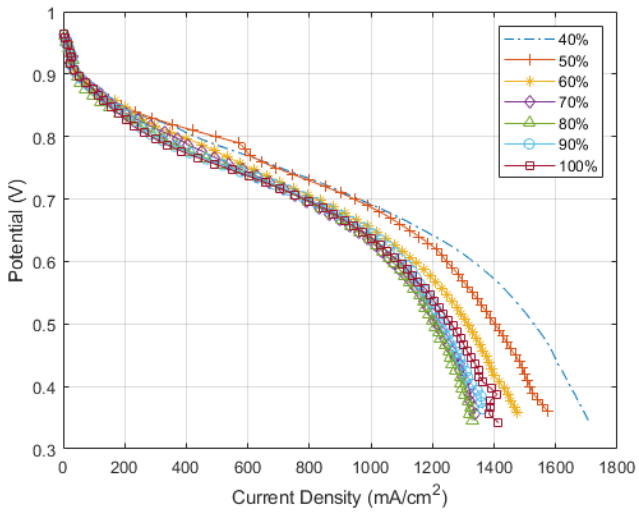

(a)

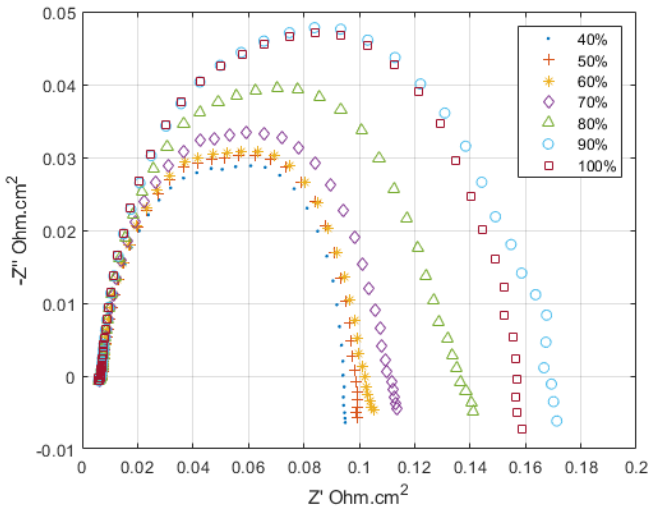

(b)

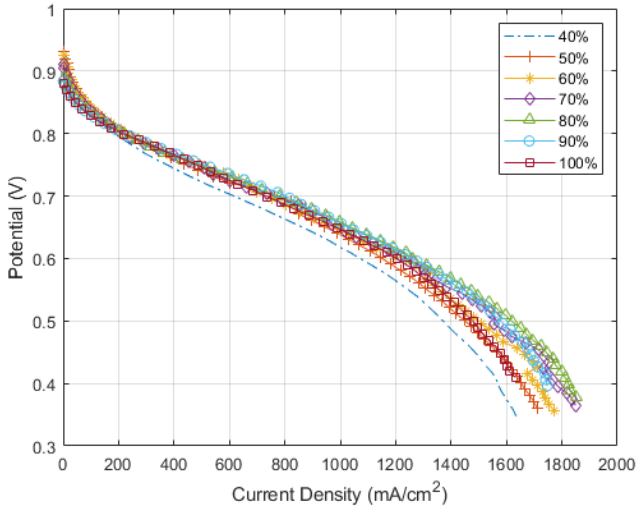

(c)

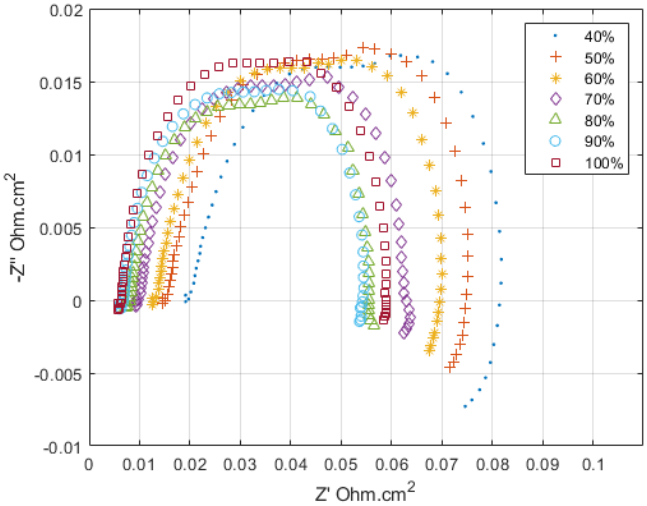

(d)

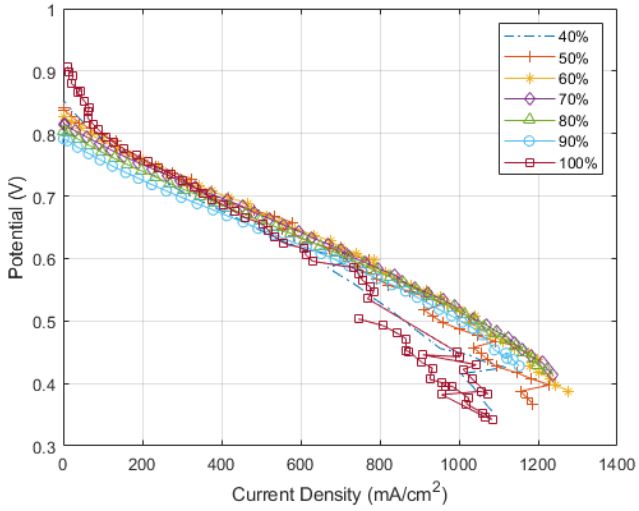

(e)

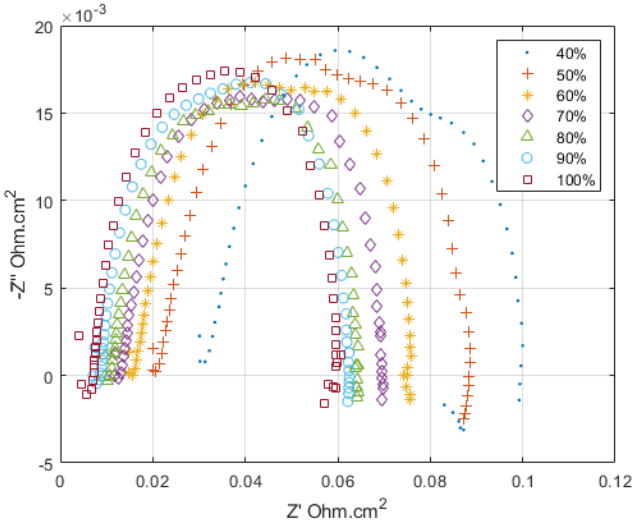

(f)

Figure 5.1: Polarisation curves and impedance spectroscopy at 0.6 V at different temperatures for the Nafion 211 membrane, across a range of relative humidities. Panels: (a) 80°C, (b) 80°C, (c) 100°C, (d) 100°C, (e) 120°C, and (f) 120°C.

to the 100% relative humidity condition. The EIS results (Figure 5.1d) confirmed the increase in the ohmic resistance of the cell with reducing relative humidity. Moreover, it is important to note the reduction in OCV for the cell compared to that achieved at 80°C. The results at 120°C show a similar performance trend to that seen at 100°C but with reduced total cell performance. The EIS results in Figure 5.1f demonstrate the further increase in ohmic resistance compared to the other temperatures due to dehydration. Again, there is a further reduction in OCV compared to the other temperatures, which can be related to reducing the Nernst potential and increasing hydrogen crossover with increasing temperature. The EIS results shown in Figure 5.1 were used to obtain a relationship for the membrane resistance at the different operating conditions [162, 211, 241, 242]. The typical equivalent circuit method [208] was not used as it fails to account for the complex resistances in the catalyst layer, contact resistances between fuel cell components, and separate ionic and electronic flow resistances. The high frequency and low frequency intercepts are available in Table 5.1. The Lambda values were then calculated using equation 3.31 from the HFR value and the calculated Lambda values are displayed in Figure 5.2.

Table 5.1: High frequency (HFR) and low frequency (LFR) intercepts varying with temperature ($\Omega \cdot cm^2$)

$\boldsymbol{Temperature}$ (°C)	**80**		**100**		**120**	
$\boldsymbol{Relative\ humidity}$ (%)	$\boldsymbol{HFR}$	$\boldsymbol{LFR}$	$\boldsymbol{HFR}$	$\boldsymbol{LFR}$	$\boldsymbol{HFR}$	$\boldsymbol{LFR}$
30	0.0077	0.0958	0.0275	0.0879	0.0451	0.1213
40	0.0075	0.0946	0.0197	0.0814	0.0313	0.0994
50	0.0072	0.0988	0.0151	0.0747	0.0207	0.0885
60	0.0071	0.1021	0.0125	0.0697	0.0155	0.0750
70	0.0070	0.1117	0.00987	0.0635	0.0119	0.0695
80	0.0069	0.1365	0.00799	0.0555	0.0108	0.0643
90	0.0068	0.1667	0.00686	0.0542	0.0072	0.0625
100	0.0067	0.1569	0.00637	0.0590	0.0067	0.0597

The lambda here calculated from the HFR uses equation 3.29, this equation has an exponential temperature term to account for the fact that this is a thermally activated process where temperature will scale the conductivity due in part to the increased ionic mobility and diffusion coefficient. This means conductivity should increase exponentially with temperature for similar relative humidity. However it can be seen from the data that there is not the increase expected for constant relative humidity. The mobility of water within the membrane means that at different temperatures for a constant relative humidity a lower dissolved water content is seen, so despite the same amount of water being available as vapour to equilibrate with the membrane less water can remain bound to the membrane structure due to the temperature.

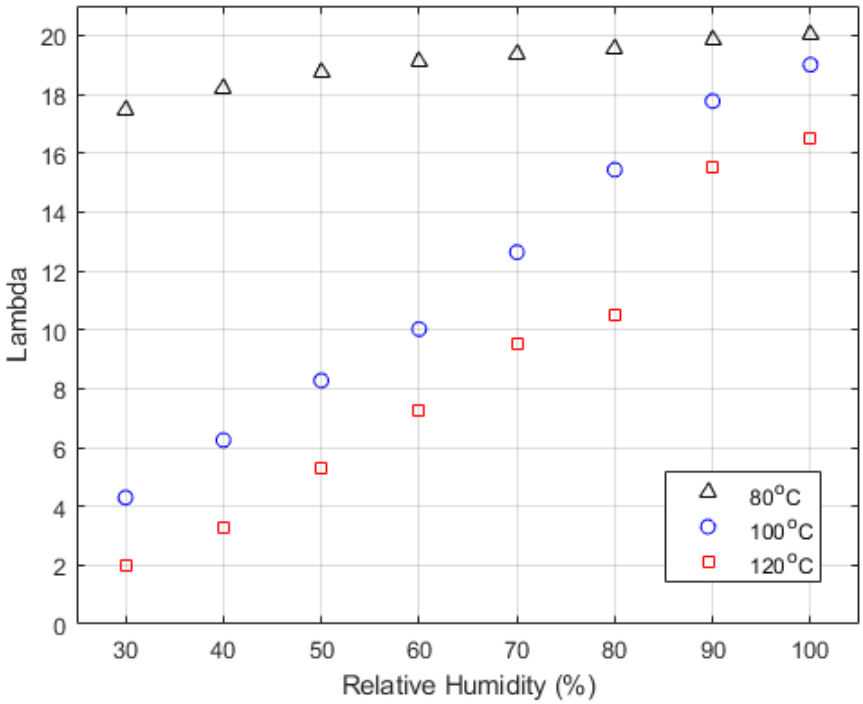

Figure 5.2: Converted HFR to equivalent lambda vs relative humidity

Figure 5.2 shows the calculated Lambda from measured HFR. The procedure of converting the high frequency resistance involves taking the measured resistance and convert-

ing it to a conductivity using Poullets law in equation 3.35. It is then possible to take the calculated conductivity and use the inverse of equation 3.29 a relationship from Dobson et al. [195], that gives conductivity as a function of Lambda, to calculate lambda from the membrane conductivity.

It is then possible to calculate the activity using the inverse of equation 3.31 which is the relationship between activity and Lambda from Dobson et al. [195]. The result of the calculation is available in Table 5.2. The values shown in that table appear to be above one, this is possibly due to the presence of a non steady-state system, which can be seen where activities above 1 are measured consistently for the cell operating at 80° C. A non steady-state system would imply that the water balance within the membrane is not at equilibrium, causing greater conductivity than expected. The cells were operated such that they did not rest at OCV between experiment steps and they would operate at 0.6 V so that the water production could remain in as close to steady state as possible however there still appear to be some non-steady state effects present, as seen in the table below.

Table 5.2: Calculated activity from HFR, across various relative humidities and temperatures

Relative humidity (%)	Temperature (ºC)		
	80	100	120
100	1.182	1.119	1.044
90	1.179	1.0961	1.015
80	1.174	1.0475	0.8770
70	1.171	0.9760	0.8404
60	1.166	0.8906	0.7317
50	1.159	0.8152	0.5889
40	1.149	0.6934	0.3506
30	1.133	0.5037	0.1882

Figure 5.3 shows the equation expressed by Dobson et al. [195] the relationship was defined for vapour activities up to 1, representing 100% relative humidity. However, most models extend the meaning of activity to include both liquid and vapour as a means of

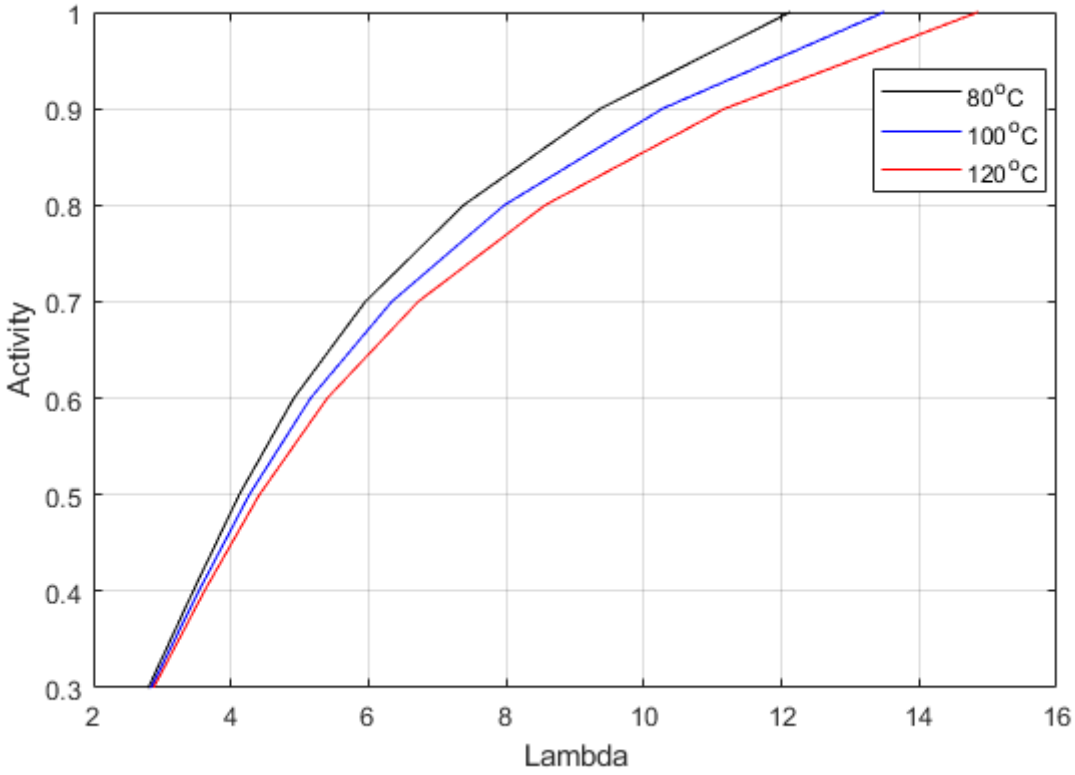

Figure 5.3: Predicted lambda vs water activity (a) from Eq. 3.31 at varied temperatures

introducing a pseudo-two-phase approximation [181, 188, 190, 193]. The approximation ignores liquid water's momentum contribution and treats it as extra vapour. In this way the converted values from HFR are used to understand the maximum activity that should be calculated for the model. In cases where the lambda is greater than 12 (80°C) and 15 (100°C), the model might imply that the activity is greater than 1. This would indicate a state of flooding or semi-saturation of the catalyst layer, typically flooding is defined as so much water as to introduce additional mass transfer resistance, where as there might be a lot of water within the catalyst layer that is moving slowly out, but does not hamper performance instead because of the increased conductivity, improves performance.

Figure 5.4 shows how the model was calculated, the lambda values were taken from the experiments and tabulated, and the model was run using a maximum function when

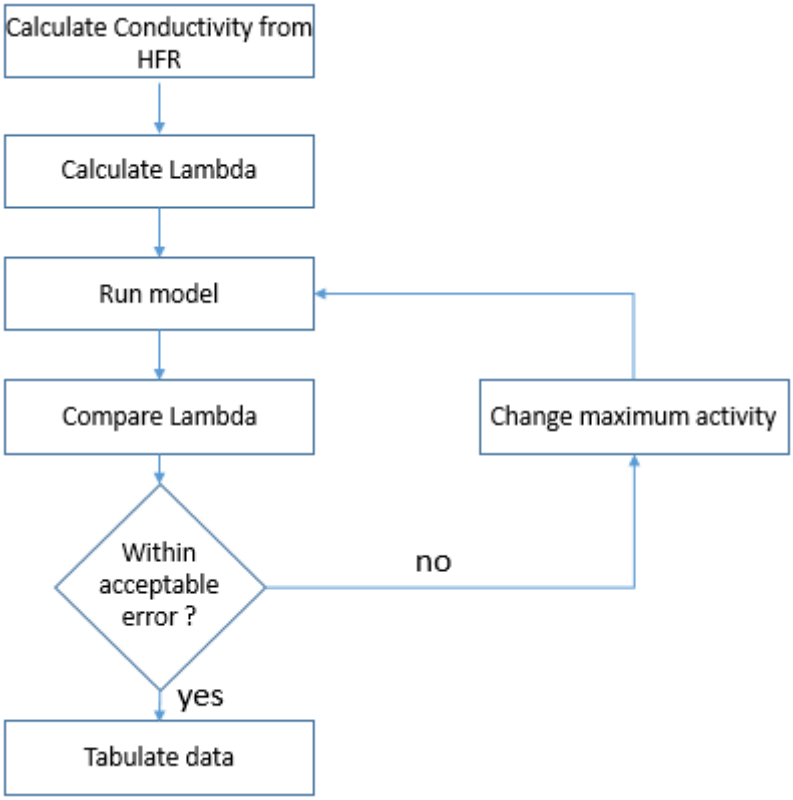

Figure 5.4: Algorithm used to solve for lambda from the model

solving for activity effectively ensuring that the activity did not surpass a maximum value. This max value was adjusted by iteration until the model had a good fit with the experimental data, the value calculated from the lambda was then tabulated and compared to the experimental data. The COMSOL model uses molecular transport physics which is optimised for gases, a maximum activity was imposed in order to prevent the water at the boundary of the membrane and catalyst layer interface from being excessively over-predicted by COMSOL.

Figure 5.5 shows the Lambda values calculated from the experimentally determined high-frequency resistance (HFR) compared to the water content values calculated from the COMSOL model using equation 3.31. The measured values seem to differ from the expected values from the function in figure 5.3, this is likely because the practical fuel

cell is designed with hydrophobic layers in order to increase the water retention of the membrane under low humidity operations. The maximum water activity was used as a fitting parameter. The measured water content was taken at 0.6 V, so similarly, the model used 0.6 V. As discussed above, the lumped Lambda shown in this figure is slightly higher than the actual lambda.

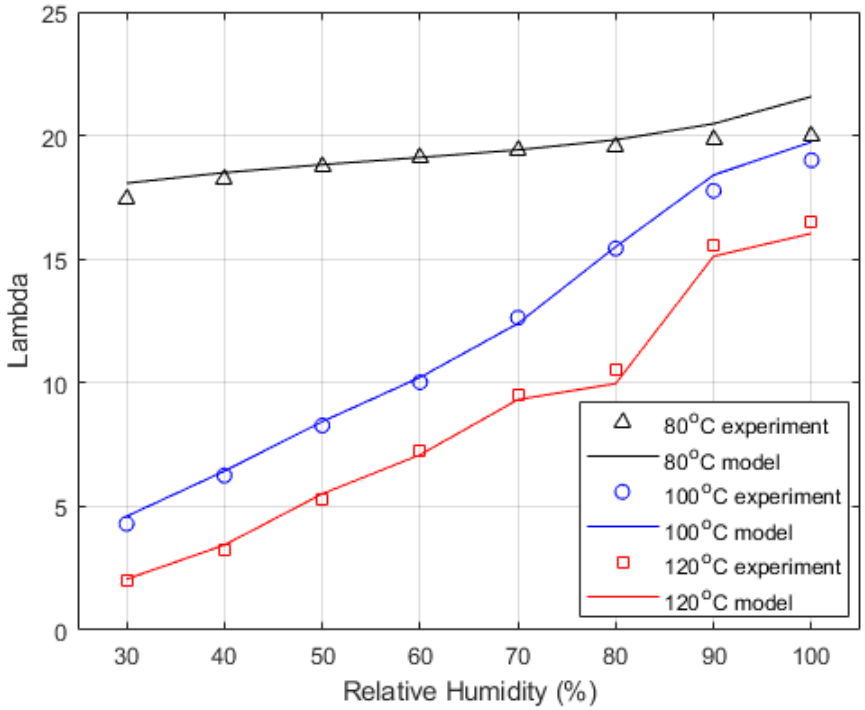

Figure 5.5: Measured (from HFR impedance spectroscopy) and converted to lambda from equation
3.29 and predicted water content (λ) from the developed model versus relative humidity.

Table 5.3 shows the fitting parameter (i.e. water activity) values used to generate the corrected water content within the membrane. The higher temperatures show a reduction in the maximum water activity, which is expected, as higher temperatures increase the saturation pressure of the water vapour.

Table 5.3: The fitted water activity used in the model for each relative humidity and temperature

Relative Humidity(%)	80°C	100°C	120°C
40	1.2	0.92	0.4
50	1.2	0.97	0.8
60	1.2	1.02	0.9
70	1.2	1.07	1
80	1.2	1.15	1.07
90	1.2	1.2	1.17
100	1.2	1.2	1.17

Figure 5.6 demonstrates the model's accuracy in predicting the polarisation curve using the derived membrane properties against the experimental results. The model shows excellent representation of the experimental results in the ohmic region at all temperatures as seen in the parity plots. There is clearly a lack of solid prediction at either the kinetic or mass transport regions. At 120°C, the model predicts the slope of the ohmic region very well. The kinetic and mass transport regions are more poorly replicated, this is probably because the mass transport resistances are based on the increase of water saturation which predicts a flooding behaviour with high relative humidity, while the kinetic parameters do not account for the crossover of reactant. Parameters like exchange current density and henry's law constant change with temperature however these parameters were assumed constant which is also why the model doesn't adequately account for those regions.

Table 5.4: R-squared Values for modelling fits in figure 5.6

Temperature (°C)	**RH 100**	**RH 70**	**RH 40**
80	0.989	0.968	0.939
100	0.931	0.952	0.989
120	0.839	0.967	0.838

Table 5.4 shows the R squared fits for each of the modelling fits in figure 5.6. There is a reasonably good fit considering the poor replication of the kinetic and mass transport regions of the polarisation curves.

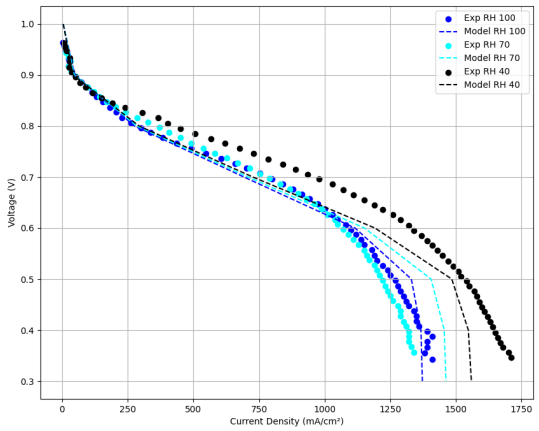

(a)

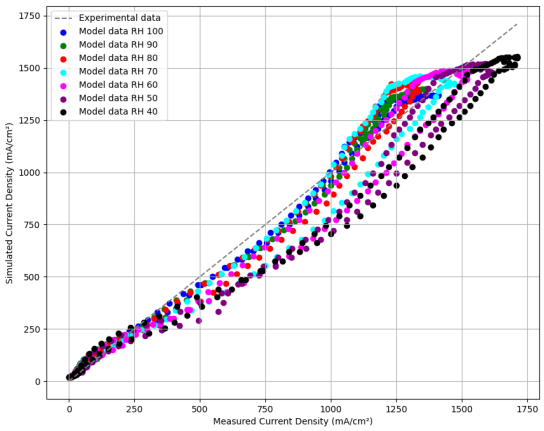

(b)

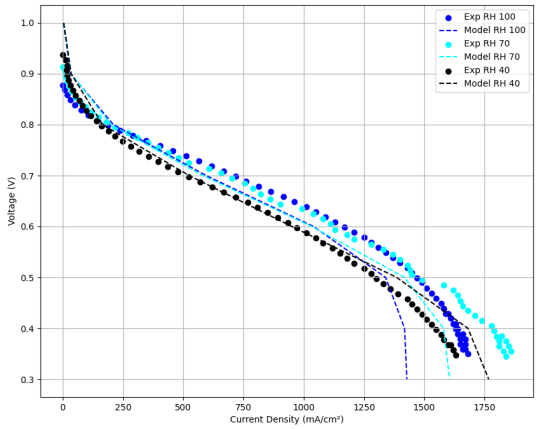

(c)

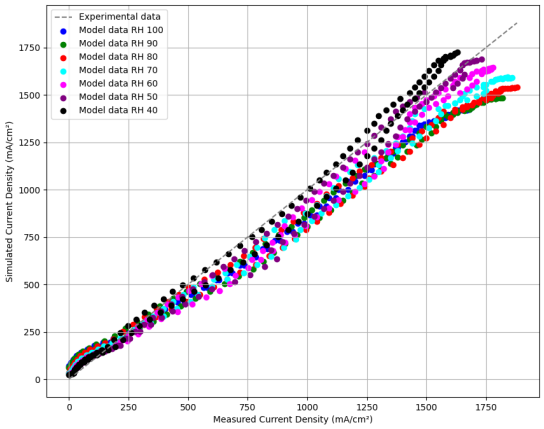

(d)

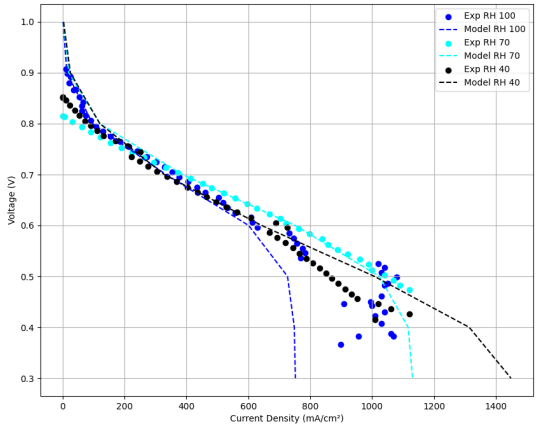

(e)

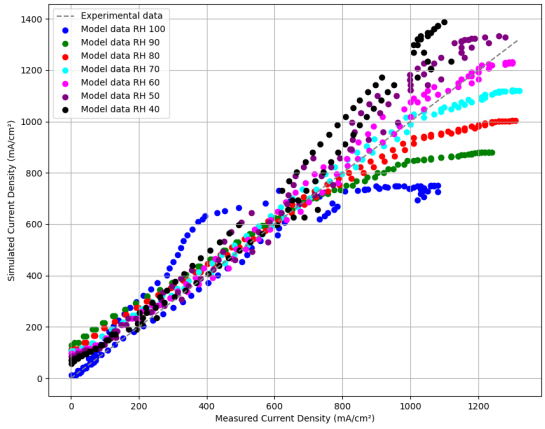

(f)

Figure 5.6: Polarisation curves and parity plots of modelling and experimental data at 80°C (a) and (b), 100°C (c) and (d), 120°C (e) and (f)

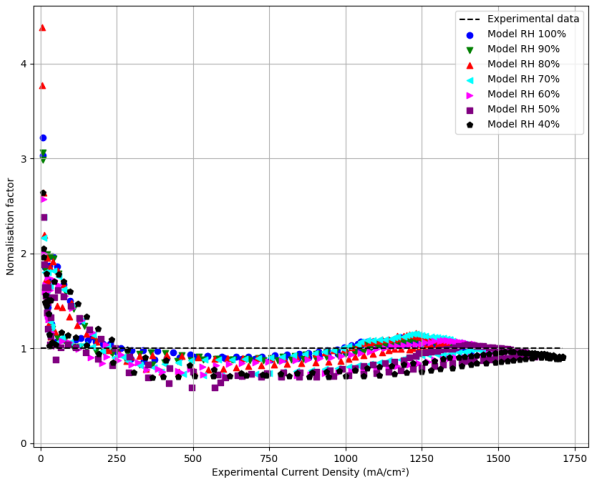

(a)

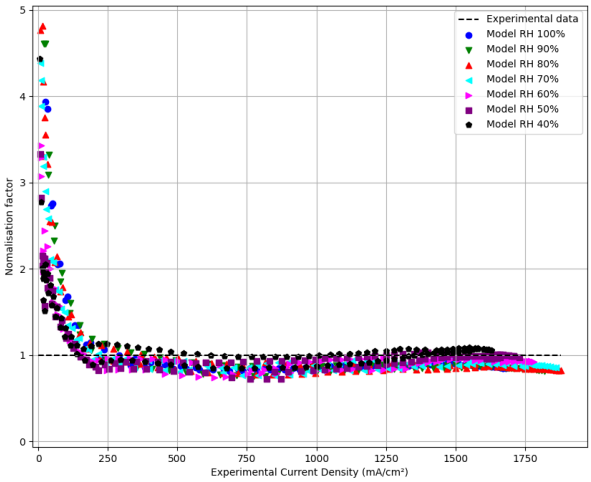

(b)

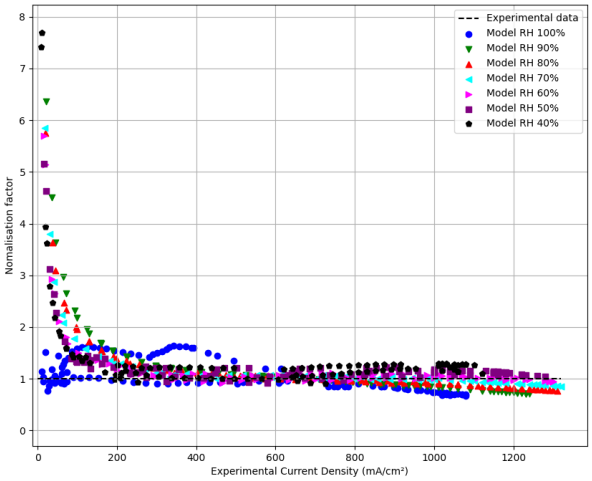

(c)

Figure 5.7: Normalisation factor based on current density for each temperature and relative humidity condition

Figure 5.7 shows the normalisation factor based on the current density, against the experimental current density. This gives a measure of the goodness of fit for the model, the criticism of this measure is that it will over-exaggerate when there is a large difference between small numbers, and under-exaggerate when the numbers are larger, it shows that there is a reasonable prediction for the higher relative humidities and as the relative

humidity becomes smaller the prediction is poor.

5.4 Discussion and model predictions

This work showed that the empirical relationship derived for Nafion 211 [47] for lambda vs water activity is valid up to 120°C at high relative humidity. The model showed good agreement with the experimental results in the ohmic region of the polarisation curve. The change in the shape of the water distribution shown in Figure 5.5 between 80°C, 100°C, and 120°C is due to several factors. The inlet gas stream's relative humidity and general thermodynamic conditions govern the membrane's water content stability. As shown in the steam table in table A.1, the enthalpy of vaporisation decreases with temperature, and the liquid enthalpy increases with temperature, making it much easier to produce water vapour at higher temperatures. Pressure has a different effect and affects the quality of steam; the higher the pressure, the higher the boiling temperature, which changes the ratio of liquid to vapour. The back pressure in the streams was maintained at 3 bara and the saturation pressure (Ps) is temperature dependent. So, the mol fraction of water in each gas stream increases significantly with temperature, which means that without the significant back pressure adjustment, the water severely reduces the oxygen content at the cathode.

Table 5.5: Cathode oxygen content Vs Temperature at 100% relative humidity

T (°C)	P (bar)	Psat (bar)	mol fraction H_2O	mol fraction air	mol fraction O_2
80	3	0.474	0.158	0.841	0.176
100	3	1.014	0.338	0.661	0.139
120	3	1.987	0.662	0.337	0.071

Table 5.5 shows that the oxygen content at 80°C is approximately 2.5 times greater

than the value at 120°C. Increasing the temperature for a Nafion membrane, which requires high hydration levels, causes a significant issue in terms of cathode oxygen content. The table also shows that the water content doubles from 80°C to 100°C and then doubles again from 100°C to 120°C; this is probably why the high-temperature tests typically have lower performance than the lower temperature tests. Performance is hampered at high temperatures by the proportion of the gas stream occupied by water; this water takes up space that could be occupied by oxygen and increases the likelihood of flooding in the cell. It also means that the mass flow rate of water required to keep the membrane fully hydrated is much greater than at 80°C, increasing the likelihood of dehydration. Especially considering temperatures above the boiling point of water, higher pressure testing is required to improve the oxygen content of the cathode gas stream and achieve the desired relative humidity. The impedance analysis of the 80°C and 100°C agreed nicely with the literature [119, 162, 211, 241]. However, the high relative humidity data in Figure 5.1d&f shows the development of a second semi-circle, indicating that there is a shift in the dominating resistance at 0.6V which would imply that the analysis does not strictly apply or that the mass transport losses have increased to such a point as they are starting to dominate in this voltage region. This is especially apparent at 120°C. The flooding physics used in the model do not represent the observed behaviour [126, 223]. The model overestimates the mass transport region of the polarisation curve; therefore dehydration and greater mass transport resistance physics are a better fit. This was confirmed with the EIS showing the development from a single semi-circle, indicating a dominating ohmic resistance, to two semi-circles, indicating a mix of mass transport and ohmic resistance. The intercept between the two semi-circles represents the limit of the ohmic resistance,

and the low-frequency intercept now shows the mass transport resistance.

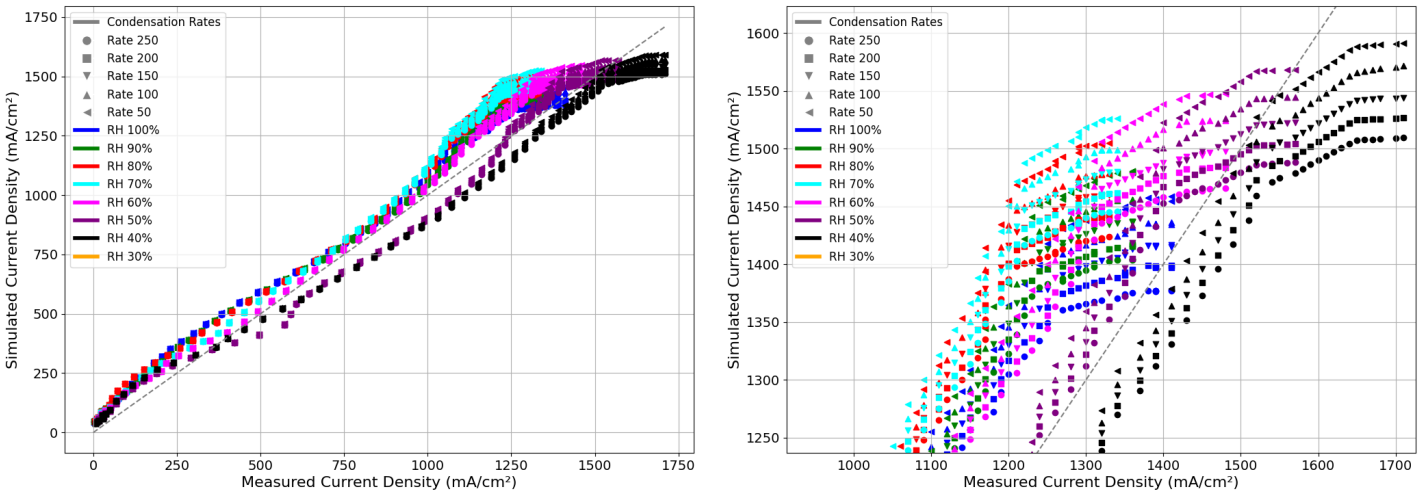

(a) (b)

Figure 5.8: (a) Example effect of condensation rate on current density in model, (b) zoomed view of mass transport region. This example data is for 80°C

Figure 5.8 shows the effect of changing the value of gamma in equations 3.39 and 3.40, gamma represents the condensation rate at which water will precipitate out from high relative humidity vapour. It is a product of the condensation rate constant and the saturation specific area to give an amount of vapour condensed per unit area. The value of condensation rate was varied by a factor of 50 to 250 $m^3 \cdot m^{-2}$. The effect of this parameter was shown in the plot, where it can be seen that the rate change does not alter the shape of the mass transport region but rather makes it act at lower current densities reducing the current density sooner. This shows that the chosen physics are probably not acting in the experiment and hence why the model does not replicate the behaviour appropriately.

Further work into the specifics of the mass transport region would be needed to develop the correct relationship that is being observed. This work is intended to focus on the membrane and ohmic region so it falls outside of the scope.

The lambda was stable for 80°C, this was not seen at higher temperatures, and there was a more dramatic drop off in lambda as RH decreased. It showed that lower humidity conditions will affect performance significantly; the key is hydration, but as discussed above, the increase in temperature will also change the oxygen available to react.

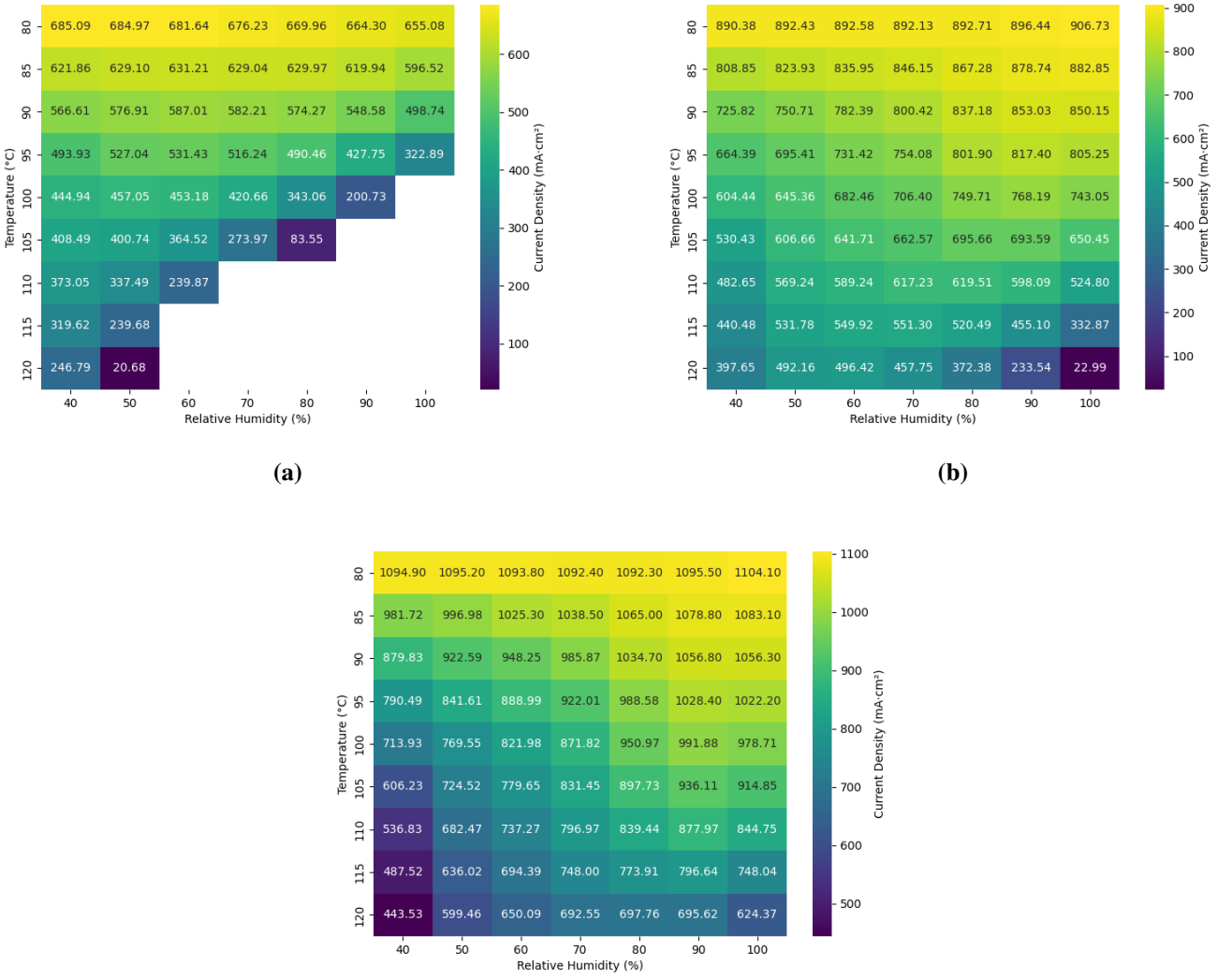

(a) **(b)**

(c)

Figure 5.9: Heat map tables of the model prediction results for 0.6 V, 40-100% RH, 80 to 120°C (a) 1 bar, (b) 2 bar, (c) 3 bar

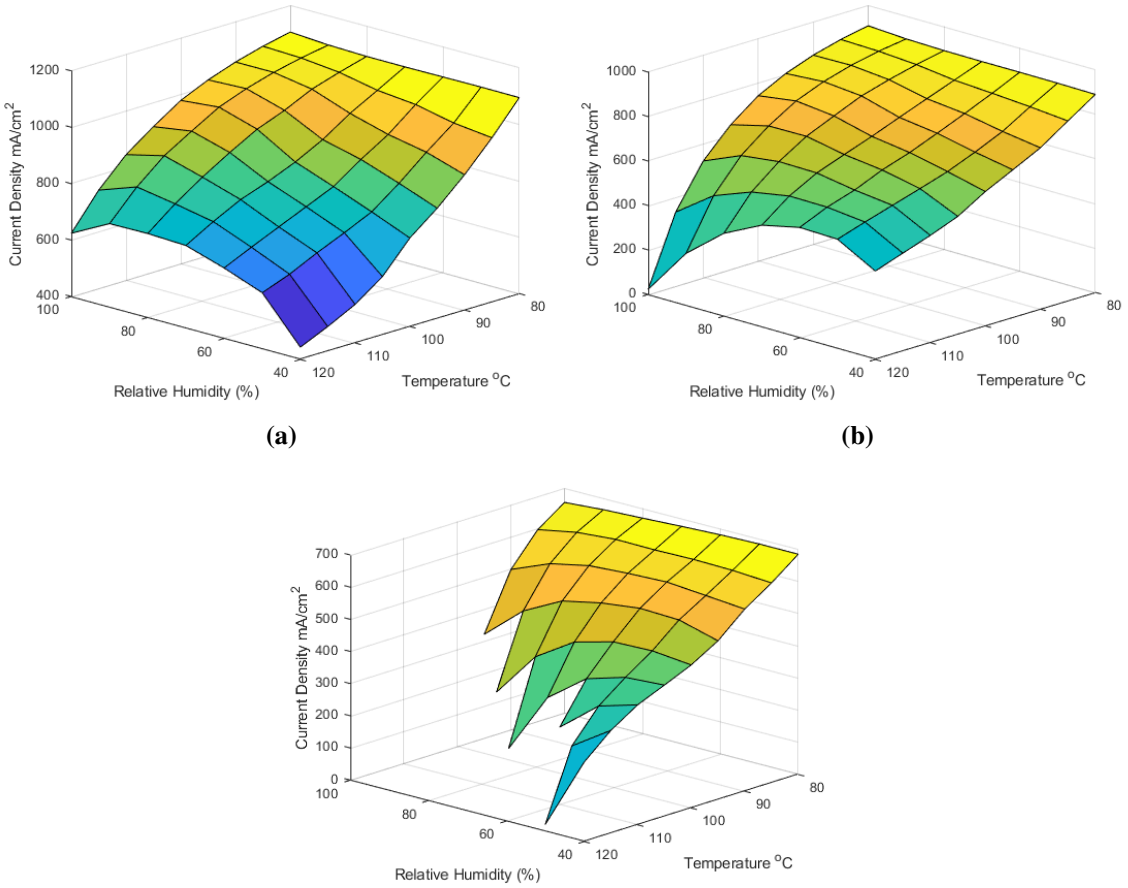

Figure 5.10: Surface plots of model current density prediction data at 0.6V across 40 to 100% RH, 80 to 120°C, and a) 1 bar, b) 2 bar, c) 3 bar pressure.

The model can predict the fuel cell's performance at many combinations of different operating conditions; Figure 5.9 shows the current density obtained at a cell voltage of 0.6 V and variety of temperatures, relative humidity, and pressure. It can be noted that the performance is similar between 80°C and 100°C. At 120°C, the performance is significantly reduced, most likely because of the reduced oxygen content mentioned above. 0.6 V was chosen as the performance parameter as it is closely tied to the membrane performance. The colour shading in the table indicates high performance (green), and low performance (red). The empty spaces in Figure 5.9 at 1 bar pressure represent the fact that it is impossible to achieve those relative humidity conditions at 1 bar pressure, as the

saturation pressure exceeds the total pressure. Hence, we see a significant improvement between the 2 bar and 3 bar data.

There is particularly poor performance at higher temperatures at 1 and 2 bar, because it is very close to the saturation point. This reduced the amount of available oxygen considerably as illustrated in Table 5.5. It shows a halving of the mol fraction between 80 and 120 °C, this is no doubt the primary reason for the poor performance. Figure 5.10 shows the model prediction data in surface plots. Blue in the surface plot represents high performance, and yellow represents low performance. Generally, higher pressure and lower temperature are better for the ohmic region. It appears that higher temperatures generally decrease performance; however, this is only true in the ohmic region; it appears that higher temperatures have lower limiting currents due to reduced oxygen partial pressure from the larger mol fraction of water present to maintain the relative humidity at high temperatures. Although 120°C was greatly affected by the membrane's increased resistance and reduced performance. While this work demonstrated that there is merit to operating Nafion-based fuel cells at higher temperatures, it is essential to acknowledge the accompanying challenges and limitations. The necessity for higher pressures to maintain operation not only requires more energy for air pumps but also increases the energy needed to vaporize water for achieving higher humidity levels, coupled with a required increase in airflow rate. Furthermore, our data indicated that despite these efforts, fuel cell performance was suboptimal within the operating voltage range of 0.8 to 0.6V, even without the challenges posed by reductions in oxygen partial pressure. These factors underscore the complexities and trade-offs involved in optimizing fuel cell operations under elevated temperature conditions.

5.5 Conclusions

This comprehensive examination of Polymer Electrolyte Fuel Cells (PEFCs), particularly with Nafion 211 membranes under various operational conditions, has elucidated several critical aspects pertinent to enhancing fuel cell performance and durability across elevated temperature ranges. Empirical relationships that relate activity to lambda (λ) and ionic conductivity have been extended to higher operational temperatures (up to 120°C). This adaptation is crucial as it highlights the importance of accurately fitting parameters such as activity and lambda in modeling and operational strategies, especially when regular operational theories begin to falter at intermediate temperatures.

The key findings and implications from this study include:

- Temperature and Membrane Hydration: It is evident that as temperature increases, membrane hydration decreases, significantly impacting the performance due to increased ohmic resistance. The highest performance experimentally was achieved at 100°C, where temperature improvements facilitated mass transport and mitigated flooding phenomena. However, beyond this threshold, performance declines due to dehydration and loss of ionic conductivity.

- Humidity and Pressure Effects: Relative humidity and operational pressure are pivotal in maintaining optimal membrane performance. The experimental results and the model predictions align in suggesting that higher pressures enhance performance by maintaining a better balance of water content without sacrificing the available oxygen. This is critical as the study shows potential benefits in high-pressure operations beyond the traditional limit of 80°C.

- Degradation Mechanisms and Material Innovation: Insights into degradation mechanisms underpin the need for developing new materials or modifying existing PFSA membranes to enhance their thermal stability and water retention capabilities. The interactions between thermal, mechanical, and chemical degradation pathways underscore the necessity for robust, durable membrane formulations.

- Advanced Modelling Techniques: The adaptation of predictive models to incorporate realistic operational variables (temperature, humidity, and pressure) has proven essential. The model's accuracy in the ohmic region of the polarisation curve suggests its utility for pre-emptive adjustments in design and operation of PEFCs.

While this work demonstrated that there is merit to operating Nafion-based fuel cells at higher temperatures, it is essential to acknowledge the accompanying challenges and limitations. The necessity for higher pressures to maintain operation not only requires more energy for air pumps but also increases the energy needed to vaporize water for achieving higher humidity levels, coupled with a required increase in airflow rate. Furthermore, our data indicated that despite these efforts, fuel cell performance was suboptimal within the operating voltage range of 0.8 to 0.6V, even without the challenges posed by reductions in oxygen partial pressure. These factors underscore the complexities and trade-offs involved in optimizing fuel cell operations under elevated temperature conditions.

In conclusion, this research outlines a clear trajectory for advancing PEFC technology through targeted improvements in membrane materials, operational strategies, and predictive modeling. By addressing these challenges and leveraging the detailed insights obtained, the development of more robust, efficient, and durable PEFC systems is distinctly achievable, marking a significant step forward in sustainable energy technologies.

Further exploration into the specifics of high-pressure scenarios could open new avenues for surpassing current temperature and performance limitations in fuel cell technologies.

CHAPTER SIX

SEMI-EMPIRICAL MODELLING OF GRAPHENE COMPOSITE MEMBRANE MATERIALS

6.1 Introduction

Polymer electrolyte fuel cells (PEFCs) are limited in operating temperature by their electrolyte material [243, 244]. Current research is focused on developing membranes with superior performance parameters such as reduced thickness [39], decreased hydrogen crossover [49, 127, 198, 226], and enhanced conductivity [99, 110, 236, 245]. Detailed discussions on these developments are found in sections 2.1, 2.2, and 2.5, with a comprehensive summary in table 2.1.

Nafion, with its robust performance characteristics and chemical stability across a range of temperatures (-10 to 80°C) [108, 246], remains the preferred polymer for many PEFCs. It consists of a polytetrafluoroethylene (PTFE) backbone with side chains ending in a sulphonic acid group [139, 163]. Nafion's ionic conductivity depends on maintaining high water content within the membrane [34, 242], limiting its upper operational temper-

ature to 80°C.

Composite membranes enhance Nafion's inherent weaknesses, like mechanical stability and high-temperature performance [32, 247]. These composites typically combine a polymer matrix with various fillers such as carbons [247–249], inorganics [87, 90], and organics [90, 245], which improve properties like hydration at elevated temperatures [112, 248] and mechanical strength [100, 236].

Increasing fuel cell operating temperatures offers several benefits, including enhanced kinetics of the oxygen reduction reaction (ORR) [114], improved water management [125], and increased tolerance to impurities [129]. However, higher temperatures also pose challenges such as dehydration of the membrane [146], which can reduce its conductivity. Additionally, exceeding the polymer's glass transition temperature could destabilize its structure, increasing permeability to gases and liquids [133, 134].

Graphene oxide, a derivative of graphene with hydrophilic properties due to oxidized groups, has shown promise as a filler in composite membranes for intermediate temperature fuel cells [97, 247, 249]. Its ability to retain water at elevated temperatures could address some of the hydration issues associated with higher operating temperatures.

Modeling is instrumental in accelerating the design and development of advanced membrane materials by enabling the exploration of parameters beyond the reach of current experimental techniques, thus reducing costs [46]. For instance, the widely used sorption model by Springer et al. [188], based on earlier work [189], has played a crucial role despite its limitations, such as the confined temperature range and pressure conditions. The absence of a comprehensive model for composite membranes underscores the need for further research in this area, which could incorporate empirical data from various

innovative composite membranes reported in the literature [44, 80, 97].

6.2 Methods

In this work, Nafion membranes with a graphene oxide filler (Nanoinnova) were created by solution casting. They were made using the methodology detailed in section 3.1.1. 4 wt% graphene oxide was added and mixed into the Nafion solution before it is added to the glassware. The membrane electrode assemblies were also made using method detailed in section 3.1.2, but two gas diffusion electrodes (Johnson Matthey GDE 0.4 mg PT loading) were used instead of spraying the membrane with catalyst ink.

The fuel cell testing was performed using the protocol detailed in section 3.1.5, the testing was performed at 80, 100, and 120°C to show its effectiveness across the temperature range.

The model is constructed in the same way as detailed in section 3.2, the only difference is that the water sorption behaviour is investigated using 2 different methods.

This model is based on only 4 wt% graphene oxide. This was part of a collaboration with Ibrahim et al. [97] where previous work was done to understand a good ratio of filler to ionomer garnering a benefit for intermediate temperature operation. Ibrahim et al. supplied the MEAs for testing. As a result of that, this work was done taking freshly made materials and attempting to model the benefits seen with the composite membranes.

6.3 Experimental results

Figure 6.1 shows the OCV with changing relative humidity for each temperature. Figure 6.2 shows the polarisation and impedance data for the experimental composite GO-Nafion membrane fuel cells. The general trend of the 80°C data shows that performance decreased with decreasing relative humidity. The impedance spectra show a shift at both x-intercepts and a slight shape change as relative humidity approaches 40%. As is well reported in literature, these shape changes indicate differences in the dominating resistance at 0.6V. The ohmic resistance (HFR) increases with decreasing RH; the mass transfer resistance (the second semi-circle) increases with increasing RH; the charge transfer resistance (the first semi-circle) decreases with increasing RH. Without further investigation it is inappropriate to say more about the type of resistance change or what process is dominating the shape change. However, the high frequency intercept of the spectra is well understood to be the lumped electronic and ionic resistances of the fuel cell; considering the construction of the model the membrane resistance is a lumped parameter so the HFR fits well.

The general trend for the 100°C data shows a greater sensitivity to the change of relative humidity; the performance at high relative humidity is the best performance of the cell at any condition. As relative humidity decreases below 80%, the polarisation curves show instability likely due to dehydration of the membrane. When the membrane undergoes dehydration, the dissolved water either evaporates or flows out of the membrane reducing its conductivity. Drying occurs when the membrane loses a critical amount of water, hindering the transport of protons; hence the large decrease in performance at 40% RH. The impedance spectra mirror the observations in the polarisation curves; they show

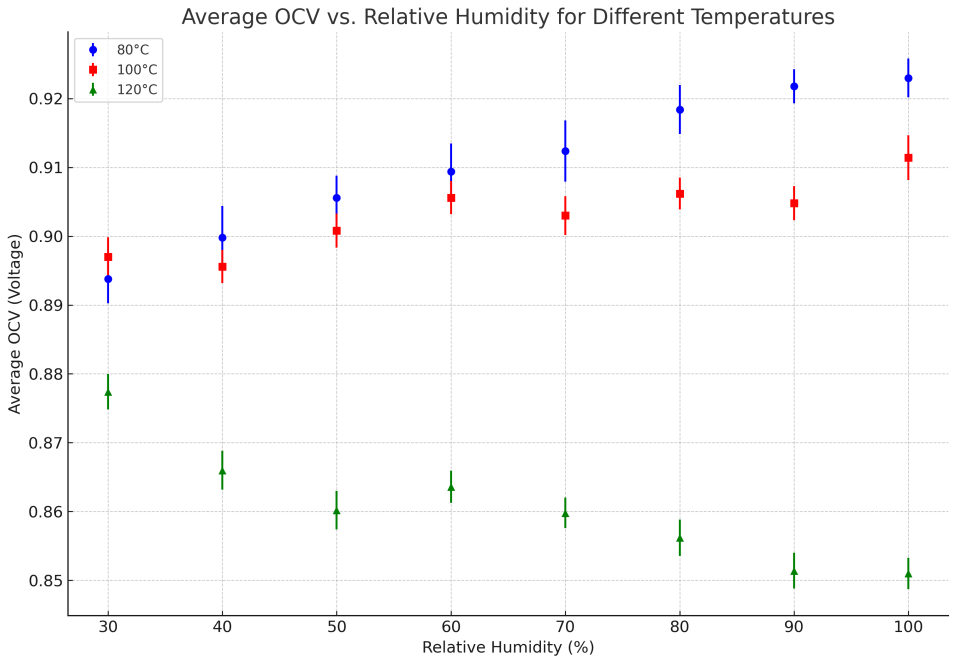

Figure 6.1: Open circuit potential vs Relative humidity, for various temperatures

a drop in HFR in line with the drop in current density of the polarisation curves. It should be noted that the low frequency x-intercept shifts far more significantly indicating an increase in the resistance of the cell indicating phenomena associated with dehydration of the membrane, which could be due to a resistance in the ionic portion of the charge transfer resistance.

The 120°C data shows a similar relative drop in performance as the 100°C data; the overall performance is less than the data obtained at the other temperatures. This drop in overall performance is probably due to several processes, the first is crossover of reactants; crossover of reactants increases with temperature, typically it is most evident at open circuit voltage as seen in Figure 6.1. Second largest effect is membrane dehydration and drying. Third, the drying of the ionomer at will cause a drop in the resistance associated with charge transfer. The impedance data again mirrors the trend in the polarisation

curves. The HFR shows an increase in line with the decrease in current density, as well as other features shifting as other effects might dominate, such as the low frequency intercept which indicates an increase of the charge transfer and mass transport resistances.

Table 6.1: High frequency (HFR) and low frequency (LFR) intercepts varying with temperature ($\Omega \cdot cm^2$)

$\boldsymbol{Temperature}$ (°C)	**80**		**100**		**120**	
$\boldsymbol{Relative\ humidity}$ (%)	$\boldsymbol{HFR}$	$\boldsymbol{LFR}$	$\boldsymbol{HFR}$	$\boldsymbol{LFR}$	$\boldsymbol{HFR}$	$\boldsymbol{LFR}$
40	0.06	0.125	0.08	0.18	0.096	0.225
50	0.04	0.085	0.056	0.125	0.07	0.155
60	0.03	0.064	0.046	0.095	0.045	0.11
70	0.023	0.059	0.032	0.071	0.036	0.085
80	0.02	0.06	0.026	0.061	0.03	0.072
90	0.019	0.063	0.02	0.053	0.022	0.062
100	0.018	0.069	0.015	0.056	0.019	0.057

Table 6.1 shows the high and low frequency intercepts from the impedance spectra in figure 6.2. There is a general trend of increasing high frequency resistance with decreasing relative humidity, as well as an increase in the low frequency resistance with increasing relative humidity. There is also a trend that as the temperature increases so does the low frequency resistance. The charge transfer and mass transfer resistance magnitudes have an obvious interplay as the temperature and relative humidity increase. this is shown by the shifting of which semi-circle dominates in the Nyquist plot.

Figure 6.2 shows changes in the kinetic region of the polarisation curve, this is mainly due to ionomer dehydration in the catalyst layer. While the membrane has improved water retention due to the presence of GO the ionomer has not leading to a slight drop in the performance in the kinetic region.

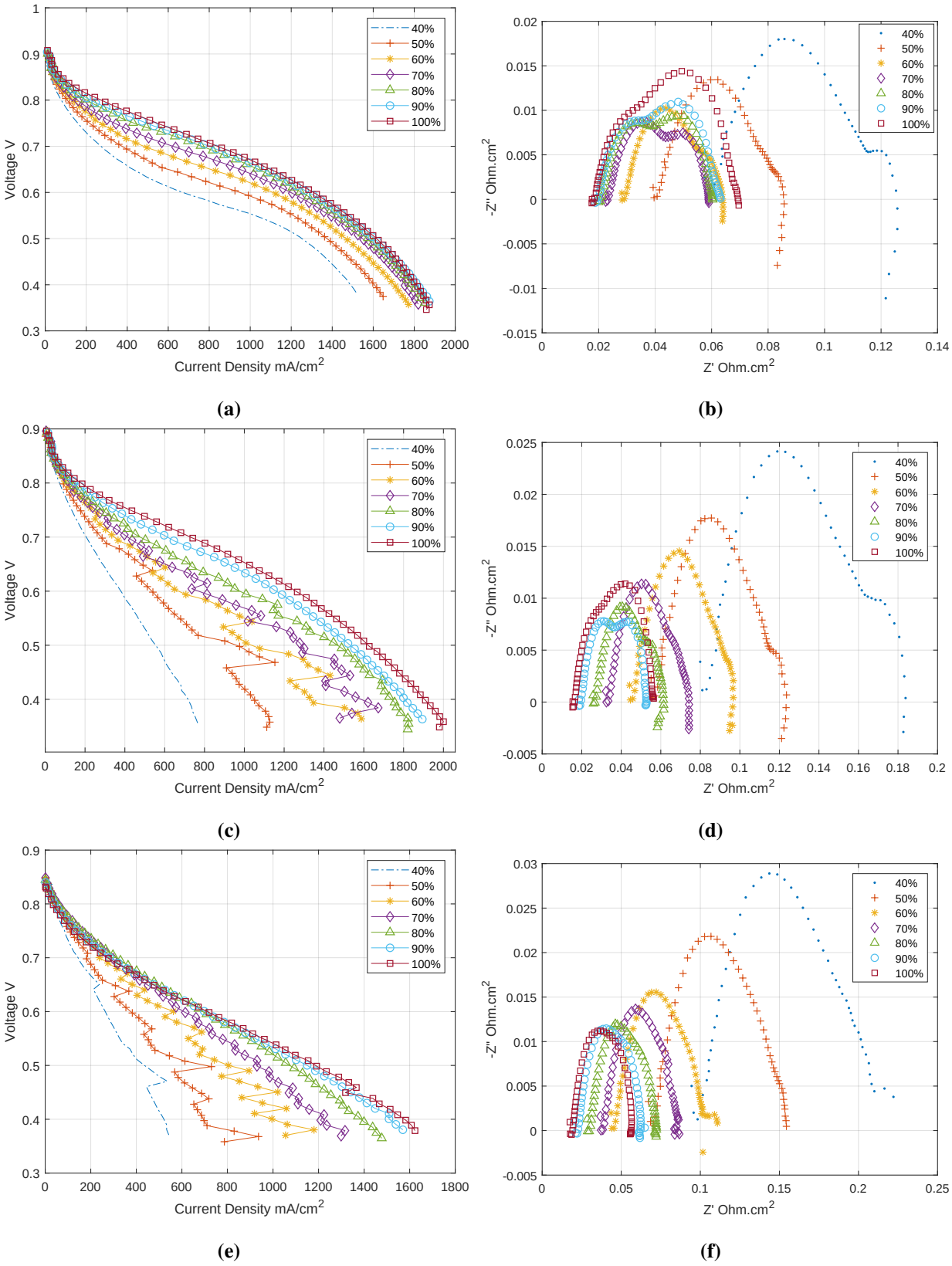

Figure 6.2: Polarisation curves (a,c,e) and Impedance spectra (b,d,f) of the prepared GO-Nafion composite membrane at 80°C (a,b), 100°C (c,d), and 120°C (e,f). Impedance spectra were taken at a voltage of 0.6 V.

6.4 Modelling – Water Sorption

Predicting the properties of composite materials is a well-defined topic of materials science. The classical approach is called the rule of mixtures and it was derived to predict the material properties of a polymer composite by using series and parallel models to create a range of possible values using the equations 6.1 and 6.2 [250, 251].

$$MP_{composite} = MP_{Filler} * f + MP_{matrix} * (1 - f) \tag{6.1}$$

$$MP_{composite} = \left(\frac{f}{MP_{Filler}} + \frac{(1 - f)}{MP_{matrix}} \right)^{-1} \tag{6.2}$$

For a two-component composite the material property MP is defined by; the series model in Equation 6.1 and the parallel model in Equation 6.2. The volume fraction of the filler (f) and the matrix ($1 - f$) is used to estimate the proportion of the material's contribution to the property of interest. Normally these equations are applied to characteristics such as modulus, mass density, tensile strength, thermal conductivity, and electronic conductivity. There are no known examples in the literature of predicting ionic conductivity through this method; however, it follows the same logic as electrical conductivity so could be valid. Nafion has many properties which are linked to performance: water sorption, ionic conductivity, mechanical strength, and electrical resistance, to name a few. When combined with graphene oxide, the main properties of interest for fuel cell modelling are water uptake and conductivity. Graphene is known to have a small ionic conductivity which is treated as negligible in this case. So, for conductivity, Equations 6.1 and 6.2 can be reduced to include the terms which deal with the matrix material, i.e. Nafion. In the case of water uptake, graphene oxide is a known hydrophilic material; it associates with

water with a high affinity owning to the oxygen content of the sheets, which means that the effect of graphene is observed in the water uptake. Graphene oxide (GO) demonstrates higher proton conductivity than pristine graphene due to its surface functional groups that introduce nano- and atomic-scale roughness, reducing energy barriers for proton transport. Experimental findings reveal that monolayer GO's proton permeability is greater than pristine graphene, highlighting the significant impact of these structural modifications on enhancing conductivity[252]. Wu et al.[252] showed that the proton conductance was 110 $\pm$ 70 mScm^{-2}; it is not clear what the dimensions of their samples are so it is difficult to compare the measured conductance with the conductivity. Nafion's conductivity lies between 10 - 40 Sm^{-1} depending on hydration. In Nafion, the ionic conductivity is closely linked to the water content of the membrane, so the graphene oxide has little interaction with ionic conductivity in terms of providing acid sites to conduct protons. It does provide extra water though, which encourages better proton transport through the membrane. Therefore, an effect of the graphene on the performance of the membrane via its hydrophilic properties can be seen. It therefore follows that it is better to lump the effect of the graphene into purely its effect on the lambda value by using the series version of the rule of mixtures.

$$\lambda_{composite} = \lambda_{Nafion} * (1 - f) + \lambda_{graphene} * (f) \tag{6.3}$$

To calculate $\lambda_{composite}$, the high-frequency resistance is converted into the equivalent membrane conductivity using equation 3.35. That conductivity data is then converted into the equivalent lambda value using equation 3.29, giving the total expected lambda value. λ_{Nafion} is calculated using the equation set out for dispersion cast Nafion membranes by

Dobson et al. [195] as follows:

$$\lambda_{Nafion} = (1 + 0.2352a^2 \cdot \left(\frac{T-30}{30}\right)) \cdot (14.22a^3 - 18.92a^2 + 13.41a) \tag{6.4}$$

$\lambda_{graphene}$ was calculated by rearranging equation 6.3 and using the $\lambda_{composite}$ and λ_{Nafion} values calculated from equations 3.29 and 6.4 respectively. Lambda is usually calculated as the number of water molecules per acid side group molecules. Since graphene doesn't have any acid side groups, the definition is extended to include the contribution of water that the graphene provides. It can be thought of as an equivalent lambda, where the value is the amount it provides if it were an equivalent Nafion membrane.

$$\lambda_{composite} = ((1+0.2352a^2 \cdot \left(\frac{T-30}{30}\right)) \cdot (14.22a^3 - 18.92a^2 + 13.41a)) * (1-f) + \lambda_{graphene} * (f) \tag{6.5}$$

Equation 6.5 shows the combined mathematical form of the rule of mixtures with the dobson equation for the behaviour of Nafion membrane water sorption. This equation was rearranged to make the water sorption behaviour of the graphene the subject.

The caveat to this approach is that there are other mechanisms at play that influence the ability of the membrane to conduct protons, such as the tortuosity, interactions between graphene oxide and sulphonic acid side groups, particle size and dispersion of the particles across the material. This set of equations ignores those effects and assumes that the bulk properties are similar throughout the full structure.

6.4.1 Polynomial model

Equations 6.6, 6.7, 6.8 below and their R^2 values in Table 6.2 were created by plotting data in Microsoft Excel, then using the 3rd order polynomial line for each trace at each temperature with the intercept set to zero. The resulting coefficients for each term were averaged and the solver function was applied to see if some multiple of the average would fit the data giving equation 6.15, and the lines were retraced and R^2 values calculated using the sum squared difference method.

$$\lambda_{\text{graphene 80°C}} = -58.34a_w^3 + 79.721a_w^2 - 16.606a_w \tag{6.6}$$

$$\lambda_{\text{graphene 100°C}} = -21.375a_w^3 + 35.649a_w^2 - 10.942a_w \tag{6.7}$$

$$\lambda_{\text{graphene 120°C}} = -27.822a_w^3 + 43.059a_w^2 - 15.465a_w \tag{6.8}$$

R^2 was used to evaluate the model's goodness of fit. It is calculated using the equation below:

$$R^2 = 1 - \frac{\sum_{i=1}^{n}(y_i - \hat{y}_i)^2}{\sum_{i=1}^{n}(y_i - \bar{y})^2} \tag{6.9}$$

where y_i is the observed value, $\hat{y}_i$ is the predicted value, $\bar{y}$ is the mean of the observed values, and n is the total number of observations.

The numerator $\sum_{i=1}^{n}(y_i - \hat{y}_i)^2$ represents the residual sum of squares (RSS), while the denominator $\sum_{i=1}^{n}(y_i - \bar{y})^2$ represents the total sum of squares (TSS). R^2 thus quantifies the proportion of the variance in the observed values explained by the model.

Table 6.2 shows the fit of the converted HFR data to the 3rd-order polynomial fits.

Table 6.2: Calculated value of R^2 for equations 6.6, 6.7, 6.8 at 80°C, 100°C, and 120°C respectively

Temperature (°C)	80	100	120
R^2	0.988	0.98	0.931

Equations 6.6 and 6.7 show the best fits, the intercept was chosen to be at zero to align with the physics that at low water contents the lambda should be low and close to zero. The idea of factoring out the sorption isotherm revealed that the behaviour revealed roughly that the 100°C and 120°C equations were similar, and the coefficients of the 80°C were almost a factor of 2 larger. This arose to the idea that the isotherm value must be different to the one for Nafion which is to be expected.

For the next iteration, the $\lambda_{graphene}$ value was evaluated as it is, the data was plotted again in Excel and a line of best fit was applied using a 3rd order polynomial. The following equations were calculated:

$$\lambda_{\text{graphene 80°C}} = -771.55a_w^3 + 1093.8a_w^2 - 234.29a_w \tag{6.10}$$

$$\lambda_{\text{graphene 100°C}} = -229.35a_w^3 + 423.47a_w^2 - 128.82a_w \tag{6.11}$$

$$\lambda_{\text{graphene 120°C}} = -367.24a_w^3 + 576.91a_w^2 - 197.66a_w \tag{6.12}$$

Table 6.3: Calculated value of R^2 for equations 6.10, 6.11, 6.12 at 80°C, 100°C, and 120°C respectively

Temperature (°C)	80	100	120
R^2	0.995	0.987	0.951

Table 6.3 shows the R^2 values for fitting the data to equations 6.10, 6.11, and 6.12. The fitting is slightly better than the first isotherm method, considering the form displayed in equation 6.13.

$$\lambda_{Graphene} = (b(T)) \cdot (Aa^3 + Ba^2 + Ca) \tag{6.13}$$

In an attempt to derive a relationship between the equations so that an isotherm component be determined, to understand the variance with temperature, the sum of the squared differences for each temperature's prediction of lambda were taken and summed together to create an objective function. 6 parameters for 24 data points were used in the solver and allowed to float to find the best fit. The upper and lower bounds of A, B, and C were found by looking at the values of the coefficients of each of the temperatures and given a 5% larger range. The model was fitted by looking at all the values simultaneously to the structure of equation 6.13 and each temperature has its own b coefficient. This was then used with the Solver plugin, using the evolutionary solver and the following conditions:

$$SSD = \Sigma(x_{calc} - x_{measured})^2 \tag{6.14}$$

Table 6.4: Initial values, conditions, and final values used in the evolutionary non-linear non-smooth solver

Variable	Initial value	Upper bound	Lower bound	Final value
Coefficient A	-456.047	-217.883	-810.128	-348.97
Coefficient B	701.06	1148.49	410.846	518.25
Coefficient C	-186.923	-122.38	-246.01	-122.379
$b_{80°C}$	1	100	0	2.12
$b_{100°C}$	1	100	0	1.08
$b_{120°C}$	1	100	0	0.324

Table 6.4 shows the initial values and conditions given to the non-linear evolutionary solver as well as the result of the solver. The solver settings were then adjusted to increase the mutation rate from 0.0075 to 0.1 and the population size increased from 100 to 400, this is to check for local minima and to ensure that the model has actually found the best

fit rather than just a good fit. The following equation 6.15 represents the result of the solver and it is displayed in Figure 6.3 for each temperature and the final R^2 fitting for the modelled vs experimental data is displayed in Table 6.5

Displayed in Figure 6.3 is the $\lambda_{composite}$ for each temperature.

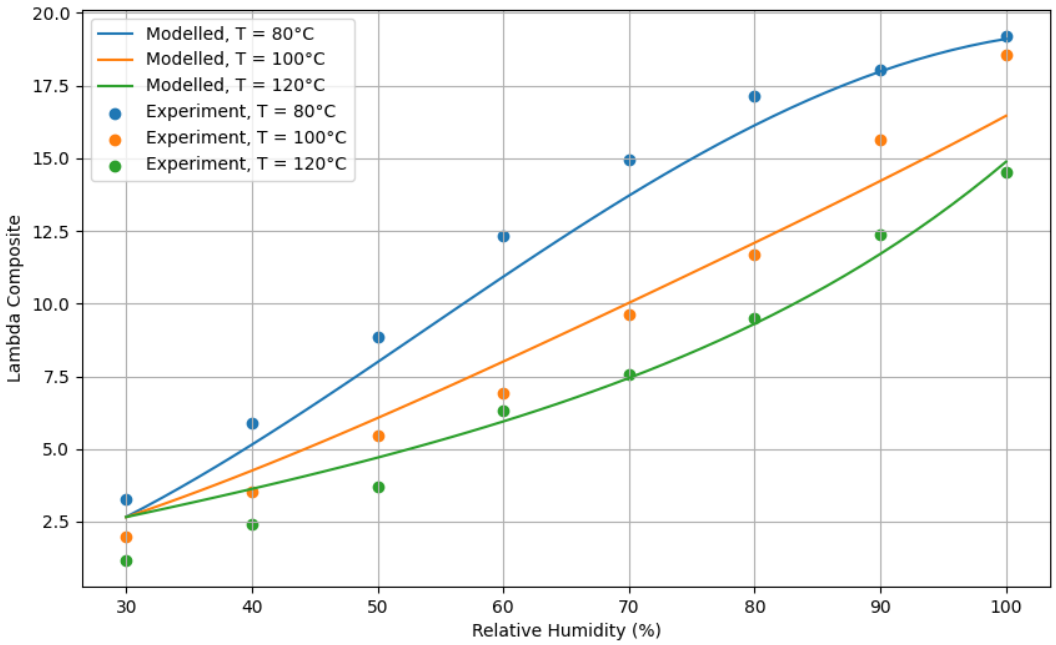

Figure 6.3: Calculated composite lambda from experimental data vs lambda calculated with predicted function from Eq. 6.15 overlaid

Figure 6.3 shows the measured HFR converted into lambda compared to the polynomial model made from the calculated contribution of graphene to lambda from the rule of mixtures. The contribution of the material is not all positive, indicating that when combined with high temperatures it aids in the dehydration of the membrane rather than its expected effect of improving the water retention. This also challenges the definition of equivalent lambda in this model. The polynomial model was only fit using data down to 30 % RH which shows in the turning point around that part of the experimental data.

Equation 6.15 is an approximate fit for $\lambda_{graphene}$ mimicking the original equation

shape of the Dobson et al. fit.

$$\lambda_{\text{composite}} = \left[\left(1 + 0.2352a^2 \cdot \frac{T-30}{30}\right) \cdot \left(14.22a^3 - 18.92a^2 + 13.41a\right)\right] \cdot (1-f) + \lambda_{\text{graphene}} \cdot f,$$

$$\text{where} \quad \lambda_{\text{graphene}} = b(T) \cdot \left(-348.97a_w^3 + 518.25a_w^2 - 122.379a_w\right). \tag{6.15}$$

The model assumed a similar equation form as Equation 6.4. The values in equation 6.15 were solved for simultaneously, including a unique value for the b at each temperature. The b parameter is present because it is assuming that the activity itself is temperature independent. The b value has an inverse temperature dependence; it is not obvious what shape the dependence has, and there are not enough data points to discern this with any confidence. Further experimentation could facilitate the extension of this model to predict for temperature in addition to activity The R^2 test is used as a method of determining the variance of the modelled data against the experimental data, as displayed in Table 6.5.

Table 6.5: Calculated value of R^2 for the modelling data fit

Temperature (°C)	80	100	120
R^2	0.988	0.963	0.965

The R^2 result shows that the fit was reasonable for 80 and 100°C cases. It was a poor fit for 120°C, this is likely because the solver is choosing a minimum based on the total sum squared difference which happened to favour the 80°C model. The squared difference of larger values is larger than smaller values with a similar magnitude of difference.

The model was checked for its sensitivity to the assumption that the intercept would be zero, i.e. that the conductivity would go to zero when there is no water present. This

was challenged by running the model with an additional term as seen in Equation 6.16

$$\lambda_{Graphene} = (b(T)) \cdot (Aa^3 + Ba^2 + Ca + c) \tag{6.16}$$

By including the additional c term in the equation we are allowing the model to choose an intercept that best fits the data. The solver parameters were updated and once a local minima was found we changed the settings as above to ensure that this was the best fit possible. The updated parameter settings were constructed in the same way as before, by using excel to calculate the equation of the best fit 3rd order polynomial. Then taking those equations including a non-zero intercept and using the average as an inital value and the upper and lower bounds as the maximum and minimum values $\pm$ 5%. The values in Table 6.6 were generated.

Table 6.6: Initial values, conditions, and final values used in the evolutionary non-linear non-smooth solver, with extra term in equation

Variable	Initial value	Upper bound	Lower bound	Final value
Coefficient A	-425.837	-191.558	-748.115	-478.42
Coefficient B	640.3	1023.76	357.89	704.40
Coefficient C	-148.89	-89.24	-192.81	-157.019
Coefficient c	-7.257	-0.8798	-14.8974	-2.735
$b_{80°C}$	1	100	0	1.503
$b_{100°C}$	1	100	0	0.768
$b_{120°C}$	1	100	0	0.229

Table 6.6 shows the settings of the evolutionary solver used to determine if adding an intercept term to the equation would improve the overall fitting, determined by R^2 as done for the above fitting.

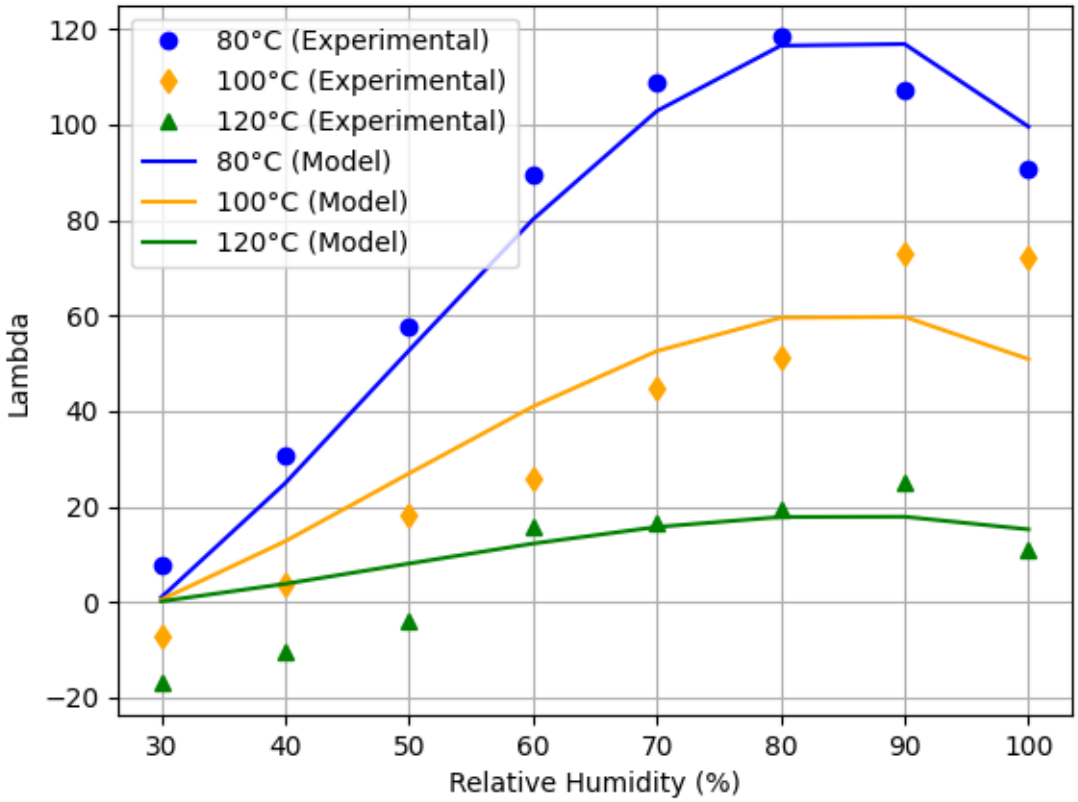

Figure 6.4: Calculated contribution of pure graphene to composite lambda with predicted function including non-zero intercept overlaid

Figure 6.4 shows the adjusted model fit with non-zero intercept value. Generally the fitting looks the same as before, indicating that the optimal result calculated before is not sensitive to the value of the intercept.

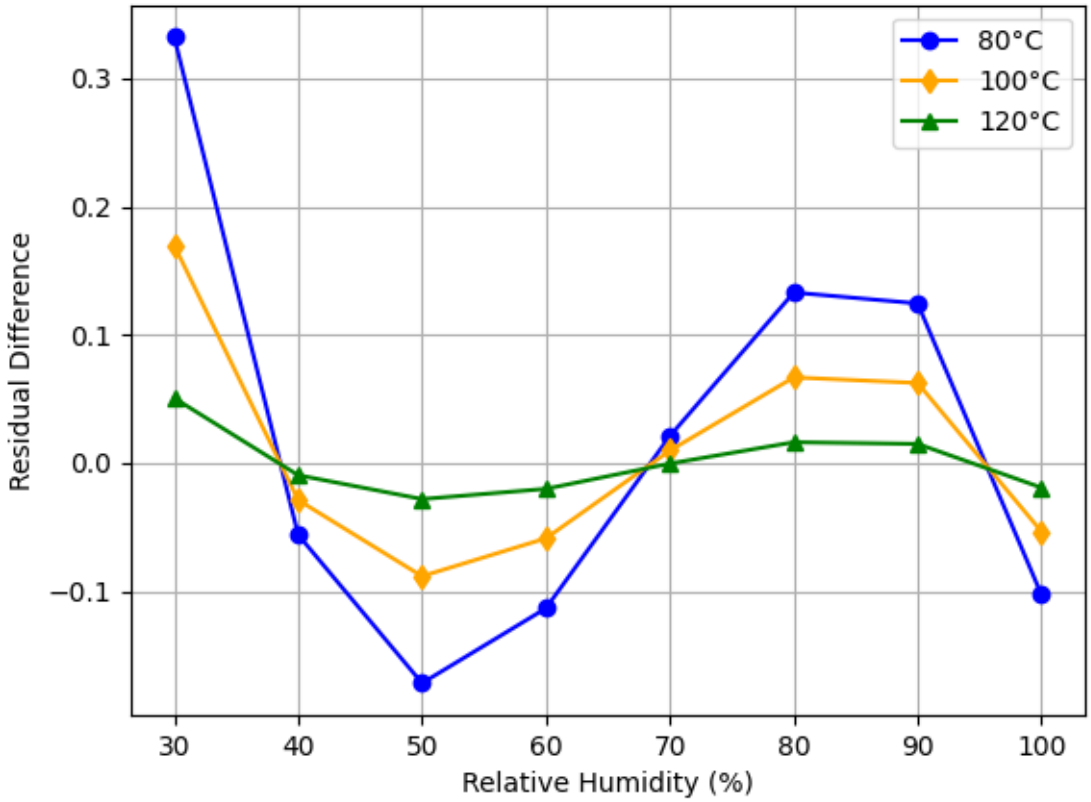

Figure 6.5: Residual difference between model with and without non-zero intercept for each temperature

Figure 6.5 shows the difference between the two models to see the sensitivity to the non-zero intercept. It appears to have made almost no effect in the R^2 parameter available in Table 6.7. In general R squared is a good indicator if the correct mathematical shape has been chosen to represent the behaviour modelled, with the caveat that there might be similar values of R squared for any mathematical shapes due to using the square root of the variance. Those shapes could have similar residual sum of the squares which would lead to difficult differentiation between the fits. In this case the polynomial model doesn't show a good R squared fit especially in the low actitivity region. The plotted variance agrees with this point with large inconsistent variance across the modelled domain.

Table 6.7: Calculated value of R^2 for the modelling data fit

Temperature (°C)	80	100	120
R^2	0.963	0.808	0.565

6.4.2 Power Law model

The second method for describing material properties assumes the variance is purely in the water sorption behaviour, the conductivity relationship will be similar to that of pure Nafion, and graphene's effects are purely limited to influencing the water sorption. A power law model is chosen because the shape of the data most resembles a power law model. Counter to literature it might stand that a power law fit is more reasonable than a polynomial fit. So the HFR data was taken and the water sorption parameter lambda was derived using Pouillet's law (equation 3.35 and equation 3.29).

$$y = ba_w^c \tag{6.17}$$

Equation 6.17 shows an example power law model, where b and c are coefficients to be determined.

Figure 6.6 shows the HFR data converted into the water sorption parameter lambda using Pouillet's law to convert resistance to conductivity, and then using equation 3.29 to convert conductivity into lambda. Overlaid on the graph are the best fit trend lines assuming that the water sorption behaves as a power law equation.

Table 6.8: Parameters for best-fit lines determined with Excel solver function

	Coefficient b	Coefficient c	R^2
80°C	20.71	1.19	0.955
100°C	18.56	1.85	0.997
120°C	14.76	1.89	0.997

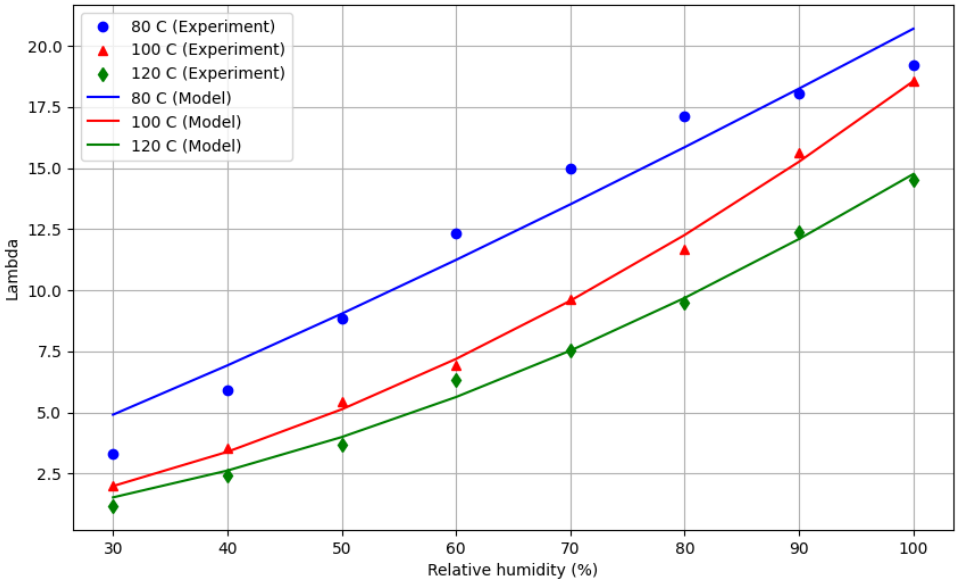

Figure 6.6: Experimental HFR data converted to Lambda (water sorption) vs water activity, Experimental values converted using Equation 3.29, power law modelling best fit from equation 6.17

To generate the values in table 6.8 the power law model coefficients were initially set to 1, and the SSD was calculated for the data vs the model. Minimising the total SSD was used as a fitting parameter for the Solver function the coefficients b and c were free and the solver was allowed to choose freely without constraint.

when evaluating the model parameters there was an interesting possibility, since the beginning of the 80°C data looked like a similar power law fit to the other temperatures: by excluding the final 3 points it was possible to create the fits seen in figure 6.7. while the last 3 points clearly do not follow the behaviour there is good agreement for data below 80% relative humidity. The reason there would not be good agreement with those points at 80 °C, is that below 100 °C some of the water can exist more easily as liquid within the cell, which means the membrane is much more likely to reach is sorption limit and therefore deviate away from this power law behaviour.

Figure 6.8 shows how the coefficients vary with temperature. It appears that the b

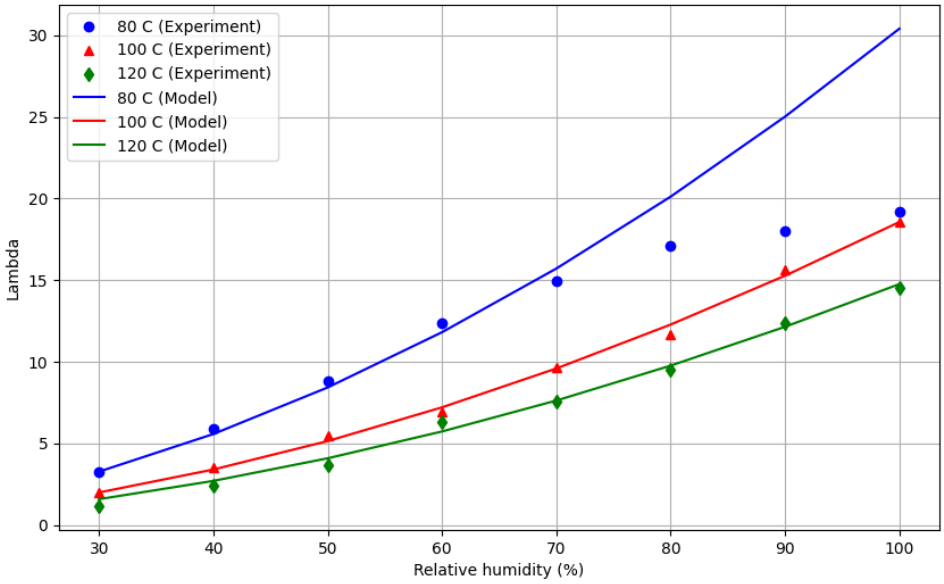

Figure 6.7: Power law individual fits for each temperature, excluding the last 3 points of the 80 °C data.

coefficient is inverse to temperature. The C coefficient was fixed at 1.85. To represent changes in the b coefficient, the value of the temperature change is considered.

Table 6.9: Changes in Temperature term from sorption isotherm suggested by dobson

	(T-To)/To
80°C	1.6667
100°C	2.3333
120°C	3.0

Table 6.9 shows the values of the temperature change, to evaluate if there are any patterns in the change of the temperature that will align with the changes in the coefficients.

By fitting the inverse of the Dobson temperature term it is possible to fit the data using a fixed coefficient k.

$$b = k/((T - To)/To) \tag{6.18}$$

Equation 6.18 uses the same form that Dobson reported in their temperature coeffi-

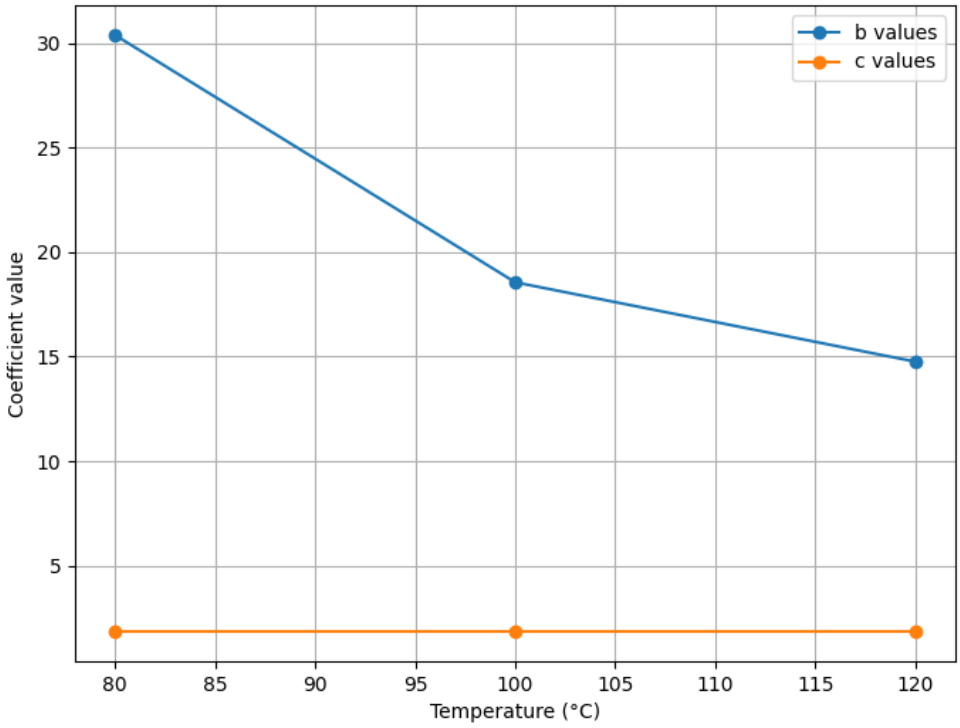

Figure 6.8: Model coefficients variance with temperature

cient. However in this function the inverse is used to emulate the inverse relationship with temperature. The dobson temperature form was adpoted along with a scalar coefficient k which was found to be 47.508. Using this equation and excluding the last three points from the 80°C, it was possible to generate the fit shown in figure 6.9.

Table 6.10: R^2 fitting parameter for the model against the experimental data at each temperature for the best fit and the suggested coefficients from equation 6.18 *for 80°C the last 3 points have been ignored when calculating R^2

Temperature (°C)	80	100	120
Best fit R2	0.988*	0.997	0.994
Assumed physics R^2	0.966*	0.960	0.971

The R^2 parameter displayed in Table 6.10 shows good confidence across all temperatures and the 80°C data below 80% relative humidity. This makes sense as the shape of the experimental data shows that it approaches an asymptote, which is not accounted for

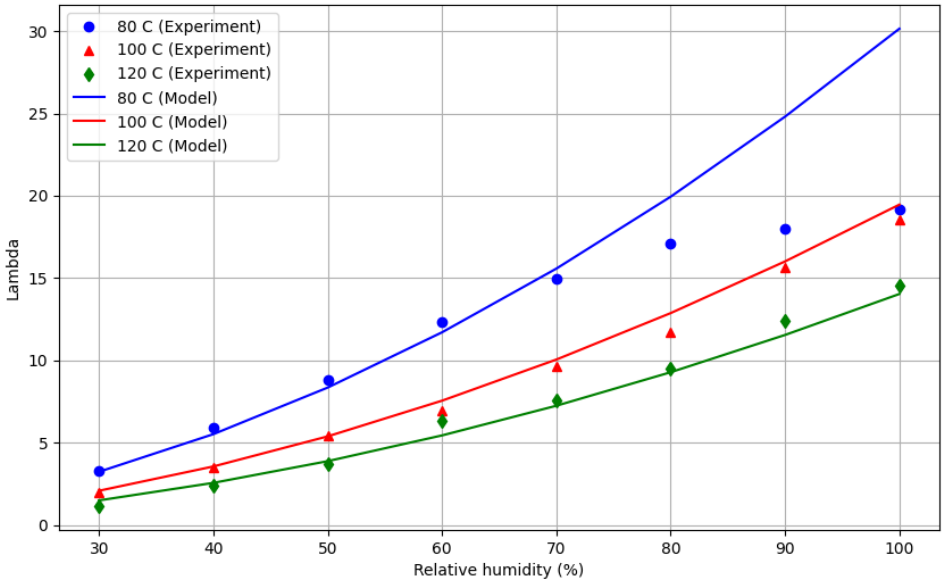

Figure 6.9: Power law model fit excluding high relative humidity at 80 °C

in the general power law used in equation 6.17. Missing some of the data out to generate a good fit is reasonable if the fit is within the model range. in order to fit all of the data from the experiment it makes little sense to bring this model forward to be used in COMSOL at a fuel cell level. However this could be a good basis for future work on modelling the water sorption physics, it can also provide function for anyone attempting to model values around these temperatures.

6.5 Modelling – Fuel cell

Using a single cell fuel cell model as described in section 3.2, the polynomial model in equation 6.16 and table 6.6. The model was run and the results plotted against the experimental data. The reference exchange current density was used to fit the model, using the total R squared as a target parameter. A best fit was difficult to achieve in all

temperature ranges due to the variation in the water model. It did not have a best fit for 120°C which is evident in the data. As with the previous use of the model, the mass transport regions often come in too strongly and they often under-predicts at low values of relative humidity because they are dependant on the concentration of water. Figure 6.10 shows the modelling fit to the experimental data at 80°C. Generally the modelling fit is good; the model replicated the experimental data at all of the relative humidities. There is a small difference in the activation and mass transport regions; however, this is to be expected as the model's focus is the membrane.

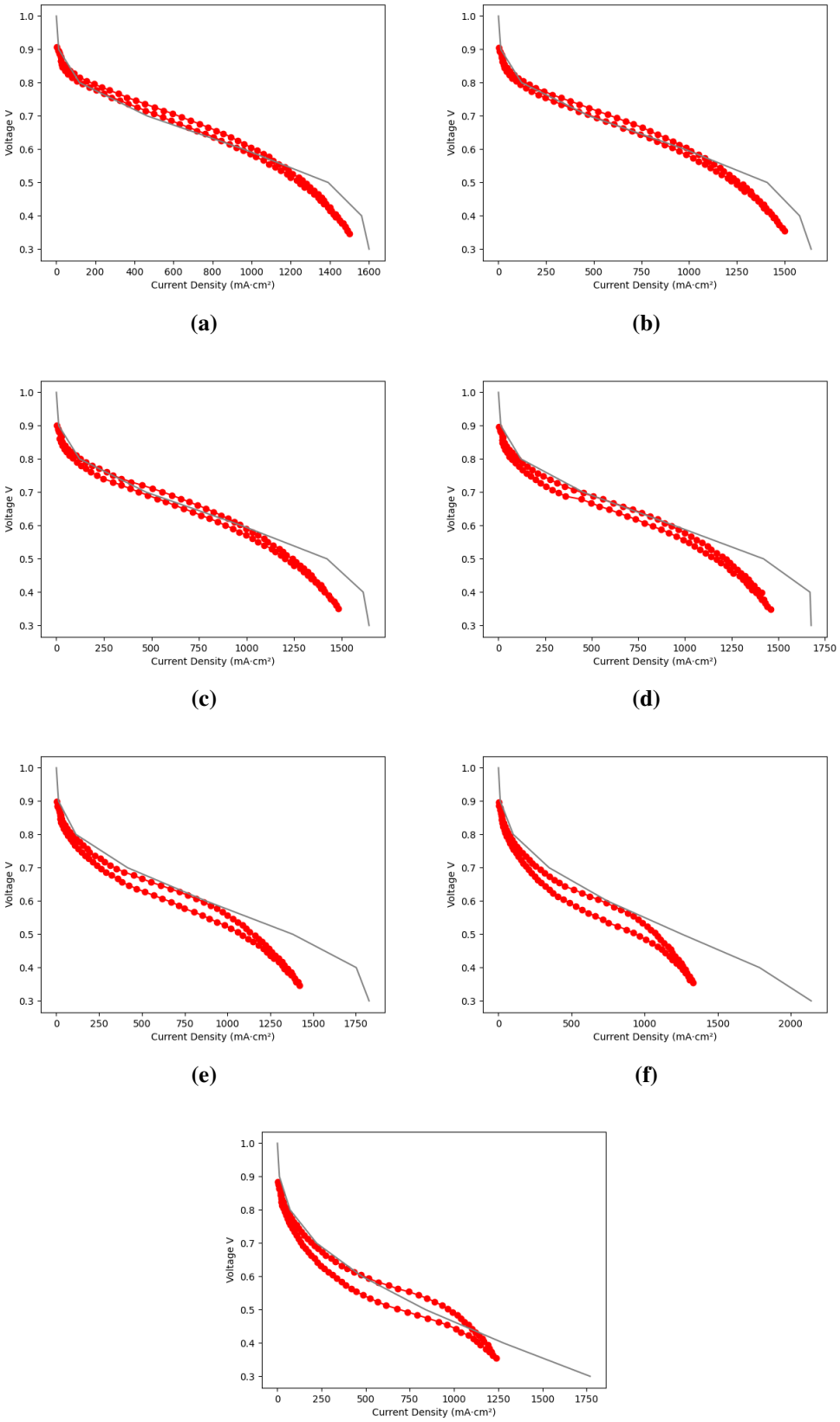

Figure 6.10: Modelling fit compared to the experimental data at 80°C and relative humidity 40%-100% (a-g).

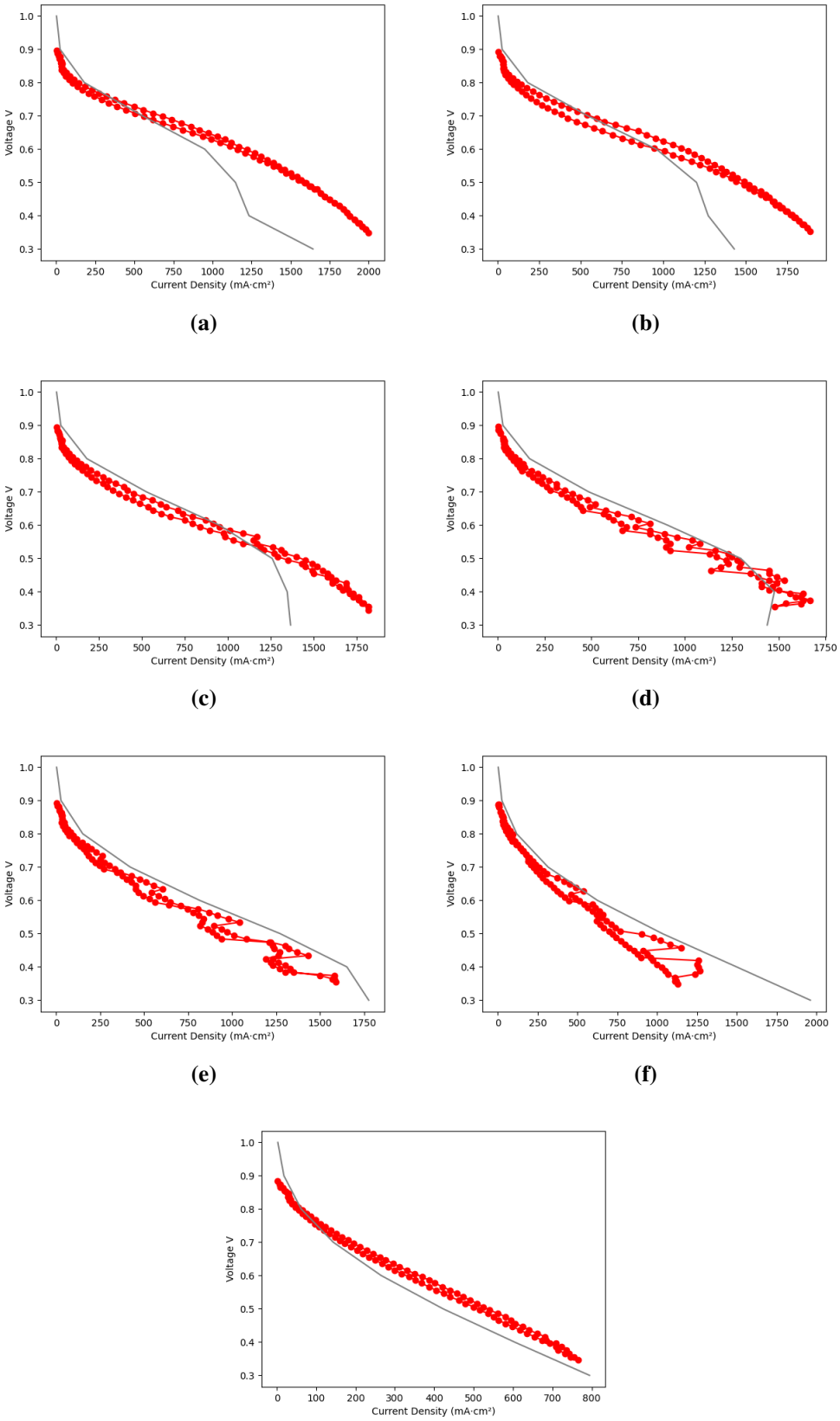

Figure 6.11: Modelling fit compared to the experimental data at 100°C and relative humidity 40%-100% (a-g).

Figure 6.11 shows the modelling fit of the experimental data at 100°C. Like the previous figure, the model shows a reasonable fit for the experimental data. For the high relative humidities, the model over-predicts the mass transport resistance and does not follow the experimental behaviour. Generally, the behaviour in the ohmic region is okay; the overall fitting of the model is poorer than the 80°C.

Figure 6.12 shows the results of the model for the 120°C, it appears the model is very poor at predicting the behaviour for this temperature. It is difficult to say if the fitting at any of the relative humidities are valid given the general poorness of fit.

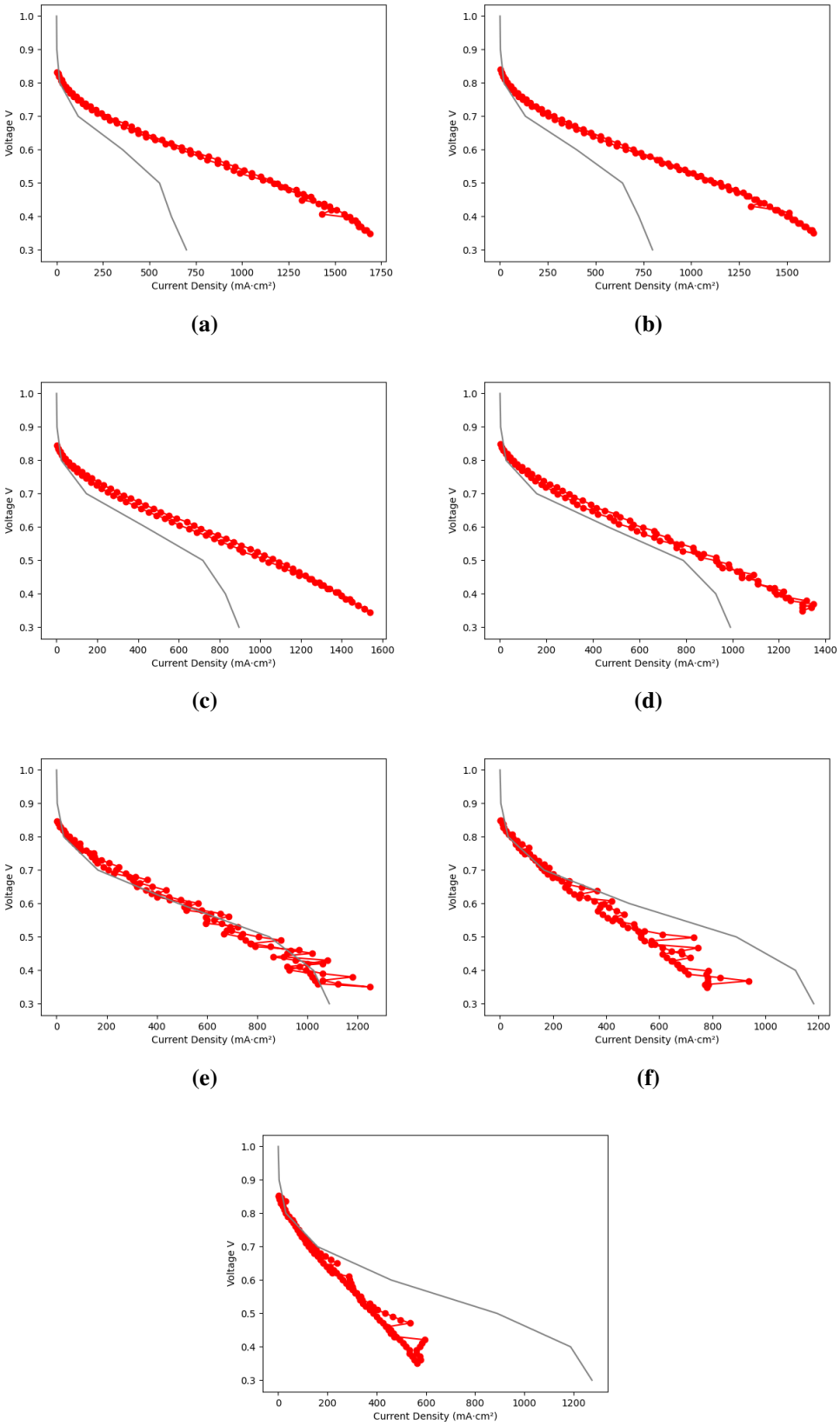

Figure 6.12: Modelling fit compared to the experimental data at 120°C and relative humidity 40%-100% (a-g).

Table 6.11: Calculated value of R^2 for the modelling data fit to the experimental data by relative humidity.

Temperature (°C)	80	100	120
Relative Humidity (%)			
100	0.971	0.745	0.082
90	0.970	0.839	0.318
80	0.949	0.901	0.561
70	0.908	0.941	0.847
60	0.804	0.841	0.972
50	0.667	0.637	0.258
40	0.937	0.923	-2.69*

Table 6.11 shows the R squared fits for the model runs against relative humidity. The first thing to notice is the negative value for the 40% relative humidity and 120°C. This value is likely negative because of how poor the fit is; some of the values predicted by the model are 2.5 times larger than the experimental data. When considering the form of the equation to calculate R squared, if the difference between the values is much larger than the variance of the experimental data, then the fraction becomes top-heavy and above 1. The trend described above appears to be confirmed by the R-squared numbers. Generally, the fitting at 80°C was the best, with 100°C fitting okay considering the mass transport inconsistencies, with 120°C being the worst.

Figure 6.13 shows the modelling data plotted against the experimental data generated by using the model coefficients from the polynomial model. The data at 80°C shows the best fit, with the 100°C model data showing good fit for the ohmic region with poor prediction of values in the mass transport region. Here it can be seen that the 120°C data is converging from the experimental data. This confirms the above observations about poor fitting.

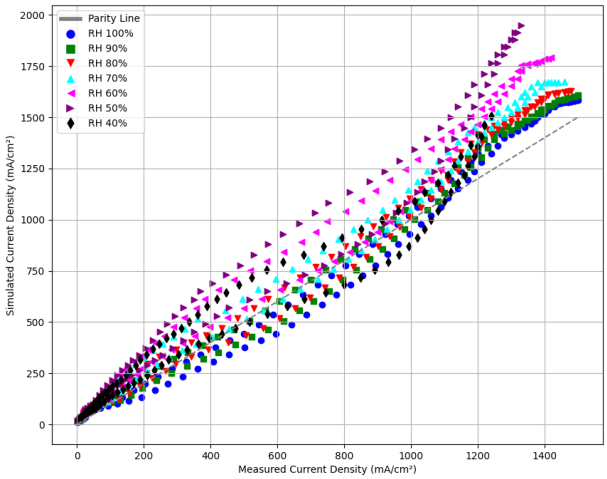

(a)

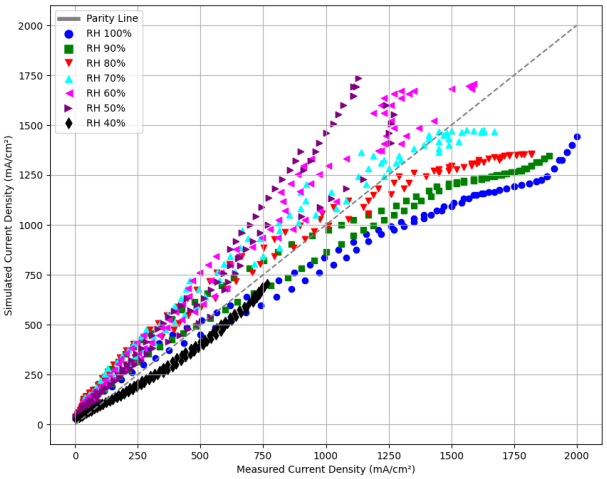

(b)

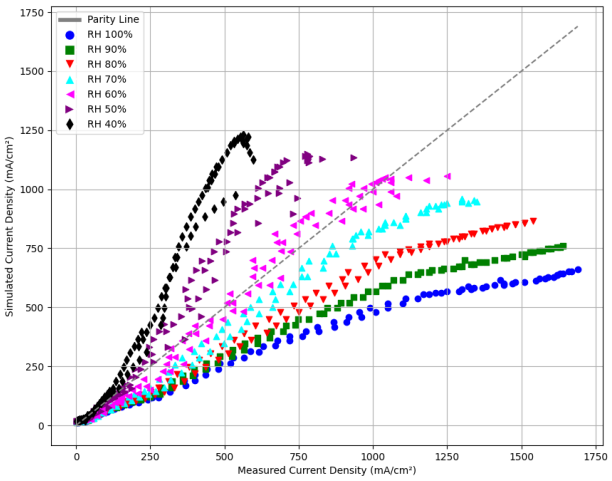

(c)

Figure 6.13: Parity plots for (a) 80°C, (b) 100°C, (c) 120°C at 40-100% RH

6.6 Conclusion

In this chapter, the performance of composite graphene oxide-Nafion (GO-Nafion) membranes was investigated experimentally and through modelling for polymer electrolyte fuel cells (PEFCs) operating at intermediate temperatures. The experimental work in-

volved fabricating GO-Nafion membranes by solution casting, incorporating 4 wt% graphene oxide as a filler material. The polarization curves and impedance spectra at 80°C, 100°C, and 120°C were used to evaluate the performance of these membranes at different relative humidity levels. The results showed that GO-Nafion membranes exhibited improved water retention and overall performance at elevated temperatures compared to pure Nafion, although significant performance degradation occurred at lower relative humidity due to membrane dehydration.

6.6.1 Experimental Observations

- 80°C Results: At 80°C, the polarization curves indicated that GO-Nafion membranes maintained their performance across a wide range of relative humidity levels (40-100%). The impedance spectra revealed that the ohmic resistance (HFR) increased with decreasing relative humidity, consistent with water loss and increased membrane resistance.

- 100°C Results: At 100°C, the polarization curves showed higher sensitivity to relative humidity changes, with significant performance loss below 80% RH due to membrane dehydration. The impedance spectra supported these observations, showing a substantial increase in HFR at low humidity levels.

- 120°C Results: At 120°C, the GO-Nafion membranes exhibited the lowest overall performance across all humidity levels. The polarization curves revealed a pronounced decrease in performance due to dehydration, reactant crossover, and proximity to Nafion's glass transition temperature. The impedance spectra further indicated high HFR and mass transport resistance.

6.6.2 Modelling Approaches

Two modelling approaches were considered to predict the performance of the GO-Nafion membranes.

- Polynomial Model:
  - The polynomial model was based on a rule-of-mixtures approach using equations derived from Dobson et al. The graphene oxide content was included as a filler in the Nafion matrix.
  - The model equations predicted the water sorption behaviour of the composite membranes, approximating the water content parameter, λ, as a function of relative humidity.
  - This model accurately predicted performance at 80°C ($R^2 > 0.96$) and 100°C ($R^2 > 0.84$), but struggled at 120°C ($R^2 < 0.57$) due to the complex interplay of dehydration and reactant crossover.
- Power-Law Model:
  - The power-law model assumed that the water sorption behaviour of the composite membranes followed a power-law relationship.
  - This model exhibited a reasonable fit across all temperatures, with coefficients determined via fitting to experimental data.
  - The coefficients showed a consistent trend with temperature, although the model lacked a clear physical basis and hence was not used further for full fuel cell modelling.

6.6.3 Fuel Cell Modelling

The polynomial model was incorporated into a full single-cell fuel cell model. The reference exchange current density was used to fit the model, and the results were compared to experimental data. The following key observations were made:

- 80°C Modelling: The model predictions aligned well with experimental data across all relative humidity levels, achieving an $R^2 > 0.96$ for most conditions.
- 100°C Modelling: The model predictions showed reasonable agreement with experimental data, though the mass transport region was overestimated at high humidity levels.
- 120°C Modelling: The model struggled to accurately predict performance at 120°C, particularly at low relative humidity. The model overestimated mass transport resistance, indicating limitations in accurately capturing dehydration effects at this temperature.

6.6.4 Summary

Overall, this chapter provides valuable insights into the potential of composite GO-Nafion membranes for intermediate temperature polymer electrolyte fuel cells and presents a comprehensive modelling framework. The polynomial model, based on a rule-of-mixtures approach, offers a promising method to predict the water sorption behavior and performance of composite membranes. However, further refinement is needed to improve predictive accuracy at higher temperatures. Future work could explore advanced water sorption models and include more comprehensive mass transport effects to achieve bet-

ter predictive accuracy across all temperature ranges. This chapter lays the groundwork for future developments in composite membrane design and modelling, ultimately aiming to enhance the performance of polymer electrolyte fuel cells operating at intermediate temperatures.

CHAPTER SEVEN

SUMMARY, CONCLUSIONS AND OUTLOOK

7.1 Summary

This thesis presents a comprehensive examination of Polymer Electrolyte Fuel Cells (PEFCs), particularly focusing on innovative membrane designs and materials aimed at improving performance across intermediate temperature ranges. Through detailed experimental studies and advanced modelling approaches, significant insights were gained into the behavior of patterned and composite membranes.

7.2 Conclusions

7.2.1 Patterned Membranes

The research presented in the patterned membranes chapter highlights the successful implementation of steel molds modified by the Laser Induced Periodic Surface Structures (LIPSS) technique to fabricate patterned membranes. These membranes demonstrated en-

hanced performance characteristics, particularly in the mass transport and ohmic regions of the polarization curve. The contact angle measurements and subsequent SEM analysis confirm the effective replication of microscale patterns onto the membrane surfaces, which significantly influenced their hydrophobic properties and surface morphology.

Key findings include:

- Sharklet Pattern Performance: The sharklet patterned membranes exhibited up to a 4-fold increase in power density, with marked improvements observed across varying relative humidity conditions. The sharklet pattern maintained higher catalytic efficiency, as evidenced by an electrochemical surface area (ECSA) increase of approximately 10% compared to the flat membrane.

- Impedance Spectroscopy: Reduced high-frequency resistance in the sharklet pattern implied lower ohmic losses and enhanced ionic conductivity.

- Hydrogen Crossover: Despite higher hydrogen crossover in the sharklet pattern, overall cell performance was not adversely affected due to the membrane's ability to maintain hydration and conductivity.

- Pattern Optimization: Other patterns like the lotus and lines demonstrated limitations under low humidity conditions, highlighting the need for careful optimization of feature size and depth.

In conclusion, the sharklet pattern emerges as a particularly promising design, enhancing both mechanical and transport properties of the membrane, thus supporting sustained performance under a variety of operational conditions.

7.2.2 Nafion 211 Membranes and Numerical Studies

This comprehensive examination of Nafion 211 membranes under various operational conditions elucidated several critical aspects pertinent to enhancing fuel cell performance and durability across elevated temperature ranges. Empirical relationships relating activity to lambda (λ) and ionic conductivity were extended to higher operational temperatures (up to 120°C). This adaptation underscores the importance of accurately fitting parameters like activity and lambda in modeling and operational strategies, particularly when regular operational theories falter at intermediate temperatures.

Key findings include:

- Temperature and Membrane Hydration: Performance peaks at 100°C due to improved mass transport and mitigation of flooding, but declines beyond this threshold due to dehydration and reduced ionic conductivity.

- Humidity and Pressure Effects: Higher pressures enhance performance by maintaining a better water balance without sacrificing oxygen availability. High-pressure operations offer potential benefits beyond the traditional 80°C limit.

- Degradation Mechanisms and Material Innovation: Developing new materials or modifying existing PFSA membranes to improve thermal stability and water retention is crucial.

- Advanced Modelling Techniques: Adapting predictive models to incorporate realistic operational variables has proven essential for pre-emptive adjustments in the design and operation of PEFCs.

In conclusion, this research outlines a clear trajectory for advancing PEFC technol-

ogy through targeted improvements in membrane materials, operational strategies, and predictive modeling.

7.2.3 Composite GO-Nafion Membranes

In this chapter, the performance of composite graphene oxide-Nafion (GO-Nafion) membranes was investigated experimentally and through modelling for polymer electrolyte fuel cells (PEFCs) operating at intermediate temperatures. The results showed that GO-Nafion membranes exhibited improved water retention and overall performance at elevated temperatures compared to pure Nafion, although significant performance degradation occurred at lower relative humidity due to membrane dehydration.

Key findings include:

- 80°C Results: GO-Nafion membranes maintained performance across a wide range of relative humidity levels (40-100%) at 80°C.
- 100°C Results: At 100°C, significant performance loss occurred below 80% RH due to membrane dehydration.
- 120°C Results: GO-Nafion membranes exhibited the lowest overall performance across all humidity levels at 120°C due to dehydration, reactant crossover, and proximity to Nafion's glass transition temperature.

Two modelling approaches were considered to predict the performance of the GO-Nafion membranes:

- Polynomial Model: Based on a rule-of-mixtures approach, this model accurately predicted performance at 80°C ($R^2 > 0.96$) and 100°C ($R^2 > 0.84$), but struggled

at 120°C ($R^2 < 0.57$).

- Power-Law Model: Exhibited a reasonable fit across all temperatures but lacked a clear physical basis, limiting its applicability for full fuel cell modelling.

In conclusion, the polynomial model, based on a rule-of-mixtures approach, offers a promising method to predict the water sorption behavior and performance of composite membranes. Further refinement is needed to improve predictive accuracy at higher temperatures.

7.3 Outlook

This thesis contributes to the development of electrolyte membranes for fuel cells by presenting new insights into intermediate temperature and low humidity operation. By investigating patterning, it was shown that electrolyte membranes can have enhanced power density by retaining greater quantities of water while improving the exchange of products and reactants at the cathode. This work was published in the journal Polymers [253].

New insights into intermediate temperature operation ($\leq$ 120°C) were gleaned from extending previous relationships to include a greater temperature range. This elucidated important information about carefully matching operational temperature and pressure, as well as giving guidance on the modifications required to enable intermediate temperature modelling. This work was published in the journal Membranes [254].

Finally, the first model for composite membranes and a methodology which can be built upon to develop these materials further were proposed.

7.4 Future Directions:

This work could be built upon in the following ways:

- Further refining the sharklet pattern and exploring the scalability of this approach, ensuring the repeatability and reliability of these patterns in larger-scale fuel cell systems.
- Developing new materials or modifying existing PFSA membranes to improve thermal stability and water retention capabilities.
- Creating a method to measure the empirical water sorption relationship of membranes at temperatures between 90°C and 120°C and pressures from atmospheric to 3 bar.
- Exploring high-pressure scenarios to surpass current temperature and performance limitations in fuel cell technologies.
- Incorporating advanced mass transport phenomena into models for better prediction of performance at high temperature and low RH.

By addressing these challenges and leveraging the detailed insights obtained, the development of more robust, efficient, and durable PEFC systems is distinctly achievable, marking a significant step forward in sustainable energy technologies.

APPENDIX ONE

APPENDIX

A.1 Steam Tables

Table A.1: Saturated Steam Properties vs. Pressure from [**Haar1984ThermodynamicUnits**]

P (bar)	T (°C)	V (m^3/kg)	ρ (kg/m^3)	h' (kJ/kg)	h' (kcal/kg)	h" (kJ/kg)	h" (kcal/kg)	L (kJ/kg)	L (kcal/kg)	s" (kJ/kg K)
0.02	17.51	67.006	0.015	73.45	17.54	2533.64	605.15	2460.19	587.61	1.8644
0.03	24.10	45.667	0.022	101.00	24.12	2545.64	608.02	2444.65	583.89	1.8694
0.04	28.98	34.802	0.029	121.41	29.00	2554.51	610.13	2433.10	581.14	1.8736
0.05	32.90	28.194	0.035	137.77	32.91	2561.59	611.83	2423.82	578.92	1.8774
0.06	36.18	23.741	0.042	151.50	36.19	2567.51	613.24	2416.01	577.05	1.8808
0.07	39.02	20.531	0.049	163.38	39.02	2572.62	614.46	2409.24	575.44	1.8840
0.08	41.53	18.105	0.055	173.87	41.53	2577.11	615.53	2403.25	574.01	1.8871
0.09	43.79	16.204	0.062	183.28	43.78	2581.14	616.49	2397.85	572.72	1.8899
0.10	45.83	14.675	0.068	191.84	45.82	2584.78	617.36	2392.94	571.54	1.8927
0.20	60.09	7.650	0.131	251.46	60.06	2609.86	623.35	2358.40	563.30	1.9156
0.30	69.13	5.229	0.191	289.31	69.10	2625.43	627.07	2336.13	557.97	1.9343
0.40	75.89	3.993	0.250	317.65	75.87	2636.88	629.81	2319.23	553.94	1.9506
0.50	81.35	3.240	0.309	340.57	81.34	2645.99	631.98	2305.42	550.64	1.9654
0.60	85.95	2.732	0.366	359.93	85.97	2653.57	633.79	2293.64	547.83	1.9790
0.70	89.96	2.365	0.423	376.77	89.99	2660.07	635.35	2283.30	545.36	1.9919
0.80	93.51	2.087	0.479	391.73	93.56	2665.77	636.71	2274.05	543.15	2.0040
0.90	96.71	1.869	0.535	405.21	96.78	2670.85	637.92	2265.65	541.14	2.0156
1.00	99.63	1.694	0.590	417.51	99.72	2675.43	639.02	2257.92	539.30	2.0267
1.10	102.32	1.549	0.645	428.84	102.43	2679.61	640.01	2250.76	537.59	2.0373
1.20	104.81	1.428	0.700	439.36	104.94	2683.44	640.93	2244.08	535.99	2.0476
1.30	107.13	1.325	0.755	449.19	107.29	2686.98	641.77	2237.79	534.49	2.0576
1.40	109.32	1.236	0.809	458.42	109.49	2690.28	642.56	2231.86	533.07	2.0673
1.50	111.37	1.159	0.863	467.13	111.57	2693.36	643.30	2226.23	531.73	2.0768
1.60	113.32	1.091	0.916	475.38	113.54	2696.25	643.99	2220.87	530.45	2.0860
1.70	115.17	1.031	0.970	483.22	115.42	2698.97	644.64	2215.75	529.22	2.0950
1.80	116.93	0.977	1.023	490.70	117.20	2701.54	645.25	2210.84	528.05	2.1037
1.90	118.62	0.929	1.076	497.85	118.91	2703.98	645.83	2206.13	526.92	2.1124
2.00	120.23	0.885	1.129	504.71	120.55	2706.29	646.39	2201.59	525.84	2.1208
2.20	123.27	0.810	1.235	517.63	123.63	2710.60	647.42	2192.98	523.78	2.1372
2.40	126.09	0.746	1.340	529.64	126.50	2714.55	648.36	2184.91	521.86	2.1531
2.60	128.73	0.693	1.444	540.88	129.19	2718.17	649.22	2177.30	520.04	2.1685
2.80	131.20	0.646	1.548	551.45	131.71	2721.54	650.03	2170.08	518.32	2.1835
3.00	133.54	0.606	1.651	561.44	134.10	2724.66	650.77	2163.22	516.68	2.1981
3.50	138.87	0.524	1.908	584.28	139.55	2731.63	652.44	2147.35	512.89	2.2331
4.00	143.63	0.462	2.163	604.68	144.43	2737.63	653.87	2132.95	509.45	2.2664

List of References

1. Friend, A. M. Population, technology and lifestyle: The transition to sustainability. *Ecological Economics* **10,** 84–86. ISSN: 09218009 (1994).

2. Glasson, J., Therivel, R. & Chadwi, A. *Introduction To Environmental Impact Assessment* 392. ISBN: 9780203023068 (2005).

3. Cook, J. *et al.* Consensus on consensus: a synthesis of consensus estimates on human-caused global warming. *Environmental Research Letters* **11,** 048002. ISSN: 1748-9326 (Apr. 2016).

4. Lykkeskov, A. *et al.* Environmental Research Letters Quantifying the consensus on anthropogenic global warming in the scientific literature The Moral Justification Behind a Climate Tax on Beef in Denmark Quantifying the consensus on anthropogenic global warming in the scientif. *Environ. Res. Lett* **8,** 24024–7. ISSN: 1748-9326 (June 2013).

5. Doran, P. T. & Zimmerman, M. K. *Examining the scientific consensus on climate change* 2009.

6. Oreskes, N. BEYOND THE IVORY TOWER: The Scientific Consensus on Climate Change. *Science* **306,** 1686–1686. ISSN: 0036-8075 (Dec. 2004).

7. Kingsford, R. T. & Watson, J. E. M. What hope for biodiversity in the face of anthropogenic climate change in Oceania? *Pacific Conservation Biology* **17,** 166–167. ISSN: 10382097 (July 2011).

8. Esteban, M. & Portugal-Pereira, J. Post-disaster resilience of a 100% renewable energy system in Japan. *Energy* **68,** 756–764. ISSN: 03605442 (Apr. 2014).

9. Shimizu, S. *CHP Market & Policy Movement in Japan* 2013.

10. Zhang, M. M., Zhou, D. Q., Zhou, P. & Chen, H. T. Optimal design of subsidy to stimulate renewable energy investments: The case of China. *Renewable and Sustainable Energy Reviews* **71,** 873–883. ISSN: 18790690 (May 2017).

11. Huang, B., Mauerhofer, V. & Geng, Y. Analysis of existing building energy saving policies in Japan and China. *Journal of Cleaner Production* **112,** 1510–1518. ISSN: 09596526 (2015).

12. European Commission. *The Road from Paris: assessing the implications of the Paris Agreement and accompanying the proposal for a Council decision on the signing, on behalf of the European Union, of the Paris agreement adopted under the United Nations Framework Convention on Cl* tech. rep. (2016), 1–10.

13. Wiedmann, T., Minx, J. & Pertsova, C. C. *Ecological Economics Research Trends* 1. ISBN: 6312317269 (Nova Science Publishers, 2008).

14. Mitchell, C. & Connor, P. Renewable energy policy in the UK 1990-2003. *Energy Policy* **32,** 1935–1947. ISSN: 03014215 (Nov. 2004).

15. Warshay, M. & Prokopius, P. R. The fuel cell in space: yesterday, today and tomorrow. *Journal of Power Sources* **29,** 193–200. ISSN: 03787753 (1990).

16. Ladewig, B. P., Jiang, S. P. & Yan, Y. *Materials for Low-Temperature Fuel Cells* 1–250. ISBN: 9783527644308 (2015).

17. Abuadmah, H. Fuel Cells Versus Heat Engines: A Perspective of Thermodynamic and Production Efficiencies (2012).

18. Rheinländer, P. J., Herranz, J., Durst, J. & Gasteiger, H. A. Kinetics of the Hydrogen Oxidation/Evolution Reaction on Polycrystalline Platinum in Alkaline Electrolyte Reaction Order with Respect to Hydrogen Pressure. *Journal of The Electrochemical Society* **161,** F1448–F1457. ISSN: 0013-4651 (Oct. 2014).

19. Momirlan, M. & Veziroglu, T. N. The properties of hydrogen as fuel tomorrow in sustainable energy system for a cleaner planet. *International Journal of Hydrogen Energy* **30,** 795–802. ISSN: 03603199 (2005).

20. Zuttel, A. Materials for hydrogen storage. *Mater. Today* **6,** 24–33. ISSN: 13697021 (2003).

21. Gordon, J. A., Balta-Ozkan, N. & Nabavi, S. A. Socio-technical barriers to domestic hydrogen futures: Repurposing pipelines, policies, and public perceptions. *Applied Energy* **336,** 120850. ISSN: 0306-2619 (Apr. 2023).

22. Faulkner, L. R. Understanding electrochemistry: Some distinctive concepts. *Journal of Chemical Education* **60,** 262–264. ISSN: 00219584 (1983).

23. Larminie, J. & Dicks, A. *Fuel cell systems explained: Second edition* 1–406. ISBN: 9781118878330 (2013).

24. OpenStax CNX. *Potential, Kinetic, Free, and Activation Energy - Biology - OpenStax CNX* 2019.

25. Agaesse, M. T. *et al. Simulations of one and two-phase flows in porous microstructures, from tomographic images of gas diffusion layers of proton exchange membrane fuel cells* PhD thesis (Universite de toulouse, 2016).

26. Robert, M. *Impact of degradation and aging on properties of PFSA membranes for fuel cells / Impact des dégradations et du vieillissement sur les propriétés des membranes PFSA pour piles à combustible* PhD thesis (2021).

27. Kusoglu, A. & Weber, A. Z. New Insights into Perfluorinated Sulfonic-Acid Ionomers. *Chemical Reviews* **117,** 987–1104. ISSN: 15206890 (Feb. 2017).

28. Mauritz, K. A. & Moore, R. B. State of understanding of Nafion. *Chemical Reviews* **104,** 4535–4585. ISSN: 00092665 (Oct. 2004).

29. Miyake, T. & Rolandi, M. in *Green Materials for Electronics* 235–253 (2018).

30. Taherkhani, Z., Abdollahi, M. & Sharif, A. A Thermodynamic Approach to Model Proton Conductivity of Nafion-117 Membranes: Temperature and Water Content Effects. *Journal of the Electrochemical Society* **162,** F1096–F1100. ISSN: 0013-4651 (July 2015).

31. Williams, R. J. P. The Problem of Proton Transfer in Membranes. *J. theor. Biol* **219,** 389–396 (2002).

32. Branco, C. M., Sharma, S., De Camargo Forte, M. M. & Steinberger-Wilckens, R. *New approaches towards novel composite and multilayer membranes for intermediate temperature-polymer electrolyte fuel cells and direct methanol fuel cells* 2016.

33. Costamagna, P. & Srinivasan, S. Quantum jumps in the PEMFC science and technology from the 1960s to the year 2000: Part I. Fundamental scientific aspects. *Journal of Power Sources* **102,** 242–252. ISSN: 03787753 (Dec. 2001).

34. Zawodzinski, T. A., Springer, T. E., Uribe, F. & Gottesfeld, S. Characterization of polymer electrolytes for fuel cell applications. *Solid State Ionics* **60,** 199–211. ISSN: 01672738 (Mar. 1993).

35. Morris, D. R. & Sun, X. Water-sorption and transport properties of Nafion 117 H. *Journal of Applied Polymer Science* **50,** 1445–1452. ISSN: 10974628 (Nov. 1993).

36. Kocha, S. S., Yang, J. D. & Yi, J. S. Characterization of gas crossover and its implications in PEM fuel cells. *AIChE Journal* **52,** 1916–1925. ISSN: 15475905 (May 2006).

37. Marr, C. & Li, X. Composition and performance modelling of catalyst layer in a proton exchange membrane fuel cell. *Journal of Power Sources* **77,** 17–27. ISSN: 03787753 (Jan. 1999).

38. Mo, S. *et al. Recent Advances on PEM Fuel Cells: From Key Materials to Membrane Electrode Assembly* Aug. 2023.

39. Kim, Y. S. *et al.* Origin of toughness in dispersion-cast Nafion membranes. *Macromolecules* **48,** 2161–2172. ISSN: 15205835 (2015).

40. Klingele, M., Breitwieser, M., Zengerle, R. & Thiele, S. Direct deposition of proton exchange membranes enabling high performance hydrogen fuel cells. *Journal of Materials Chemistry A* **3,** 11239–11245. ISSN: 20507496 (2015).

41. Transactions, E. C. S. & Society, T. E. Direct Membrane Deposition – A Fast and Simple Technique for Membrane Electrode Assembly Manufacturing M. Klingele. **80,** 571–576. ISSN: 19385862 (2017).

42. Abouzari-Lotf, E. *et al.* Highly durable polybenzimidazole composite membranes with phosphonated graphene oxide for high temperature polymer electrolyte membrane fuel cells. *Journal of Power Sources* **412,** 238–245. ISSN: 03787753 (Feb. 2019).

43. Kim, A. R., Gabunada, J. C. & Yoo, D. J. Amelioration in physicochemical properties and single cell performance of sulfonated poly(ether ether ketone) block copolymer composite membrane using sulfonated carbon nanotubes for intermediate humidity fuel cells. *International Journal of Energy Research* **43,** 2974–2989. ISSN: 1099114X (June 2019).

44. Di Noto, V., Boaretto, N., Negro, E. & Pace, G. *New inorganic-organic proton conducting membranes based on Nafion and hydrophobic fluoroalkylated silica nanoparticles* in *Journal of Power Sources* **195** (Elsevier, Dec. 2010), 7734–7742.

45. Commer, P., Hartnig, C., Seeliger, D. & Spohr, E. *Modeling of proton transfer in polymer electrolyte membranes on different time and length scales* in *Molecular Simulation* **30** (2004), 755–763. ISBN: 0892-7022.

46. Dickinson, E. J. & Smith, G. Modelling the proton-conductive membrane in practical polymer electrolyte membrane fuel cell (Pemfc) simulation: A review. *Membranes* **10,** 1–53. ISSN: 20770375 (Nov. 2020).

47. Peron, J. *et al.* Properties of Nafion® NR-211 membranes for PEMFCs. *Journal of Membrane Science* **356,** 44–51. ISSN: 03767388 (July 2010).

48. Tse, Y. L. S., Herring, A. M., Kim, K. & Voth, G. A. Molecular dynamics simulations of proton transport in 3M and nafion perfluorosulfonic acid membranes. *Journal of Physical Chemistry C* **117,** 8079–8091. ISSN: 19327447 (Apr. 2013).

49. Zhang, H., Li, J., Tang, H., Lin, Y. & Pan, M. Hydrogen crossover through perfluorosulfonic acid membranes with variable side chains and its influence in fuel cell lifetime. *International Journal of Hydrogen Energy* **39,** 15989–15995. ISSN: 03603199 (Sept. 2014).

50. Giner-Sanz, J. J., Ortega, E. M. & Pérez-Herranz, V. *Hydrogen crossover and internal short-circuit currents experimental characterization and modelling in a proton exchange membrane fuel cell* in *International Journal of Hydrogen Energy* **39** (Pergamon, Aug. 2014), 13206–13216.

51. Omosebi, A. & Besser, R. S. Electron beam patterned Nafion membranes for DMFC applications. *Journal of Power Sources* **228,** 151–158. ISSN: 03787753 (2013).

52. Liu, C. Y. & Sung, C. C. A review of the performance and analysis of proton exchange membrane fuel cell membrane electrode assemblies. *Journal of Power Sources* **220,** 348–353. ISSN: 03787753 (Dec. 2012).

53. Matos, B. R. *et al.* Nafion-based composite electrolytes for proton exchange membrane fuel cells operating above 120 °c with titania nanoparticles and nanotubes as fillers. *Journal of Power Sources* **196,** 1061–1068. ISSN: 03787753 (Feb. 2011).

54. D'Epifanio, A. *et al.* Composite nafion/sulfated zirconia membranes: Effect of the filler surface properties on proton transport characteristics. *Chemistry of Materials* **22,** 813–821. ISSN: 08974756 (Feb. 2010).

55. Singh, Y. *et al.* Ex situ characterization and modelling of fatigue crack propagation in catalyst coated membrane composites for fuel cell applications. *International Journal of Hydrogen Energy* **44,** 12057–12072. ISSN: 03603199 (May 2019).

56. Üregen, N., Pehlivanoğlu, K., Özdemir, Y. & Devrim, Y. Development of polybenzimidazole/graphene oxide composite membranes for high temperature PEM fuel cells. *International Journal of Hydrogen Energy* **42,** 2636–2647. ISSN: 03603199 (Jan. 2017).

57. Ibrahim, Y. & Hilal, N. *A Critical Assessment of Surface-Patterned Membranes and Their Role in Advancing Membrane Technologies* Dec. 2023.

58. Debe, M. K., Schmoeckel, A. K., Vernstrom, G. D. & Atanasoski, R. High voltage stability of nanostructured thin film catalysts for PEM fuel cells. *Journal of Power Sources* **161,** 1002–1011. ISSN: 03787753 (Oct. 2006).

59. Debe, M. K. Effect of Electrode Surface Area Distribution on High Current Density Performance of PEM Fuel Cells. *Journal of The Electrochemical Society* **159,** B54. ISSN: 00134651 (Jan. 2012).

60. Sinha, P. K., Gu, W., Kongkanand, A. & Thompson, E. Performance of Nano Structured Thin Film (NSTF) Electrodes under Partially-Humidified Conditions. *Journal of The Electrochemical Society* **158,** B831. ISSN: 00134651 (July 2011).

61. Debe, M. K. Tutorial on the Fundamental Characteristics and Practical Properties of Nanostructured Thin Film (NSTF) Catalysts. *Journal of The Electrochemical Society* **160,** F522–F534. ISSN: 0013-4651 (2013).

62. Kim, S. M. *et al.* Prism-patterned Nafion membrane for enhanced water transport in polymer electrolyte membrane fuel cell. *Journal of Power Sources* **317,** 19–24. ISSN: 03787753 (2016).

63. Zhou, Z. *et al.* Molded, high surface area polymer electrolyte membranes from cured liquid precursors. *Journal of the American Chemical Society* **128,** 12963–12972. ISSN: 00027863 (2006).

64. Yildirim, M. H., te Braake, J., Aran, H. C., Stamatialis, D. F. & Wessling, M. Micro-patterned Nafion membranes for direct methanol fuel cell applications. *Journal of Membrane Science* **349,** 231–236. ISSN: 03767388 (Mar. 2010).

65. Jeon, Y. *et al.* Interface-designed Membranes with Shape-controlled Patterns for High-performance Polymer Electrolyte Membrane Fuel Cells. *Scientific reports* **5,** 16394. ISSN: 2045-2322 (Nov. 2015).

66. Kim, K. H. *et al.* The effects of Nafion® ionomer content in PEMFC MEAs prepared by a catalyst-coated membrane (CCM) spraying method. *International Journal of Hydrogen Energy* **35,** 2119–2126. ISSN: 03603199 (Mar. 2010).

67. Yu, H., Roller, J. M., Mustain, W. E. & Maric, R. Influence of the ionomer/carbon ratio for low-Pt loading catalyst layer prepared by reactive spray deposition technology. *Journal of Power Sources* **283,** 84–94. ISSN: 03787753 (June 2015).

68. Chaparro, A. M., Gallardo, B., Folgado, M. A., Martín, A. J. & Daza, L. PEMFC electrode preparation by electrospray: Optimization of catalyst load and ionomer content. *Catalysis Today* **143,** 237–241. ISSN: 09205861 (May 2009).

69. Jeon, S. *et al.* Effect of ionomer content and relative humidity on polymer electrolyte membrane fuel cell (PEMFC) performance of membrane-electrode assemblies (MEAs) prepared by decal transfer method. *International Journal of Hydrogen Energy* **35,** 9678–9686. ISSN: 03603199 (Sept. 2010).

70. Suzuki, A. *et al.* Ionomer content in the catalyst layer of polymer electrolyte membrane fuel cell (PEMFC): Effects on diffusion and performance. *International Journal of Hydrogen Energy* **36,** 2221–2229. ISSN: 03603199 (Feb. 2011).

71. El-Kharouf, A., Mason, T. J., Brett, D. J. & Pollet, B. G. *Ex-situ characterisation of gas diffusion layers for proton exchange membrane fuel cells* Nov. 2012.

72. El-kharouf, A. *UNDERSTANDING GDL PROPERTIES AND PERFORMANCE IN POLYMER University of Birmingham Research Archive* PhD thesis (2014).

73. Chu, H. S., Yeh, C. & Chen, F. Effects of porosity change of gas diffuser on performance of proton exchange membrane fuel cell. *Journal of Power Sources* **123,** 1–9. ISSN: 03787753 (Sept. 2003).

74. Nam, J. H., Lee, K. J., Hwang, G. S., Kim, C. J. & Kaviany, M. Microporous layer for water morphology control in PEMFC. *International Journal of Heat and Mass Transfer* **52,** 2779–2791. ISSN: 00179310 (May 2009).

75. Lim, C. & Wang, C. Y. Effects of hydrophobic polymer content in GDL on power performance of a PEM fuel cell. *Electrochimica Acta* **49,** 4149–4156. ISSN: 00134686 (Sept. 2004).

76. Shimpalee, S., Beuscher, U. & Van Zee, J. W. Analysis of GDL flooding effects on PEMFC performance. *Electrochimica Acta* **52,** 6748–6754. ISSN: 00134686 (Aug. 2007).

77. Soboleva, T., Malek, K., Xie, Z., Navessin, T. & Holdcroft, S. PEMFC catalyst layers: The role of micropores and mesopores on water sorption and fuel cell activity. *ACS Applied Materials and Interfaces* **3,** 1827–1837. ISSN: 19448244 (2011).

78. Mardle, P., Fernihough, O. & Du, S. Evaluation of the scaffolding effect of Pt nanowires supported on reduced graphene oxide in PEMFC electrodes. *Coatings* **8,** 48. ISSN: 20796412 (Jan. 2018).

79. Wang, X., Li, W., Chen, Z., Waje, M. & Yan, Y. Durability investigation of carbon nanotube as catalyst support for proton exchange membrane fuel cell. *Journal of Power Sources* **158,** 154–159. ISSN: 03787753 (July 2006).

80. Di Noto, V., Gliubizzi, R., Negro, E., Vittadello, M. & Pace, G. Hybrid inorganic-organic proton conducting membranes based on Nafion and 5 wt.% of MxOy (M = Ti, Zr, Hf, Ta and W). Part I. Synthesis, properties and vibrational studies. *Electrochimica Acta* **53,** 1618–1627. ISSN: 00134686 (Dec. 2007).

81. Di Noto, V. *et al.* Hybrid inorganic-organic proton conducting membranes based on Nafion and 5 wt% of MxOy (M = Ti, Zr, Hf, Ta and W). Part II: Relaxation phenomena and conductivity mechanism. *Journal of Power Sources* **187,** 57–66. ISSN: 03787753 (Feb. 2009).

82. Adjemian, K. T. *et al.* Function and characterization of metal oxide-nafion composite membranes for elevated-temperature H 2/O 2 PEM fuel cells. *Chemistry of Materials* **18,** 2238–2248. ISSN: 08974756 (May 2006).

83. Saccà, A., Gatto, I., Carbone, A., Pedicini, R. & Passalacqua, E. ZrO2-Nafion composite membranes for polymer electrolyte fuel cells (PEFCs) at intermediate temperature. *Journal of Power Sources* **163,** 47–51. ISSN: 03787753 (Dec. 2006).

84. Sahu, A. K., Selvarani, G., Pitchumani, S., Sridhar, P. & Shukla, A. K. A Sol-Gel Modified Alternative Nafion-Silica Composite Membrane for Polymer Electrolyte Fuel Cells. *Journal of The Electrochemical Society* **154,** B123. ISSN: 00134651 (Dec. 2007).

85. Griffin, A. *et al. Scalable methods for directional assembly of fillers in polymer composites: Creating pathways for improving material properties* Sept. 2022.

86. Costamagna, P., Yang, C., Bocarsly, A. B. & Srinivasan, S. Nafion® 115/zirconium phosphate composite membranes for operation of PEMFCs above 100 °C. *Electrochimica Acta* **47,** 1023–1033. ISSN: 00134686 (Jan. 2002).

87. Saccà, A. *et al.* Composites Nafion-titania membranes for Polymer Electrolyte Fuel Cell (PEFC) applications at low relative humidity levels: Chemical physical properties and electrochemical performance. *Polymer Testing* **56,** 10–18. ISSN: 01429418 (Dec. 2016).

88. Xu, G. *et al.* In-situ sulfonation of targeted silica-filled Nafion for high-temperature PEM fuel cell application. *International Journal of Hydrogen Energy* **44,** 29711–29716. ISSN: 03603199 (Nov. 2019).

89. Xu, G. *et al.* Non-destructive fabrication of Nafion/silica composite membrane via swelling-filling modification strategy for high temperature and low humidity PEM fuel cell. *Renewable Energy* **153,** 935–939. ISSN: 18790682 (June 2020).

90. Oh, K., Kwon, O., Son, B., Lee, D. H. & Shanmugam, S. Nafion-sulfonated silica composite membrane for proton exchange membrane fuel cells under operating low humidity condition. *Journal of Membrane Science* **583,** 103–109. ISSN: 18733123 (Aug. 2019).

91. Pineda-Delgado, J. L. *et al.* Synthesis and evaluation of HfO2 as a prospective filler in inorganic-organic hybrid membranes based on Nafion for PEM fuel cells. *Nanotechnology* **30,** 105707. ISSN: 13616528 (Jan. 2019).

92. He, D. *et al.* Engineered Graphene Materials: Synthesis and Applications for Polymer Electrolyte Membrane Fuel Cells. *Advanced Materials* **29,** 1601741. ISSN: 15214095 (May 2017).

93. Sahu, A. K. *et al.* Sulfonated Graphene-Nafion Composite Membranes for Polymer Electrolyte Fuel Cells Operating under Reduced Relative Humidity. *Journal of Physical Chemistry C* **120,** 15855–15866. ISSN: 19327455 (July 2016).

94. Lee, D. C., Yang, H. N., Park, S. H. & Kim, W. J. Nafion/graphene oxide composite membranes for low humidifying polymer electrolyte membrane fuel cell. *Journal of Membrane Science* **452,** 20–28. ISSN: 03767388 (Feb. 2014).

95. Lee, D. C., Yang, H. N., Park, S. H., Park, K. W. & Kim, W. J. Self-humidifying Pt-graphene/SiO2 composite membrane for polymer electrolyte membrane fuel cell. *Journal of Membrane Science* **474,** 254–262. ISSN: 18733123 (Jan. 2015).

96. Yang, H. N., Lee, W. H., Choi, B. S. & Kim, W. J. Preparation of Nafion/Pt-containing TiO2/graphene oxide composite membranes for self-humidifying proton exchange membrane fuel cell. *Journal of Membrane Science* **504,** 20–28. ISSN: 18733123 (Apr. 2016).

97. Ibrahim, A., Hossain, O., Chaggar, J., Steinberger-Wilckens, R. & El-Kharouf, A. GO-nafion composite membrane development for enabling intermediate temperature operation of polymer electrolyte fuel cell. *International Journal of Hydrogen Energy* **45,** 5526–5534. ISSN: 03603199 (Feb. 2020).

98. Kumar, P., Bharti, R. P., Kumar, V. & Kundu, P. P. in *Progress and Recent Trends in Microbial Fuel Cells* 47–72 (Elsevier, Jan. 2018). ISBN: 9780444640178.

99. Xue, C. *et al.* Graphite oxide/functionalized graphene oxide and polybenzimidazole composite membranes for high temperature proton exchange membrane fuel cells. *International Journal of Hydrogen Energy* **39,** 7931–7939. ISSN: 03603199 (May 2014).

100. Kannan, R. *et al.* Artificially designed membranes using phosphonated multiwall carbon nanotube-polybenzimidazole composites for polymer electrolyte fuel cells. *Journal of Physical Chemistry Letters* **1,** 2109–2113. ISSN: 19487185 (July 2010).

101. Cheddie, D. F. & Munroe, N. D. A two-phase model of an intermediate temperature PEM fuel cell. *International Journal of Hydrogen Energy* **32,** 832–841. ISSN: 03603199 (2007).

102. Bouchet, R., Miller, S., Duclot, M. & Souquet, J. L. *A thermodynamic approach to proton conductivity in acid-doped polybenzimidazole* in *Solid State Ionics* **145** (Elsevier, Dec. 2001), 69–78.

103. Razaq, M., Razaq, A., Yeager, E., DesMarteau, D. D. & Singh, S. Perfluorosulfonimide as an Additive in Phosphoric Acid Fuel Cell. *Journal of The Electrochemical Society* **136,** 385–390. ISSN: 0013-4651 (1989).

104. Mamlouk, M., Sousa, T. & Scott, K. A High Temperature Polymer Electrolyte Membrane Fuel Cell Model for Reformate Gas. *International Journal of Electrochemistry* **2011,** 1–18. ISSN: 2090-3537 (2011).

105. Scharifker, B. R., Zelenay, P. & Bockris, J. O. The Kinetics of Oxygen Reduction in Molten Phosphoric Acid at High Temperatures. *Journal of The Electrochemical Society* **134,** 2714–2725. ISSN: 0013-4651 (Nov. 1987).

106. Biyikoğlu, A. *Review of proton exchange membrane fuel cell models* Sept. 2005.

107. Zhou, Z. *et al.* Polybenzimidazole-based polymer electrolyte membranes for high-temperature fuel cells: Current status and prospects. *Energies* **14.** ISSN: 19961073 (2021).

108. Yin, B. *et al.* Construction of Stable Wide-Temperature-Range Proton Exchange Membranes by Incorporating a Carbonized Metal–Organic Frame into Polybenzimidazoles and Polyacrylamide Hydrogels. *Small,* 2103214. ISSN: 1613-6810 (Sept. 2021).

109. Lee, K. S., Spendelow, J. S., Choe, Y. K., Fujimoto, C. & Kim, Y. S. An operationally flexible fuel cell based on quaternary ammonium-biphosphate ion pairs. *Nature Energy* **1.** ISSN: 20587546 (2016).

110. Jang, S. *et al.* Prism patterned TiO2 layers/Nafion® composite membrane for elevated temperature/low relative humidity fuel cell operation. *Journal of Industrial and Engineering Chemistry* **90,** 327–332. ISSN: 22345957 (Oct. 2020).

111. Antolini, E. *Graphene as a new carbon support for low-temperature fuel cell catalysts* July 2012.

112. Kumar, R., Mamlouk, M. & Scott, K. Sulfonated polyether ether ketone-sulfonated graphene oxide composite membranes for polymer electrolyte fuel cells. *RSC Advances* **4,** 617–623. ISSN: 20462069 (Nov. 2014).

113. Song, C. *et al.* PEM fuel cell reaction kinetics in the temperature range of 23-120 °C. *Electrochimica Acta* **52,** 2552–2561. ISSN: 00134686 (2007).

114. Xu, H., Song, Y., Kunz, H. R. & Fenton, J. M. Effect of Elevated Temperature and Reduced Relative Humidity on ORR Kinetics for PEM Fuel Cells. *Journal of The Electrochemical Society* **152,** A1828. ISSN: 00134651 (July 2005).

115. Wakabayashi, N., Takeichi, M., Itagaki, M., Uchida, H. & Watanabe, M. Temperature-dependence of oxygen reduction activity at a platinum electrode in an acidic electrolyte solution investigated with a channel flow double electrode. *Journal of Electroanalytical Chemistry* **574,** 339–346. ISSN: 15726657 (Jan. 2005).

116. Holewinski, A. & Linic, S. Elementary Mechanisms in Electrocatalysis: Revisiting the ORR Tafel Slope. *Journal of The Electrochemical Society* **159,** H864–H870. ISSN: 0013-4651 (2012).

117. Xu, C. *et al.* A polybenzimidazole/sulfonated graphite oxide composite membrane for high temperature polymer electrolyte membrane fuel cells. *Journal of Materials Chemistry* **21,** 11359–11364. ISSN: 09599428 (July 2011).

118. Parthasarathy, A., Srinivasan, S., Appleby, A. J. & Martin, C. R. Pressure Dependence of the Oxygen Reduction Reaction at the Platinum Microelectrode/Nafion Interface: Electrode Kinetics and Mass Transport. *Journal of The Electrochemical Society* **139,** 2856–2862. ISSN: 0013-4651 (Oct. 1992).

119. Li, Q., He, R., Gao, J.-A., Jensen, J. O. & Bjerrum, N. J. The CO Poisoning Effect in PEMFCs Operational at Temperatures up to 200°C. *Journal of The Electrochemical Society* **150,** A1599. ISSN: 00134651 (2003).

120. Dhar, H. P., Christner, L. G. & Kush, A. K. Nature of CO Adsorption during H 2 Oxidation in Relation to Modeling for CO Poisoning of a Fuel Cell Anode. *Journal of The Electrochemical Society* **134,** 3021–3026. ISSN: 0013-4651 (Dec. 1987).

121. Han, P. & Bartels, D. M. Temperature dependence of oxygen diffusion in H2O and D2O. *Journal of Physical Chemistry* **100,** 5597–5602. ISSN: 00223654 (Mar. 1996).

122. Yakovlev, Y. V. *et al.* Ionomer content effect on charge and gas transport in the cathode catalyst layer of proton-exchange membrane fuel cells. *Journal of Power Sources* **490,** 229531. ISSN: 0378-7753 (Apr. 2021).

123. Ji, M. & Wei, Z. *A review of water management in polymer electrolyte membrane fuel cells* Nov. 2009.

124. Ge, S. & Wang, C.-Y. Liquid Water Formation and Transport in the PEFC Anode. *Journal of The Electrochemical Society* **154,** B998. ISSN: 00134651 (July 2007).

125. Li, H. *et al. A review of water flooding issues in the proton exchange membrane fuel cell* 2008.

126. Li, A., Chan, S. H. & Nguyen, N. t. Anti-flooding cathode catalyst layer for high performance PEM fuel cell. *Electrochemistry Communications* **11,** 897–900. ISSN: 13882481 (2009).

127. Hickner, M. A., Fujimoto, C. H. & Cornelius, C. J. Transport in sulfonated poly(phenylene)s: Proton conductivity, permeability, and the state of water. *Polymer* **47,** 4238–4244. ISSN: 00323861 (2006).

128. Knights, S. D., Colbow, K. M., St-Pierre, J. & Wilkinson, D. P. *Aging mechanisms and lifetime of PEFC and DMFC* in *Journal of Power Sources* **127** (2004), 127–134.

129. De Beer, C., Barendse, P. S., Pillay, P., Bullecks, B. & Rengaswamy, R. Classification of high-temperature PEM fuel cell degradation mechanisms using equivalent circuits. *IEEE Transactions on Industrial Electronics* **62,** 5265–5274. ISSN: 02780046 (Aug. 2015).

130. Yan, W. M., Chen, C. Y. & Liang, C. H. Comparison of performance degradation of high temperature PEM fuel cells with different bipolar plates. *Energy* **186,** 115836. ISSN: 03605442 (Nov. 2019).

131. Hartnig, C. & Schmidt, T. J. On a new degradation mode for high-temperature polymer electrolyte fuel cells: How bipolar plate degradation affects cell performance. *Electrochimica Acta* **56,** 4237–4242. ISSN: 00134686 (Apr. 2011).

132. LaConti, A. B., Hamdan, M. & McDonald, R. C. in *Handbook of Fuel Cells* (2010). ISBN: 0471499269.

133. Calleja, G., Jourdan, A., Ameduri, B. & Habas, J. P. *Where is the glass transition temperature of poly(tetrafluoroethylene)? A new approach by dynamic rheometry and mechanical tests* in *European Polymer Journal* **49** (Pergamon, Aug. 2013), 2214–2222.

134. Osborn, S. J. *et al.* Glass transition temperature of perfluorosulfonic acid ionomers. *Macromolecules* **40,** 3886–3890. ISSN: 00249297 (May 2007).

135. Paddison, S. J. Proton conduction in PEMs: Complexity, cooperativity and connectivity. *Topics in Applied Physics* **113,** 385–412. ISSN: 03034216 (2009).

136. Kornyshev, A. A. & Spohr, E. *Proton transport in polymer electrolyte membranes using theory and classical molecular dynamics* 2009.

137. Elliott, J. A. *Atomistic structural modelling of ionomer membrane morphology* 2009.

138. Kreuer, K. D. *On solids with liquidlike properties and the challenge to develop new proton-conducting separator materials for intermediate-temperature fuel cells* 2002.

139. Li, Q., He, R., Jensen, J. O. J. & Bjerrum, N. J. N. Approaches and Recent Development of Polymer Electrolyte Membranes for Fuel Cells Operating above 100 °C. *Chemistry of materials* **15,** 4896–4915. ISSN: 08974756 (Dec. 2003).

140. Deluca, N. W. & Elabd, Y. A. *Polymer electrolyte membranes for the direct methanol fuel cell: A review* Aug. 2006.

141. Gebel, G. & Diat, O. *Neutron and X-ray scattering: Suitable tools for studying lonomer membranes* Apr. 2005.

142. Elliott, J. A., Hanna, S., Elliott, A. M. & Cooley, G. E. Atomistic simulation and molecular dynamics of model systems for perfluorinated ionomer membranes. *Physical Chemistry Chemical Physics* **1,** 4855–4863. ISSN: 14639076 (Jan. 1999).

143. Paddison, S. J. The modeling of molecular structure and ion transport in sulfonic acid based ionomer membranes. *Journal of New Materials for Electrochemical Systems* **4,** 197–207. ISSN: 14802422 (2001).

144. Ismail, M. S., Ingham, D. B., Ma, L., Hughes, K. J. & Pourkashanian, M. Effects of catalyst agglomerate shape in polymer electrolyte fuel cells investigated by a multi-scale modelling framework. *Energy* **122,** 420–430. ISSN: 03605442 (Mar. 2017).

145. Hwang, S. S., Lee, P. H. & Han, S. S. Three-dimensional transport modeling for Proton Exchange Membrane(PEM) fuel cell with micro parallel flow field. *Sensors* **8,** 1475–1487. ISSN: 14248220 (2008).

146. Nam, J. H. & Kaviany, M. Effective diffusivity and water-saturation distribution in single- and two-layer PEMFC diffusion medium. *International Journal of Heat and Mass Transfer* **46,** 4595–4611. ISSN: 00179310 (2003).

147. Ismail, M. S., Ingham, D. B., Hughes, K. J., Ma, L. & Pourkashanian, M. Effective diffusivity of polymer electrolyte fuel cell gas diffusion layers: An overview and numerical study. *International Journal of Hydrogen Energy* **40,** 10994–11010. ISSN: 03603199 (July 2015).

148. Elliott, J. A. & Hanna, S. A model-independent maximum-entropy method for the inversion of small-angle X-ray diffraction patterns. *Journal of Applied Crystallography* **32,** 1069–1083. ISSN: 00218898 (Dec. 1999).

149. Din, X. D. & Michaelides, E. E. Transport Processes of Water and Protons through Micropores. *AIChE Journal* **44,** 35–47. ISSN: 00011541 (Jan. 1998).

150. Dyakov, Y. A. & Tovbin, Y. K. Molecular dynamics study of the cations, water molecules, and polymer chains in Nafion type membranes. *Russian Chemical Bulletin* **44,** 1186–1189. ISSN: 15739171 (1995).

151. Paddison, S. J. & Zawodzinski, T. A. Molecular modeling of the pendant chain in Nafion®. *Solid State Ionics* **113-115,** 333–340. ISSN: 01672738 (Dec. 1998).

152. Paddison, S. J. & Elliott, J. A. On the consequences of side chain flexibility and backbone conformation on hydration and proton dissociation in perfluorosulfonic acid membranes. *Physical Chemistry Chemical Physics* **8,** 2193–2203. ISSN: 14639076 (May 2006).

153. Urata, S. *et al.* Intermolecular interaction between the pendant chain of perfluorinated ionomer and water. *Physical Chemistry Chemical Physics* **6,** 3325–3332. ISSN: 14639076 (July 2004).

154. Cui, S. T., Siepmann, J. I., Cochran, H. D. & Cummings, P. T. Intermolecular potentials and vapor-liquid phase equilibria of perfluorinated alkanes. *Fluid Phase Equilibria* **146,** 51–61. ISSN: 03783812 (May 1998).

155. Urata, S. *et al.* Molecular dynamics simulation of swollen membrane of perfluorinated ionomer. *Journal of Physical Chemistry B* **109,** 4269–4278. ISSN: 15206106 (2005).

156. Vishnyakov, A. & Neimark, A. V. Molecular Simulation Study of Nafion Membrane Solvation in Water and Methanol. *Journal of Physical Chemistry B* **104,** 4471–4478. ISSN: 15206106 (May 2000).

157. Vishnyakov, A. & Neimark, A. V. Molecular dynamics simulation of microstructure and molecular mobilities in swollen nation membranes. *Journal of Physical Chemistry B* **105,** 9586–9594. ISSN: 10895647 (Oct. 2001).

158. Cormanich, R. A., O'Hagan, D. & Bühl, M. Hyperconjugation Is the Source of Helicity in Perfluorinated n-Alkanes. *Angewandte Chemie - International Edition* **56,** 7867–7870. ISSN: 15213773 (July 2017).

159. Holt, D. B. & Farmer, B. L. *Modeling of helix reversal defects in polytetrafluoroethylene: I. Force field development and molecular mechanics calculations* in *Polymer* **40** (Elsevier, July 1999), 4667–4672.

160. Holt, D. B., Farmer, B. L., Macturk, K. S. & Eby, R. K. Fluoropolymer force fields derived from semiempirical molecular orbital calculations. *Polymer* **37,** 1847–1855. ISSN: 00323861 (May 1996).

161. Zawodzinski, T. A., Davey, J., Valerio, J. & Gottesfeld, S. The water content dependence of electro-osmotic drag in proton-conducting polymer electrolytes. *Electrochimica Acta* **40,** 297–302. ISSN: 00134686 (Feb. 1995).

162. Lefebvre, M. C., Martin, R. B. & Pickup, P. G. Characterization of Ionic Conductivity Profiles within Proton Exchange Membrane Fuel Cell Gas Diffusion Electrodes by Impedance Spectroscopy. *Electrochemical and Solid-State Letters* **2,** 259. ISSN: 10990062 (June 1999).

163. Elliott, J. A. & Paddison, S. J. Modelling of morphology and proton transport in PFSA membranes. *Physical Chemistry Chemical Physics* **9,** 2602–2618. ISSN: 14639076. arXiv: 0402594v3 [cond-mat] (2007).

164. Costamagna, P., Grosso, S. & Di Felice, R. Percolative model of proton conductivity of Nafion® membranes. *Journal of Power Sources* **178,** 537–546. ISSN: 03787753 (Apr. 2008).

165. Spohr, E. *Molecular dynamics simulations of Proton transfer in a model nafion pore* in *Molecular Simulation* **30** (2004), 107–115. ISBN: 0892702301000.

166. Wöhr, M. *et al.* Dynamic modelling and simulation of a polymer membrane fuel cell including mass transport limitation. *International Journal of Hydrogen Energy* **23,** 213–218. ISSN: 0360-3199 (Mar. 1998).

167. Yi, J. S. An Along-the-Channel Model for Proton Exchange Membrane Fuel Cells. *Journal of The Electrochemical Society* **145,** 1149. ISSN: 00134651 (1998).

168. Huang, J., Li, Z. & Zhang, J. *Review of characterization and modeling of polymer electrolyte fuel cell catalyst layer: The blessing and curse of ionomer* 2017.

169. Kone, J. P., Zhang, X., Yan, Y., Hu, G. & Ahmadi, G. Three-dimensional multiphase flow computational fluid dynamics models for proton exchange membrane fuel cell: A theoretical development. *Journal of Computational Multiphase Flows* **9,** 3–25. ISSN: 17574838 (2017).

170. Springer, T. E., Wilson, M. S. & Gottesfeld, S. Modeling and Experimental Diagnostics in Polymer Electrolyte Fuel Cells. *Journal of The Electrochemical Society* **140,** 3513–3526. ISSN: 0013-4651 (Dec. 1993).

171. Enderby, J. A. Water absorption by polymers. *Transactions of the Faraday Society* **51,** 106–116. ISSN: 00147672 (1955).

172. Wadsö, L. & Jannasch, P. Water vapor sorption thermodynamics of the nafion ionomer membrane. *Journal of Physical Chemistry B* **117,** 8561–8570. ISSN: 15205207 (July 2013).

173. Kocherbitov, V. Salt-saturated salt solution as a standard system for sorption calorimetry. *Thermochimica Acta* **421,** 105–110. ISSN: 00406031 (Nov. 2004).

174. ToolBox, E. Properties of Saturated Steam - Pressure in Bar. *Engineering ToolBox,* 5–9 (2015).

175. Von Schroeder, P. Z. Über Erstarrungs- und Quellungserscheinungen von Gelatine. *Phys. Chem.* **45,** 75 (1903).

176. Legras, M., Hirata, Y., Nguyen, Q. T., Langevin, D. & Métayer, M. Sorption and diffusion behaviors of water in Nafion 117 membranes with different counter ions. *Desalination* **147,** 351–357. ISSN: 00119164 (Sept. 2002).

177. Pushpa, K. K., Nandan, D. & Iyer, R. M. Thermodynamics of water sorption by perfluorosulphonate (Nafion-117) and polystyrene-divinylbenzene sulphonate (Dowex 50W) ion-exchange resins at 298 ± 1 K. *Journal of the Chemical Society, Faraday Transactions 1: Physical Chemistry in Condensed Phases* **84,** 2047–2056. ISSN: 03009599 (Jan. 1988).

178. Broka, K. & Ekdunge, P. Modelling the PEM fuel cell cathode. *Journal of Applied Electrochemistry* **27,** 281–289. ISSN: 0021891X (1997).

179. Hinatsu, J. T., Mizuhata, M. & Takenaka, H. Water Uptake of Perfluorosulfonic Acid Membranes from Liquid Water and Water Vapor. *Journal of The Electrochemical Society* **141,** 1493–1498. ISSN: 0013-4651 (June 1994).

180. Pasaogullari, U., Wang, C.-Y. & Chen, K. S. Two-Phase Transport in Polymer Electrolyte Fuel Cells with Bilayer Cathode Gas Diffusion Media. *Journal of The Electrochemical Society* **152,** A1574. ISSN: 00134651 (July 2005).

181. Kulikovsky, A. A. Quasi-3D Modeling of Water Transport in Polymer Electrolyte Fuel Cells. *Journal of The Electrochemical Society* **150,** A1432. ISSN: 00134651 (Sept. 2003).

182. Karpenko-Jereb, L. *et al.* A novel membrane transport model for polymer electrolyte fuel cell simulations. *International Journal of Hydrogen Energy* **39,** 7077–7088. ISSN: 03603199 (Apr. 2014).

183. Jeck, S., Scharfer, P. & Kind, M. Absence of Schroeder's paradox: Experimental evidence for water-swollen Nafion® membranes. *Journal of Membrane Science* **373,** 74–79. ISSN: 03767388 (May 2011).

184. Schneider, N. S. & Rivin, D. Steady state analysis of water vapor transport in ionomers. *Polymer* **51,** 671–678. ISSN: 00323861 (Feb. 2010).

185. Onishi, L. M., Prausnitz, J. M. & Newman, J. Water-nafion equilibria. Absence of schroeder's paradox. *Journal of Physical Chemistry B* **111,** 10166–10173. ISSN: 15206106 (Aug. 2007).

186. Yuan, X., Wang, H., Colin Sun, J. & Zhang, J. *AC impedance technique in PEM fuel cell diagnosis-A review* Dec. 2007.

187. Chen, L., Chen, Y. & Tao, W. Q. Schroeder's paradox in proton exchange membrane fuel cells: A review. *Renewable and Sustainable Energy Reviews* **173,** 113050. ISSN: 18790690 (Mar. 2023).

188. Springer, T. E. Polymer Electrolyte Fuel Cell Model. *Journal of The Electrochemical Society* **138,** 2334. ISSN: 00134651 (1991).

189. Yeo, S. C. & Eisenberg, A. Physical properties and supermolecular structure of perfluorinated ion-containing (nafion) polymers. *Journal of Applied Polymer Science* **21,** 875–898. ISSN: 10974628 (Apr. 1977).

190. Meier, F. & Eigenberger, G. Transport parameters for the modelling of water transport in ionomer membranes for PEM-fuel cells. *Electrochimica Acta* **49,** 1731–1742. ISSN: 00134686 (Apr. 2004).

191. Kusoglu, A. *et al.* Constitutive response and mechanical properties of PFSA membranes in liquid water. *Journal of Power Sources* **195,** 483–492. ISSN: 03787753 (2010).

192. Mittelsteadt, C. K. & Liu, H. in *Handbook of Fuel Cells* (2010).

193. Weber, A. Z. & Newman, J. Modeling transport in polymer-electrolyte fuel cells. *Chemical Reviews* **104,** 4679–4726. ISSN: 00092665 (2004).

194. Ramousse, J., Deseure, J., Lottin, O., Didierjean, S. & Maillet, D. Modelling of heat, mass and charge transfer in a PEMFC single cell. *Journal of Power Sources* **145,** 416–427. ISSN: 03787753 (Aug. 2005).

195. Dobson, P., Lei, C., Navessin, T. & Secanell, M. Characterization of the PEM Fuel Cell Catalyst Layer Microstructure by Nonlinear Least-Squares Parameter Estimation. *Journal of The Electrochemical Society* **159,** B514–B523. ISSN: 0013-4651 (2012).

196. Wiezell, K., Gode, P. & Lindbergh, G. Steady-State and EIS Investigations of Hydrogen Electrodes and Membranes in Polymer Electrolyte Fuel Cells. *Journal of The Electrochemical Society* **153,** A759. ISSN: 00134651 (Feb. 2006).

197. Neubrand, W. in, 479–479 (Stuttgart, 1999). ISBN: 3-89722-216-7.

198. Cheng, X. *et al.* Hydrogen crossover in high-temperature PEM fuel cells. *Journal of Power Sources* **167,** 25–31. ISSN: 03787753 (May 2007).

199. Romano, J. M., Garcia-Giron, A., Penchev, P. & Dimov, S. Triangular laser-induced submicron textures for functionalising stainless steel surfaces. *Applied Surface Science* **440,** 162–169. ISSN: 01694332 (May 2018).

200. Ding, X., Fuller, T. F. & Harris, T. A. L. Effects of annealing conditions on the performance of solution cast Nafion membranes. *ECS Trans.* **41,** 1537–1544 (2011).

201. Branco, C. M. *Multilayer Membranes for Intermediate Temperature Polymer Electrolyte Fuel Cells* PhD thesis (University of Birmingham, 2017).

202. Fisher, S. & Kunin, R. Routine Exchange Capacity Determinations of Ion Exchange Resins. *Analytical Chemistry* **27,** 1191–1194. ISSN: 15206882 (1955).

203. Tsotridis, G., Pilenga, A., Marco, G. D. & Malkow, T. *EU Harmonised Test Protocols for PEMFC MEA Testing in Single Cell Configuration for Automotive Applications; JRC Science for Policy report* EUR 27632 EN, doi 10.2790/54653. ISBN: 978-92-79-54132-2 (2015).

204. Edwards, R. L. & Demuren, A. Regression analysis of PEM fuel cell transient response. *International Journal of Energy and Environmental Engineering* **7,** 329–341. ISSN: 22516832 (Sept. 2016).

205. Carter, R. N., Kocha, S. S., Wagner, F., Fay, M. & Gasteiger, H. A. Artifacts in Measuring Electrode Catalyst Area of Fuel Cells through Cyclic Voltammetry. *ECS Transactions* **11,** 403–410. ISSN: 1938-6737 (Dec. 2019).

206. Garrick, T. R., Moylan, T. E., Carpenter, M. K. & Kongkanand, A. Editors' Choice—Electrochemical Active Surface Area Measurement of Aged Pt Alloy Catalysts in PEM Fuel Cells by CO Stripping. *Journal of The Electrochemical Society* **164,** F55–F59. ISSN: 0013-4651 (Dec. 2017).

207. Kinoshita, K. & Stonehart, P. PREPARATION AND CHARACTERIZATION OF HIGHLY DISPERSED ELECTROCATALYTIC MATERIALS. *Mod Aspects Electrochem,* 183–267 (1977).

208. Yuan, X. Z., Song, C., Wang, H. & Zhang, J. *Electrochemical impedance spectroscopy in PEM fuel cells: Fundamentals and applications* 1–420. ISBN: 9781848828452 (2010).

209. Soboleva, T. *et al.* Investigation of the through-plane impedance technique for evaluation of anisotropy of proton conducting polymer membranes. *Journal of Electroanalytical Chemistry* **622,** 145–152. ISSN: 15726657 (Oct. 2008).

210. Saab, A. P., Garzon, F. H. & Zawodzinski, T. A. Determination of Ionic and Electronic Resistivities in Carbon/Polyelectrolyte Fuel-Cell Composite Electrodes. *Journal of The Electrochemical Society* **149,** A1541. ISSN: 00134651 (Oct. 2002).

211. Ren, X. & Pickup, P. G. Simulation and analysis of the impedance behaviour of electroactive layers with non-uniform conductivity and capacitance profiles. *Electrochimica Acta* **46,** 4177–4183. ISSN: 00134686 (Aug. 2001).

212. Feliu, S. *Electrochemical impedance spectroscopy for the measurement of the corrosion rate of magnesium alloys: Brief review and challenges* June 2020.

213. Ismail, M. S., Ingham, D. B., Hughes, K. J., Ma, L. & Pourkashanian, M. An efficient mathematical model for air-breathing PEM fuel cells. *Applied Energy* **135,** 490–503. ISSN: 03062619 (Dec. 2014).

214. Berning, T., Lu, D. M. & Djilali, N. *Three-dimensional computational analysis of transport phenomena in a PEM fuel cell* in *Journal of Power Sources* **106** (Elsevier, Apr. 2002), 284–294.

215. Cooper, K. Characterizing Through-Plane and In-Plane Ionic Conductivity of Polymer Electrolyte Membranes. *ECS Transactions* **41,** 1371–1380. ISSN: 1938-6737 (2011).

216. Baharlou-Houreh, N., Masaeli, N., Afshari, E. & Mohammadzadeh, K. Performance analysis of a proton exchange membrane fuel cell with the stair arrangement of obstacles in the cathode channel. *International Journal of Numerical Methods for Heat and Fluid Flow* **33,** 3940–3966. ISSN: 09615539 (Nov. 2023).

217. Sutida Marthosa. *Improvement of Electrocatalyst Performance in Hydrogen Fuel Cells by Multiscale Modelling — The University of Manchester* PhD thesis (University of Manchester, Manchester, 2012).

218. Xing, L. *et al.* A two-phase flow and non-isothermal agglomerate model for a proton exchange membrane (PEM) fuel cell. *Energy* **73,** 618–634. ISSN: 03605442 (Aug. 2014).

219. Bernardi, D. M. & Verbrugge, M. W. A Mathematical Model of the Solid-Polymer-Electrolyte Fuel Cell. *Journal of The Electrochemical Society* **139,** 2477–2491. ISSN: 0013-4651 (Sept. 1992).

220. Sun, W., Peppley, B. A. & Karan, K. An improved two-dimensional agglomerate cathode model to study the influence of catalyst layer structural parameters. *Electrochimica Acta* **50,** 3359–3374. ISSN: 00134686 (May 2005).

221. Kamaraj, A. B., Shaw, V. & Sundaram, M. M. *Novel Fabrication of Un-coated Super-hydrophobic Aluminum via Pulsed Electrochemical Surface Modification* in *Procedia Manufacturing* **1** (Elsevier B.V., 2015), 892–903.

222. Bae, J. W., Cho, Y. H., Sung, Y. E., Shin, K. & Jho, J. Y. Performance enhancement of polymer electrolyte membrane fuel cell by employing line-patterned Nafion membrane. *Journal of Industrial and Engineering Chemistry* **18,** 876–879. ISSN: 1226086X (May 2012).

223. Le Canut, J.-M., Abouatallah, R. M. & Harrington, D. A. Detection of Membrane Drying, Fuel Cell Flooding, and Anode Catalyst Poisoning on PEMFC Stacks by Electrochemical Impedance Spectroscopy. *Journal of The Electrochemical Society* **153,** A857. ISSN: 00134651 (Mar. 2006).

224. Zhou, Y., Lin, G., Shih, A. J. & Hu, S. J. Assembly pressure and membrane swelling in PEM fuel cells. *Journal of Power Sources* **192,** 544–551. ISSN: 03787753 (July 2009).

225. Kongkanand, A., Dioguardi, M., Ji, C. & Thompson, E. L. Improving Operational Robustness of NSTF Electrodes in PEM Fuel Cells. *Journal of The Electrochemical Society* **159,** F405–F411. ISSN: 0013-4651 (July 2012).

226. Baik, K. D., Hong, B. K. & Kim, M. S. Effects of operating parameters on hydrogen crossover rate through Nafion® membranes in polymer electrolyte membrane fuel cells. *Renewable Energy* **57,** 234–239. ISSN: 09601481 (Sept. 2013).

227. Pei, P. *et al.* Improved methods to measure hydrogen crossover current in proton exchange membrane fuel cell. *Applied Energy* **215,** 338–347. ISSN: 03062619 (Apr. 2018).

228. Marković, N. M., Sarraf, S. T., Gasteiger, H. A. & Ross, P. N. Hydrogen electrochemistry on platinum low-index single-crystal surfaces in alkaline solution. *Journal of the Chemical Society - Faraday Transactions* **92,** 3719–3725. ISSN: 09565000 (1996).

229. Brodt, M., Wycisk, R. & Pintauro, P. N. Nanofiber Electrodes with Low Platinum Loading for High Power Hydrogen/Air PEM Fuel Cells. *Journal of the Electrochemical Society* **160,** F744–F749. ISSN: 0013-4651 (2013).

230. Green, C. L. & Kucernak, A. Determination of the platinum and ruthenium surface areas in platinum-ruthenium electrocatalysts by underpotential deposition of copper. 2: Effect of surface composition on activity. *Journal of Physical Chemistry B* **106,** 11446–11456. ISSN: 10895647 (2002).

231. Xia, Z., Wang, Q., Eikerling, M. & Liu, Z. Effectiveness factor of Pt utilization in cathode catalyst layer of polymer electrolyte fuel cells. *Canadian Journal of Chemistry* **86,** 657–667. ISSN: 0008-4042 (2008).

232. Marinova, T. S. & Chakarov, D. V. Coadsorption of carbon monoxide and hydrogen on iridium single crystals. *Surface Science* **217,** 65–77. ISSN: 00396028 (July 1989).

233. Zhang, H. & Shen, P. K. *Recent development of polymer electrolyte membranes for fuel cells* 2012.

234. Abdul Rasheed, R. K., Liao, Q., Caizhi, Z. & Chan, S. H. *A review on modelling of high temperature proton exchange membrane fuel cells (HT-PEMFCs)* Feb. 2017.

235. Liu, Y.-H., Yi, B., Shao, Z.-G., Xing, D. & Zhang, H. Carbon nanotubes reinforced nafion composite membrane for fuel cell applications. *Electrochemical and Solid-State Letters* **9,** A356–A359 (2006).

236. Shi, S., Weber, A. Z. & Kusoglu, A. Structure/property relationship of Nafion XL composite membranes. *Journal of Membrane Science* **516,** 123–134. ISSN: 18733123 (Oct. 2016).

237. Rui, Z. & Liu, J. *Understanding of free radical scavengers used in highly durable proton exchange membranes* Dec. 2020.

238. Pollet, B. G., Kocha, S. S. & Staffell, I. Current status of automotive fuel cells for sustainable transport. *Current Opinion in Electrochemistry* **16,** 90–95. ISSN: 24519111 (Aug. 2019).

239. Sato, H., Uematsu, M., Watanabe, K., Saul, A. & Wagner, W. New International Skeleton Tables for the Thermodynamic Properties of Ordinary Water Substance. *Journal of Physical and Chemical Reference Data* **17,** 1439–1540. ISSN: 15297845 (Dec. 1988).

240. Vielstich, W., Gasteiger, H. & H. Yokokawa Eds. *Handbook of Fuel Cells: Advances in Electrocatalysis, Material, Diagnostics and Durability* (eds Vielstich,

W., Gasteiger, H. & H. Yokokawa Eds.) 1090 pages. ISBN: 978-0-471-49926-8 (Wiley, 2009).

241. Easton, E. B. & Pickup, P. G. An electrochemical impedance spectroscopy study of fuel cell electrodes. *Electrochimica Acta* **50,** 2469–2474. ISSN: 00134686 (Apr. 2005).

242. Li, G. & Pickup, P. G. Ionic Conductivity of PEMFC Electrodes. *Journal of The Electrochemical Society* **150,** C745. ISSN: 00134651 (2003).

243. Faulkner, A. J. B. L. R. *Fundamentals and Applications* **1,** 117–157. ISBN: 0471043729 (2000).

244. Moseley, P. Fuel Cell Systems Explained. *Journal of Power Sources* **93,** 285. ISSN: 03787753 (2001).

245. Alberti, G. *et al.* Novel Nafion-zirconium phosphate nanocomposite membranes with enhanced stability of proton conductivity at medium temperature and high relative humidity. *Electrochimica Acta* **52,** 8125–8132. ISSN: 00134686 (Nov. 2007).

246. Wan, Z., Chang, H., Shu, S., Wang, Y. & Tang, H. A review on cold start of proton exchange membrane fuel cells. *Energies* **7,** 3179–3203. ISSN: 19961073 (2014).

247. Enotiadis, A., Angjeli, K., Baldino, N., Nicotera, I. & Gournis, D. Graphene-based nafion nanocomposite membranes: Enhanced proton transport and water retention by novel organo-functionalized graphene oxide nanosheets. *Small* **8,** 3338–3349. ISSN: 16136810 (Nov. 2012).

248. Wang, Z., Nelson, J. K., Hillborg, H., Zhao, S. & Schadler, L. S. Graphene oxide filled nanocomposite with novel electrical and dielectric properties. *Advanced Materials* **24,** 3134–3137. ISSN: 09359648 (June 2012).

249. Chai, G. L., Shevlin, S. A. & Guo, Z. Nitrogen-mediated graphene oxide enables highly efficient proton transfer. *Scientific Reports* **7,** 5213. ISSN: 20452322 (Dec. 2017).

250. Ashby, M. F. in *Materials Selection in Mechanical Design* 299–340 (Butterworth-Heinemann, Jan. 2011). ISBN: 978-1-85617-663-7.

251. Srinivasababu, N. in *Failure Analysis in Biocomposites, Fibre-Reinforced Composites and Hybrid Composites* 109–131 (Woodhead Publishing, Jan. 2018). ISBN: 9780081022931.

252. Wu, Z. F. *et al.* Proton and molecular permeation through the basal plane of monolayer graphene oxide. *Nature Communications 2023 14:1* **14,** 1–8. ISSN: 2041-1723 (Nov. 2023).

253. Fernihough, O. *et al.* Patterned Membranes for Proton Exchange Membrane Fuel Cells Working at Low Humidity. *Polymers* **13,** 1976. ISSN: 2073-4360 (June 2021).

254. Fernihough, O., Ismail, M. S. & El-kharouf, A. Intermediate Temperature PEFC's with Nafion® 211 Membrane Electrolytes: An Experimental and Numerical Study. *Membranes* **12,** 430. ISSN: 2077-0375 (Apr. 2022).